



Quorum Quenching as a tool for biofouling control in membrane bioreactors: hydrodynamics, mass transfer, and impact on filtration

Naila Bouayed

► To cite this version:

Naila Bouayed. Quorum Quenching as a tool for biofouling control in membrane bioreactors: hydrodynamics, mass transfer, and impact on filtration. Chemical and Process Engineering. INSA de Toulouse, 2018. English. NNT : 2018ISAT0052 . tel-03625311

HAL Id: tel-03625311

<https://theses.hal.science/tel-03625311>

Submitted on 30 Mar 2022

HAL is a multi-disciplinary open access archive for the deposit and dissemination of scientific research documents, whether they are published or not. The documents may come from teaching and research institutions in France or abroad, or from public or private research centers.

L'archive ouverte pluridisciplinaire **HAL**, est destinée au dépôt et à la diffusion de documents scientifiques de niveau recherche, publiés ou non, émanant des établissements d'enseignement et de recherche français ou étrangers, des laboratoires publics ou privés.



THÈSE

En vue de l'obtention du

DOCTORAT DE L'UNIVERSITÉ DE TOULOUSE

Institut National des Sciences Appliquées de Toulouse (INSA Toulouse)

Présentée par :

Naila BOUAYED

Le vendredi 09 novembre 2018

**Quorum Quenching as a tool for biofouling control in membrane bioreactors:
hydrodynamics, mass transfer, and impact on filtration**

École doctorale et discipline ou spécialité

ED MEGEP : Génie des Procédés et Environnement

Unité de recherche

Laboratoire d'Ingénierie des Systèmes Biologiques et des Procédés (LISBP)

Directrice(s) ou Directeur(s) de Thèse

Pr. Christelle Guigui – Directrice de thèse

Dr. Christine Lafforgue-Baldas – Co-directrice de thèse

Dr. Nicolas Dietrich – Co-directeur de thèse

Jury

Pr. Christelle Wisniewski – Université Montpellier 1 - Rapporteur

Pr. José António Teixeira – Université de Minho (Braga, Portugal) - Rapporteur

Pr. Chung-Hak Lee – Université Nationale de Séoul (Corée du Sud) - Examineur

Dr. Anthony Massé – Université de Nantes - Examineur

Pr. Corinne Cabassud – INSA Toulouse - Examinatrice

Dr. Mathias Monnot – Université d'Aix-Marseille - Examineur

REMERCIEMENTS

Ces quelques mots sont pour moi l'occasion d'exprimer ma reconnaissance envers toutes les personnes qui ont contribué, de près ou de loin, à l'aboutissement de ce travail de longue haleine.

Ce travail de thèse a été réalisé au LISBP de l'INSA Toulouse, et je remercie à ce titre Nic Lindley, Carole Jouve Molina, Christelle Guigui et Arnaud Cockx, de m'avoir accueillie dans leur laboratoire et leurs équipes de recherche SOPHYE et TIM, respectivement, en m'offrant un cadre et des conditions de travail agréables.

Je remercie mes encadrants, Christelle Guigui, Christine Lafforgue-Baldas et Nicolas Dietrich, tout d'abord pour la confiance qu'ils m'ont accordée en me choisissant pour ce sujet de thèse passionnant et enrichissant et grâce auquel j'ai eu la grande chance de voyager et d'apprendre énormément. Je les remercie également pour leur accompagnement et leurs conseils durant ces 4 années mouvementées. Ma profonde gratitude revient particulièrement à Christine pour avoir toujours été à mon écoute et pour avoir toujours répondu présente pour m'apporter son aide.

Ce sujet de thèse s'est effectué en collaboration avec l'Université Nationale de Séoul, avec la participation du Professeur Chung-Hak Lee, que je tiens à remercier pour les nombreux encouragements qu'il m'a témoignés, ainsi que pour l'excellent accueil qu'il m'a réservé, avec ses étudiants, au sein de son laboratoire. Je le remercie aussi de m'avoir fait le grand honneur de prendre part à l'évaluation de mon travail et d'avoir fait le déplacement pour ma soutenance de thèse.

Un grand merci aux membres de mon jury de soutenance qui ont accepté de juger mon travail et pour les retours constructifs qu'ils m'ont faits. Je remercie le Professeur Christelle Wisniewski et le Professeur José Antonio Teixeira d'avoir pris le temps de rapporter mon travail. Je leur exprime également ma gratitude, ainsi qu'aux autres membres, Anthony Massé, Corinne Cabassud, et Mathias Monnot, pour leurs questions pertinentes et la discussion riche qui a suivi la soutenance de thèse.

Ce travail de thèse n'aurait pu voir le jour sans l'aide, qu'elle soit technique, scientifique ou morale, apportée par nombre de personnes auxquelles je suis profondément reconnaissante. Au premier rang desquelles, les étudiants et stagiaires qui ont travaillé à mes côtés : je remercie vivement Anthony, ChangLiang, Nicolas et Prantik d'avoir contribué à la production et à l'interprétation de résultats. Je remercie également tous les étudiants qui ont apporté leur contribution à ce projet et que j'ai eu grand plaisir à encadrer.

J'aimerais exprimer mes plus sincères remerciements au personnel technique du laboratoire sans qui la thèse n'aurait pu se faire. Je remercie chaleureusement José et Bernard pour la construction et l'instrumentation de mon pilote, mais aussi et surtout, pour leur expertise et leur sympathie. Je salue également l'aide précieuse que m'a apportée Manon par sa réactivité et son efficacité, et qui a permis de solutionner un nombre incalculable de problèmes techniques. Ma

profonde gratitude va évidemment à Aurore et Nathalie qui, au-delà de la formation et du support technique qu'elles m'ont apportés, ont été d'une grande aide en m'apportant tout leur soutien et leurs encouragements, dans des moments difficiles. Pour ces raisons, je vous remercie les filles et vous dois beaucoup. De la même manière, je remercie Claude d'avoir partagé ses connaissances avec moi et de ne jamais avoir compté son temps lorsque j'ai eu besoin de son aide précieuse : cela a été un réel plaisir de travailler avec toi et je te remercie de m'avoir toujours exprimé ton soutien. Je pense également à Colette, Christophe, Mansour, Julie, et Jean-Christophe Rouch qui m'ont ponctuellement apporté leur appui.

Je tiens à remercier tous les enseignants-chercheurs du département GPE avec qui j'ai eu la chance d'interagir. Je remercie particulièrement Jérôme d'avoir pris de son temps pour m'éclairer sur la partie DTS, ainsi que Maria et Alain Liné de m'avoir plus d'une fois reçue dans leurs bureaux pour répondre à mes questions. Je remercie sincèrement tous ceux qui m'ont simplement témoigné leur sympathie dans les couloirs du hall ou lors d'une pause café ; je pense notamment à Maria, Aras, Arnaud, ..., je remercie également Gilles et Stéphanie de m'avoir fait confiance en me confiant des enseignements. Je remercie également Yolaine et Etienne d'avoir cru en moi en étant les premiers à m'ouvrir les portes de l'INSA et du laboratoire. Ma profonde gratitude s'adresse tout particulièrement à Dominique qui m'a accompagnée sur la partie enseignements et qui a été d'un soutien infaillible pendant ces 4 années de thèse : je te suis très reconnaissante Domi de m'avoir toujours ouvert ta porte, et d'avoir toujours fait tout ton possible pour m'apporter ton aide amicale.

Je ne saurais oublier mes camarades doctorants qui ont partagé avec moi cette aventure et qui m'ont apporté tout leur soutien. Je les remercie pour les fous rires, les pauses café, les sorties, les soirées, les weekends...et pour les séances de psychanalyse gratuites ! A ce titre, un grand merci à mes collègues de bureau : Paul, Angélica, Noémie, Nga et Manel : merci de m'avoir écoutée, je pense que notre solidarité nous a énormément aidés à (sur)vivre (à) la thèse ! De la même manière, je remercie tous mes autres camarades, Mourad, Maider, Ana, Nouredine, Laura, Mathias, Claire, Christelle L., Ana, Allan, Elsa, David, Qiuming, Marine, Maxime, Xiaomin, Alberto, Ibrahima, Flavie, Mathilde,...et tous les autres : j'ai été très contente de faire votre connaissance et garderai un excellent souvenir de vous tous.

Enfin, je remercie infiniment mes proches qui, sans contribuer directement à ce travail, ont eu un rôle capital par leur appui sans faille. Je ne remercierai jamais assez mes parents qui m'ont transmis la valeur et l'amour du travail et dont la fierté a toujours été mon principal moteur. Je les remercie, ainsi que mes sœurs et mes beaux-frères d'avoir toujours cru en moi et de m'avoir toujours encouragée. Je remercie mes neveu et nièce qui, sans le savoir, ont été ma seule bouffée d'oxygène pendant ces années de dur labeur et d'implication totale.

J'exprime pour finir ma profonde gratitude à mon partenaire de vie, qui est la personne qui y a toujours cru, lorsque moi-même n'y croyais plus. Tu as été mon pilier pendant toute cette expérience, tu m'as transmis ta force et m'a toujours poussée à me dépasser. Tu as fait preuve de grande patience et de compréhension, et je ne te remercierai jamais assez d'avoir été là.

RESUME

Dans un contexte où le colmatage des membranes demeure être le principal frein au large développement des Bioréacteurs à Membrane (BAM), le Quorum Quenching (QQ) est récemment apparu comme une solution innovante de contrôle du colmatage. Depuis 2009, le QQ fait l'objet d'un intérêt croissant dans la recherche où la plupart des études ont prouvé son efficacité, sans pour autant caractériser tous les mécanismes impliqués dans son action. Pourtant, en appliquant une nouvelle technique de contrôle du colmatage, il semble indispensable de s'assurer de sa plus-value par rapport à l'existant et de vérifier que les autres aspects du BAM ne s'en retrouvent pas altérés. C'est dans cette optique, et après une synthèse bibliographique, que ce travail s'inscrit, avec comme principal objectif la compréhension des mécanismes découlant de l'application du QQ supporté par des particules (« QQ media ») aux BAM. L'étude s'est portée sur l'hydrodynamique et le transfert de matière comme axes originaux, car ces phénomènes physiques sont d'une importance cruciale pour la performance du BAM. Une approche expérimentale a été développée et conduite sur un BAM à air-lift (18L), pour atteindre les objectifs de l'étude :

Il résulte de l'application du QQ au BAM un réacteur multiphasique complexe. La première partie est consacrée à la caractérisation multi-échelle de l'hydrodynamique du réacteur par des techniques optiques (caméra, PIV). L'effet de l'ajout des « QQ media » a ainsi pu être évalué aux échelles globale (DTS, mélange, rétention gazeuse) et locale (taille de bulles, champs de vitesse liquide, contraintes de cisaillement à la membrane). La variation des paramètres opératoires a permis l'étude du comportement intrinsèque des QQ media en termes de fluidisation. Les résultats ont montré que la fluidisation était favorisée à fort débit d'air et pour la plus grande largeur de « riser » de l'air-lift. Aussi, la fluidisation des « QQ cylindres creux et feuilles » s'est avérée plus efficace que celle des « QQ billes » à même débit d'air. Les expériences ont mis en évidence un faible effet des « QQ media » sur les grandeurs globales du réacteur (la rétention gazeuse, la vitesse moyenne d'écoulement, le temps de mélange), mais un effet négatif à l'échelle locale, notamment en présence de « QQ feuilles » (profil de vitesses dans le « riser », contraintes de cisaillement à la membrane).

L'action du QQ est basée sur une réaction enzymatique. Or, comme dans toute réaction (bio)chimique, le transfert de matière peut-être un paramètre-clé à étudier, pour identifier les étapes limitantes de la réaction globale. L'objectif de la seconde partie est de caractériser le transfert depuis/vers les « QQ media », en utilisant une molécule modèle et des méthodes optiques. Les effets de l'hydrodynamique et de la forme des « QQ media » sur le transfert de matière ont pu être appréciés, en déterminant un coefficient de transfert et des flux transférés. A fraction volumique de « QQ media » égale, le flux transféré en présence de « QQ feuilles » est le plus important du fait de leur plus grande surface d'échange.

Enfin, la dernière partie de cette étude s'est focalisée sur la confrontation des différents résultats pour finalement établir un lien entre l'hydrodynamique, le transfert de matière et le colmatage de la membrane. Des essais de filtration d'une suspension modèle (bentonite) ont été réalisés, et l'effet mécanique des « QQ media » sur la réduction du colmatage a été étudié. Les résultats ont révélé l'efficacité des « QQ feuilles » pour réduire le colmatage de la membrane.

Au global, ce travail contribue à une meilleure compréhension des mécanismes impliqués dans l'application du QQ aux BAM, d'un point de vue purement physique. Le choix de cet axe original a également permis d'identifier des pistes d'amélioration conduisant cette solution prometteuse qu'est le QQ supporté par des particules, vers une application optimale et une réduction efficace du colmatage.

Mots-clés : Bioréacteurs à membrane, Quorum Quenching, Air-lift, Hydrodynamique, Transfert de matière, Filtration, Colmatage.

ABSTRACT

In a context where membrane fouling is the main limitation restraining the wide application of Membrane Bioreactors (MBRs), Quorum Quenching (QQ) recently appeared as a new biological paradigm for biofouling mitigation. Since 2009, QQ has been the subject of wide investigation and numerous authors focused on demonstrating its efficiency to reduce biofouling, without exploring the mechanisms involved in its application. Though, when applying an innovative biofouling control technique, it seems essential to provide an added value without impairing the other operating parameters of the MBR. Within this scope, and on the basis of a literature review, the present work aims to better understand the mechanisms involved in the application of particles (media)-mediated QQ to MBRs. This was achieved by addressing original directions, hydrodynamics and mass transfer, two physical phenomena of great importance in the MBR operation. An experimental approach was developed using a lab-scale airlift MBR (18 L) with the view to meeting the main objectives of this work:

The application of QQ to the MBR results in a multiphase reactor, therefore, the first objective of this work consisted in leading a multi-scale characterization of the hydrodynamics in such a system. Using optical techniques (camera, PIV), the effect of the addition of solid QQ media in suspension was assessed at the global scale (RTD, mixing, gas hold-up) and the local scale (bubble size, liquid velocity field, membrane shear stress). The investigation of different operating conditions also allowed characterizing the inherent fluidization behavior of the QQ media. It was found that the fluidization of QQ media was favored under high aeration and wide riser configuration. In addition, the fluidization of QQ sheets and hollow cylinders was found to be more efficient than that of QQ beads. The experiments showed that the addition of the QQ media had insignificant effect on the reactor at the global scale (gas hold-up, average liquid velocity, mixing time), but could have negative effect at the local scale, especially in presence of QQ sheets (liquid velocity profile, membrane shear stress).

The QQ activity is based on an enzymatic reaction, and as in every (bio)chemical reaction, the mass transfer is a key-parameter to investigate for determining the limiting step of the global reaction. Thus, the objective of the second part of this work was to characterize, using a model molecule and optical methods, the mass transfer from/towards the QQ media. The effects of the hydrodynamics and the shape of QQ media on the mass transfer were evaluated, via the determination of a mass transfer coefficient and a transferred flux under different operating conditions. Under the same volume fraction of QQ media, the greater transferred flux was obtained in presence of QQ sheets owing to their bigger exchange surface.

Finally, the last part of this study was dedicated to link the obtained results and come to a nexus between the hydrodynamics, the mass transfer and the membrane fouling. With this view, filtration experiments

were carried out with a model suspension (bentonite) and the mechanical effect of the addition of QQ media was studied in terms of fouling mitigation. The QQ sheets appeared to be the most efficient shape to mitigate membrane fouling.

The present study is a contribution to a better understanding of the mechanisms involved in the QQ application to MBRs, from a purely physical perspective. Choosing this original research direction, also allowed identifying valuable ways of improvement to move the promising technology of media-mediated QQ towards an optimal application and an effective mitigation of biofouling.

Key-words: Membrane Bioreactors, Quorum Quenching, Airlift, Hydrodynamics, Mass transfer, Filtration, Membrane fouling.

TABLE OF CONTENTS

GENERAL INTRODUCTION	1
CHAPTER I. CONTEXT AND STRATEGY OF THE STUDY	5
RESUME EN FRANCAIS	6
I.1. Literature review	7
I.1.1. Introduction.....	7
I.1.2. History of bacterial QQ	9
I.1.3. Isolation of QQ bacteria	10
I.1.4. Activity of QQ bacteria	10
I.1.5. Methods for entrapping QQ bacteria in MBRs	12
I.1.6. Localization of the activity of the QQ bacteria in the MBR.....	14
I.1.7. Performance of the bacterial QQ-MBR.....	16
I.1.8. Effect of bacterial QQ on the MBR performance at macroscopic scale	20
I.1.9. Effect of bacterial QQ on the MBR performance at microscopic scale	25
I.1.10. Effect of the operating conditions on the effectiveness of bacterial QQ.....	26
I.2. Concluding remarks and scientific strategy of the thesis	33
CHAPTER II. MATERIALS AND METHODS	37
II.1. Introduction	38
II.2. Experimental set-up	38
II.2.1. Lab-scale Air-Lift Membrane Bioreactor (ALMBR).....	38
II.2.2. Implementation of Quorum Quenching (QQ) media	42
II.3. Varying operating parameters.....	43
II.3.1. Inter-membrane distance.....	43
II.3.2. Aeration	43
II.3.3. Volume fraction of QQ media	44
II.4. Characterization of the hydrodynamics.....	45
II.4.1. Evaluation of the QQ media fluidization by camera (images).....	45
II.4.2. Characterization of the QQ media and bubbles by shadowgraphy	49
II.4.3. Characterization of the liquid flow by PIV	54
II.5. Characterization of the circulation and mixing performances.....	61
II.5.1. Residence Time Distribution measurement	61
II.5.2. Mixing time measurement	65
II.6. Characterization of the mass transfer by a tracer technique.....	68
II.6.1. Selection of the tracer (Rose Bengal Lactone).....	68
II.6.2. Preparation of the solution	68
II.6.3. Calibration curve (spectrophotometry)	69
II.6.4. Mass transfer in the jar-tests	70
II.6.5. Mass transfer in the lab-scale reactor.....	71
II.7. Filtration test for the study of membrane fouling	80
II.7.1. Principle, setup and experimental protocol.....	80
II.7.2. Model suspension (bentonite)	81
II.7.3. Pressure monitoring for the TMP determination	83
II.7.4. Permeability measurement.....	83

II.7.5. Fouling characterization.....	83
CHAPTER III. HYDRODYNAMICS CHARACTERIZATION OF THE ALMBR/QQ-ALMBR.....	85
<i>RESUME EN FRANCAIS</i>	86
<i>III.1. Introduction</i>	87
<i>III.2. Background</i>	88
III.2.1. Characterization of the hydrodynamics at the global-scale	88
III.2.2. Characterization of the hydrodynamics at the local-scale.....	98
III.2.3. Literature review on the hydrodynamics characterization of multiphase systems	104
<i>III.3. Material and methods</i>	109
III.3.1. ALMBR/QQ-ALMBR operation.....	109
III.3.2. Gas hold-up measurement.....	110
III.3.3. Assessment of the fluidization of QQ media	110
III.3.4. Camera for the characterization of gas and solid phases	111
III.3.5. PIV for the characterization of the liquid phase.....	112
III.3.6. Experimental procedure	114
<i>III.4. Results and discussion</i>	115
III.4.1. Global characterization of the hydrodynamics of the ALMBR/QQ-ALMBR.....	115
III.4.2. Local characterization of the hydrodynamics of the ALMBR/QQ-ALMBR.....	129
<i>III.5. Conclusions and perspectives</i>	151
CHAPTER IV. MIXING AND CIRCULATION PERFORMANCE OF THE ALMBR/QQ-ALMBR ...	153
<i>RESUME EN FRANCAIS</i>	154
<i>IV.1. Introduction</i>	155
<i>IV.2. Background</i>	156
IV.2.1. Characterization of the short-term mixing performance	156
IV.2.2. Definition of mixing time and measurement techniques	156
IV.2.3. Characterization of the long-term mixing performance.....	160
<i>IV.3. Materials and methods</i>	169
IV.3.1. QQ-ALMBR operation	169
IV.3.2. Mixing time measurement	170
IV.3.3. RTD measurement	171
IV.3.4. Experimental procedure	172
<i>IV.4. Results and discussion</i>	172
IV.4.1. Characterization of the short-term mixing performance of the ALMBR/QQ-ALMBR.....	172
IV.4.2. Characterization of the long-term mixing performance of the ALMBR/QQ-ALMBR	176
<i>IV.5. Conclusions and perspectives</i>	195
CHAPTER V. MASS TRANSFER PHENOMENA INVOLVED IN THE QQ-MBR.....	197
<i>RESUME EN FRANÇAIS</i>	198
<i>V.1. Introduction</i>	199
<i>V.2. Background</i>	200
V.2.1. Mass transfer fundamentals	200
V.2.2. Literature review on mass transfer in QQ-MBRs	202

V.3.	<i>Materials and methods</i>	204
V.3.1.	Selection and preparation of the dye solution	204
V.3.2.	QQ media.....	204
V.3.3.	Jar-test setup and spectrophotometry for the mass transfer study from the liquid to the QQ media 205	
V.3.4.	Experimental setup and camera technique for the mass transfer study from the QQ media to the liquid 206	
V.4.	<i>Theoretical aspects of the mass transfer kinetics</i>	207
V.4.1.	Liquid-solid mass transfer.....	207
V.4.2.	Solid-Liquid mass transfer	210
V.5.	<i>Results and discussion</i>	211
V.5.1.	Calculation of the diffusion coefficient of the Rose Bengal Lactone	211
V.5.2.	Liquid-solid mass transfer from the liquid to the QQ media	212
V.5.3.	Solid-liquid mass transfer from the QQ media to the liquid	222
V.6.	<i>Conclusions and perspectives</i>	231
CHAPTER VI. EFFECT OF QQ MEDIA ON FOULING AND GENERAL DISCUSSION		235
RESUME EN FRANCAIS		236
VI.1.	<i>Introduction</i>	237
VI.2.	<i>Membrane fouling in the ALMBR/ QQ-ALMBR</i>	237
VI.2.1.	Fouling in the ALMBR.....	238
VI.2.2.	Fouling in the QQ-ALMBR.....	243
VI.3.	<i>Mechanisms involved in the physical effect of QQ media for membrane fouling mitigation</i>	246
VI.3.1.	Summary and consistency of the results	246
VI.3.2.	Relationship between the fouling mitigation effect and the physical aspects of QQ media	254
VI.4.	<i>Interest of the study for membrane fouling mitigation through a biological effect</i>	255
VI.5.	<i>Conclusions and perspectives</i>	258
GENERAL CONCLUSION AND PERSPECTIVES		259
APPENDICES		265

LIST OF FIGURES

Figure 0: Number of papers published in journals investigating/reviewing QQ as a biofouling mitigation technique for MBRs.....	3
Figure I-1 : Structure of an N-acyl-L-homoserine lactones (AHL) molecule (R1 can be an oxo or a hydroxyl group; R2 can be a carbon chain from C1 to C15).	7
Figure I-2 : AHL degradation by lactonase produced by <i>Rhodococcus</i> sp. BH4.....	11
Figure I-3 : AHL degradation by acylase produced by <i>Pseudomonas</i> sp. 1A1.....	12
Figure I-4 : (a) Polyethylene (PE) microbial vessel, (b) ceramic microbial vessel (CMV) (c) sodium alginate beads, (d) sodium alginate hollow cylinders, (e) sodium alginate sheets, and (d) Rotating Microbial Carrier Frame (RMCF) [52], for the QQ bacteria entrapping.	13
Figure I-5 : Localization of the Quorum Quenching (QQ) activity of <i>Rhodococcus</i> sp. BH4 entrapped in a microbial vessel or sodium alginate beads in a lab-scale membrane bioreactor (MBR).....	14
Figure I-6 : Localization of the QQ activity of <i>Pseudomonas</i> sp. 1A1 entrapped in a microbial vessel in a lab-scale MBR.	15
Figure I-7 : Schematic representation of the TMP profiles obtained in control MBR (solid line) and QQ MBR (dotted line).....	20
Figure II-1 : (a) Internal-loop split-cylinder (b) internal-loop draft-tube and (c) external-loop ALR...	39
Figure II-2 : Air-lift Membrane Bioreactor.	39
Figure II-3 : Diagram of the lab-scale Air-Lift Membrane Bioreactor (ALMBR).....	40
Figure II-4 : Process flow and instrumentation diagram of the lab-scale Air-Lift Membrane Bioreactor (ALMBR).	41
Figure II-5: Photographs of the Quorum Quenching (a) beads (b) hollow cylinders and (c) sheets.....	42
Figure II-6 : Selection of the observation windows for (a) the study of the fluidization (b) the shadowgraphy.....	46
Figure II-7 : Experimental procedure for the study of the QQ media fluidization.....	46
Figure II-8 : Series of images recorded for the determination of the fluidization rate of beads introduced at 0.45 % v/v and under an air flowrate of $0.90 \text{ Nm}^3 \cdot \text{h}^{-1} \cdot \text{m}^{-2}$	47
Figure II-9 : Shadowgraphy setup for the hydrodynamics characterization of the reactor.	49
Figure II-10 : Experimental procedure for the study of the hydrodynamics in presence of QQ media.	50
Figure II-11 : Flow chart of the image processing program used for the determination of the bubble size and the bubble and QQ media velocity.	51
Figure II-12 : Series of images recorded at the top of the membrane (Window I) for the determination of the properties of bubbles generated in the ALMBR under an air flowrate of $0.90 \text{ Nm}^3 \cdot \text{h}^{-1} \cdot \text{m}^{-2}$ with a riser width of 15 mm (the time between two consecutive images of a series is 5 ms).....	53
Figure II-13 : Principle of the PIV technique. (a) Frame recorded at the time (t). (b) Frame recorded at the instant ($t + \Delta t$). (c) Velocity field deduced from the cross-correlation between the pair of frames (a) and (b).	55
Figure II-14 : PIV setup for the hydrodynamics characterization of the reactor.....	56
Figure II-15 : Example of zoomed-in PIV frames for the configuration of the settings (<i>the red arrow represents the displacement of the circled particle</i>).....	56
Figure II-16 : Image processing steps on DynamicStudio. (a) Raw image. (b) Gridded image with a mask applied on it. (c) Raw velocity field resulting from the cross-correlation. (d) Smoothed velocity field resulting from the moving average validation.	58
Figure II-17 : Schematic matrix resulting from the digitalization of each PIV image.	58

Figure II-18 : Example of horizontal liquid flow profile of vertical velocities, obtained in the ALMBR at Window I, with a riser width of 7 mm and under an air flowrate of $0.75 \text{ Nm}^3 \cdot \text{h}^{-1} \cdot \text{m}^{-2}$.	59
Figure II-19 : Example of shear stress evolution obtained in the ALMBR at the Window III with a riser width of 15 mm and under an air flowrate of $0.90 \text{ Nm}^3 \cdot \text{h}^{-1} \cdot \text{m}^{-2}$.	60
Figure II-20 : Conductivity standard curve of NaCl.	62
Figure II-21 : Experimental setup for the RTD measurement.	62
Figure II-22 : Experimental procedure for the study of the RTD in presence of QQ media.	63
Figure II-23 : Example of (a) Conductivity and (b) concentration curves, obtained in the ALMBR under an air flowrate of $0.75 \text{ Nm}^3 \cdot \text{h}^{-1} \cdot \text{m}^{-2}$ with a riser width of 15 mm.	63
Figure II-24 : Conductivity curves obtained in the ALMBR in presence of QQ beads and under an SADm of $0.90 \text{ Nm}^3 \cdot \text{h}^{-1} \cdot \text{m}^{-2}$.	65
Figure II-25 : Experimental setup for the mixing time measurement.	66
Figure II-26 : Example of raw signal of the light intensity through the aerobic tank of the ALMBR under an air flowrate of $0.90 \text{ Nm}^3 \cdot \text{h}^{-1} \cdot \text{m}^{-2}$.	67
Figure II-27 : Light spectrum of Rose Bengal Lactone.	69
Figure II-28 : Spectrophotometry calibration curve of the Rose Bengal Lactone.	70
Figure II-29 : Jar-tests experiments for the study of the transfer into the QQ media.	71
Figure II-30 : Fresh QQ (a) beads (b) hollow cylinders (c) sheets and stained QQ (d) beads (e) hollow cylinders and (f) sheets, after the 24 h jar-test experiment.	71
Figure II-31 : Experimental setup for the visualization of the mass transfer in the MBR.	72
Figure II-32 : Camera calibration curve of the Rose Bengal Lactone.	73
Figure II-33: Comparison of the ratios of the absorbance to the optical pathway obtained by the spectrophotometer and the camera technique.	74
Figure II-34 : Flow chart of the image processing program used for the mass transfer experiments.	75
Figure II-35 : Example of images recorded during the mass transfer from the QQ sheets to the liquid under an air flowrate of $0.75 \text{ Nm}^3 \cdot \text{h}^{-1} \cdot \text{m}^{-2}$. (a) Average flat image obtained prior to the experiment. (b) Raw and (b') final processed image obtained at 32.5 min. (c) Raw and (c') final processed image obtained at 32.5 min.	76
Figure II-36 : Example of (a) intensity (b) absorbance and (c) concentration curves obtained for the mass transfer experiment from the QQ sheets to the liquid under an air flowrate of $0.75 \text{ Nm}^3 \cdot \text{h}^{-1} \cdot \text{m}^{-2}$.	78
Figure II-37 : Experimental procedure for the study of the mass transfer from the QQ media to the liquid phase of the ALMBR.	79
Figure II-38 : Experimental setup for the filtration experiment.	80
Figure II-39: Turbidity calibration curve for bentonite.	82
Figure II-40 : Size distribution curve of the bentonite suspension used to feed the ALMBR (for he experiment run under an SADm of $0.75 \text{ Nm}^3 \cdot \text{h}^{-1} \cdot \text{m}^{-2}$).	82
Figure III-1: Experimental setup of ALMBR studied by Prieske et al. (2008) [110].	93
Figure III-2: Shape regimes for bubbles in free motion through infinite and stationary liquid media [118].	100
Figure III-3: Terminal velocity for air bubbles rising in stationary water at 20°C [118].	101
Figure III-4: Velocity profiles using PIV in a 3x3 hollow fiber module under two different liquid axial flowrates (0.0067 and $0.0267 \text{ m} \cdot \text{s}^{-1}$) [121].	102
Figure III-5: Example of membrane shear stress profile measured with a shear stress meter located in the middle of the membrane, under an aeration of $4.8 \text{ L} \cdot \text{min}^{-1}$ [124].	103
Figure III-6 : Experimental setup and observation windows for (a) the assessment of the fluidization of QQ media (b) the PIV and camera measurements.	110

Figure III-7 : Camera setup for the characterization of the hydrodynamics of the reactor.	111
Figure III-8 : Definition of the minimal horizontal distance to the membrane to characterize the QQ media position in the riser. The images were recorded in window II (Figure III-6(b)) with a riser width of 15 mm, under an SADm of $1.00 \text{ Nm}^3 \cdot \text{h}^{-1} \cdot \text{m}^2$, in presence 0.45 % v/v of (a) QQ beads (b) QQ hollow cylinders and (c) QQ sheets.....	112
Figure III-9 : PIV setup for the characterization of the hydrodynamics of the reactor.	113
Figure III-10 : Example of determination of the liquid superficial velocity in the riser and the velocity profile, from a time-averaged velocity field recorded in the ALMBR at the top of the membrane (window I) with $Dr = 7 \text{ mm}$ and under an air flowrate of $1.0 \text{ Nm}^3 \cdot \text{h}^{-1} \cdot \text{m}^2$	113
Figure III-11: Average gas hold-up in the riser of the ALMBR for two riser widths.	115
Figure III-12: Average liquid velocity in the riser of the ALMBR for two riser widths.....	118
Figure III-13: Comparison of the experimental average liquid velocities in the riser and the calculated ones by the model of Prieske et al. (2008) [110], for the two riser widths.	120
Figure III-14: Fluidization rate of the QQ media introduced at different volume fractions and measured under different air flowrates with a riser width (Dr) of 15 mm.	122
Figure III-15: Average gas hold-up in the riser of the QQ-ALMBR for a riser width of 15 mm and in presence of QQ beads at 0.45 % v/v.	125
Figure III-16 : Average vertical liquid velocity in the riser of the QQ-ALMBRs for a riser width of 15 mm and for different volume fractions of QQ media (<i>the error bars were not represented for the data from the QQ-ALMBRs not to clutter the plot, but were about 50 % on average</i>).	127
Figure III-17 : Average bubble size in terms of circle equivalent-diameter obtained in the ALMBR for the two riser widths and under different air flowrates.	130
Figure III-18: Example of images recorded at window I under an air flowrate of $1.0 \text{ Nm}^3 \cdot \text{h}^{-1} \cdot \text{m}^2$ and with a riser width of (a) 7 mm and (b) 15 mm.	131
Figure III-19: Average bubble velocity in the ALMBR for the two riser widths and under different air flowrates.	132
Figure III-20 : Experimental horizontal profiles of vertical velocity in the two configurations of ALMBR, under different air flowrates.	135
Figure III-21 : (a) PIV image, (b) shear stress evolution at the local point ($x_{\text{membrane}}, y_{\text{middle}}$) and (c) its derived shear stress peak distribution, taken at the bottom of the reactor (window III) under an SADm of $0.90 \text{ Nm}^3 \cdot \text{h}^{-1} \cdot \text{m}^2$ and with a riser width of 15 mm.....	137
Figure III-22 : Cumulative distribution of local membrane shear stress peak in the ALMBR under different air flowrates and in different observation windows.....	139
Figure III-23 : Average minimal distance to the membrane of QQ media at a volume fraction of 0.45 % v/v with a riser width of 15 mm and under different air flowrates.	141
Figure III-24: Average media velocity in the riser part under different air flowrates.	142
Figure III-25 : Average bubble size obtained in the QQ-ALMBR for a riser width of 15 mm, a volume fraction of 0.45 % v/v and under different air flowrates (<i>the error bars were not represented for the data from the QQ-ALMBRs not to clutter the plot</i>).	144
Figure III-26 : Average bubble velocity obtained in the QQ-ALMBR for a riser width of 15 mm, a volume fraction of 0.45 % v/v and under different air flowrates (<i>the error bars were not represented for the data from the QQ-ALMBRs not to clutter the plot</i>).	145
Figure III-27: Experimental horizontal profiles of vertical velocity, in the QQ-ALMBRs in presence of 0.45 % v/v of QQ media, with a riser width of 15 mm and under different air flowrates.....	146

Figure III-28: Cumulative distribution of local membrane shear stress peak in the QQ-ALMBRs with a volume fraction of QQ media of 0.45 % v/v, under different air flowrates and in different observation windows.	148
Figure IV-1 : (a) Single tubular riser ALMBR and (b) double tubular riser ALMBR, studied by Xu and Yu (2008) [145].....	159
Figure IV-2 : Typical RTD profiles obtained as a response to a pulse injection in (a) MBRs, (b) ALRs [151].	166
Figure IV-3 : RTD measurement in the case of (a) an MBR or an ALMBR (as in the present study) and (b) an ALR.....	166
Figure IV-4 : Experimental setup for (a) the RTD measurement (b) the mixing time measurement..	171
Figure IV-5 : Mixing time in the ALMBR under different air flowrates.	173
Figure IV-6 : Mixing time in the QQ-ALMBR under different air flowrates.	175
Figure IV-7: Experimental RTD curves obtained in the ALMBR under different air flowrates.	177
Figure IV-8 : Usual models applied to the ALMBR under different air flowrates.	180
Figure IV-9 : Scheme of the modelling of the reactor as two stirred tanks-in-series with different volumes, with a recirculation between the two tanks and potential dead zones.....	181
Figure IV-10 : Specific theoretical model with $m = 1$ applied to the ALMBR under different air flowrates.	183
Figure IV-11 : Experimental RTD curves obtained in the ALMBR/QQ-ALMBRs under different air flowrates.	186
Figure IV-12 : Specific theoretical model applied to the QQ-ALMBRs under different air flowrates ad without dead zones ($m = 1$).	189
Figure IV-13 : Optimized specific theoretical model applied to the QQ-ALMBRs under different air flowrates and with optimized parameters (m and Qr).	192
Figure V-1 : CLSM images of cylinders entrapping (a) <i>E.coli</i> JB525 and (b) both <i>E.coli</i> JB525 and <i>Rhodococcus</i> sp. BH4 [12].	202
Figure V-2 : CLSM images of the edge of beads entrapping (a) <i>E.coli</i> JB525 and (b) both <i>E.coli</i> JB525 and <i>Rhodococcus</i> sp. BH4. CLSM images of the center of beads entrapping (c) <i>E.coli</i> JB525 and (d) both <i>E.coli</i> JB525 and <i>Rhodococcus</i> sp. BH4 [14].	203
Figure V-3: Photographs of the QQ (a) beads (b) hollow cylinders and (c) sheets.....	204
Figure V-4: Jar-test setup for the study of the mass transfer from the liquid phase to the QQ media.	206
Figure V-5: Experimental setup for the study of the mass transfer from the QQ media to the liquid phase.....	207
Figure V-6 : Illustrative representation of the transfer of the Rose Bengal Lactone from the liquid solution to the QQ media, in the jar-test experiments.	208
Figure V-7 : Illustrative representation of the transfer of the Rose Bengal Lactone from the QQ media to the liquid, in the aerobic tank of the lab-scale MBR.....	210
Figure V-8 : 3D-representation of the molecular conformation of the Rose Bengal Lactone.	211
Figure V-9 : Transferred amount of Rose Bengal Lactone in the QQ sheets overtime, for three repeated experiments.	213
Figure V-10 : Transferred amount of Rose Bengal Lactone in the QQ media overtime (from Experiment 1).	214
Figure V-11 : Identification of the adsorption model for the experimental data from Experiment 1.	215
Figure V-12 : Concentration of the Rose Bengal Lactone in the liquid phase overtime for the Experiment 1.	217

Figure V-13 : Illustrative representation of the liquid-solid mass transfer of the Rose Bengal Lactone from the liquid to the QQ (a) beads (b) hollow cylinders and (c) sheets.	220
Figure V-14 : Concentration of the Rose Bengal Lactone at the surface of the QQ media overtime.	221
Figure V-15 : Effect of the hydrodynamics on the normalized released amount of Rose Bengal Lactone in the liquid phase for the three different shapes of QQ media.	224
Figure V-16 : Initial (over the first 90 s) evolution of the concentration of Rose Bengal Lactone in the liquid phase from QQ beads under three air flowrates.	225
Figure V-17 : Mass transfer coefficients under different air flowrates and for the three shapes of QQ media.	227
Figure V-18 : Effect of the shape of the QQ media on the normalized concentrations of Rose Bengal Lactone in the liquid phase for the three different air flowrates.	228
Figure V-19 : Transfer of the Rose Bengal Lactone from the surface of the membrane to the QQ media in the MBR under an SADm of $0.75 \text{ Nm}^3 \cdot \text{h}^{-1} \cdot \text{m}^{-2}$	233
Figure VI-1 : (a) Permeability and (b) normalized permeability versus the permeate volume obtained for the filtration of bentonite in the ALMBR under an SADm of $0.75 \text{ Nm}^3 \cdot \text{h}^{-1} \cdot \text{m}^{-2}$	238
Figure VI-2 : Proportions of resistances resulting from the filtration of bentonite in the ALMBR under an SADm of $0.75 \text{ Nm}^3 \cdot \text{h}^{-1} \cdot \text{m}^{-2}$	240
Figure VI-3 : Repeatability of the experiment conducted in the ALMBR under an SADm of $0.75 \text{ Nm}^3 \cdot \text{h}^{-1} \cdot \text{m}^{-2}$, in terms of permeability and normalized permeability versus the permeate volume.	241
Figure VI-4 : Normalized permeability curves obtained for the experiments conducted in the ALMBR under the SADm of 0.75 and $1.00 \text{ Nm}^3 \cdot \text{h}^{-1} \cdot \text{m}^{-2}$	242
Figure VI-5 : Normalized permeability curves obtained for the experiments conducted in the ALMBR/ QQ-ALMBR under the different operating conditions.	244
Figure VI-6 : Normalized permeability curves obtained for the experiments conducted in the QQ-ALMBRs under the air flowrates of 0.75 and $1.00 \text{ Nm}^3 \cdot \text{h}^{-1} \cdot \text{m}^{-2}$	245
Figure VI-7 : Correlation between the number of fluidized QQ media and the mixing time in the aerobic tank of the ALMBR.	251
Figure VI-8 : Correlation between the number of fluidized QQ media and the effective volume in the aerobic tank of the ALMBR.	251
Figure VI-9 : Correlation between the Sherwood number and the liquid-Reynolds number obtained for the mass transfer of Rose Bengal Lactone from three shapes of QQ media to the liquid phase of the ALMBR.	254
Figure VI-10 : Characteristic times of the QQ-ALMBR operation.	256
Figure A-II-1-VI-11 : Flow-chart of extraction, purification, identification and quantification of AHLs [164].	266
Figure A-III-1-VI-12 : Correlations between the correction factor Δ and the shape factor k' , deduced from the values in Table A-III-1-1.	270
Figure A-III-1-VI-13 : Correlations between the correction factor Δ and the equivalent-Galilei number, deduced from the values in Table A-III-1-1.	271
Figure A-IV-2-VI-14 : Illustrative example for the determination of the gap between an experimental and a theoretical curve.	276

LIST OF TABLES

Table I-1 : QQ bacteria isolated and applied for biofouling control in MBRs.....	10
Table I-2 : Effect of <i>Rhodococcus</i> sp. BH4-mediated Quorum Quenching on membrane biofouling mitigation in MBRs inoculated with activated sludge (AS), under continuous mode and using hollow fibers (HF) or flat sheet (FS) membrane as the filtration module.	17
Table I-3 : Effect of other bacteria-mediated Quorum Quenching on membrane biofouling mitigation in MBRs inoculated with AS, under continuous mode and using submerged polyvinylidene fluoride (PVDF) hollow fibers as the filtration module.....	19
Table II-1 : Physical properties of the QQ media.....	43
Table II-2 : Ranges of variation of the operating parameters of the ALMBR/ QQ-ALMBR.	44
Table II-3 : Tools and physical magnitudes used for the characterization of the hydrodynamics.	45
Table II-4 : Determination of the fluidization rate corresponding to the conditions presented in Figure II-8.....	48
Table II-5 : Bubble size (mm) deduced from the processing of the images presented in Figure II-12.	53
Table II-6 : Values of Δt selected for each air flowrate.	57
Table II-7 : Tracer recovery for each experiment.	64
Table II-8 : Mixing time (s) for three replicates.....	67
Table II-9 : Physico-chemical properties of the Rose Bengal Lactone.	68
Table II-10 : Spectrophotometer and camera-deduced optical parameters for standard solutions of Rose Bengal Lactone.....	73
Table III-1: Gas-liquid flowing regimes in confined environments.....	91
Table III-2: Fluidization regimes for solid particles in three-phase ALRs based on the observations of Fan et al. (1984) [112] (<i>the white circles represent bubbles and the dark ones represent solid particles</i>).....	96
Table III-3 : Selected studies of the hydrodynamics in Air-Lift Reactors (ALRs) and Air-Lift Membrane Bioreactors (ALMBRs).....	105
Table III-4: Operating parameters for the ALMBR/ QQ-ALMBR.....	114
Table III-5: Correlation ($y = ax^2 + bx + c$) parameters for the average gas hold-up in the ALMBR presented in Figure III-11.....	116
Table III-6: Average liquid velocities in the riser under different operating conditions.....	117
Table III-7: Correlation (Equation III-42) parameters for the average liquid velocity in the ALMBR presented in Figure III-12.....	119
Table III-8: Parameters and results of the model of Prieske et al. (2008) [110] calculated for the two riser widths of the present study.....	119
Table III-9: Reynolds numbers based on the superficial velocities in the riser, for the two riser widths and the different air flowrates.	121
Table III-10 : Average liquid velocities in the riser and the down-comer for the two riser widths and under different air flowrates.	121
Table III-11: Projected areas A_p and calculated terminal falling velocities U_{tp} for the three shapes of QQ media (<i>the hollow cylinders and sheets were considered to fall horizontally</i>).....	123
Table III-12: Experimental and calculated minimum fluidization gas velocities for the three shapes of QQ media at different volume fractions (<i>the model of Petrovic is based on a total fluidization of particles, whereas the experimental values of the present work correspond to a partial fluidization</i>).	124

Table III-13: Theoretical example of a spherical bubble and a spherical cap having the same projected area but different volumes.....	131
Table III-14 : Correlation parameters for the liner trend curve ($y = ax + b$) presented in Figure III-19.	133
Table III-15: Average bubble size, slip velocities and calculated terminal velocities for the two riser widths and under different air flowrates.....	133
Table III-16 : Comparison of the average QQ media velocities to the average liquid velocity and the bubble velocity obtained in the riser ($Dr = 15$ mm) under the same conditions.....	143
Table IV-1 : Summary of studies characterizing the short-term mixing performance in multiphase reactors.	157
Table IV-2 : Summary of studies on the long-term mixing performance in multiphase reactors.	165
Table IV-3 : Operating conditions for the ALMBR/QQ-ALMBR.....	170
Table IV-4 : Average mixing and circulation times measured in the QQ-ALMBR.	174
Table IV-5 : Qualitative and quantitative criteria for the RTD analysis.	178
Table IV-6 : RTD parameters calculated from the experimental results for the ALMBR.	178
Table IV-7 : Optimized m parameter for the specific theoretical model applied to the ALMBR under different air flowrates.	183
Table IV-8 : RTD parameters calculated for the ALMBR/QQ-ALMBR.....	185
Table IV-9: Discrepancies between the experimental RTD curve and the specific theoretical model applied to the QQ-ALMBRs under different air flowrates (with $m = 1$).	188
Table IV-10 : Optimized m parameter for the specific theoretical model applied to the QQ-ALMBRs under different air flowrates.	190
Table V-1 : Properties of QQ media.	205
Table V-2 : Calculated diffusion coefficients for the Rose Bengal Lactone molecule.	211
Table V-3 : Final amounts (qe) of Rose Bengal Lactone transferred in the QQ media after 24 h, for three repeated experiments.	212
Table V-4 : Linear correlation parameters (for Experiment 1) and parameters of the pseudo-second order kinetics model for the adsorption of Rose Bengal Lactone into QQ media.....	215
Table V-5 : External liquid-solid mass transfer parameters for the three QQ media shape (under 90 rpm and solid:liquid ratio of 1:9).	218
Table V-6 : Sherwood numbers for the mass transfer of Rose Bengal Lactone from the liquid to the different shapes of QQ media.....	219
Table V-7 : QQ media properties in the QQ-ALMBR under different air flowrates.	222
Table V-8 : Time te required to reach 96 % of the equilibrium of solid-liquid mass transfer for the three shapes of QQ media.	223
Table V-9 : Parameters of the kinetics model and Sherwood numbers for the solid-liquid mass transfer of Rose Bengal Lactone from the QQ media to the liquid under different air flowrates (<i>the Sh numbers were calculated with the diffusion coefficient $D = 3.92 \times 10^{-10} \text{ m}^2 \cdot \text{s}^{-1}$</i>).	226
Table VI-1 : Initial conditions and results for the two identical experiments run in the ALMBR under an SADm of $0.75 \text{ Nm}^3 \cdot \text{h}^{-1} \cdot \text{m}^{-2}$	240
Table VI-2 : Initial conditions for the experiments run in the ALMBR under two different air flowrates.	242
Table VI-3 : Initial conditions and comparison criteria deduced from the experiments run in the ALMBR/QQ-ALMBR under different operating conditions.	243
Table VI-4 : Summary of the main experimental results obtained at a volume fraction of 0.45 % v/v.	247

Table VI-5 : QQ media and liquid velocities measured with different methods.....	253
Table A-III-2-VI-6: Different heights of baffles tested for the study of the fluidization of QQ media under a riser width Dr of 7 mm.....	272
Table A-IV-2-VI-7 : Example for the determination of the gap between an experimental and a theoretical curve.	277
Table A-VI-2-VI-8 : Fluidization rates, numbers and surfaces of the QQ media.	278

NOMENCLATURE

Latin letters

Symbol	Description	Unit
1A1	QQ bacteria <i>Pseudomonas</i> sp. 1A1	-
A	Wetted area of the flow	m^2
a	Channel radius	m
A or $A(t)$	Absorbance of the solution in the reactor	-
A_b	Free area available for the liquid flow between the riser and the down-comer in the airlift reactor	m^2
A_d	Cross-section of the down-comer in the airlift reactor	m^2
A_m	Membrane area	m^2
A_{MM}	Free area available for the liquid flow between the membrane plates in a module of the ALMBR	m^2
A_p	Projected area	m^2
A_r	Cross-section of the riser in the airlift reactor	m^2
BH4	QQ bacteria <i>Rhodococcus</i> sp. BH4	-
C or $C(t)$	Tracer concentration in the liquid phase of the reactor	$mg.L^{-1}$ or $g.L^{-1}$
C_0	Initial tracer concentration in the liquid phase of the reactor	$mg.L^{-1}$ or $g.L^{-1}$
C_1 or $C_1(t)$	Tracer concentration in the outlet of the anoxic tank of the reactor	$mg.L^{-1}$ or $g.L^{-1}$
C_2 or $C_2(t)$	Tracer concentration in the outlet of the aerobic tank of the reactor	$mg.L^{-1}$ or $g.L^{-1}$
C_{in} or $C_{in}(t)$	Tracer concentration in the feed for the RTD measurement	$mg.L^{-1}$ or $g.L^{-1}$
$C_l(t)$	Concentration of the tracer (Rose Bengal Lactone) in the liquid phase of the reactor	$mg.L^{-1}$ or $mg.m^{-3}$
C_{out} or $C_{out}(t)$	Tracer concentration in the permeate	$mg.L^{-1}$ or $g.L^{-1}$
$C_s(t)$	Concentration of the tracer (Rose Bengal Lactone) at the surface of the solid phase (QQ media)	$mg.L^{-1}$ or $mg.m^{-3}$
D	Dispersion coefficient in the dispersion RTD model	$m^2.s^{-1}$
D or D_{AB}	Diffusion coefficient of solute A into the solvent B	$m^2.s^{-1}$
d_a	Circle-equivalent bubble diameter (having the same projected area A_p)	m
D_d	Down-comer characteristic dimension (diameter/width)	m
d_e	Volume-equivalent bubble diameter (having the same bubble volume V_b)	m
D_h	Hydraulic diameter	m
d_{MM}	Distance between the membrane plates in a module of the ALMBR	m
d_p	Particle diameter	m
D_r	Riser characteristic dimension (diameter/width)	m
E or $E(t)$	RTD probability function	s^{-1} , min^{-1} , h^{-1} or $days^{-1}$
E_{exp} or $E_{exp}(t)$	Experimental RTD probability function	s^{-1} , min^{-1} , h^{-1} or $days^{-1}$
$E\ddot{o}$	Eötvös number	-
E_{th} or $E_{th}(t)$	Theoretical RTD probability function	s^{-1} , min^{-1} , h^{-1} or $days^{-1}$
f_p	Fraction of tracer recovered after the time t_p	%

Symbol	Description	Unit
g	Gravitational acceleration	m.s^{-2}
h_D	total liquid height in the reactor	m
h_L	total liquid height in the reactor	m
I or $I(t)$	Light intensity through the solution in the reactor	-
I_0	Light intensity through the blank (water)	-
I_t	Intensity of turbulence	-
J	Permeate flux	$\text{L.h}^{-1}.\text{m}^{-2}$ or m.s^{-1}
K	Correlation constant	-
k	Boltzmann constant	$\text{m}^2.\text{kg.s}^{-2}.\text{K}^{-1}$
k_1	Constant of the pseudo-first order kinetics model for adsorption	s^{-1}
k_2	Constant of the pseudo-second order kinetics model for adsorption	$\text{g.mg}^{-1}.\text{s}^{-1}$
K_B	Frictional loss coefficient at the bottom of the airlift reactor	(-)
k_c	Global mass transfer coefficient	m.s^{-1}
k_{ls}	Liquid-solid mass transfer coefficient	m.s^{-1}
K_{MM}	Resistance coefficient of the membrane module in the ALMBR	(-)
k_{sl}	Solid-liquid mass transfer coefficient	m.s^{-1}
K_T	Frictional loss coefficient at the top of the airlift reactor	(-)
L	Length	m
l	Optical pathway in Beer-Lambert law	cm
L_p	Permeability of the membrane	$\text{L.h}^{-1}.\text{m}^{-2}.\text{bar}^{-1}$
$L_{p, \text{cleaned}}$	Permeability of the membrane after mechanical cleaning	$\text{L.h}^{-1}.\text{m}^{-2}.\text{bar}^{-1}$
$L_{p, \text{fouled}}$	Permeability of the membrane after filtration	$\text{L.h}^{-1}.\text{m}^{-2}.\text{bar}^{-1}$
$L_{p, \text{initial}}$	Permeability of the membrane prior to filtration	$\text{L.h}^{-1}.\text{m}^{-2}.\text{bar}^{-1}$
L_{p0}	Initial permeability of the membrane	$\text{L.h}^{-1}.\text{m}^{-2}.\text{bar}^{-1}$
l_{MM}	Height of the membrane module in the ALMBR	m
M	Morton number	-
m	Dead zone index	-
M_B	Molecular weight of the solvent B	g.mol^{-1}
M_s	Mass of the solid phase in the reactor	g or kg
n	Short-circuiting rate	-
N	Number of stirred tanks-in-series	-
N_{FM}	Number of fluidized QQ media (set in suspension)	-
N_A	Transferred flux of the solute A	$\text{g.s}^{-1}.\text{m}^{-2}$
N_{TM}	Total number of QQ media introduced in the reactor	-
P	Wetted perimeter of the flow	m
P_i	Inlet pressure of the MBR	bar
P_p	Permeate pressure	bar
$q(t)$	Adsorbed quantity of solute per mass unit of solid (QQ media)	mg.g^{-1}
Q_{permeate}	Permeate flowrate	L.h^{-1}
q_e	Adsorbed quantity of solute per mass unit of solid at the equilibrium	mg.g^{-1}
Q_g	Gas (air) flowrate	$\text{Nm}^3.\text{h}^{-1}$
Q_i	Feed flowrate	L.h^{-1} or $\text{m}^3.\text{h}^{-1}$
Q_r	Recirculation flowrate (from the aerobic tank to the anoxic tank)	L.h^{-1} or $\text{m}^3.\text{h}^{-1}$
R	Back-mixing rate in the tanks-in-series with backmixing RTD model	-
R_{irr}	Irreversible fouling resistance	m^{-1}
R_m	Membrane (specific) resistance	m^{-1}

Symbol	Description	Unit
R_{rev}	Reversible fouling resistance	m^{-1}
R_t	Total (membrane + cake) resistance after filtration	m^{-1}
r_A	Molecular radius	m
R_c	Bubble curvature radius	m
Re	Reynolds number	-
Re_b	Bubble-Reynolds number	-
Re_m	Mix (gas and liquid) Reynolds number	-
Re_{MM}	Reynolds number inside the membrane module in the ALMBR	-
S	Cross-section opened to the free passage of air	m^2
S_{FM}	Surface of fluidized QQ media (set in suspension)	m^2
$SADm$	Specific Aeration Demand based on the membrane surface	$Nm^3.h^{-1}.m^{-2}$
$SADp$	Specific Aeration Demand based on the permeate flowrate	-
Sc	Schmidt number	-
Sh	Sherwood number	-
S_s	Total exchange surface of the QQ media	m^2
t	Time	s, min, h or days
T	Temperature	$^{\circ}C$ or K
t_{50}	Time to recover 50 % of the tracer injected for the RTD	h
t_c	Circulation time	s
t_m	Mixing time	s
TMP	Transmembrane Pressure	bar
t_p	Time to reach the peak of the RTD distribution	h
u	Velocity	$m.s^{-1}$
U_b	Bubble velocity	$m.s^{-1}$
U_{gmf}	Minimum fluidization gas velocity	$m.s^{-1}$
U_{gr}	Superficial gas velocity in the riser of the airlift reactor	$m.s^{-1}$
U_{gs}	Superficial gas velocity	$m.s^{-1}$
U_l	Liquid velocity	$m.s^{-1}$
u_l'	Liquid velocity fluctuation	$m.s^{-1}$
U_{lmf}	Minimum fluidization liquid velocity	$m.s^{-1}$
U_{lr}	Average liquid velocity in the riser of the airlift reactor	$m.s^{-1}$
U_{mr}	Mix (gas and liquid) velocity in the riser	$m.s^{-1}$
U_{sr}	Average solid velocity in the riser of the airlift reactor	$m.s^{-1}$
U_{tp}	Terminal velocity of a particle in free motion in a liquid	$m.s^{-1}$
V	Volume of the reactor	m^3 or L
V_1	Volume of the anoxic tank of the ALMBR	L or m^3
V_2	Volume of the aerobic tank of the ALMBR	L or m^3
V_A	Molecular volume of the solute A	$cm^3.mol^{-1}$
V_b	Bubble volume	m^3
V_d	Volume of the down-comer in the airlift reactor	m^3 or L
V_{eff}	Effective volume of the reactor	L or m^3
V_g	Volume of gas in the reactor	Nm^3
V_{gd}	Volume of gas in the down-comer of the airlift reactor	Nm^3
V_{gr}	Volume of gas in the riser of the airlift reactor	Nm^3
V_l	Volume of the liquid phase in the reactor	L or m^3
$V_{permeate}$	Permeate volume	L

Symbol	Description	Unit
V_r	Volume of the riser in the airlift reactor	m ³ or L
V_s	Volume of solid in the reactor	m ³ or L
V_s	Volume of the solid phase in the reactor (QQ media)	L or m ³
χ	Association parameter in Wilke and Chang correlation	-

Greek letters

Symbol	Description	Unit
α (Chapter IV)	Ratio of volumes in the two tanks-in-series RTD model	
α (Chapter III)	Constant in the correlation of Bello et al. (1984)	-
β	Constant in the correlation of Bello et al. (1984)	-
ΔP	Pressure difference	Pa or bar
Δt	Time step	s, min, h or days
ε_g	Gas hold-up in the reactor	(%)
ε_{gd}	Gas hold-up in the down-comer of the airlift	(%)
ε_{gr}	Gas hold-up in the riser of the airlift	(%)
ε_l	Liquid hold-up in the reactor	(%)
ε_{lr}	Liquid hold-up in the riser of the airlift	(%)
ε_s	Solid hold-up in the reactor	(%)
ε_{sd}	Solid hold-up in the down-comer of the airlift	(%)
ε_{sr}	Solid hold-up in the riser of the airlift	(%)
ε_λ	Molar attenuation coefficient in Beer-Lambert law	cm.L.mol ⁻¹ or cm.L.g ⁻¹
θ	Dimensionless time	-
θ_m	Dimensionless mixing time	-
μ	Mean residence time deduced from the RTD	h
μ_l	Dynamic viscosity of the liquid	Pa.s
ν_l	Kinematic viscosity of the liquid	m ² .s ⁻¹
ρ_g	Gas density	kg.m ⁻³
ρ_l	Liquid density	kg.m ⁻³
ρ_r	Mean density in the riser	kg.m ⁻³
ρ_s	Solid density	kg.m ⁻³
σ	Surface tension	N.m ⁻¹
σ_t	Standard deviation to the average liquid velocity	m.s ⁻¹
σ^2	Variance of the RTD	h ²
τ	Theoretical (hydraulic) residence time in the reactor	h
φ	Shear stress	Pa

Abbreviations

Symbol	Description
AHL(s)	Acyl-Homoserine Lactone(s)
ALMBR(s)	Airlift Membrane Bioreactor(s)
ALR(s)	Airlift Reactor(s)
CEBs	Cell Entrapping Beads
CLSM	Confocal Laser Scanning Microscopy

Symbol	Description
CMOS	Complementary Metal-Oxide-Semiconductor
CMV	Ceramic Microbial Vessel
FS	Flat sheet membrane
HF	Hollow fiber membrane
MBR(s)	Membrane Bioreactor(s)
MM	Membrane module
PAC	Powdered Activated Carbon
PE	Polyethylene
PES	Polyether Sulfone
PIV	Particle Image Velocimetry
PVDF	Polyvinylidene Fluoride
QQ	Quorum Quenching
QS	Quorum Sensing
RTD	Residence Time Distribution
SAD	Specific Aeration Demand
TAB	Total Attached Biomass
WW	Wastewater
WWT	Wastewater Treatment

GENERAL INTRODUCTION

Water is a fundamental resource, essential to life, though seriously threatened by the current human activity. Water availability is nowadays a crucial concern, and one of the reasons to that, according to the United Nations, is the water pollution caused by the intensive agriculture, and the untreated urban and industrial wastes. In 2017, the UNESCO estimated to 80 % the global proportion of wastewater released in the ecosystem without being treated or reused. As a consequence, about 25 % of people on the planet (according to WHO/UNICEF 2015), use drinking water contaminated with pollutants and faeces, exposing themselves to serious diseases. As an example, in 2018, on the other side of the Mediterranean Sea (in Algeria), a cholera epidemic spread because of the lack of water management systems.

Providing a good water quality appears as the major challenge of the future decades to preserve the human health and the ecosystem. A major part of the solution will inevitably involve the development and the deployment of efficient wastewater treatment and/or reuse processes. Among the existing advanced wastewater treatment processes, Membrane bioreactors (MBRs) are considered as the most effective technology. In comparison to other conventional wastewater treatment processes, MBRs provide excellent water quality with a smaller footprint, and a great potential for water reuse [1].

However, membrane (bio)fouling remains the major bottleneck that still thwarts the wide application of MBRs. Membrane fouling is a term that encompasses all the phenomena inducing the deterioration of the membrane performance by a severe loss of permeability, which further results in higher energy consumption to maintain the process productivity, and heightened need to clean or replace the membrane, finally leading to a substantial increase in the operating costs.

Several membrane cleaning methods have been developed to date and can be classified into physical, chemical, and biological methods [2]. The physical and chemical cleaning methods used to date have been demonstrated to efficiently remove biofouling. However, they can seriously damage the membrane and lead, by this way, to a significant increase in the operating costs [3]. As a consequence, biological anti-biofouling methods have been recently widely investigated for their high effectiveness and their low toxicity using natural plant extracts, nitric oxide gas, enzymes, or energy uncoupling [4].

A number of studies on biofouling have demonstrated that its formation is controlled by a bacterial communication system named Quorum Sensing (QS) [5]. QS is mediated by signal molecules that are produced and detected by bacteria to regulate their behaviors. With the continuous progress in understanding QS mechanisms, Quorum Quenching (QQ), which consists in targeting the QS communication by disrupting it, has appeared as a promising option to fight biofilm formation, bringing new hopes to research on biofouling control strategies.

QQ application to mitigate biofouling in MBRs was firstly developed in 2009 in Seoul National University (South Korea). Since then, research has witnessed a growing interest for membrane biofouling control via QQ application, as it is possible to notice in the figure below.

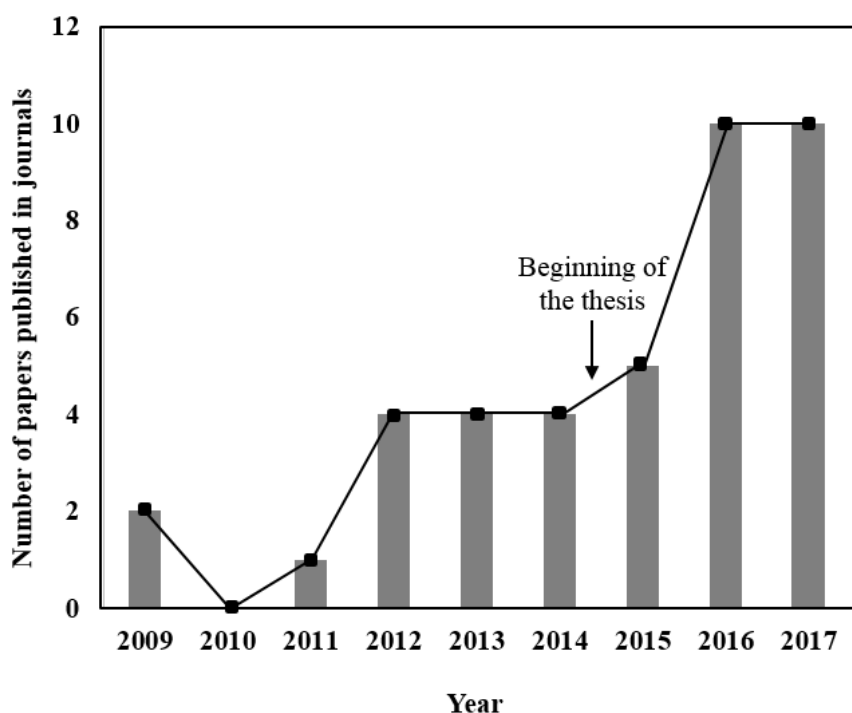


Figure 0: Number of papers published in journals investigating/reviewing QQ as a biofouling mitigation technique for MBRs.

Over the last decade, research focused on proving the undeniable effectiveness of QQ to mitigate membrane biofouling, on the basis of MBR-related indicators that demonstrated the resulting effect on biofouling, such as; the TMP rise, the amounts of EPS, biofilm, AHLs ...etc. However, when developing innovative techniques with the view to improving existing ones, it seems essential to ensure that the innovation only leads to an upgraded result, without affecting the former technique in any way. For this reason, previous research studies have strongly centered their efforts on verifying that the application of QQ did not impair the biodegradation performance of the MBR, mostly by determining the COD and TKN removal efficiencies. In addition, some studies recently focused on identifying the potential changes induced by the QQ application on the microbial community of the MBR [6–8].

The application of QQ to MBRs requires the addition of QQ activity carriers. Several methods to carry the QQ activity were developed and will be further presented in the literature review (Chapter I). Among these methods, the most recent one consists in using sodium alginate particles (QQ media) entrapping QQ bacteria that have the capability to disrupt the QS signal via QQ enzymes. The QQ media are free-moving particles that were developed in a variety of shapes (spheres, cylinders, hollow cylinders, sheets)

and sizes, and were reported to be efficient to mitigate fouling via a double-action [9–14]: the biological effect based on the QQ enzymatic reaction disrupting the QS, and the physical washing effect due to the addition of the suspended QQ media that mechanically cleanse the cake layer on the membrane. With this double-action, two main aspects appear as crucial: the **hydrodynamics** (because the addition of QQ media transforms the MBR into a multi-phase reactor and the interactions between the different phases should be characterized) and the **mass transfer** (since the QQ reaction involves the meeting between the QQ enzymes produced in the QQ media and the signal molecules of QS). Nevertheless, these two aspects were not deeply investigated so far.

In this context, the present study was proposed in 2014 as a thesis topic for the very first time in the “Laboratoire d’Ingénierie des Systèmes Biologiques et des Procédés” LISBP, with the willingness to couple the laboratory expertise (in chemical engineering and membrane science) to the application of QQ to MBRs, in interaction with the Korean team. More specifically, the intentions were mainly:

- To study the QQ application in a new configuration of MBR (air-lift MBR) that was reported to exhibit a particular hydrodynamics behavior that is favorable to fouling mitigation. The originality is also to use a flat sheet membrane for QQ application, when most of the studies reported to date dealt with hollow fibers.
- To bring complementary results to the ones reported in the literature, in particular by targeting the aforementioned physical aspects involved in the QQ application (hydrodynamics, mass transfer).

The present work mainly aims to contribute to the optimization of QQ, adopting an original scientific strategy based upon the study of the physical phenomena involved in what clearly appeared as a promising paradigm for biofouling control in MBRs.

For that purpose, a strong effort was made to review the state of the art, for a deep understanding of the context before establishing the strategy of this work. Therefore, Chapter I not only gives an overview of the literature, but also the scientific objectives of this thesis. After the presentation of the materials and methods in Chapter II, the hydrodynamics aspects are developed in the Chapters III and IV, respectively by characterizing the three phases (gas, liquid and solid) of the system and studying the mixing and flowing behavior in the reactor. Chapter V focuses on the study of the mass transfer involved in the media-based QQ application, and finally Chapter VI deals with the assessment of the physical effect of QQ media to mitigate fouling.

The outline of the thesis as well as the contents of each part will be more deeply explained after a deep understanding of the state-of-the-art, at the end of the next chapter.

CHAPTER I. CONTEXT AND STRATEGY OF THE STUDY

RESUME EN FRANCAIS

Le Quorum Quenching (QQ) est apparu ces dernières années comme une méthode innovante et efficace de lutte contre le colmatage dans les bioréacteurs à membrane, et fait l'objet d'un intérêt croissant dans le monde de la recherche. Ce premier chapitre présente le contexte général de l'étude ainsi que les directions scientifiques qui ont été choisies pour ce travail. L'intérêt de ce chapitre est donc double :

- Dans un premier temps, il est de dresser un état de l'art exhaustif de l'application du QQ comme outil de contrôle du colmatage des membranes. A cet effet, la première partie est consacrée aux notions fondamentales du QQ, à son application aux bioréacteurs à membrane, à son efficacité pour limiter le colmatage, et enfin, à l'effet des conditions opératoires sur cette efficacité. Pour appuyer cette synthèse bibliographique sur le sujet, un travail d'analyse et d'harmonisation de l'information issue des publications parues entre 2009 et 2018 a été effectué et synthétisé sous forme de tableaux de résultats normalisés. A partir des données de la littérature, des critères de discussion ont été définis en s'axant sur les paramètres du procédé. Aussi, les zones d'ombre et interrogations sur le sujet ont pu être identifiées. Une partie de cet état de l'art a été publiée sous forme d'article de revue dans le journal *Membranes* en 2016.

- Dans un second temps, il est de positionner la stratégie scientifique de la thèse en regard du contexte posé par l'état de l'art. En s'appuyant sur les verrous identifiés et en prenant une approche « procédé » comme angle de vue, les questions scientifiques traitées dans la présente étude sont explicitées, et ses principaux objectifs énoncés.

Le présent chapitre s'appuie sur de fortes notions de biologie qui sont indispensables à la bonne compréhension du processus du QQ, mais aussi, à l'identification des mécanismes qui restent inexploqués jusqu'à présent (tels que le transfert de matière mis en jeu dans le QQ). Cependant, la bibliographie relative à chacune des notions et points scientifiques abordés sera développée en tête de chaque chapitre de résultats.

I.1. Literature review

I.1.1. Introduction

Membrane fouling is partly attributed to biofouling, which is defined as the complex combination of several mechanisms: deposition and accumulation of biosolids from the mixed liquor (microbial cells, microbial flocs), microbial growth on the membrane, pore clogging by microorganisms and adsorption of secreted microbial products, which results in the formation of a complex biocake on the membrane. A major part of the biocake is composed of biofilm, which refers to the bacterial tendency to grow as a confined population forming cell clusters embedded in a self-produced slimy matrix composed of extracellular polymeric substances (EPS) [15,16]. According to Wisniewski and Grasmick (1998) [17], the soluble fraction of EPS plays a major role in the global membrane fouling.

In the last decade, several studies have focused on demonstrating the involvement of Quorum Sensing (QS) in biofouling, as reviewed by Lade et al. (2014) [18,19] and Siddiqui et al. (2015) [20]. QS is defined as cell-to-cell communication enabling the bacteria to harmonize their behavior and to function as a coordinated social cluster. QS, which was first described by Fuqua et al. (1994) [21] as the bacterial capability to express certain phenotypes only when a certain cell density threshold is reached, is actually based on the ability of bacteria to produce, release, assess and respond to chemical signals called autoinducers. Three different types of autoinducers have been identified to date: *N*-acyl-L-homoserine lactones (acyl-HSLs or AHLs) for Gram-negative communication, autoinducing peptides (AIPs) for Gram-positive bacteria and furanosyl borate diesters known as AI-2 signals for interspecies communication.

In MBRs, the Gram-negative proteobacteria phylum was demonstrated to be the most abundant among the myriad MBR-living bacteria [7,22,23]. Thus, the prevalent bacterial communication in MBRs is believed to be Gram-negative QS which is ensured through AHLs as autoinducers. These molecules are composed of a lactone ring and an acylated chain containing 4 to 18 carbons as reviewed by Lade et al. (2014) [18] (Figure I-1).

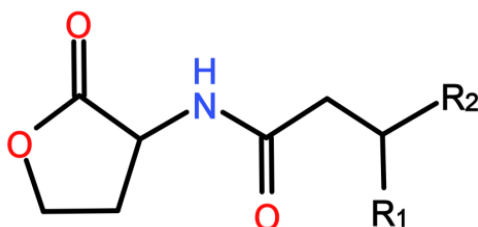


Figure I-1 : Structure of an *N*-acyl-L-homoserine lactones (AHL) molecule (R1 can be an oxo or a hydroxyl group; R2 can be a carbon chain from C1 to C15).

AHL-mediated QS in Gram-negative bacteria is based on the biosynthesis of AHLs in the intracellular compartment, then on their accumulation both in the intracellular and the extracellular environment because of their small molecular weights. At high cell density, the extracellular concentration of AHLs increases until it reaches a threshold, beyond which bacteria can sense them and then activate the transcription of certain target genes [24–28].

AHL-mediated QS has been proved to be involved in biofilm formation in various ways for a number of bacterial species [29–37]. A few studies on biofouling control in MBRs have focused on the potential relationship between AHLs and biofilm on the membrane. Yeon et al. (2009) [38] were the first to provide evidence of the occurrence of AHL-mediated QS in MBRs by proving the presence of different AHLs in the biocake formed on the membrane surface. Using a biological assay (based on *A.tumefaciens* A136 as a reporter strain), the amount of AHLs was found to range from 0 to 50 ng/mg of biocake [38]. This result has been confirmed [11,13,39–42] and then taken to the next step with the determination of a correlation between the AHL amount and the transmembrane pressure (TMP) level [38,41]. Hence, the occurrence of AHL-mediated QS has not only been highlighted but has also been demonstrated to be closely related to biofouling in MBRs.

With this observation, a novel biofouling mitigation strategy based on QS inhibition, i.e., Quorum Quenching (QQ), was then developed. As its name implies, QQ refers to any mechanism that can effectively disrupt QS communication [43]. In theory, QS inhibition can be achieved by targeting either the generation of AHLs, the AHL molecule itself, or the AHL reception, as reviewed by Rasmussen and Givskov [44]. In the particular case of biofouling in MBRs, QQ through destruction of the AHL molecules has been the most investigated mechanism. In essence, QQ can be achieved using several QS inhibitors (QSIs), among which natural compounds, such as piper betle extract (PBE) [41,45] and AHL-degrading enzymes or bacteria, have been preferred over synthetic QSIs for application to MBRs. To date, the degradation of AHLs is the most appreciated and the most commonly applied method for biofouling mitigation in MBRs, and this has been achieved by using either a purified QQ enzyme (porcine kidney acylase I [6,38,46–48]) or bacteria that produce a QQ enzyme (QQ bacteria). The former technique is referred to as “enzymatic QQ” in opposition to the latter, which is known as “bacterial QQ”.

Recently, three interesting reviews have given overviews of the QS and QQ mechanisms, together with summaries of all the QSIs and all the QS-based ways to mitigate membrane biofouling in general [18–20]. However, these reviews do not plainly explain biofouling in MBRs: the links between QQ and the physical phenomena of the MBR process are not explored in depth, and the recent trends in QS-based biofouling mitigation are not fully supported by comparative data in terms of QQ efficiency.

The present chapter gives a literature overview on the QQ principle and application, and part of it was published as a review paper in the journal Membranes in 2016. A special emphasis will be placed on the application of bacterial QQ to mitigate membrane biofouling in MBRs for WWT.

To date, the literature reports several QQ bacteria having the capacity to mitigate biofouling in MBRs. These bacteria appear to have different modes of action to mitigate membrane biofouling, which are mostly attributed to the nature and the localization of the QQ enzymes they produce. Thus, we propose to discuss the relationship between the bacterial QQ and the MBR process here, taking the different points of view offered by the confrontation of the different QQ bacteria. In that way, for each QQ strain, the mode of action will be explained by giving details about the nature and the localization of the QQ enzyme it produces. The use of QQ bacterial consortia will also be included in this summary. The QQ effectiveness will be further discussed by analyzing the effects of bacterial QQ on the physical phenomena related to biofouling in MBRs at both the macroscopic and microscopic scales. Then, the effects of the MBR operating conditions on QQ effectiveness will be examined to try to highlight potentially optimal conditions for bacterial QQ application in MBRs. Finally, some concluding remarks and perspectives will be presented in the last part as directions for future research, and the selected scientific strategy for the present work will be presented.

1.1.2. History of bacterial QQ

The application of bacterial QQ by means of QQ-enzyme-producing bacteria was developed to overcome practical barriers related to the use of a purified enzyme, such as the purification costs and the loss of the enzyme activity. Oh et al. (2012) [11] were the first to experiment bacterial QQ in a lab-scale MBR. For that purpose, a batch-type MBR was supplemented with a genetically modified *E.coli* strain harboring the *aiiA* gene, coding for the production of a QQ enzyme. As a result, 30 % of reduction in the TMP level was observed, and the time for the TMP to reach 25 kPa was extended by approximately 40 %. The use of this recombinant *E.coli* has further led to similar results in a continuous mode, demonstrating the potential of bacterial QQ to mitigate biofouling in lab-scale MBRs. However, the use of such a recombinant strain is hardly conceivable because of its very poor chances of survival in a real MBR at the industrial scale. Considering the significant number of natural QQ bacteria that have been identified to date (reviewed by Czajkowski and Jafra [49] and Lade et al. (2014) [18]), the isolation of an indigenous QQ bacterium from a real MBR appeared to be the most reasonable method. Thus, several strains were isolated, characterized and reported in the literature. Some of these bacteria were found to produce QQ endoenzymes (produced and kept inside the microbial cells), whereas some others produce exoenzymes (produced inside the microbial cells and then released out). These bacteria were either used as a single QQ strain or in a bacterial QQ consortium, to evaluate their potential to reduce biofouling. Table I-1 presents the main QQ bacteria that were identified to date and tested for their potential to mitigate biofouling in MBRs.

Table I-1 : QQ bacteria isolated and applied for biofouling control in MBRs.

QQ Strains		QQ enzyme		Reference
Name	Source	Type	Localization	
<i>Rhodococcus</i> sp. BH4	MBR	Lactonase	Endoenzyme	[9–14,39,40,50–54]
<i>Pseudomonas</i> sp.	MBR	Acylase	Exoenzyme	[55–58]
<i>Bacillus</i> sp. T5	Saltern area	Lactonase	Endoenzyme	[59,60]
<i>Enterobacter cloaca</i>	MBR	Acylase	Exoenzyme	[57,58]
<i>Delftia</i> sp.	MBR	Acylase	Exoenzyme	[57]
<i>Microbacterium</i> sp.	MBR	n.a.	n.a.	[58]
<i>Enterococcus</i> sp. HEMM-1	MBR	Lactonase	n.a.	[61]

I.1.3. Isolation of QQ bacteria

The QQ bacteria reported in the literature (Table I-1) were isolated from different sources, using an enrichment culture method as described in details by Oh et al. (2012) [11]. This method was in particular, used to isolate *Rhodococcus* sp. BH4. *Rhodococcus* sp. BH4 was the first indigenous bacterium isolated from a real MBR and identified by a 16S rRNA as Gram-positive strain showing high activity against C8-HSL. Its QQ potential to reduce biofouling in MBRs was widely tested and reported in the literature. Similarly, Yu et al. (2016) [62] isolated a whole consortium of QQ bacteria from activated sludge samples.

I.1.4. Activity of QQ bacteria

The QQ bacteria were proved to exert their quenching activity via the production of QQ enzymes. Several QQ enzymes could degrade the AHL molecules at different sites of the AHL molecules (Figure I-1), as reported in the literature [63,64]. In the case of the QQ bacteria used for biofouling control, two main classes of QQ enzymes were identified: acylase and lactonase (Table I-1).

Two different examples of QQ bacteria, producing each of the two enzymes are developed in the following. The two bacteria *Rhodococcus* sp. BH4 and *Pseudomonas* sp. 1A1 were selected for deeper discussion for two main reasons: firstly because they were commonly used as QQ bacteria for biofouling control in MBRs, and secondly because the differences between them are interesting to explore, since *Rhodococcus* sp. BH4 produce an internal lactonase (endoenzyme), whereas *Pseudomonas* sp. 1A1 produce an external acylase (exoenzyme). These two strains have sufficiently different characteristics to cover a wide spectrum of QQ bacteria activities.

I.1.4.1. Lactonase activity of *Rhodococcus* sp. BH4

For *Rhodococcus* sp. BH4, a genetic comparison with the known *Rhodococcus erythropolis* W2 was conducted and revealed the presence of the same AHL-lactonase gene [50]. Hence, the QQ activity of *Rhodococcus* sp. BH4 against AHLs is strongly believed to be ensured by lactonase. However, some additional research may be needed, since other strains belonging to the *Rhodococcus* genus have been

found to produce other kinds of AHL-degrading enzymes, such as acylases and oxidoreductases [65–67].

Lactonase has the capacity to degrade AHLs by opening the lactone ring according to the enzymatic reaction presented in Figure I-2.

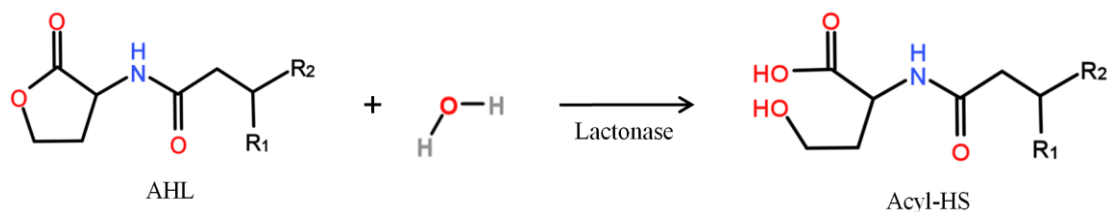


Figure I-2 : AHL degradation by lactonase produced by *Rhodococcus* sp. BH4.

This mode of action suggests that lactonase can theoretically degrade a wide range of AHLs regardless of the acyl chain lengths and the substitutions on the third carbon (R1 group on Figure I-2), evoking a non-selective QQ activity. However, it has been reported that lactonase from *Rhodococcus* sp. BH4 has a lower degrading activity against AHLs with an additional oxo group on the third carbon, compared to the same AHLs with no substitutions [68]. In addition, for AHLs with an oxo group, the lactonase activity increases with the length of the acyl chain, which finally suggests a greater affinity for some AHLs than for others [50,68]. It has been demonstrated that the lactonase activity may be impaired under acidic pH or at high temperature [68]. In addition, the latter study has revealed that the catalytic activity of some lactonases can be totally inhibited by the presence of certain metal ions such as Cu^{2+} and Ag^{+} at 0.2 mM [69]. Thus, when using *Rhodococcus* sp. BH4 as a lactonase-producing strain for biofouling mitigation in an MBR, it can be of great interest to check that the amounts of Cu^{2+} and Ag^{+} in the MBR are below the inhibition limit of 0.2 mM that has been reported [68]. Finally, a potential drawback of using lactonase from *Rhodococcus* sp. BH4 as a QQ enzyme is that the AHL degradation reaction is reversible under acidic pH. However, the rebinding can be avoided by a chemical modification of the opened ring (substitution or reduction) [44].

I.1.4.2. Acylase activity of Pseudomonas sp. 1A1

For *Pseudomonas* sp. 1A1, a genetic analysis revealed the presence of an AHL-acylase homologue gene, which implies that the QQ activity of this strain towards AHLs is most likely ensured by an acylase [55]. This finding is consistent with a previous study investigating the QQ enzyme produced by another *Pseudomonas* strain (PAO1) [70].

Acylase is known to degrade AHLs by hydrolyzing the amine bond between the acyl chain and the lactone ring to produce homoserine lactones and fatty acids (Figure I-3).

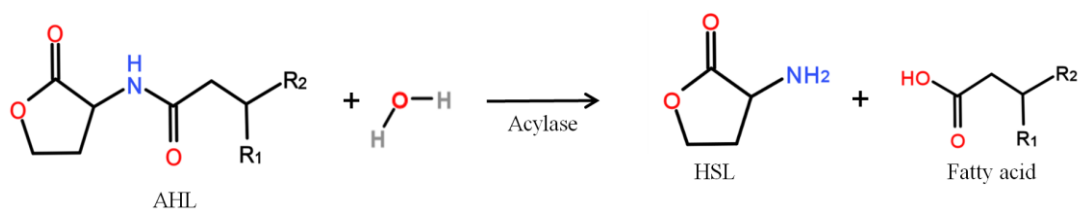


Figure I-3 : AHL degradation by acylase produced by *Pseudomonas* sp. 1A1.

Concerning the enzymatic activity of acylase from *Pseudomonas* sp. 1A1, it has been proved that the longer the acyl side chain is, the greater is the degradation rate, for both substituted and unsubstituted AHLs ranging from C6 to C12 [55]. Similar results have been obtained when characterizing an acylase from *Anabaena* sp. PCC7120, which confirms that the acylase activity depends on the side chain length [71]. Furthermore, it is highly probable that the activity of acylase from *Pseudomonas* sp. 1A1 is dependent on pH and temperature, as has been demonstrated for a purified porcine kidney acylase [72].

1.1.5. Methods for entrapping QQ bacteria in MBRs

After the identification of the QQ bacteria, their implementation in MBRs was carried out to assess their potential to mitigate biofouling by interfering with AHL signal molecules. For that purpose, different entrapping methods were used, in order to avoid loss of cells with the withdrawal of excess sludge from the MBR, as well as to protect them against the attack of other microorganisms cohabiting in the MBR. QQ bacteria were added using different entrapping methods: microbial vessels, sodium alginate capsules/media and a Rotating Microbial Carrier Frame (RMCF).

- Microbial vessels were designed to maintain the QQ bacteria immobilized using a porous material permitting the free diffusion of AHLs and nutrients through the vessel. For example, Oh et al. (2012) [11] used a module composed of 10-cm long polyethylene (PE) hollow fibers (HF) to encapsulate the *Rhodococcus* sp. BH4 cells (Figure I-4(a)). The module was then submerged and held in a fixed place in the MBR. The initial amounts of *Rhodococcus* sp. BH4 cells inserted in microbial vessels ranged from approximately 130 to 450 mg.L⁻¹ of the total working volume [10,11,50]. The volume of the vessel itself represented less than 0.08 % of the MBR volume. For *Pseudomonas* sp. 1A1, two types of materials were used for these vessels: PE and ceramic. As for *Rhodococcus* sp. BH4, Cheong et al. (2013) [55] made PE vessels using microporous HF (0.4 μm). They also designed a ceramic microbial vessel (CMV) consisting of a monolithic microporous module (0.45 μm) with a total length of 10 cm and composed of several lumens into which the cells were injected using a sterile syringe (Figure I-4(b)). The initial quantities of *Pseudomonas* sp. 1A1 cells tested varied from approximately 200 to 700 mg 1A1/L of the total working volume.

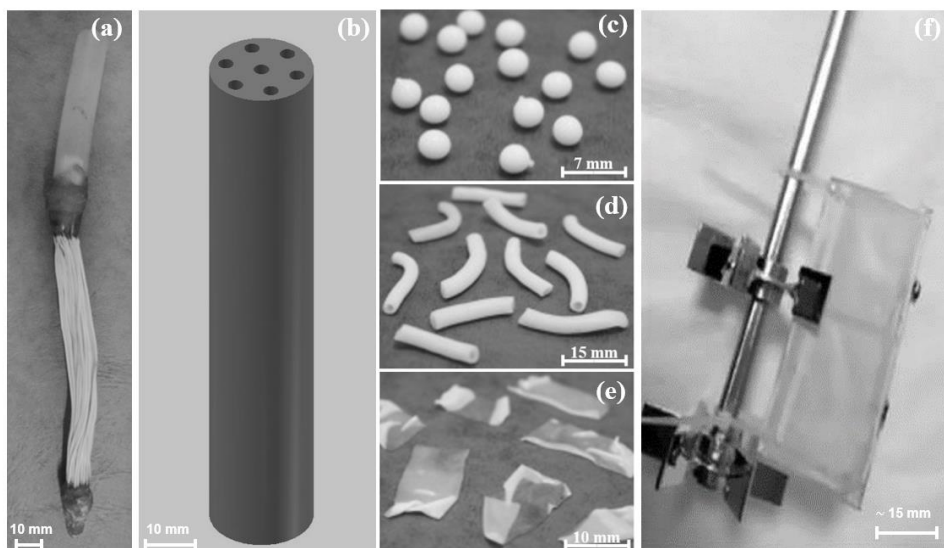


Figure I-4 : (a) Polyethylene (PE) microbial vessel, (b) ceramic microbial vessel (CMV) (c) sodium alginate beads, (d) sodium alginate hollow cylinders, (e) sodium alginate sheets, and (f) Rotating Microbial Carrier Frame (RMCF) [52], for the QQ bacteria entrapment.

- Sodium alginate capsules (QQ media) were first developed for entrapping *Rhodococcus* sp. BH4. They were prepared by dripping a mixture of a *Rhodococcus* sp. BH4 suspension and a sodium alginate solution through a nozzle into a CaCl_2 solution to obtain spherical Cell Entrapping Beads (CEBs) as described by Kim et al. (2013) [39] (Figure I-4(c)). In that case, the amount of *Rhodococcus* sp. BH4 entrapped in the beads was around 6 mg BH4/g sodium alginate. Kim et al. (2015) [9] further developed macrocapsules by coating the CEBs with a microporous polymer layer for better resistance to harsh conditions resulting from the use of real WW. Recently, Lee et al. (2016) [13] developed QQ beads made of a mixture of polyvinyl alcohol and sodium alginate to reinforce their stability in real WW. Finally, in the last years Lee et al. (2016) [12,14,73] developed new shapes of sodium alginate capsules, such as cylinders and sheets (Figure I-4(d) and (e)), in order to increase the exchange surface for the same volume of QQ media inserted in the MBR. Unlike the microbial vessel, the sodium alginate media could move freely when inserted in the MBR.

- Recently, an RMCF (Figure I-4(f)) has been developed as a new entrapping technology for *Rhodococcus* sp. BH4, using a polycarbonate frame and four cubbyholes covered with a polyvinylidene fluoride (PVDF) microfiltration membrane, and packed with a *Rhodococcus* sp. BH4 suspension using a syringe. The RMCF was then set into the MBR similarly to a mechanical stirring device, submerged in the membrane tank [51,52].

Given the variety of entrapping methods, the localization of the QQ activity and the question of the mass transfer of the main molecules involved in the QQ reaction is addressed in the following.

I.1.6. Localization of the activity of the QQ bacteria in the MBR

The localization of the enzymatic (QQ) reaction depends on several parameters at different scales. At the cell scale, the main aspect to take into account is the type of enzyme produced by the QQ bacteria, as two types were identified to date: endoenzymes or exoenzymes (Table I-1). On the other hand, at the process scale, the key factor to consider is the entrapping method used for the addition of QQ bacteria in the MBR. In order to better understand where the QQ enzymatic reaction could possibly take place in the MBR, two different cases are discussed in the following.

I.1.6.1. Localization of the activity of endoenzyme-producing QQ bacteria in the MBR

To date, the best-known example of endoenzyme-producing QQ bacteria is *Rhodococcus* sp. BH4. The measurement of the enzymatic activities of the supernatant and the pellets from the same sample of *Rhodococcus* sp. BH4 has revealed that its QQ activity is based on the production of an intracellular AHL-lactonase, which indicates that the enzymatic degradation of AHLs takes place inside the *Rhodococcus* sp. BH4 cells [50]. This implies that, when *Rhodococcus* sp. BH4 is implemented in an MBR for membrane biofouling control, the AHLs from either the mixed liquor or the biocake on the membrane are transported by convection towards the entrapping element, diffuse through this porous element towards the *Rhodococcus* sp. BH4 cells and then through the cell membrane to be hydrolyzed in their intracellular compartment, as schematically presented in Figure I-5.

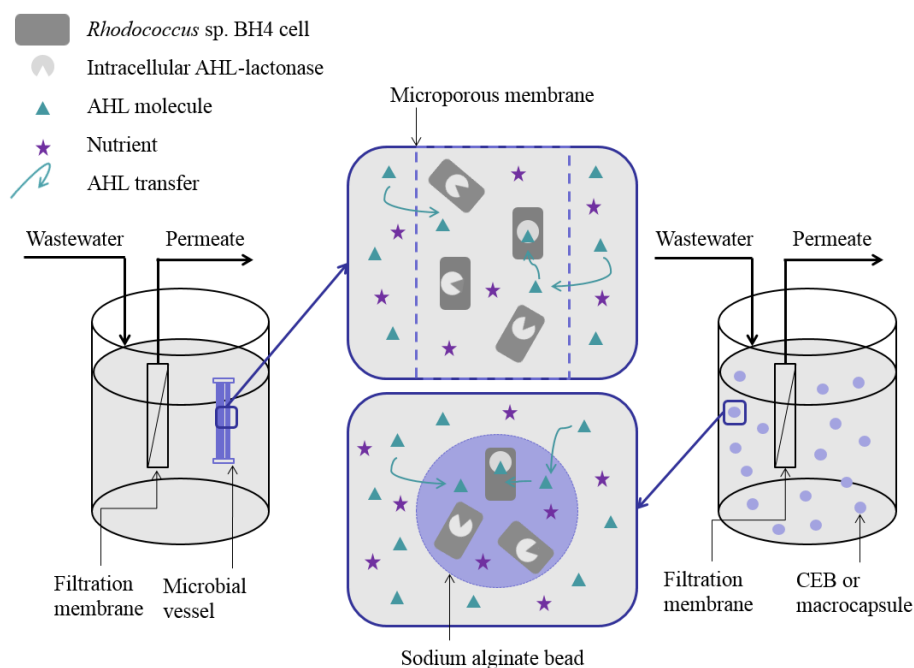


Figure I-5 : Localization of the Quorum Quenching (QQ) activity of *Rhodococcus* sp. BH4 entrapped in a microbial vessel or sodium alginate beads in a lab-scale membrane bioreactor (MBR).

When the microbial vessel is used as an entrapping element, the *Rhodococcus* sp. BH4 cells are held in a fixed place in the MBR and the convective forces created by the aeration and the suction are expected to drive the AHLs towards the immobilized *Rhodococcus* sp. BH4 cells.

The latest technology for encapsulating the QQ bacteria (RMCF) is not represented in Figure I-5 but it is noteworthy that the rotation motion of this module is believed to prevent the settling of cells in the module and to generate additional shear forces in the MBR, which may promote the AHL transport.

Finally, in the case of sodium alginate media (Figure I-4(c), (d) and (e)), it can be assumed that the free motion of the media in the MBR enhances the probability that AHLs will encounter the *Rhodococcus* sp. BH4 cells. Nevertheless, the complex structure of the sodium alginate core could slow down the diffusion of AHLs through the media. Therefore, the localization of the QQ activity is key information that can significantly impact the performances of these entrapping techniques. Some attempts were made in the literature in that way, and achieved the visualization of the transfer of AHLs through sodium alginate particles [12,14]. The mass transfer will be more deeply discussed in the present study (Chapter V).

1.1.6.2. Localization of the activity of exoenzyme-producing QQ bacteria in the MBR

Pseudomonas sp. 1A1 is chosen as an example in the following because unlike lactonase from *Rhodococcus* sp. BH4, acylase produced by *Pseudomonas* sp. 1A1 has been proved to be an exoenzyme [55]. This finding has been further reinforced by the fact that acylases released from *Pseudomonas* sp. 1A1 continued to accumulate in the extracellular medium even when the concentration of dead cells started to increase. Thus, the acylase produced by *Pseudomonas* sp. 1A1 is believed to spread freely out of the cells, to bind to, and hydrolyze AHLs everywhere in the reactor or on the membrane surface as well as inside or outside the entrapping device. An illustrative representation is presented in Figure I-6.

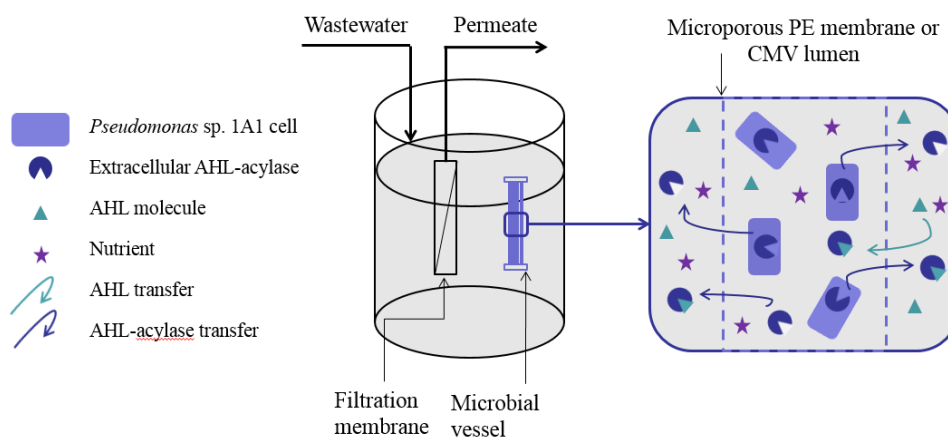


Figure I-6 : Localization of the QQ activity of *Pseudomonas* sp. 1A1 entrapped in a microbial vessel in a lab-scale MBR.

1.1.7. Performance of the bacterial QQ-MBR

Once isolated, the strains that were found to have a QQ activity were applied in MBRs under a wide variety of operating conditions. In parallel to the QQ-MBRs, control MBRs were systematically run in all the reported studies, with the aim to highlight the added value of QQ to mitigate membrane biofouling. In the present section, a comprehensive summary of all the studies reported to date is tabulated, distinguishing *Rhodococcus* sp. BH4 as a QQ bacteria (because of its wide application) in Table I-2, from the other QQ strains in Table I-3.

Table I-2 gathers together all the studies on the effectiveness of *Rhodococcus* sp. BH4 in reducing biofouling in MBRs. In the reported studies, entrapped BH4 cells were introduced in different lab-scale MBRs (working volume < 5 L), a semi-pilot MBRs (working volume of 35 L) and pilot-scale MBRs (working volume ≥ 80 L) operated in a continuous mode. The MBRs were inoculated with AS from WWT plants, and hollow fibers (HF) or Flat Sheets (FS) were used to ensure the WW filtration.

In Table I-3, the effectiveness of other QQ bacteria to mitigate membrane biofouling is presented. All the reported studies were performed in lab-scale MBRs (working volume ≤ 5 L) running in a continuous mode and using submerged PVDF HF as filtration modules.

A wide variability can be observed in the way results are expressed in these studies. Hence, important efforts were made in this work to:

- **Select relevant information from the reported studies in terms of operating conditions and results.**
- **Define appropriate criteria allowing the assessment of the biofouling extent, based on particular points of the TMP or on the amount of biofilm produced.**
- **Standardize the results in terms of percentages with respect to the control MBR performance to better highlight the contribution of QQ to biofouling reduction. The calculation used to convert results into percentages is presented in Equation I-1, where $P\%$ is the standardized result in percentages; M is one of the properties measured to characterize biofouling (TMP, EPS amount...); the minus sign (–) stands for the reduction of biofouling by QQ. The standardization of results also allowed including all the studies in an overall discussion and drawing global trends.**

$$P\% = -\frac{M_{control\ MBR} - M_{QQ\ MBR}}{M_{control\ MBR}} \times 100 \quad I-1$$

The content of Table I-2 and Table I-3 will be discussed, considering different parameters that will be explained in the following.

(AS), under continuous mode and using hollow fibers (HF) or flat sheet (FS) membrane as the filtration module.

[illegible]

Table I-2: *continuation.*

MBR/QQ-MBR design							MBR/QQ-MBR operation							Resulting QQ effect expressed in % of the control MBR											Reference	N ^o
Reactor volume (L)	Membrane				Rhodococcus sp. BH4									Permeate flux (L/m ² h)	Air supply (m3/h)	Filtration/relaxation	Run time (d)	Number of cycles		TMP			Time for TMP to reach			
	Geometry	Configuration	Area (cm ²)	Pore size (µm)	Entrapping method	Inserted quantity of BH4 cells in the reactor (mg/L)	For control MBR	For QQ MBR	After 1 day of operation	At the end of the 1st cycle	At the end of operation	The breaking point	25 kPa					40 kPa	Proteins	Polysaccharides	Proteins	Polysaccharides				
Synthetic wastewater																										
5	HF	S	100	n.a	RMCF (8 mg BH4/cm ³ RMCF)	n.c.	60	n.a.	-	30	1	1	- 63 %	- 52 %	- 52 %	-	-	-	-	-32%	~ 0 %	-	-	[52]	16	
2	FS	S	152	0.4	QQ cylinders (~ 170/reactor 0.5 % of the working volume)	n.c.	20	0.06	-	~ 6	3	1	- 72 %	- 79 %	+ 21 %	-	+ 273 % (+ 4 d)	-	-	-	-	-	-	[12]	17	
3	HF	S	186	n.a	QQ cylinders (1 % of the working volume)	n.c.	21	0.12	-	~ 20	4	1	- 63 %	- 89 %	- 82 %	+ 170 %	+ 434 %	+ 366 %	-	-	-	-	-	[14]	18	
Real wastewater																										
2.5	HF	S	155	0.04	Macrocapsules (500/reactor)	n.c.	30	0.06	-	22	3	1	- 23 %	- 87 %	- 21 %	+ 1135 %	+ 750 % (+ 19 d)	+ 667 % (+ 19.7 d)	- 48 w% after a 9 days cycle	-	-	- 53 %	- 88 %	[9]	19	
80	FS	S	9000	0.4	QQ beads (~ 19000/reactor)	~ 4000	20	0.27	10 min/ 2 min	14	2	1	n.c.	- 83 %	- 81 %	+ 590 %	+ 470 %	-	- 86 % after 14 days	- 52 %	- 85 %	- 21 %	-	[13]	20	
35	HF	S	7000	0.1	QQ beads (~ 6500/reactor ➔ 0.5 % of the working volume ➔)	n.c.	16.5	n.a.	8 min/2 min	~ 55	4	1	0 %	- 83 %	- 57 %	+ 300 %	+ 286 %	-	-	- 71 %	- 67 %	-	-	[53]	21	
35	HF	S	7000	0.1	QQ beads (~ 6500/reactor ➔ 0.5 % of the working volume ➔)	n.c.	16.5	n.a.	8 min/1 min/1 min backwashing	~ 70	3	1	0 %	- 83 %	- 20 %	-	+ 220 %	-	-	- 52 %	- 62 %	-	-	[53]	22	

S: submerged; **E:** External submerged (side-stream); **Numbers:** Taken from the literature; **Numbers:** Calculated with the data available in the literature;

n.a.: Not available data; **n.c.:** Not calculable value with the provided data.

Table I-3 : Effect of other bacteria-mediated Quorum Quenching on membrane biofouling mitigation in MBRs inoculated with AS, under continuous mode and using submerged polyvinylidene fluoride (PVDF) hollow fibers as the filtration module.

MBR/QQ-MBR design						MBR/QQ-MBR operation						Resulting QQ effect expressed in % of the control MBR												Reference	N ^o
Reactor volume (L)	Membrane			QQ bacteria																					
	Configuration	Area (cm ²)	Pore size (µm)	Strain(s)	Entrapping method	Inserted quantity of QQ strain(s) in the reactor (mg/L)	Permeate flux (L/m ² h)	Filtration/relaxation	Run time (d)	Number of cycles		TMP			Time for TMP to reach			TAB in biofilm	SMP in mixed liquor		EPS in biofilm				
										For control MBR	For QQ MBR	After 1 day of operation	At the end of the 1st cycle	At the end of operation	The breaking point	25 kPa	40 kPa		Proteins	Polysaccharides	Proteins	Polysaccharides			
2.5	S	155.2	0.04	<i>Pseudomonas</i> sp. 1A1	PE vessels (4/reactor)	192	25	-	7.8	2	2	- 15 %	- 71 %	- 79 %	+ 180 %	+ 134 % (+ 2.6 d)	+ 150 % (+ 3.1 d)	-	-	-	-	-	[55]	1	
3.0	S	210	0.04	<i>Pseudomonas</i> sp. 1A1	CMV under inner flow feeding mode (1/reactor)	706.8	30	-	2.1	1	1	- 15 %	- 77 %	- 77 %	-	-	-	- 63 w%	-	-	-	-	[56]	2	
3.0	S	210	0.04	<i>Pseudomonas</i> sp. 1A1	CMV under inner flow feeding mode (1/reactor)	706.8	25	-	9.4	1	1	- 22 %	- 76 %	- 76 %	-	-	-	-	-	-	-	-	[56]	3	
3.0	S	210	0.04	<i>Pseudomonas</i> sp. 1A1	CMV under inner flow feeding mode (1/reactor)	266.4	35	-	6	2	2	- 25 %	- 60 %	- 56 %	-	-	-	-	- 6 %	- 62 %	- 77 %	- 37 %	[56]	4	
3.0	S	210	0.04	<i>Pseudomonas</i> sp. 1A1	CMV under normal feeding mode (1/reactor)	266.4	35	-	6	2	2	- 5 %	- 44 %	- 25 %	-	- 3 %	-	-	- 2 %	- 51 %	- 31 %	- 36 %	[56]	5	
4.5	S	90	n.a.	<i>Bacillus</i> sp. T5	PVDF vessel	n.c.	18.5	-	10	1	1	- 49 %	- 40 %	- 40 %	-	-	-	-	-	-	-	-	[59]	6	
4.5	S	88	n.a.	<i>Bacillus</i> sp. T5	CEBs	n.c.	48	-	13	1	1	- 69 %	- 77 %	- 77 %	-	-	-	-	-	-	-	-	[60]	7	
5	S	700	0.05	<i>Enterobacter cloaca</i> , <i>Delftia</i> sp., <i>Pseudomonas</i> sp.	CEBs (400/reactor ➔ 2 % of the working volume)	n.c.	20	8 min/2 min	40	3	1	- 42 %	- 86 %	- 41 %	+ 203 %	+ 198 %	-	-	-	-	- 57 %	- 45 %	[57]	8	
5	S	700	0.05	<i>Rhodococcus</i> sp. BH4, <i>Delftia</i> sp., <i>Pseudomonas</i> sp.	CEBs (400/reactor ➔ 2 % of the working volume)	n.c.	20	8 min/2 min	35	3	1	- 42 %	- 84 %	0%	+ 175 %	+ 175 %	-	-	-	-	- 51 %	- 31 %	[57]	9	
3.2	S	470	0.04	Enterobacter cloaca QQ13 + Microbacterium sp. QQ1 + <i>Pseudomonas</i> sp. QQ3 + <i>Rhodococcus</i> sp. BH4 + (AI-2-degrading-) <i>Escherichia coli</i> ΔlsrRΔluxS	PAC-alginate beads (5 % of the working volume)	n.c.	15	-	19	1	1	- 19 %	- 92 %	- 92 %	+ 448 %	+ 389 %	-	-	- 61 %	- 93 %	-	-	[58]	10	

S: submerged; **Numbers:** Taken from the literature; **Numbers:** Calculated with the data available in the literature; **n.a.:** Not available data; **n.c.:** Not calculable value with the provided data.

1.1.8. Effect of bacterial QQ on the MBR performance at macroscopic scale

The effect of QQ on the MBR performance at macroscopic scale is discussed here in terms of TMP, characteristics of the mixed liquor, and biodegradation efficiencies.

The TMP was chosen because it is without any doubt the most monitored property in studies of biofouling in MBRs, most likely because it is an excellent indicator of biofouling and it can be easily measured continuously during the MBR operation, providing key-information on the biofouling kinetics. For these reasons, all the studies reporting the effectiveness of QQ to mitigate biofouling are at least partly based on the comparison of the TMP profiles. Before giving numerical results, the general shape of the TMP profile in MBRs is illustrated in Figure I-7, then the possible modifications resulting from the implementation of bacterial QQ are proposed and as well as the information that can be deduced from the comparison of the two shapes.

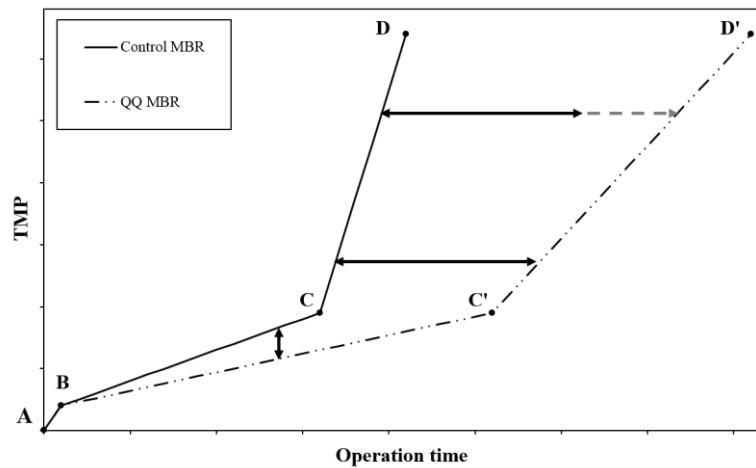


Figure I-7 : Schematic representation of the TMP profiles obtained in control MBR (solid line) and QQ MBR (dotted line).

Figure I-7 presents a schematic illustration of the TMP profiles during MBR operation at constant flux. The fouling phenomenon is now recognized by the MBR community as a three-stage process. Initially, a short-term increase in TMP is observed, from point A to point B, and can probably be attributed to initial pore blocking and the adsorption of solutes from the mixed liquor. Next, a slow long-term rise takes place between points B and C, and is due to the progressive deposition of biosolids (cells and microbial flocs) on the membrane surface and the progressive formation of biofilm. Finally, at point C, called the breaking point, a striking increase, called the TMP jump, indicates a severe loss of permeability [74–76]. The occurrence of the TMP jump depends on the operating conditions and is believed to be caused by sudden changes in local flux or in the biocake architecture and EPS composition [76–81]. Once point D is reached, the filtration process is stopped and the membrane is either cleaned

with a view to reusing it, or changed. The time at which point D is reached is defined as a cycle, and several cycles usually take place during an MBR run.

With the implementation of QQ bacteria to reduce biofouling in MBRs, the second stage of the TMP rise-up is expected to be significantly slowed down from point B to point C', and the occurrence of the TMP jump (at the breaking point) would thus be delayed (Figure I-7). Moreover, the TMP jump from point C' to point D' could be expected to be attenuated, indicating that the addition of QQ bacteria could lead to modified biofouling behavior with temporal and spatial variations in both the progressive biofouling stage and the TMP jump stage. Nevertheless, one particular case could be that the TMP jump in the QQ MBR (C'D' section in Figure I-7) was parallel to that in the control MBR (CD section in Figure I-7), which could imply that QQ only slows down the progressive biofouling stage with no major changes in the TMP jump stage.

In the studies reported in Table I-2 and Table I-3, the initial TMP did not exceed 10 kPa (it ranged from approximately 3 to 10 kPa). For all these studies, it was possible to identify the kind of TMP evolution presented in Figure I-7. However, the first short-term increase stage (AB section in Figure I-7), which takes place relatively quickly, was not clearly identifiable, especially for the studies carried out in the long-term operation.

In order to know which of these stages is the most affected by bacterial QQ, we chose to distinguish between the effect on the progressive biofouling stage (section BC' in Figure I-7) and the effect on the TMP jump (section C'D' in Figure I-7).

Hence, the analysis of the TMP profiles with the latter approach, combined with the characterization of the mixed liquor and the biodegradation efficiencies, are expected to provide information about the direct effects of QQ on the physical phenomena in the MBR at macroscopic scale.

1.1.8.1. Effect on the progressive biofouling stage

For the assessment of the bacterial QQ effect on the progressive biofouling stage, it may be interesting to take into account the vertical gap between the BC and BC' sections at a certain time (Figure I-7). In this case, the arbitrary time of 1 day was selected, because it is the time by which the steady progressive biofouling stage was set in all the studies considered in Table I-2 and Table I-3. This gap would then represent the TMP reduction induced by QQ after 1 day of MBR operation.

In the studies run with synthetic WW and *Rhodococcus* sp. BH4 as QQ bacteria, a significantly reduced TMP value was noted (references n° 1, n° 3, n° 7 to 12 and n° 14 to 18 in Table I-2) with more than 50 % reduction after 1 day of operation. Besides, for some of the studies monitoring longer operation times (≥ 5 days) (references n° 4 to 6 in Table I-2), the TMP reduction was less pronounced, with less than 25 % reduction. When QQ-MBRs were run with real wastewater during more than 14 days (references n° 19 to 22 in Table I-2), the TMP reduction was also less pronounced after 1 day of operation. With

these results, it appears that *Rhodococcus* sp. BH4-mediated QQ effectively slows down the progressive biofouling stage, which indicates that *Rhodococcus* sp. BH4 probably expresses its QQ activity from the very early phase of the MBR operation (during the first day). However, this effect is less visible for longer operation times.

For the other QQ bacteria, the TMPs measured in QQ-MBRs ranged between 5 % and 69 % lower than that in control-MBRs, after 1 day of operation (references n°1 to 10 in Table I-3). These values indicate that, as well as *Rhodococcus* sp. BH4, the other QQ bacteria have a marked effect on the progressive biofouling stage, indicating a relatively early QQ activity of the considered QQ strains/consortia. Nevertheless, it seems that this effect is less pronounced than that of *Rhodococcus* sp. BH4, since the TMP reduction is lower than 50 %, in most of the cases.

1.1.8.2. Effect on the TMP jump

For the evaluation of the QQ effect on the TMP jump, two criteria have been defined and selected. The first criterion is the comparison of the times t and t' corresponding to the times for reaching the breaking points C and C', respectively (Figure I-7), which provide a quantitative information about the TMP jump postponement. The second criterion is the comparison of the slopes of the sections CD and C'D' which were calculated with the points at 25 kPa and 40 kPa that were found to belong to the TMP jump stage for most long-term operations.

In presence of *Rhodococcus* sp. BH4 as QQ bacteria, the analysis of the breaking points according to the first criterion reveals that the time at which the TMP jump occurs is successfully delayed, by at least 170 % (corresponding almost to a twofold postponement) [14] (references n° 18 in Table I-2).

For the second criterion, only some long-term MBR operations with running times around 20 days were taken into account (references n° 5 and 19 in Table I-2) since the filtration in shorter operations is usually stopped before (or right after) the breaking point is reached. The time delays to reach the two points of 25 kPa and 40 kPa with QQ were approximately the same for Kim et al. (2013,2015) [9,39] (references n° 5 and 19 in Table I-2), which refers to similar slopes (around 160 kPa/day for Kim et al. (2013) [39] and 25 kPa/day for Kim et al. (2015) [9]) for the sections CD and C'D' (Figure I-7). This indicates that *Rhodococcus* sp. BH4-mediated QQ seems to have no effect on the TMP jump stage in these two cases. In contrast, for Lee et al. (2016) [13] and Maqbool et al. (2015) [40] (references n° 6 and 20 in Table I-2), the point of 40 kPa was not actually reached and a less pronounced TMP jump was recorded (data not shown), which indicates a substantial effect of *Rhodococcus* sp. BH4-mediated QQ on the TMP jump.

Studying the effect of *Rhodococcus* sp. BH4-mediated QQ on the TMP jump in addition to its effect on the progressive biofouling stage may give interesting insight into how the QQ effectiveness might evolve over time in the MBR. According to these results, it seems that *Rhodococcus* sp. BH4-mediated QQ

tends to be globally more effective in inducing modifications of the TMP profile during the first progressive biofouling stage than during the TMP fast jump stage, which could be attributed to a potential loss of the QQ effectiveness. Another potential explanation could be that another type of QS-controlled biofouling (e.g., AI-2-controlled QS for interspecies communication), against which the *Rhodococcus* sp. BH4 cells have no effect, becomes predominant over the AHL-controlled one. However, further research would be needed to clarify these assumptions. All these results taken together with the number of cycles of the control MBRs compared to the QQ MBRs clearly indicate that the implementation of *Rhodococcus* sp. BH4-mediated QQ substantially reduces the membrane cleaning frequency.

Cheong et al. (2013,2014) [55,56] investigated the effectiveness of *Pseudomonas* sp. 1A1 to mitigate biofouling in MBRs for running times ranging from 6 to 13 days. Concerning the comparison of the times t and t' at which the breaking points C and C' were reached for the control and the QQ MBR, respectively (Figure I-7), the time elapsing before the TMP jump was observed to increase by 180% (corresponding to an almost threefold postponement) (reference n° 1 Table I-3). When consortia of QQ bacteria were implemented (references n° 8 to 10 in Table I-3), the effect on the delay of the breaking point was even more visible, with up to a 450 % increase (reference n° 10 in Table I-3). Thus, when comparing these studies (Table I-3), it appears that the use of QQ consortia leads to the most pronounced effect on the TMP jump, probably because of the complementarity of the QQ bacteria that results in a stronger activity. When comparing the slopes corresponding to the TMP jump sections CD and $C'D'$ (Figure I-7), the times necessary to attain the pressures of 25 kPa and 40 kPa in presence of *Pseudomonas* sp. 1A1, were both seen to be delayed by approximately 3 days (reference n° 1 in Table I-3). Although these results reveal that other bacteria-mediated QQ does indeed have an effect on biofouling, more research is needed to unravel how the effectiveness of each of these bacteria evolves over time.

1.1.8.3. Effect on the mixed liquor characteristics

It is important to evaluate the effect of QQ on the mixed liquor characteristics, particularly in terms of EPS and AHL amounts, since these are good indicators of biofouling.

EPS are well-known to be closely related to biofouling in MBRs since they are the “glue” that holds the biofilm cell clusters attached to the membrane [16]. In other words, a noticeable increase in the amount of EPS in the MBR is correlated with a heightened biofouling phenomenon. The total quantity of EPS in the mixed liquor can be divided into soluble microbial products (SMP) and EPS bound to the microbial flocs. In principle, these fractions need to be collected separately to be further analyzed (for more details on EPS extraction methods, see Domínguez et al. (2010) [82]).

With the implementation of *Rhodococcus* sp. BH4 as a QQ bacterium, Maqbool et al. (2015) [40] determined the amount of SMP in the mixed liquor by analyzing the supernatant from an AS sample (reference n° 6 in Table I-2). A 90 % reduction in the SMP amount was recorded after 80 days of

operation, indicating that *Rhodococcus* sp. BH4-mediated QQ had a strong effect on the EPS production. In addition, significant reductions in the amounts of proteins (from 32 to 71 %) and polysaccharides (from 62 to 85 %) in the mixed liquor were obtained (references n° 16 and n° 20 to 22 in Table I-2). It is important to quantify this effect since it has been shown that, in some cases, the solutes and colloids in the supernatant play a more important role in biofouling than the biological pellets [83,84]. Nevertheless, it is still worth mentioning that slight reductions in the amounts of bound EPS were obtained with the application of BH4 mediated-QQ, with -32 % and -5 % in the loosely-bound EPS (LB-EPS) and the tightly-bound EPS, respectively [40]. Lee et al. (2016) [13] also recorded an average reduction of 17 % in the amount of bound EPS in mixed liquor.

Concerning the amount of AHLs in the mixed liquor, given that these signal molecules are usually produced at very low concentrations (in the range of picograms to nanograms per liter) and that they are present as a complex mixture with different compounds, an extraction procedure is necessary before the quantification [85,86]. Several quantification methods to measure the AHL concentration after their extraction have been reported to date and are summarized by Siddiqui et al. (2015) [20]. Maqbool et al. (2015) [40] extracted the AHLs from the supernatant of a broth sample then analyzed them using HPLC. A much smaller AHL concentration was observed in the QQ-MBR than in the control MBR (qualitative results). Hence, Maqbool et al. (2015) [40] came to the conclusion that the implementation of *Rhodococcus* sp. BH4 leads to a biofouling reduction via the destruction of AHLs in the mixed liquor, which is consistent with previous studies [38]. This result shows that monitoring the AHL concentration in the mixed liquor could help evaluate the progress of the QQ activity in MBRs. However, no information about the evolution of this concentration during the MBR operation is provided in the studies noted in Table I-2, probably because of the very low amounts, which would make the quantification laborious.

Recently, Lee et al. (2016) [13] showed that QQ could have an effect on the floc size of the AS. In a pilot-scale MBR of 80 L, they recorded a 17% reduction in the average floc size. However, in a three-stage MBR of a total working volume of 450 L, composed of three tanks of 150 L (anoxic, aerobic and membrane tank), QQ did not lead to major differences in floc size in each tank. Thus, there is no clear trend yet about the influence of *Rhodococcus* sp. BH4-mediated QQ on the floc size of the mixed liquor.

Concerning the effect of the other QQ bacteria reported to date on the sludge characteristics, it has only been assessed in terms of SMP. Cheong et al. (2014) [56] have reported a 60 % reduction in the amount of polysaccharides, whereas the reduction in proteins was merely 6 % (references n° 4 and 5 in Table I-3), when *Pseudomonas* sp. 1A1 was used as a QQ strain. These results suggest that *Pseudomonas* sp. 1A1-mediated QQ targets the QS-controlled genes in charge of the production of polysaccharides in a more pronounced way. On the other hand, Xiao et al. (2018) [58] recorded more significant reductions in both proteins (- 61 %) and polysaccharides (- 93 %) when a QQ consortia was used to control

biofouling (reference n° 10 in Table I-3). The latter result confirms the assumption that the different QQ bacteria could mitigate biofouling by targeting different QS-controlled genes, which is actually in favor of using QQ consortia rather than single QQ stains.

Given the current stage of knowledge and the few elements known so far, additional research into the effect of QQ on other properties such as zeta potential, viscosity, or Sludge Volume Index (SVI) is required to provide complementary data to understand exactly how QQ bacteria affect the mixed liquor characteristics.

1.1.8.4. Effect on the biodegradation efficiencies in the MBR

The effect on the MBR performance should obviously be evaluated to make sure the implementation of QQ does not impair the MBR treatment capacities. For 15 of the studies considered in Table I-2 (references n° 5 to 16, n° 19 and n° 21 to 22), this was assessed in terms of Chemical Oxygen Demand (COD) removal efficiencies and resulted in very negligible variations (less than a 3% modification compared to the control MBR) [9,39,40,51–53]. The fact that the COD removal efficiencies remained practically unchanged indicates that the use of *Rhodococcus* sp. BH4 as QQ bacteria induces no adverse effect on the ability of the biomass to metabolize the organic matter in the MBR. The same approach was used to assess Total Kjeldahl Nitrogen (TKN) removal and resulted in less than a 5% variation compared to the control MBR, when the *Rhodococcus* sp. BH4 cells were entrapped in CEBs, microbial vessels or RMCF (data not shown) [51]. For Lee et al. (2016) [13], neither the total nitrogen removal efficiency nor the ammonia-nitrogen (NH₄-N) removal efficiency was significantly affected when *Rhodococcus* sp. BH4-mediated QQ was used in a pilot-scale MBR. In the same way, the implementation of *Pseudomonas* sp. 1A1 or *Bacillus* sp. T5 to mitigate biofouling in an MBR resulted in negligible differences in the biodegradation efficiencies [55,56,59].

Therefore, these findings confirm that single strain-mediated QQ effectively mitigates biofouling without affecting the MBR treatment performance in terms of COD and TKN removal efficiencies. However, no information is available yet in the literature concerning the biodegradation efficiencies in presence of QQ consortia.

1.1.9. Effect of bacterial QQ on the MBR performance at microscopic scale

At microscopic scale, the effect of bacterial QQ can be highlighted by the observation and the characterization of the biocake formed on the membrane.

1.1.9.1. Effect on the amount of biofilm

Biofouling is known to result from biocake formation on the membrane surface, of which biofilm (cells + EPS) is a major component. When studying biofouling in MBRs, the observation of biocake or biofilm becomes particularly relevant to determine whether the mitigation strategy employed reduces biofilm formation effectively.

In this context, membranes are usually taken out at the end of operation and specimens are cut off to measure the Total Attached Biomass (TAB) and/or to conduct microscopic observations using Confocal Laser Scanning Microscopy (CLSM) to evaluate the biofilm morphology. In presence of *Rhodococcus* sp. BH4, an approximate 50 % (w/w) reduction in TAB has been reported after 1.7 and 9 days of operation by Oh et al. (2012) [11] and Kim et al. (2015) [9], respectively, while Kim et al. (2013) [39] recorded a 70 % reduction after only 3 days of operation, which was in accordance with the CLSM observations (references n° 1, 5 and 19 in Table I-2). Lee et al. (2016) [13] recorded the most pronounced reduction in TAB with almost 90 % after 14 days of operation (reference n° 20 in Table I-2).

Concerning the effect of other bacteria-mediated QQ at the microscopic scale, Cheong et al. (2014) [56] obtained a 60% reduction in the TAB on the membrane when *Pseudomonas* sp. 1A1 bacteria-encapsulating CMV was used in the MBR (reference n° 2 in Table I-3). Besides, Gül and Koyuncu [59] obtained significantly thinner biofilm at the end of the operation (10 days) when *Bacillus* sp. T5 was implemented as QQ bacteria in microbial vessel. These findings clearly highlight the effectiveness of bacterial QQ in reducing the amount of biofilm. However, complementary quantitative data on the biofilm thickness, porosity, etc., would be pertinent to identify possible structural modifications induced by QQ bacteria.

1.1.9.2. Effect on the biofilm composition

The biofilm composition is usually discussed in terms of EPS amounts. First, the biocake is detached from the used membrane by placing it in a water tank equipped with an air-scouring system and/or with sonication followed by an air-scouring system [39]. Finally, EPS are extracted from the biocake in suspension using the Cation Exchange Resin (CER) method developed by Jahn and Nielsen [87].

When *Rhodococcus* sp. BH4 was introduced into lab-scale MBRs to assess its QQ potential, Kim et al. (2013) [39] reported an 80 % reduction in the total amount of EPS in the biocake after only 3 days of operation (reference n° 5 in Table I-2). Lee et al. (2016) [13] obtained a 20 % reduction in the amount of proteins, whereas the amount of polysaccharides remained practically unchanged (reference n° 20 in Table I-2). On the other hand, the amounts of proteins and polysaccharides in the biocake were reduced by approximately 50 % and 90 % after 32 days of operation Kim et al. (2015) [9] (reference n° 19 in Table I-2). In presence of *Pseudomonas* sp. 1A1, the composition of biofilm, was reduced of about 80 % and 40 % in proteins and polysaccharides, respectively (reference n° 4 in Table I-3). These findings support the assumption that bacterial QQ mitigates biofouling by decreasing the EPS production in the biofilm.

1.1.10. Effect of the operating conditions on the effectiveness of bacterial QQ

It is of great interest to investigate the effects of the operating conditions on the effectiveness of bacterial QQ, in order to identify the optimal conditions that offer the most substantial mitigation of biofouling.

1.1.10.1. Effect of the initial quantity of QQ Bacteria inserted into the MBR

The quantity of *Rhodococcus* sp. BH4 initially inserted into the entrapping element in the MBR using PE microbial vessels has been studied for its potential effect on *Rhodococcus* sp. BH4-mediated QQ [50]. Oh et al. (2013) [50] reported that 13 days were required to reach the TMP of 30 kPa in a lab-scale MBR containing two PE microbial vessels packed with 8.9 g BH4/m² of the vessel surface area, whereas it took 28 days to reach the same TMP in a lab-scale MBR containing two vessels packed with 17.8 g BH4/m² of the vessel surface area (data not shown). A similar study has been reported using beads entrapping *Rhodococcus* sp. BH4 [51]. Two kinds of beads were prepared: with 1.5 mg BH4/cm³ of bead volume (beads I) and with 7.5 mg BH4/cm³ of bead volume (beads II). The two beads were placed in continuous lab-scale MBRs under the same operating conditions (references n° 7 and 8 in Table I-2). Beads I reduced the TMP by 93% (reference n° 8 in Table I-2), whereas beads II achieved almost 100% (reference n° 8 in Table I-2). This result is thus consistent with the previous study with the microbial vessels, i.e., the greater quantity gave rise to a more significant delay of biofouling whatever the QQ device. Cheong et al. (2014) [56] also experimented this effect by inserting two different initial quantities of *Pseudomonas* sp. 1A1 into the CMV: 26.5 and 70.3 mg biomass/cm³-lumen (corresponding to 266.4 and 706.8 mg biomass/L reactor respectively), both under the inner flow feeding mode. However, the permeate flux was not maintained constant for both initial quantities, which makes the results difficult to compare. Therefore, it could be interesting to evaluate the effect of the initial quantity on the QQ effectiveness, all other operating conditions the same.

1.1.10.2. Effect of the entrapping method

The mass transfer question has been further moved ahead by an analysis of the effect of the entrapping method on the *Rhodococcus* sp. BH4 efficiency in mitigating biofouling. The three entrapping methods mentioned above (microbial vessels, sodium alginate beads and RMCF) were compared under the same operating conditions with the same quantity of *Rhodococcus* sp. BH4 [51] (references n° 10 to 12 in Table I-2).

After 1 day of operation, beads were found to be the most efficient, with a reduction of 90 % in the TMP level (reference n° 10 in Table I-2) and the microbial vessel was the least efficient to reduce biofouling (reference n° 11 in Table I-2).

It is noteworthy that the TMP jump obtained with the beads seems to be the most pronounced, with only a 14 % fall in the TMP at the end of operation. This observation still remains unexplained, though Köse-Mutlu et al. (2015) [51] proposed a global assessment of the BH4 QQ effectiveness based on the ratio between the areas under the TMP curves. Consequently, based on these ratios, it was concluded that the more mobile the QQ device is, the more efficient is the biofouling mitigation via *Rhodococcus* sp. BH4-mediated QQ. This can be attributed to the higher probability of contacts between QQ media and AHL molecules promoted by the movement of QQ media. Another reason would be that the free movement

of the beads induces collisions between beads and membrane, resulting in a physical cleaning of the membrane in addition to the QQ effect, which thus enhances biofouling mitigation. This is consistent with previous studies demonstrating that vacant beads (with no QQ bacteria) or other inert particles also had the ability to reduce biofouling through a physical washing action that considerably delayed the time before the TMP jump was reached [39,88].

Also with the recent development of new sodium alginate media, the effect of the shape and size of the capsules has also been investigated [12,14,73]. Lee et al. (2016) [12] developed QQ beads and QQ hollow cylinders (Figure I-4) in various sizes and compared their QQ activity as well as their physical washing effect. It was found that the QQ activity tended to increase with the exchange surface for both shapes. In addition, the cylinders shape was identified as more favorable for a physical washing effect on the membrane owing to its bigger contact surface with the membrane. These results were further confirmed by Lee et al. (2016) [14] and Nahm et al. (2017) [73], when both of the QQ cylinders and sheets (with bigger exchange surface than beads) were found to have an enhanced capacity to mitigate biofouling in MBRs than QQ beads. Thus, in the case of free moving sodium alginate QQ media, the importance of the shape was clearly highlighted, and attributed to the bigger exchange surface that promotes the biological activity on the one hand (by fostering the mass transfer of AHLs towards and the core of QQ media), and the physical cleaning of the membrane surface on the other hand.

Nevertheless, very few information about the latter effect was reported in the literature, which is why the present work focuses on providing a better understanding, considering the different aforementioned aspects: the hydrodynamics, the mass transfer, and the physical cleaning. More details will be given in the strategy of the thesis.

1.1.10.3. Effect of the microbial vessel design

The effect of the microbial vessel material on the QQ effectiveness has also been investigated [50]. Four kinds of microbial vessels were designed, with different materials, pore sizes, surface areas and inner volumes. Each of the four vessels was packed with the same quantity of QQ bacteria (30 mg BH4/vessel). The influence of the microbial vessel design on the QQ effectiveness was evaluated for approximately 40 days of operation in MBRs with a working volume of 20 L. At certain times, the vessels were removed from the MBR to measure their QQ activity based on the degradation rate of C8-HSL over 45 days. The modified polyethersulfone (PES) membrane, which had the largest inner volume (0.98 mL), was found to offer the highest QQ activity, with around 60 % after 45 days. In comparison, the PE membrane and the two PVDF membranes with smaller inner volumes (0.20, 0.31 and 0.29 mL, respectively) only resulted in 20 % to 45 % after 45 days. This was attributed to the fact that the largest volume offered more space for the *Rhodococcus* sp. BH4 growth.

I.1.10.4. Effect of the location of the microbial vessel in the MBR

The effect of the specific location of the microbial vessel inside the MBR is another important factor that has been investigated. Jahangir et al. (2012) [10] designed a side-stream MBR (or external submerged MBR) with a total working volume of 2.8 L consisting of a bioreactor tank (2 L) and a membrane tank (0.8 L), with continuous recirculation between the two tanks. The operating conditions are noted in Table I-2 (references n° 2 and 3). In order to highlight the significance of the location of *Rhodococcus* sp. BH4 strain in the MBR, the microbial vessel was placed either in the bioreactor tank or in the membrane tank to carry out a comparative study in terms of TMP level. An overall enhancement of the *Rhodococcus* sp. BH4-mediated QQ activity was obtained when the microbial vessel was near the membrane, with a 50 % reduction in the TMP after 1 day of operation and about an 80 % reduction at the end of the operation. The corresponding reductions were approximately 20 % and 35 % when the microbial vessel was in the bioreactor. The time required to reach a TMP of 25 kPa was extended by 160 % when the vessel was in the membrane tank, whereas, it was delayed by only 110 % when the vessel was in the bioreactor. Therefore, the closer the microbial vessel is to the membrane, the greater is the capacity of *Rhodococcus* sp. BH4 to mitigate biofouling through QQ activity. It can be assumed that the AHLs in the biofilm on the membrane surface play a more significant role in biofouling than the AHLs from the mixed liquor. In addition, the importance of the question of mass transfer is raised again with this experiment since the nearer the QQ enzyme (intracellular AHL-lactonase) was to its substrate (AHLs from biofilm), the more pronounced was the biofouling mitigation in the QQ MBR.

I.1.10.5. Effect of the recirculation rate in a side-stream MBR

With the same side-stream MBR as above (or external submerged MBR), Jahangir et al. (2012) [10] considered the *Rhodococcus* sp. BH4-mediated QQ effectiveness as a function of the recirculation rate between the two tanks. For that purpose, the recirculation rate was set to 75, 150 and 300 times the permeate flowrate, and the effect on QQ effectiveness was assessed in terms of TMP. It was found that the QQ effectiveness increased with the recirculation rate, for both of the microbial vessel positions (data not shown). Besides, the QQ effectiveness appeared to be much more enhanced by an increased recirculation rate when the microbial vessel was in the membrane tank, than when it was in the bioreactor. These results again reinforce the significance of molecules transport, since they indicate that a greater recirculation rate promotes the transport of AHLs from the biofilm on the membrane surface so that they can be degraded inside the microbial vessel.

I.1.10.6. Effect of combined physical and/or chemical cleaning methods

Some studies focused recently on the combination of bacterial QQ with different physical methods for biofouling mitigation. Weerasekara et al. (2014) [42] investigated the coupling of *Rhodococcus* sp. BH4-mediated QQ with two physical cleaning modes: relaxation and air backpulse. The former consisted in a short break (1 min) after 19 or 29 min of filtration, while the latter consisted in injecting compressed air into the lumen side of the membrane for 20 s. In MBRs equipped with *Rhodococcus* sp. BH4-

entrapping microbial vessels, TMP monitoring over approximately 20 days of operation revealed that the QQ+air backpulse combination gave rise to a more significant biofouling reduction than QQ+relaxation (data not shown).

Weerasekara et al. (2016) [54] also combined the effect of BH4-mediated QQ with simple backwashing and chemically enhanced backwashing (using chlorine). The comparison of the TMP profiles revealed that the effect was more pronounced when chlorine was added in the backwashing flux with a reduction of 46 % after 14 days of operation, when only 33 % of reduction in the TMP was obtained after 9 days of operation with simple backwashing. The effect on membrane fouling was also characterized by quantifying the amount of biofilm, which was found to be reduced by 26 % and 36 % with the application of backwashing and chlorine-enhanced backwashing, respectively. Also, it was showed that the concentration of chlorine could further heighten the effect of QQ to mitigate biofilm formation, with – 60 % and – 50 % in the TMP level and the biofilm amount, respectively, after 48 days of operation. From these results, Weerasekara et al. (2016) [54] concluded that the effect of BH4-mediated QQ was even higher when chlorine was injected, and this was attributed to the capacity of chlorine to reduce chemical fouling which complements the action of QQ on the physical fouling.

Very recently, Xiao et al. (2018) [58] evaluated the coupled antifouling effect of Powdered Activated Carbon (PAC) together with QQ by entrapping a QQ consortium in sodium alginate/PAC media. This combination resulted in significant reduction of the TMP with more than 90 % at the end of the operation.

Although the added value of the PAC on the QQ efficiency was not clearly investigated in the latter study [58], the aforementioned results prove that the combination of bacterial QQ to conventional cleaning methods (physical and/or chemical) is a promising method for biofouling control in MBRs leading to excellent results in terms of TMP and biofilm amount.

1.1.10.7. Effect of the permeate flux

The effect of the permeate flux on the *Rhodococcus* sp. BH4-mediated QQ effectiveness was also investigated with beads as the entrapping method. Köse-Mutlu et al. (2015) [51] reported that an increase in the permeate flux from 30 to 50 L/m²·h severely impacted the *Rhodococcus* sp. BH4-mediated QQ effectiveness in terms of TMP reduction at the end of operation (– 97 % at 30 L/m²·h versus – 14 % at 50 L/m²·h). This can be explained by the fact that the formation of biocake is facilitated by the driving forces created with a high permeate flux. Another possible explanation is that the transport of AHLs from the biocake to the entrapped *Rhodococcus* sp. BH4 cells can be strongly counteracted by a high permeate flux.

In addition to the previous operating conditions, it could be of interest to investigate the effects of other parameters such as the aeration rate or the total working volume on the effectiveness of the *Rhodococcus* sp. BH4-mediated QQ with a view to identifying the optimal value for QQ efficiency.

From evaluations of the permeate flux using *Pseudomonas* sp. 1A1, it has been reported that a decrease in the permeate flux from 30 L/m²·h to 25 L/m²·h gives rise to slower biofouling (references n° 2 and 3 in Table I-3). As presented in Table I-3, the *Pseudomonas* sp. 1A1 effect on biofouling mitigation seems to be unchanged, since the TMP was reduced by approximately 80 % at the end of the MBR operation with the addition of QQ, under both of the permeate fluxes. Thus, modification of the permeate flux seemed to have no specific effect on the QQ effectiveness, but did have an effect on the biofouling kinetics in both the control and the QQ MBRs.

1.1.10.8. Effect of the feeding mode in case of CMV for entrapping Pseudomonas sp. 1A1

When a CMV was used as an entrapping device, the feeding mode made a significant difference in the performance of the QQ MBR [56]. The CMV was composed of a central lumen surrounded by six other lumens in a circle, into each of which *Pseudomonas* sp. 1A1 was inserted Figure I-4(b). The experiments carried out with 266.4 mg/L of *Pseudomonas* sp. 1A1 initially inserted into the MBR and with a permeate flux of 35 L/m²·h, showed that the inner flow feeding mode (i.e., MBR fed through the central lumen of the submerged CMV) resulted in an overall enhancement of the QQ effectiveness compared to the normal feeding mode (directly in the MBR tank) (references n° 4 and 5 in Table I-3). The TMP rise-up corresponding to the inner flow feeding mode was substantially delayed compared with that corresponding to the normal feeding flow, the TMP being approximately 60 % at the end of the operation for the inner mode, versus 25 % lower for the normal mode. In addition, the effect on the mixed liquor and the biocake composition in terms of EPS was more pronounced when the inner flow feeding mode was used (references n° 4 and 5 in Table I-3). Under the normal mode, *Pseudomonas* sp. 1A1 lost most of its QQ effectiveness over time with, with a 25% reduction in the TMP at the end of the operation, versus about 50% at the end of the first cycle (reference n° 5 in Table I-3), whereas the *Pseudomonas* sp. 1A1 activity remained practically unchanged under the inner mode (reference n° 4 in Table I-3).

In conclusion, the inner flow feeding mode gave rise to enhanced QQ activity of *Pseudomonas* sp. 1A1. Cheong et al. (2014) [56] attributed these observations to the higher viability of the encapsulated cells that occurred with relatively fresher feed by the inner flow feeding mode. In fact, the inner feeding is believed to enhance the mass transfer of nutrients from the feed to the *Pseudomonas* sp. 1A1 encapsulated cells, promoting the growth of the bacteria as well as their acylase production. However, it can also be assumed that the inner flow feeding mode would foster the transport of acylases by driving them from the CMV lumens to the mixed liquor, thereby increasing their probability of encountering and degrading the signal molecules of AHL molecules. The latter hypothesis would need to be confirmed by a comparative study of acylase mass transfer through the CMV in the two feeding modes.

1.1.10.9. Effect of the geometry of the filtration module

When using a multi-layer HF module for filtration and QQ beads or sheets as entrapping methods, Nahm et al. (2017) [73] showed that the physical washing effect of the QQ media was significantly greater on the outer fibers of the module than on its inner fibers. This finding indicates that the use of bacterial QQ entrapped in free-moving media could be of particular interest in presence of single-layer HF modules, rather than multi-layer ones, so that the total membrane area is entirely exposed to the cleaning effect of the QQ media.

1.1.10.10. Effect of the organic loading rate of the MBR

Waheed et al. (2017) [89] studied the effect of the organic loading rate in a 450 mL MBR equipped with HF as a filtration module. The monitoring of the TMP revealed that the effect of bacterial QQ entrapped in sodium alginate beads was more pronounced when the organic loading rate was kept constant in the MBR, than when it was gradually increased during the operation. These observations were also confirmed in terms of EPS production, indicating that an increase in the organic loading rate leads to a fast fouling phenomenon, against which the activity of the QQ bacteria is harder to express. From this result, it can be concluded that the application of bacterial QQ to MBRs should be achieved under constant organic loading rate with a view to getting the maximum effectiveness to reduce biofouling.

I.2. Concluding remarks and scientific strategy of the thesis

The results presented in this literature review for the different QQ strains identified to date, highlight some interesting features of bacterial QQ for membrane biofouling mitigation in MBRs. The mode of action of the QQ strains has been discussed through the nature and the localization of their QQ activity, and their resulting effect on the MBR at both the macroscopic and the microscopic scales. Also, the confrontation of the different QQ bacteria gathered in this review helped underline some **gaps in research** on the application of QQ for membrane biofouling control.

In the following, the main conclusions of this literature review are summarized and the interrogations that remain unsolved are deduced.

The QQ strains identified and reported in the literature all showed a great potential to mitigate biofouling. It appeared that the QQ effectiveness in mitigating biofouling depends on the MBR operating conditions.

- It has been reported that, the greater the initial quantity of QQ bacteria inserted in the MBR, the more efficient bacterial QQ can be to reduce membrane biofouling, for a given biomass concentration.
- Concerning the different entrapping methods, it has been demonstrated that the mobile entrapping elements (RMCF, CEBs and macrocapsules) give rise to enhanced QQ effectiveness in comparison to the stationary microbial vessel, probably because of the shear forces they create, which would promote the transport of the AHLs and/or induce a direct physical cleaning effect of the biocake on the membrane, however, no studies answering that question were reported. In the case of suspended QQ media (CEBs and macrocapsules) the physical effect is supposedly attributed to the direct contact with the membrane surface, but the exact link between the QQ media and the mitigation of biofouling via a physical effect was not identified to date.
- With the use of the microbial vessel, it has been shown that QQ is more effective to reduce biofouling when the vessel is closer to the membrane, which indicates that AHLs from the biocake play an important role in the QQ process.
- A higher recirculation rate in a side-stream MBR has been found to result in heightened QQ effectiveness. Also, the permeate flux was identified as having a negative influence on the effectiveness of both the QQ bacteria.
- Besides, QQ was found to allow significant energy savings in MBRs. As an example, about 30 % of reduction in the specific aeration energy demand was obtained in a lab-scale QQ-MBR [42], and the filtration energy consumption was reduced by approximately 50 % in a lab-scale QQ-MBR equipped with a chlorine-based backwashing system reported by Weerasekara et al. (2016) [54]. The bacterial QQ was also found to be effective to reduce biofouling in a pilot-scale MBR fed with real wastewater.

Moreover, Lee et al. (2016) [13] recently demonstrated in a pilot-scale MBR that the application of QQ could reduce by approximately 60 % the biofouling related energy consumption. Thus, the fact that the application of bacterial QQ leads to a significant reduction in both the energy consumption and the operating costs is an additional strong advantage showing that this is a viable method that could be used, at least in the near future, as a complement to physical and/or chemical cleaning methods.

It appears that great efforts have been made to optimize the bacterial QQ process, in particular by investigating the possible relationships between QQ effectiveness and the MBR operating conditions. Nevertheless, some crucial information is still missing and future research should focus on the few gaps revealed in order to make the application of bacterial QQ conceivable for membrane biofouling mitigation in MBRs in the near future.

- The presentation of the QQ activity localization and the entrapping elements for the different QQ bacteria considered helped underline that the **transport of the main molecules** involved in the QQ process (AHLs as substrates and lactonases or acylases as QQ endo/exo-enzymes) is not completely understood yet, although some assumptions have been made in that direction [12,14]. Hence, an in-depth characterization of the transport of these molecules in the MBR should be carried out, and the influence of the MBR hydrodynamics and the variety of immobilization methods should be investigated.

- The analysis of the bacterial QQ effect on the progressive biofouling stage has given some interesting clues about the time needed for the QQ activity to become significant in the MBRs. It appears that the QQ activity takes place in the early phase (after 1 day) of the MBR operation for most of the QQ bacteria. Thus, it could be of great interest for these QQ strains to investigate which of the QQ enzyme production or the QQ enzyme transport, is the **limiting step in the QQ process** for biofouling mitigation in MBRs.

- In all the studies considered in this review, the TMP jump was successfully delayed with the application of bacterial QQ over the run times investigated. However, bacterial QQ does not completely prevent biofouling; it simply postpones its occurrence. One of the hypotheses to explain this observation could be that **other kinds of QS-controlled biofouling** become prevalent in the MBRs. Thus, the relationship between biofouling and other kinds of autoinducers present in the MBR (i.e., AIPs and AI-2s) should be more deeply investigated, and might lead to a more efficient QQ strategy to mitigate biofouling.

This literature review states the fundamentals of the bacterial QQ for biofouling mitigation in MBRs. Even though it strongly relies on biological aspects, this approach was necessary for at least two reasons: firstly, to ensure a full understanding of the context of the topic, and secondly, to define an original scientific strategy for the present work. Indeed, the present study aims to investigate the application of QQ from the original and unexplored perspective of the physical phenomena (**hydrodynamics** and **mass transfer**) involved in the MBR and QQ-MBR processes. Therefore, the following aspects were stated as the main scientific questions to answer in this work:

- With the existing entrapping methods reviewed, and more specifically the free-moving entrapping media (QQ media), the application of QQ to MBRs results in a complex multiphase system (gas, solid, liquid), for which the effect on the **hydrodynamics** was identified as the first point of interest of the study. Therefore, the **first objective** of this work will be to study the impact of the addition of QQ media on the MBR hydrodynamics, at both the global (RTD and mixing) and local (characterization of the three phases) scales, and also, considering the short and medium-term operation, based on the characteristic times of the process (mixing time, hydraulic residence time).
- On another level, the literature review also revealed the importance of the **mass transfer** for the QQ reaction. Actually, QQ is an enzymatic reaction targeting AHLs, and as every (bio)chemical reaction, the mass transfer involving the main reagents can be of critical importance for its efficiency. For these reasons, the characterization of the mass transfer through the free-moving QQ media is addressed as the **second objective** of this study, in order to determine characteristic properties given the different shapes of QQ media reported to date, and the hydrodynamics conditions investigated in this work.
- After summarizing the experimental results and discussing their consistency and the relationships between the different parts, the **third objective** of the study is to evaluate the physical anti-fouling action involved in the QQ application under given hydrodynamics conditions.

In sum, the global aim of the present work is to conduct a **purely physical study** in order to bring ways of improvement for the double effect of QQ on biofouling mitigation: the biological effect (by studying the mass transfer for the QQ reaction) and the mechanical effect (by studying the hydrodynamics), in the specific case of **free-moving QQ media** (such as QQ beads, cylinders, sheets).

In order to meet the objectives of the study, an **experimental approach** was chosen and a particular type of MBR was selected for the QQ application: **air-lift MBR** (ALMBR). To our best knowledge, QQ was never applied to such a reactor, which makes the technical originality of the present work. The outline of the thesis is organized as follows:

In **Chapter II**, the detailed description of the ALMBR will be given and the materials and methods used for its characterization will be presented.

In **Chapter III**, the main addressed questions are: how do the QQ media behave in terms of fluidization under different conditions? What is the effect of the addition of QQ media on the hydrodynamics of the ALMBR? For that purpose, the different phases of ALMBR are characterized; using shadowgraphy, the bubbles size and velocity are determined, as well as the QQ media velocity and position. Using PIV, the liquid flow is investigated by measuring velocity profiles, average velocities, and shear stress at the membrane. Additionally, the fluidization of QQ media is studied under different aeration conditions using a camera technique and measuring a fluidization rate.

In **Chapter IV**, the focus is made on determining the effect of the addition of QQ media on the mixing and circulation performances of the ALMBR. With this view, the mixing time is measured using a tracer technique in the aerated part of the ALMBR. In order to investigate the circulation performance, a Residence Time Distribution (RTD) analysis under different conditions of aeration is conducted.

In **Chapter V**, the mass transfer phenomena are addressed. Based on what was reported in the literature, the mass transfer from/towards the QQ media is considered and a tracer is used to determine characteristic magnitudes, such as the transferred flux and the mass transfer coefficient. On that basis, the different shapes of QQ media are compared.

In **Chapter VI**, the physical effect of QQ media to reduce membrane fouling is investigated by running filtration experiments, using a model suspension to consider only the effect on cake fouling. Based on the permeability measurement, the results obtained for the three shapes of QQ media are discussed, and the obtained effect is put in relationship with the previous results of the study.

Finally, the main conclusions of this work as well as future perspectives and recommendations are given in the last section of the manuscript.

CHAPTER II. MATERIALS AND METHODS

II.1. Introduction

The strategy of the present work is to study the physical aspects involved in the application of QQ in an ALMBR. To meet the different objectives in terms of characterization of hydrodynamics, mass transfer and fouling, an experimental approach was developed and based on a diversity of techniques, among which some were specifically designed for the study.

First, the lab-scale ALMBR used for this work is presented and its main components and operating conditions are given. Then, for each part of the study, the approach is presented by explaining the principle of the method, the experimental setup and procedure, the main steps and calculations followed for the data processing (if necessary). In addition, the potential sources of experimental errors were discussed for the different methods and quantified when possible.

II.2. Experimental set-up

II.2.1. Lab-scale Air-Lift Membrane Bioreactor (ALMBR)

ALMBRs result from a combination of an air-lift reactor (ALRs) with an MBR. ALRs are multiphase reactors applied in a variety of processes such as fermentation, wastewater treatment, chemical industry...etc. ALRs consist in reactors comprising two distinct compartments: the riser in which gas (usually air) is injected in the form of bubbles that rise through the liquid, and the down-comer in which the liquid describes a downward motion. The difference of densities between these two compartments induce a recirculation of the liquid flow and constitutes a particular liquid motion that is characteristic of ALRs. Several configurations of ALRs exist and can be roughly categorized into internal-loop ALRs (in which the overall liquid circulation takes place in the same section) and external-loop ALRs (in which the liquid circulation takes place in two physically separated regions) [90,91]. Schematic illustrations of the different configurations of ALRs are presented in Figure II-1. For the internal-loop ALRs, two main configurations are possible: the split-cylinder ALR comprising one riser and one down-comer separated by an internal baffle; and the draft-tube ALR where the riser and the down-comer are two concentric cylinders. The geometry of ALRs is usually characterized by the area of its main parts: the riser area A_r , the down-comer area A_d , and also A_b , the area available for the liquid flow between the riser and the down-comer at the bottom of the reactor.

The ALMBRs are ALRs equipped with a membrane module (either HF or FS) in the riser part, as presented in Figure II-2. The ALMBRs were the subject of interest in the wastewater treatment field, because of their considerable advantages such as: a more efficient heat and mass transfer, a good mixing performance as well as a lower energy consumption. With the view to reducing biofouling, ALMBRs were also widely investigated and identified as a promising configuration [92–95].

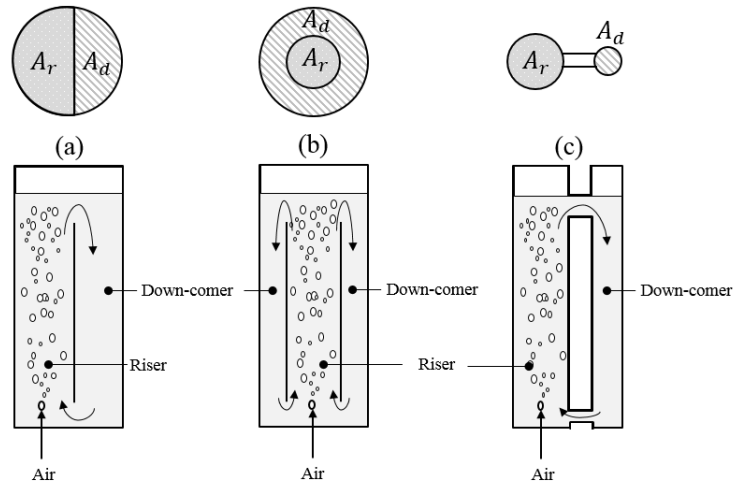


Figure II-1 : (a) Internal-loop split-cylinder (b) internal-loop draft-tube and (c) external-loop ALR.

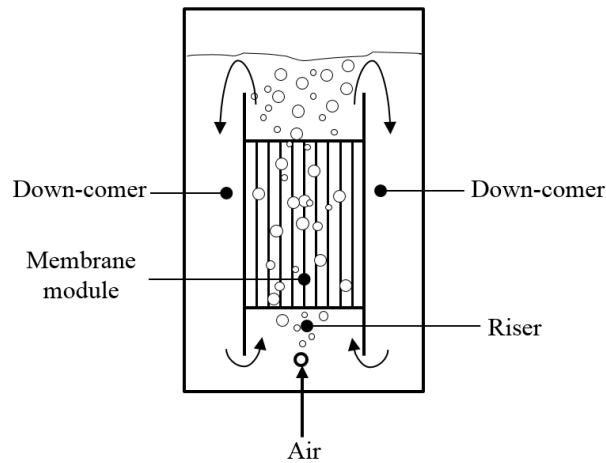
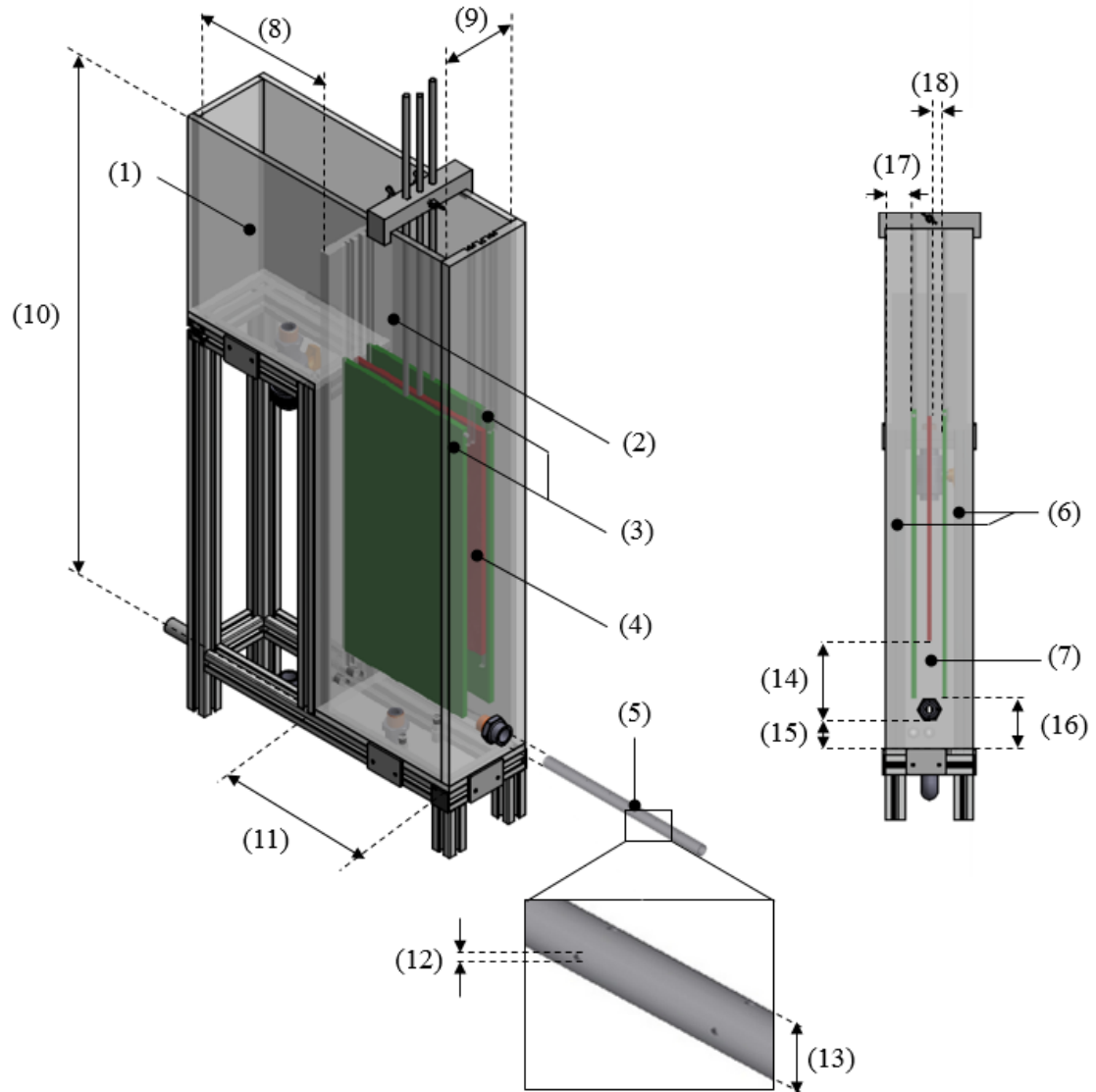


Figure II-2 : Air-lift Membrane Bioreactor.

II.2.1.1. Description of the reactor

In the present study, the experiments were carried out in a lab-scale ALMBR with a total working volume of 18 L, composed of an anoxic tank (5 L) and an aerobic tank (13 L), in a similar way to the one described by previous research work [80,96]. Figure II-3 shows the geometry of the lab-scale ALMBR, its components and the different flows in it. The membrane was submerged in the aerobic tank. The ALMBR was fed with a peristaltic pump (Masterflex L/S), in the stirred (188 rpm) anoxic tank and the overflow dropped into the aerobic membrane tank. A continuous recirculation flow from the aerobic tank to the anoxic tank was set using a peristaltic pump (Masterflex) (Figure II-4). The working flowrates, as well as the operating conditions, will be presented in the following.



MBR components

- (1) Anoxic tank (5 L)
- (2) Aerobic tank (13 L)
- (3) Baffles
- (4) Flat sheet membrane
- (5) Air sparger (perforated tube with 2 rows of 7 holes each)

Air-lift parts

- (6) Down-comer
- (7) Riser

Dimensions (mm)

- (8) 240
- (9) 116
- (10) 800
- (11) 210
- (12) 2
- (13) 8/10 (inner/outer)
- (14) 140
- (15) 20
- (16) 65
- (17) D_d (variable)
- (18) D_r (variable)

Figure II-3 : Diagram of the lab-scale Air-Lift Membrane Bioreactor (ALMBR).

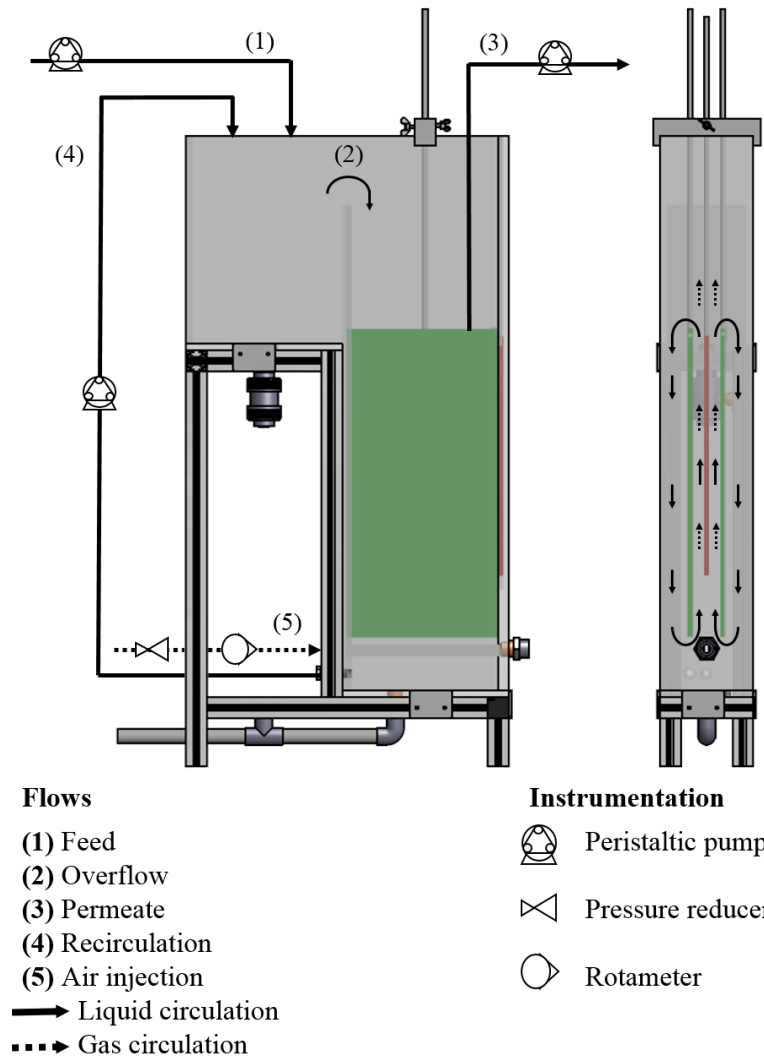


Figure II-4 : Process flow and instrumentation diagram of the lab-scale Air-Lift Membrane Bioreactor (ALMBR).

The aerobic tank was equipped with an air-sparging system consisting in a coarse air bubbles injection through a perforated plastic tube, composed of two rows of seven 2 mm-holes each (multi-orifice sparger). The air sparger was located at the bottom of membrane (Figure II-3), and the injection of air through it was measured by a calibrated rotameter (Figure II-4).

Two baffles (represented by the green plates, component (3) on Figure II-3) were set on both sides of the membrane (represented by the red plate), with a view to creating an air-lift configuration with three separated parts. As it is possible to notice on Figure II-3 and Figure II-4, three separated parts are thus created in the aerobic tank : an aerated part with an upward circulation called the riser in the center, and two non-aerated parts called the down-comer, on both sides of the riser. The circulation of fluids created by the air-lift configuration are presented on Figure II-4. The riser part has a total width of $2D_r$ and a total riser cross-sectional area (A_r), whereas the down-comer part has a total width of $2D_d$ and a total cross-sectional area (A_d).

II.2.1.2. Membrane and filtration mode

A single flat sheet membrane was used as a filtration module (represented by the red plate, component (4) on Figure II-3). The membrane was made of Polyether Sulfone (PES) and the module was 315 mm-long, 225 mm-wide and 7 mm-thick (Kubota, Japan). The average pore size was 0.2 μm and the total area 0.1 m^2 . The selected membrane only allowed the external-to-internal filtration. The permeate suction was ensured by a peristaltic pump (Masterflex), at a constant flux, and the selected permeate flux will be presented in the following.

II.2.2. Implementation of Quorum Quenching (QQ) media

II.2.2.1. Physical properties of QQ media

The QQ media used in this study were made of sodium alginate and provided by the Water Environment – Membrane Technology (WEMT) laboratory (School of Chemical and Biological Engineering, Seoul National University, South Korea). The production method consisted in dripping a homogeneous liquid alginate suspension (complemented with a QQ bacteria suspension or not) into a CaCl_2 solution to obtain solid particles, with different shapes, as reported in the literature [14,39,73]. Three different shapes of QQ media were used in this study: QQ beads, QQ hollow cylinders and QQ sheets (Figure II-5).



Figure II-5: Photographs of the Quorum Quenching (a) beads (b) hollow cylinders and (c) sheets.

The physical properties of the QQ media are summarized in Table II-1. The volume, surface, specific surface and number of particles in 1 mL were deduced from the average dimensions. The wet density was measured with a pycnometer, and the free-falling velocity was determined visually by measuring the time for a particle to reach the bottom of the reactor filled with water.

Table II-1 : Physical properties of the QQ media.

QQ media	Beads	Hollow cylinders	Sheets
Dimensions (mm)	Diameter: 3.5	Inner diameter: 1.7 Outer diameter: 3.5 Length: 27	Length: 20 Width: 10 Thickness: 0.5
Volume of a particle (mm ³)	22.5	198.5	100
Surface of a particle (mm ²)	38.5	455.8	400
Specific surface of a particle (mm ⁻¹)	1.7	2.3	4
Number of particles in 1 mL of QQ media	44	5	10
Wet density (g.cm ⁻³)	1.074 ± 0.002	1.06 ± 0.01	1.063 ± 0.004
Free-falling velocity (m.s ⁻¹)	0.035 ± 0.002	0.024 ± 0.003	0.011 ± 0.002

II.2.2.2. Addition of QQ media to the MBR

The QQ media were only introduced in the aerobic tank since the membrane was comprised in it (Figure II-3). The QQ media were indifferently introduced before or after the aeration was switched on, since this was found to have no influence on their fluidization.

II.3. Varying operating parameters

II.3.1. Inter-membrane distance

The inter-membrane represents the distance between the membrane surface and the baffle, which also corresponds to half of the total riser width ($2D_r$) (Figure II-3). This distance could be varied by changing the position of the two baffles, creating different air-lift configurations. Two inter-membrane distances were tested: $D_r = 7 \text{ mm}$ and $D_r = 15 \text{ mm}$. The rest of the geometrical characteristics of the air-lift created by these two positions are specified in Table II-2.

II.3.2. Aeration

The air flowrate in the air-sparging system was varied in this study. In MBRs, the aeration can be characterized in terms of Specific Aeration Demand (SAD), either with respect to the total membrane area A_m ($SADm$ in $\text{Nm}^3 \cdot \text{h}^{-1} \cdot \text{m}^{-2}$), or to the total permeate flux J in $\text{m} \cdot \text{s}^{-1}$ ($SADp$ unitless), according to Equations II-1 and II-2, respectively, where Q_g is the air flowrate [97].

$$SADm = \frac{Q_g}{A_m} \quad \text{II-1}$$

$$SADp = \frac{Q_g}{JA_m} \quad \text{II-2}$$

Five different values were chosen based on the literature and ranged from 0.03 to 0.10 Nm³/h (i.e. 0.30 to 1.00 in terms of SADm) and 30 to 100 Nm³/m³ permeate in terms of SADp), which fits into the range of industrial MBRs [98]. In terms of superficial gas velocity U_{gr} , defined as the ratio of the air flowrate to the cross-section of the riser A_r opened to the passage of gas (Equation II-3), the investigated conditions of aeration depended on the distance D_r , as indicated in Table II-2.

$$U_{gr} = \frac{Q_g}{A_r} \quad \text{II-3}$$

II.3.3. Volume fraction of QQ media

The selected QQ media were added to the ALMBR in different volume fractions that were reported in previous studies investigating the efficiency of QQ application to hollow fibers lab-scale to pilot-scale MBRs [9,39,40]. The selected volume fractions of QQ media were 0.06, 0.10 and 0.45 % v/v (Table II-2), and all of them corresponded to a volume of QQ media negligible compared to the total working volume of the ALMBR, in order not to generate significant differences in the global behavior of the reactor, and make the comparison with the vacant ALMBR possible.

Table II-2 : Ranges of variation of the operating parameters of the ALMBR/ QQ-ALMBR.

Operating parameters	
Air-lift	
Inter-membrane distance D_r (mm)	[7 ; 15]
Total riser width $2D_r$ (mm)	[14 ; 30]
Total down-comer width $2D_d$ (mm)	[80 ; 64]
Total riser cross sectional area A_r (m ²)	[0.00294 ; 0.0063]
Total down-comer cross sectional area A_d (m ²)	[0.0168 ; 0.01344]
A_r/A_d ratio (-)	[0.175 ; 0.469]
Liquid height h_D (m)	0.585
MBR	
Feed flow (L.h ⁻¹)	[0 ; 1.5]
Recirculation flow (L.h ⁻¹)	[0 ; 4]
Filtration flux (LMH)	[0 ; 15]
SADm (Nm ³ .h ⁻¹ .m ⁻²)	[0.3 → 1.78]
U_{gr} (m.s ⁻¹) for: $D_r = 7$ mm	[0.0028 → 0.0094]
$D_r = 15$ mm	[0.0013 → 0.0044]
QQ media	
Volume fraction (% v/v)	[0.06 ; 0.10 ; 0.45]
Total number (N_{TM}) of:	
Beads	[347 ; 578 ; 2600]
Hollow cylinders	[39 ; 65 ; 298]
Sheets	[78 ; 130 ; 585]

II.4. Characterization of the hydrodynamics

The tools used for the characterization as well as the physical magnitudes measured are summarized in Table II-3 before giving their detailed explanation in the following.

Table II-3 : Tools and physical magnitudes used for the characterization of the hydrodynamics.

Characterization tool	Characterized phase	Physical magnitude measured
Camera (images)	Solid (QQ media)	Fluidization rate
Shadowgraphy	Solid (QQ media)	Velocity
	Gas (bubbles)	Position with respect to the membrane
		Size
		Velocity
Particle Image Velocimetry (PIV)	Liquid	Velocity field
		Velocity profile
		Average velocity
		Membrane shear stress

II.4.1. Evaluation of the QQ media fluidization by camera (images)

II.4.1.1. Principle and set-up

In this study, the visualization was an important tool for the characterization of the hydrodynamics, especially in presence of QQ media. In that purpose, a camera (Canon EOS 500D) together with a lens (Canon zoom lens EF-S 18-55 mm) were used to capture images. This method was used to study the fluidization of the QQ media under different operating conditions. For this to be achieved, a 142 mm x 90 mm-window of the MBR was chosen for the visualization (Figure II-6(a)). This window was selected because the clear baffles allowed seeing the whole depth of the reactor.

II.4.1.2. Experimental protocol

The fluidization was studied for the three shapes of QQ media introduced in the three aforementioned volume fractions (0.06, 0.10 and 0.45 % v/v). The two positions for the baffles ($D_r = 7$ mm and $D_r = 15$ mm) were experienced, and a total of 8 different air flowrates were tested. The experimental procedure is summarized in Figure II-7. A total of 144 conditions were thus selected, and in each condition, 12 pictures (replicates) were taken to be analyzed.

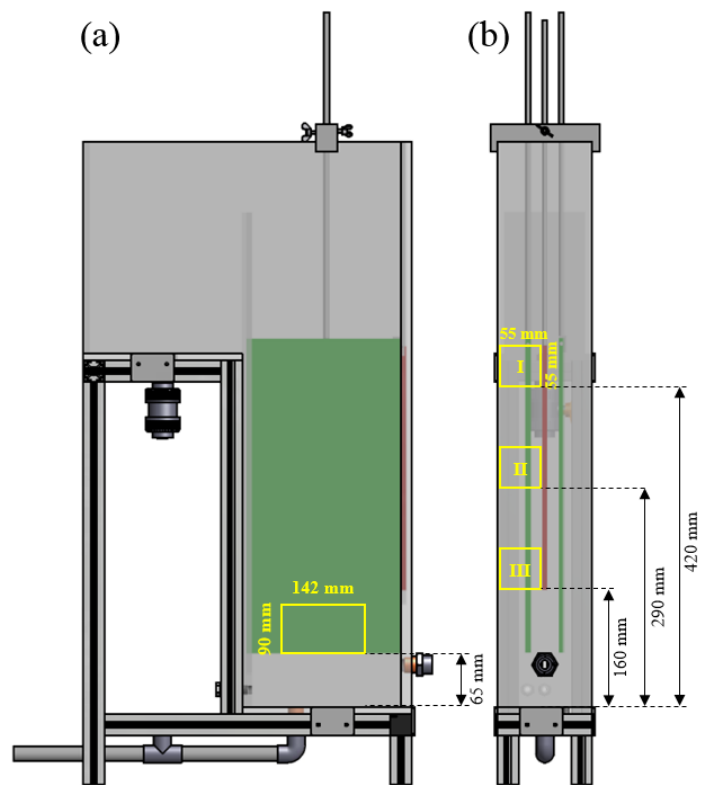


Figure II-6 : Selection of the observation windows for (a) the study of the fluidization (b) the shadowgraphy.

		Volume fraction (% v/v)	D _r (mm)	SADm (Nm ³ .h ⁻¹ .m ⁻²)
Shape				
QQ media	Beads Hollow cylinders Sheets	0.06 0.10 0.45	7 15	0.30
				0.40
				0.50
				0.75
				0.90
				1.00
				1.35
				1.78

Figure II-7 : Experimental procedure for the study of the QQ media fluidization.

II.4.1.3. Determination of the fluidization rate of QQ media

On the basis of the 10 pictures, the fluidization rate was defined in each case as the percentage of fluidized QQ media, in other words, the number of fluidized (in suspension) QQ media (N_{FM}) divided by the total number of QQ media introduced in the reactor (N_{TM}) (Equation II-4). In that way, the number of particles in each picture was counted and corresponded to the volume of the observation window (1.4 L). Making the hypothesis that the fluidized QQ media were homogeneously distributed in the aerobic tank, the number was multiplied in order to deduce the number of fluidized particles (N_{FM}) in the whole volume of the aerobic tank (13 L). The results from the 10 pictures were averaged to determine the average fluidization rate corresponding to every single operating condition. The 10 images were recorded with a 15 s-time interval between two consecutive pictures, in order to be more representative of the long-term behavior of QQ media in the reactor.

$$\text{Fluidization rate (\%)} = \frac{N_{FM}}{N_{TM}} \times 100 \quad \text{II-4}$$

II.4.1.4. Relevancy of the average fluidization rate

An example of pictures is presented in Figure II-8. This example was selected because it corresponds to the condition with the biggest discrepancies between the 10 images of a series, and was obtained in presence of QQ beads, loaded at 0.45 % v/v (2600 QQ beads in total) in the reactor, under an SADm of $0.90 \text{ Nm}^3 \cdot \text{h}^{-1} \cdot \text{m}^{-2}$.

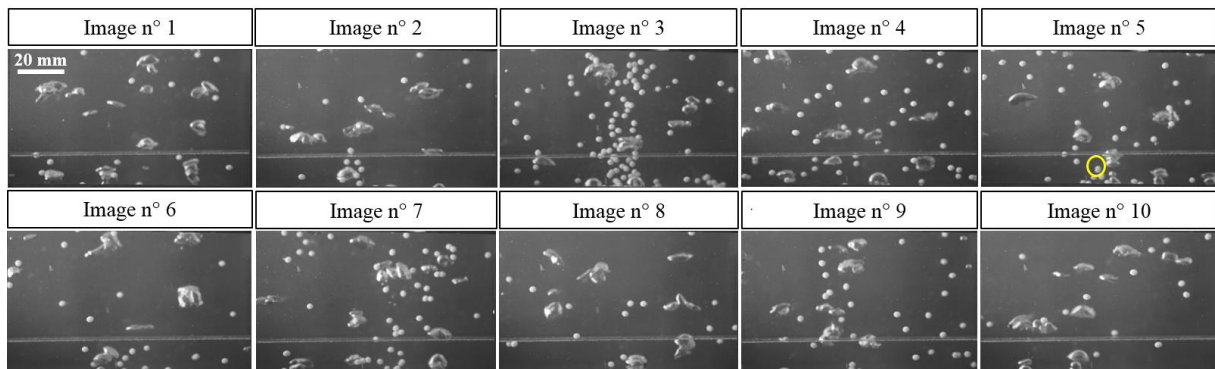


Figure II-8 : Series of images recorded for the determination of the fluidization rate of beads introduced at 0.45 % v/v and under an air flowrate of $0.90 \text{ Nm}^3 \cdot \text{h}^{-1} \cdot \text{m}^{-2}$.

The QQ beads were counted in each picture to deduce the corresponding fluidization rate, as presented in Table II-4. It is possible to observe important discrepancies from one image to another, which result in a big standard deviation representing 72 % of the average value, in terms of number of fluidized media (N_{FM}) and 72.5 % in terms of the corresponding fluidization rate.

Table II-4 : Determination of the fluidization rate corresponding to the conditions presented in Figure II-8.

Image n°	Number of QQ beads in the	N_{FM}	N_{TM}	Fluidization rate (%)
1	14	130	2600	5
2	15	139		5.3
3	95	882		33.9
4	51	473		18.2
5	32	297		11.4
6	19	176		6.8
7	49	455		17.5
8	17	157		6.0
9	31	287		11.0
10	14	130		5
Average value	33	312		12.0
Absolute standard deviation	25	226		8.7
Relative standard deviation (%)	76	72		72.5

These elements reveal the following:

- The fluidization phenomenon itself which is a random and “cyclic” phenomenon, as it appears in the image n°3 in Figure II-8, an important amount of QQ media can be suddenly set in suspension before settling back to the bottom of the reactor.
- The counting of QQ media on the images can also be misleading as it was not unusual to see QQ media almost perfectly superimposed, as presented in the circled area in the image n° 5 (Figure II-8), which makes it hard to determine whether it is one single particle or two superimposed particles.
- The simplifying assumption of the uniform distribution of QQ media in the reactor which was made to obtain the total number of fluidized QQ media in the reactor N_{FM} . This hypothesis was made because the camera technique did not allow the visualization of the whole aerobic tank, but it can be assumed that it is not fully correct. Indeed, it can be observed in Figure II-8 that the QQ beads are not uniformly distributed in every single image, therefore, not uniformly distributed in the whole reactor.

In sum, the average fluidization rate was selected as a criterion to compare the different shapes of QQ media under different conditions, but as it is demonstrated with this example (corresponding to the worst case with 72 % of relative standard deviation), it is worth keeping in mind that the fluidization rate can vary in time because of the aeration frequency and that the calculation of the average fluidization rate is based on the hypothesis of a uniform distribution of QQ media.

II.4.2. Characterization of the QQ media and bubbles by shadowgraphy

II.4.2.1. Principle

The shadowgraphy is a visualization technique used to observe and characterize non-uniformities in transparent media. The technique consists in using a camera together with a light panel to reveal the shadows of the considered system. The shadows result from a disturbance of the light rays, which is due to the difference of refractive indexes of the different elements. Some physical properties, such as the distance, the distortion, the motion, etc., can be accurately inferred from this technique. The camera is usually monitored by a computer and an acquisition software. A great number of images can be recorded by this method, and a computational program is usually used to process all of them.

II.4.2.2. Setup

In this study, the shadowgraphy technique was used in order to characterize both of the gas phase and the solid phase. The experimental setup consisted in a Complementary Metal-Oxide-Semiconductor (CMOS) camera (acA1920 - 155 μm , 1920 x 1200 pixels², 164 fps, Basler) with a 105 mm lens (Micro-NIKKOR, 105 mm, Nikon). A backlight panel (Phlox-LedW-BL, 400 x 200 mm², 24 V, 2A, Phlox) was set up against the back of the aerobic tank in order to illuminate the reactor (Figure II-9).

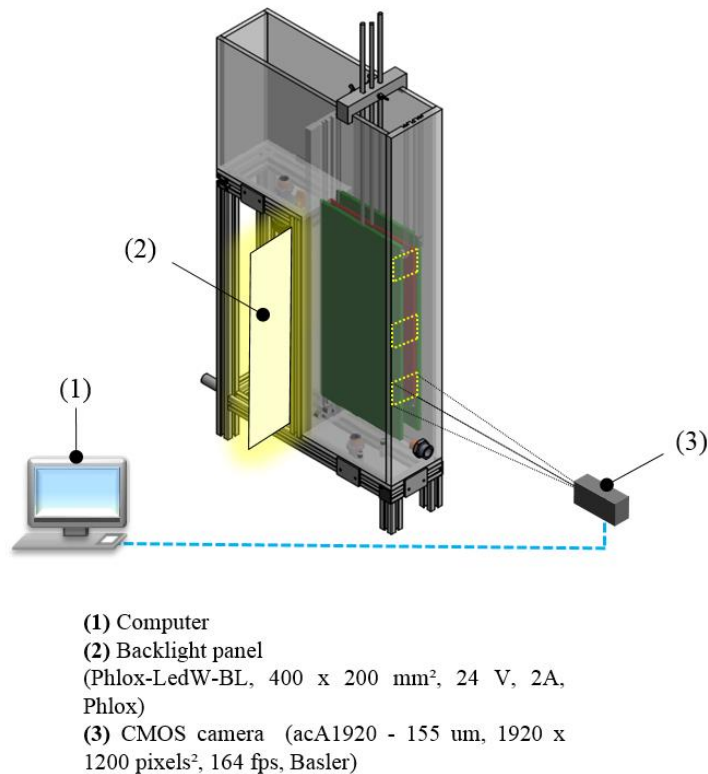


Figure II-9 : Shadowgraphy setup for the hydrodynamics characterization of the reactor.

The acquisition of pictures was set to 200 Hz and lasted 15 s. The images were acquired using the appropriate software (pylon Viewer 64-bit) and then processed using a Matlab (MathWorks, USA) program which will be further detailed. The focus was made on the median plane in the middle of the reactor, orthogonally to the camera. The images had a size of 1600x960 pixels² and were recorded in grey level. The observation was made in the previously defined windows (I, II and III on Figure II-6), located respectively at the top, the middle and the bottom of the membrane.

II.4.2.3. *Experimental protocol*

In this part of the work, the shadowgraphy technique was applied for each QQ media shape, for each of the three volume fractions, in each of the three observation windows (I, II, III), under the two possible positions for the baffles (7 and 15 mm). In each of these conditions, a total of 5 air flowrates was tested. The experimental procedure as well as the order in which the parameters were varied appear in Figure II-10. In sum, 270 different conditions were selected and tested in presence of QQ media, in addition to 30 conditions in absence of QQ media corresponding to the 3 windows, the 2 positions and the 5 air flowrates.

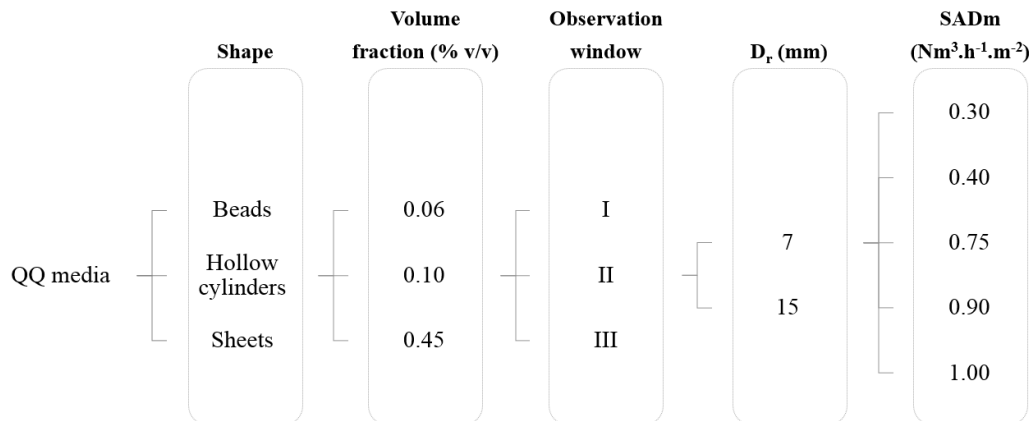


Figure II-10 : Experimental procedure for the study of the hydrodynamics in presence of QQ media.

II.4.2.4. Image processing for the determination of the hydrodynamics parameters

A Matlab (MathWorks, USA) program was used to process the shadowgraphy images and was mainly based on the operations presented in Figure II-11.

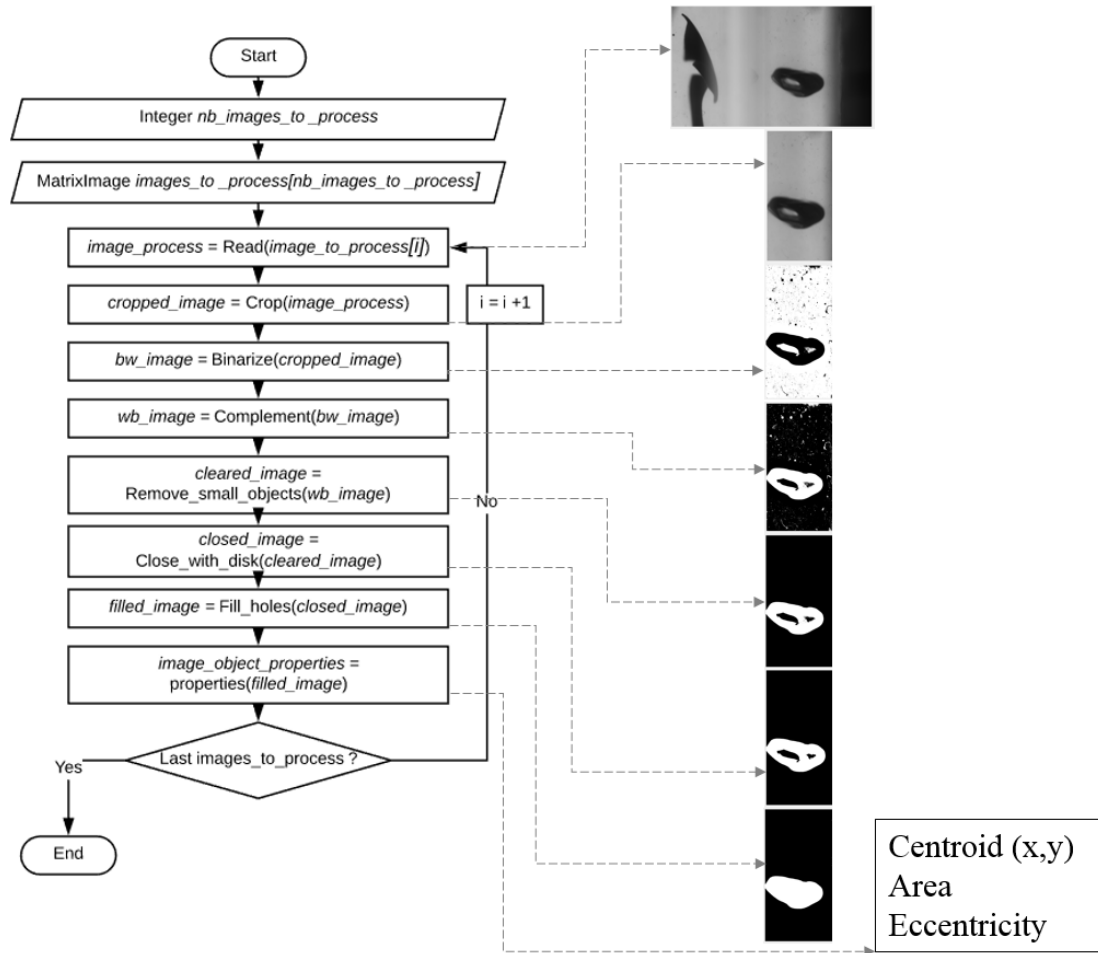


Figure II-11 : Flow chart of the image processing program used for the determination of the bubble size and the bubble and QQ media velocity.

After declaring the variables and reading the image, the first step of the program consists in cropping the image only to maintain the area corresponding to the riser space, which was in this study the area of interest (Figure II-11). Then, the grayscale image was transformed into a binary one where the object appears as a black shape and the liquid as the white medium surrounding it. The image was the “reversed” resulting in the image of a white object in a black background. The next step consists in removing the small objects from the background, in order not to take them into account as objects of interest (QQ media or bubbles). Finally, the holes in the object of interest are filled and the properties of it (barycenter, area and shape factor) are calculated and displayed. The barycenter (centroid) was localized to determine the velocity of the objects (either bubble or QQ media) between two consecutive

images of a series. The projected area of bubbles A_p was measured in each image to determine to circle-equivalent diameter d_a as the bubble size (diameter of the circle having the same projected area), according to the Equation II-5. The average properties (bubble size, bubble velocity, QQ media velocity) corresponding to each operating condition, were determined on the basis of 10 objects (bubbles or QQ media) analyzed under the considered conditions.

$$d_a = \left(\frac{4A_p}{\pi}\right)^{1/2} \quad \text{II-5}$$

The program operates exactly the same way when several objects of interest are present on the images (several bubbles and/or QQ media), and the properties of each of the object are determined and displayed.

II.4.2.5. Reliability of the method

In order to discuss the reliability of the shadowgraphy method together with the image processing, an example of image sequence is presented in Figure II-12 and corresponds to the observation of 10 bubbles generated in the MBR with a riser width of 15 mm at the top of the membrane (Window I) and under an air flowrate of $0.90 \text{ Nm}^3 \cdot \text{h}^{-1} \cdot \text{m}^{-2}$. The selected example was chosen because it shows the potential sources of error. For each bubble, 3 to 9 consecutive images (depending on the cases) were selected for the analysis.

The bubble sizes corresponding to the selected images were determined and presented in Table II-5. The bubble size was chosen to discuss the reliability because it is undeniably the parameter with the biggest error, since it is based on the hypothesis of the sphericity of bubbles, which is not validated in most cases Figure II-12.



Figure II-12 : Series of images recorded at the top of the membrane (Window I) for the determination of the properties of bubbles generated in the ALMBR under an air flowrate of $0.90 \text{ Nm}^3 \cdot \text{h}^{-1} \cdot \text{m}^{-2}$ with a riser width of 15 mm (the time between two consecutive images of a series is 5 ms).

Table II-5 : Bubble size (mm) deduced from the processing of the images presented in Figure II-12.

		Image n°								Average bubble size (mm)	Standard deviations			
		1	2	3	4	5	6	7	8		9	(mm)	(%)	
Bubble n°	1	9.21	8.89	8.62	8.43	8.21	8.04	8.06				8.5	0.4	5
	2	3.21	3.27	3.36	3.25	3.27	3.28					3.27	0.05	1
	3	11.4	11.84	12.1	12.0	12.0	12.0	12.1	12.1			12.0	0.2	2
	4	6.74	6.85	6.94	6.95	7.18	7.37	7.42				7.1	0.3	4
	5	11.7	11.84	11.8	11.7							11.81	0.07	1
	6	12.5	11.94	11.5	11.0							11.8	0.6	5
	7	14.8	14.77	14.7								14.78	0.04	0.2
	8	14.2	14.26	14.1								14.20	0.09	1
	9	9.66	9.65	9.83	10.0							9.8	0.2	2
	10	2.33	2.31	2.31	2.29	2.29	2.29	2.29	2.30	2.32		2.30	0.02	1
Average bubble size (mm)											9.5			
Standard deviations (mm)											4.3			
(%)											45			

The following elements are important to underline:

- For one series of images of the same bubble, the most significant discrepancy in terms of relative standard deviation was worth 5 % in the case of bubbles n° 1 and n° 6. As it is possible to observe in Figure II-12, the bubbles in these two cases seem to describe non-negligible deformation while rising. The deformation can be 3D, which modifies the projected (2D) area of the bubble and its size, consequently, resulting in a decreasing bubble size over the series (Table II-5). Therefore, the deformation of bubbles is one of the limitations of this method and can be misleading for the determination of bubble size.
- Over the 10 bubbles selected, the two biggest ones were bubbles n° 7 and 8 with an average size of 14.78 and 14.20 mm, respectively. However, when looking at the corresponding images, it seems that two bubbles are superimposed in these cases, which means that the resulting size does not correspond to one single bubble. These errors could be either attenuated by processing a larger number of images, or avoided by improving the processing and making it more sophisticated so it only takes into account isolated bubbles.
- The average of the sizes of the 10 bubbles was taken as the average bubble size (9.5 mm in this case) for the considered condition. However, it can be seen that the standard deviation to the average is quite important (45 %) suggesting a considerable dispersion of results. This dispersion is mainly due to the fact that the population of bubbles is heterogeneous, as a variety of shapes and sizes can be obtained in the same conditions (Figure II-12). However, this phenomenon is inherent to the system (air sparger, flowrate, geometry of the reactor) rather than to the analysis method.

II.4.3. Characterization of the liquid flow by PIV

II.4.3.1. Principle

PIV is an optical technique widely used in fluid mechanics to visualize the instantaneous velocity field of a flowing fluid. The technique consists in seeding the fluid with solid tracer particles (light reflecting or fluorescent particles) which are assumed to follow exactly the flow, owing to their small size (10 to 100 μm). The seeded fluid is then illuminated with a laser sheet (2D), and using a camera, images of the lit particles can be captured successively with a given acquisition frequency. In each acquisition, two laser pulses separated by a time Δt are emitted and a pair of frames is recorded within the same time delay Δt (frames (a) and (b) in Figure II-13). The images are then analyzed with the appropriate software. Each frame is subdivided into several interrogation areas (defined by the yellow grid in Figure II-13). The displacement of the particles from the first to the second frame is determined via a spatial cross-correlation, and the velocity vectors are finally deduced by dividing the calculated displacement by the time Δt . This procedure is repeated in each interrogation area in order to obtain the instantaneous velocity field in the entire observed region.

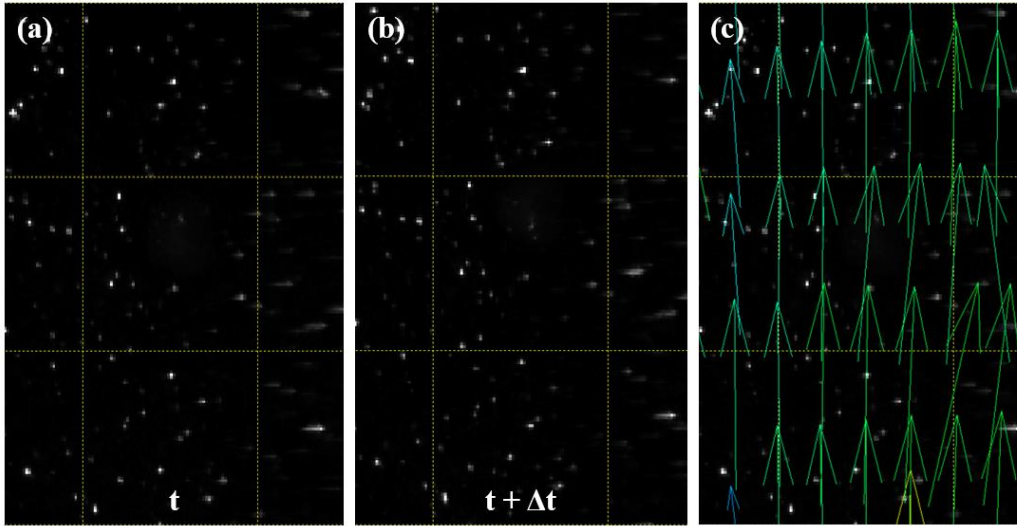


Figure II-13 : Principle of the PIV technique. (a) Frame recorded at the time (t). (b) Frame recorded at the instant ($t + \Delta t$). (c) Velocity field deduced from the cross-correlation between the pair of frames (a) and (b).

II.4.3.2. Set-up

- **Material**

In this study, the selected tracer particles were silver-coated hollow glass spheres (Dantec Dynamics, Denmark) with a density of 1.4 g.cm^{-3} , a size distribution ranging from 10 to 30 μm and an average diameter of 15 μm . The middle vertical plane of the reactor was illuminated with a laser sheet (Nd:YAG unit laser source, DualPower 200-15, class 4, Dantec Dynamics, Denmark) and a CMOS camera (FlowSense EO 4M, 2048 x 2048 pixels² (1 pixel = 27 μm), 20.4 fps, Dantec Dynamics, Denmark) was placed orthogonally to the laser sheet with a 105 mm lens (Micro-NIKKOR, 105 mm, Nikon) was mounted on it (Figure II-14). The observations were made in the previously defined windows of 55 x 55 mm² (Figure II-6). The software DynamicStudio (2015a, Dantec Dynamics, Denmark) was used for the control and synchronization of the camera and the laser, for the settings configuration (acquisition frequency, time Δt between two consecutive frames of a pair), as well as, for the image processing.

- **Settings**

The acquisition frequency was set to 10 Hz and the acquisition time to 25 s, for a total number of 250 pairs of frames. For the image analysis, the entire frame was divided into 4096 interrogation areas of 32 x 32 pixels² each (Figure II-15). The time Δt between two frames of a pair was adjusted according to the velocity induced by the different tested air flowrates, in such a way that every single tracer particle moves about 1/4 of the length of the interrogation area (in our case, about 8 pixels) (Figure II-15). For the considered range of air flowrates, this time Δt ranged between 0.5 to 5 ms.

- **Addition of the tracer particles (seeding)**

The optimal concentration of tracer particles in the fluid was adjusted in such a way that 4 to 5 particles were present in each interrogation area.

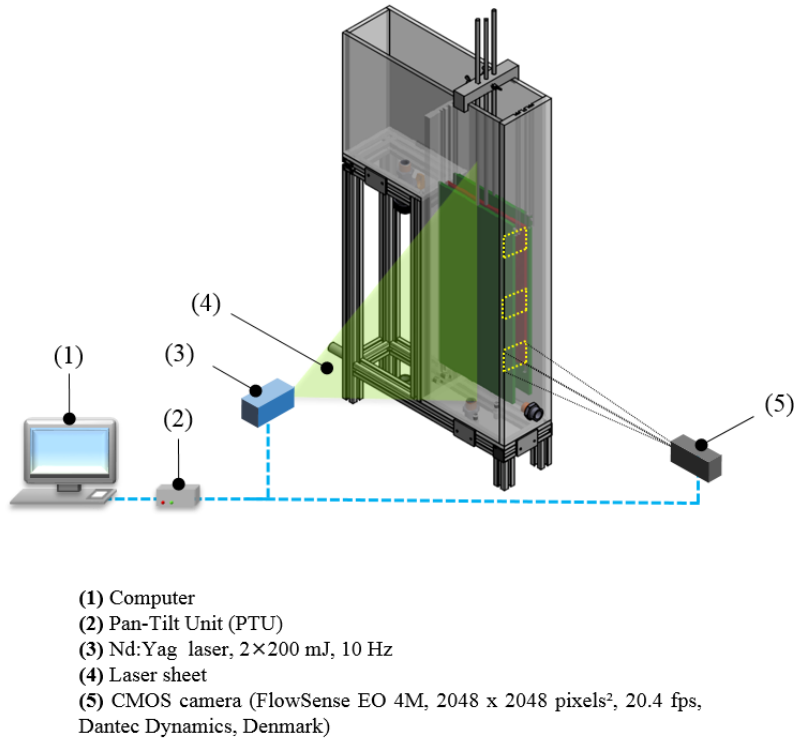


Figure II-14 : PIV setup for the hydrodynamics characterization of the reactor.

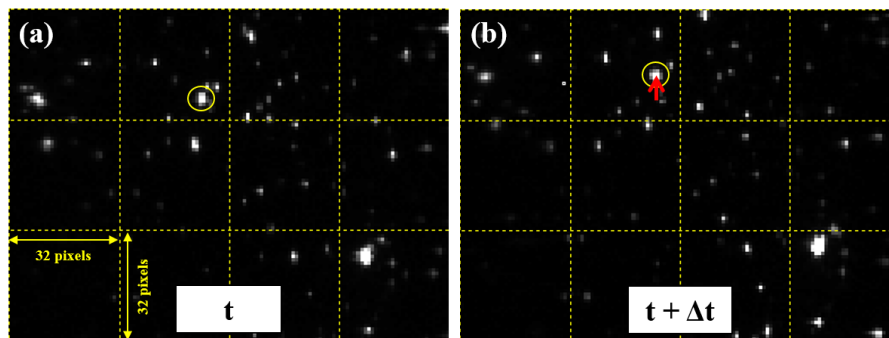


Figure II-15 : Example of zoomed-in PIV frames for the configuration of the settings (*the red arrow represents the displacement of the circled particle*).

II.4.3.3. *Experimental protocol*

The 300 operating conditions that were investigated (30 for the MBR + 270 for the QQ-MBRs) were the same as for the shadowgraphy measurement (Figure II-10). The times Δt between two frames of a pair that were selected for each air flowrate are indicated in Table II-6.

Table II-6 : Values of Δt selected for each air flowrate.

SADm ($\text{Nm}^3 \cdot \text{h}^{-1} \cdot \text{m}^{-2}$)	0.30	0.40	0.75	0.90	1.00
Δt (ms)	5	5	1	0.5	0.5

II.4.3.4. *Image and data processing for the determination of the hydrodynamics parameters*

- **Image processing**

An analysis sequence for the image processing was programmed on DynamicStudio (2015a, Dantec Dynamics, Denmark) and consisted in the following steps:

- The raw image (Figure II-16(a)) was divided into interrogation areas of 32×32 pixels². Using the appropriate mask (visually defined), the areas corresponding to the baffle and the membrane were removed from the images not to be taken into account in the analysis (Figure II-16(b)).
- The cross-correlation between the two frames of each pair was applied in each interrogation area with an overlap factor of 50 % (which means that the detection area of tracer particles is no longer limited to an interrogation area but it is extended to 50 % of the nearby areas). A first “raw” velocity field is then obtained (Figure II-16(c)).
- The moving average validation function was finally applied in order to smooth the “raw” velocity field. The function consists in replacing every velocity vector by the average of its 5 nearby vectors, and 4 iterations were performed to obtain the final velocity field (Figure II-16(d)).
- The velocity fields are then digitalized and converted into matrices of data, organized as in Figure II-17, where (X_i, Y_j) are the horizontal and vertical coordinates of the point (i, j) , U_{ij} represents the horizontal velocity vectors, V_{ij} the vertical horizontal vectors, and W_{ij} the resulting velocity vectors. The indexes i and j can take values between 1 to $n = 127$.

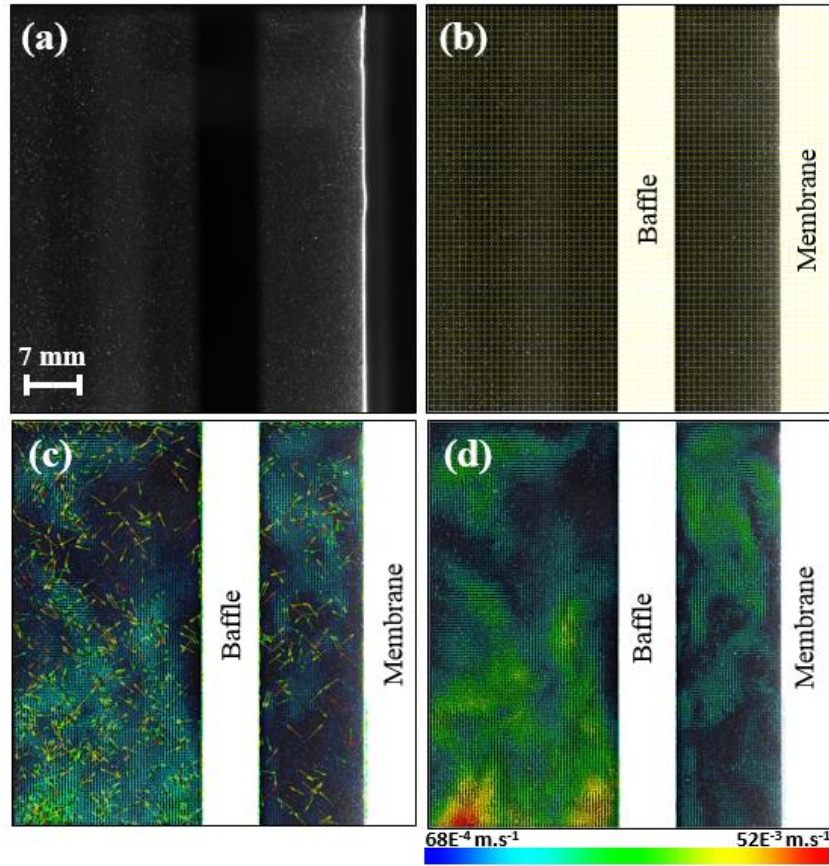


Figure II-16 : Image processing steps on DynamicStudio. (a) Raw image. (b) Gridded image with a mask applied on it. (c) Raw velocity field resulting from the cross-correlation. (d) Smoothed velocity field resulting from the moving average validation.

X_i	Y_j	U_{ij}	V_{ij}	W_{ij}
X_1	Y_1	U_{11}	V_{11}	W_{11}
\vdots	\vdots	\vdots	\vdots	\vdots
X_n	Y_1	U_{n1}	V_{n1}	W_{n1}
X_1	Y_2	U_{12}	V_{12}	W_{12}
\vdots	\vdots	\vdots	\vdots	\vdots
X_n	Y_2	U_{n2}	V_{n2}	W_{n2}
\vdots	\vdots	\vdots	\vdots	\vdots
X_1	Y_n	U_{1n}	V_{1n}	W_{1n}
\vdots	\vdots	\vdots	\vdots	\vdots
X_n	Y_n	U_{nn}	V_{nn}	W_{nn}

Figure II-17 : Schematic matrix resulting from the digitalization of each PIV image.

- **Data processing**

The matrices of data obtained from the digitalization of the velocity fields were exported to be processed on a Matlab (MathWorks, USA) program, in order to deduce information about the liquid flow. The first step was to average the 250 matrices (from the 250 images) to obtain the average flow overtime and determine several the hydrodynamics parameters, according to the approach explained in the following.

The liquid flow profile in the observed area was first determined by vertically averaging the vertical velocity vectors V_{ij} ($j = 1$ to 127) at each position X_i , according to the Equation II-6 and resulting in the example of profile presented in Figure II-18.

$$\overline{V}_i(X_i) = \frac{1}{n} \sum_{j=1}^{n=127} V_{ij} \quad \text{II-6}$$

(For $i = 1$ to 127)

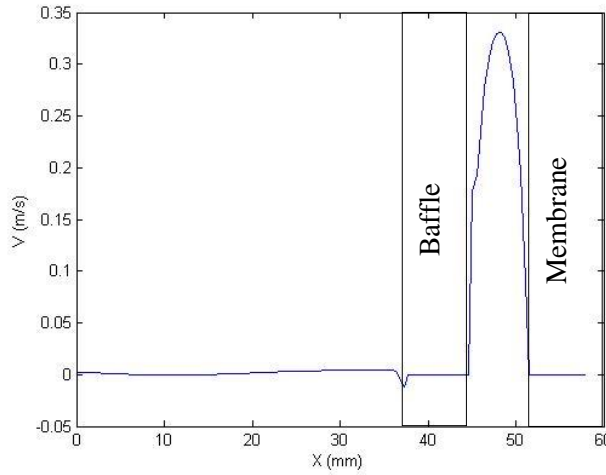


Figure II-18 : Example of horizontal liquid flow profile of vertical velocities, obtained in the ALMBR at Window I, with a riser width of 7 mm and under an air flowrate of $0.75 \text{ Nm}^3 \cdot \text{h}^{-1} \cdot \text{m}^{-2}$.

The riser part was more specifically characterized then and the average vertical velocity in the riser, named U_{lr} , was determined by horizontally averaging the values in the riser part, according to the Equation II-7, where w is the number of points in the riser space (between the baffle and the membrane).

$$U_{lr} = \frac{1}{w} \sum_{i=X_{baffle}}^{X_{membrane}} \overline{V}_i(X_i) \quad \text{II-7}$$

The membrane shear stress is another parameter used to characterize the liquid flow in the ALMBR/QQ-ALMBR. Since the time-fluctuations are valuable information for this parameter, the 250 matrices (corresponding to 250 images for each condition) were not averaged. For each image, the membrane shear stress was locally determined in one single point as presented in Figure II-19. The local membrane shear stress φ was calculated as in Equation II-8 (where μ_l is the viscosity of the liquid), and its evolution overtime (25 s) was determined (Figure II-19).

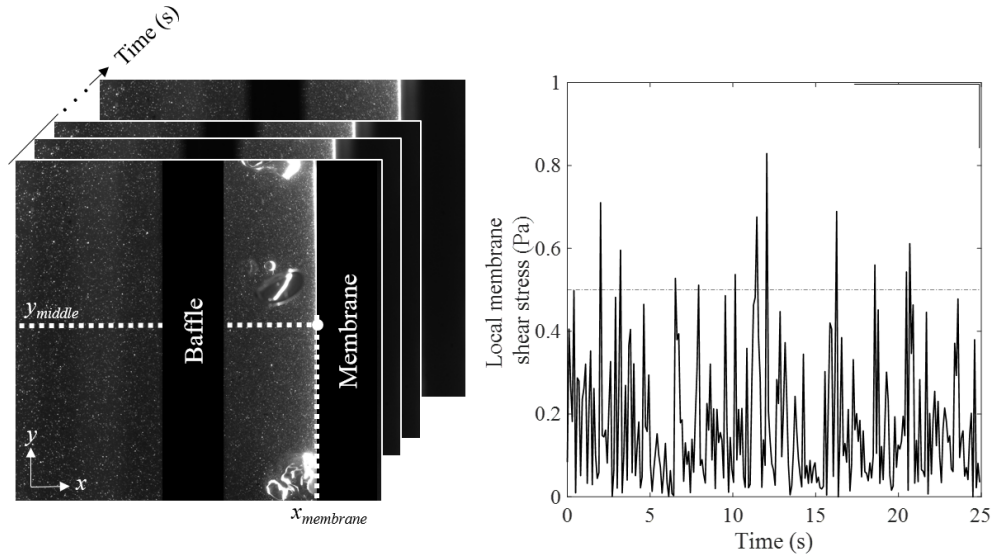


Figure II-19 : Example of shear stress evolution obtained in the ALMBR at the Window III with a riser width of 15 mm and under an air flowrate of $0.90 \text{ Nm}^3 \cdot \text{h}^{-1} \cdot \text{m}^{-2}$.

$$\varphi = \mu_l \frac{\partial V(X)}{\partial X} \Big|_{x_{membrane}, y_{middle}} \quad \text{II-8}$$

II.4.3.5. Reliability of the method

As it was previously described, the analysis of PIV data requires a succession of several steps, and errors can potentially be generated in each step.

- In the image processing, the calculations may generate errors but these errors are hardly quantifiable, since they are internal to the PIV software. Therefore, it is crucial to minimize these errors by ensuring the adequacy of the settings and correlation parameters (particles seeding, adjustment of Δt , definition of the interrogation areas...etc.)

- In the data processing, the determination of the liquid flow profile and the average liquid velocity requires averaging the velocity vectors in space. However, non-negligible dispersions

in the velocity field can be obtained. As an example, the velocity field in presence of QQ sheets in the ALMBR resulted in vertical velocity vectors ranging from 10^{-4} to 0.2 m.s^{-1} in the riser, which corresponds to a weighted average value of the vertical velocity of 0.06 m.s^{-1} and a dispersion of $\pm 0.02 \text{ m.s}^{-1}$ from the average (33 %).

II.5. Characterization of the circulation and mixing performances

II.5.1. Residence Time Distribution measurement

II.5.1.1. Principle

The Residence Time Distribution (RTD) is a method used in chemical engineering to characterize the mixing and the flowing behaviors in non-ideal reactors. The principle was first introduced by MacMullin and Weber in 1935, but was further more deeply developed by Danckwerts in 1953. The RTD is based on the determination of a probability function describing the age distribution of the fluid elements circulating in the reactor. The RTD is a global method based on a stimulus-response experiment. It usually consists in injecting a certain amount of non-reactive tracer in the feed of the reactor and measuring its amount in the output over time. The analysis of the signal and its deviation from the ideal flow patterns reveal some dysfunctions that may take place in real reactors, such as dead volumes, channeling of fluid, or recycling of fluid.

II.5.1.2. Selection and preparation of the tracer (NaCl)

A saturated (around 360 g.L^{-1}) solution was prepared by dissolving a certain amount of NaCl (Sigma-Aldrich) in the appropriate volume of tap water. The solution was stored at 4°C to be further used as a tracer.

II.5.1.3. Calibration curve (conductivity)

The concentration of NaCl was measured using a conductivity probe and a standard curve was determined prior to the experiments. For that purpose, several standard solutions with precisely known concentrations of NaCl were prepared and their conductivity was measured. The calibration curve presented in Figure II-20 was obtained. As expected, a perfectly linear correlation was found to link the conductivity to the concentration of NaCl, and the line intercepts the y-axis at the value of 0.0002 S.cm^{-1} because the NaCl solutions were prepared in tap water that naturally contains a small amount of salts.

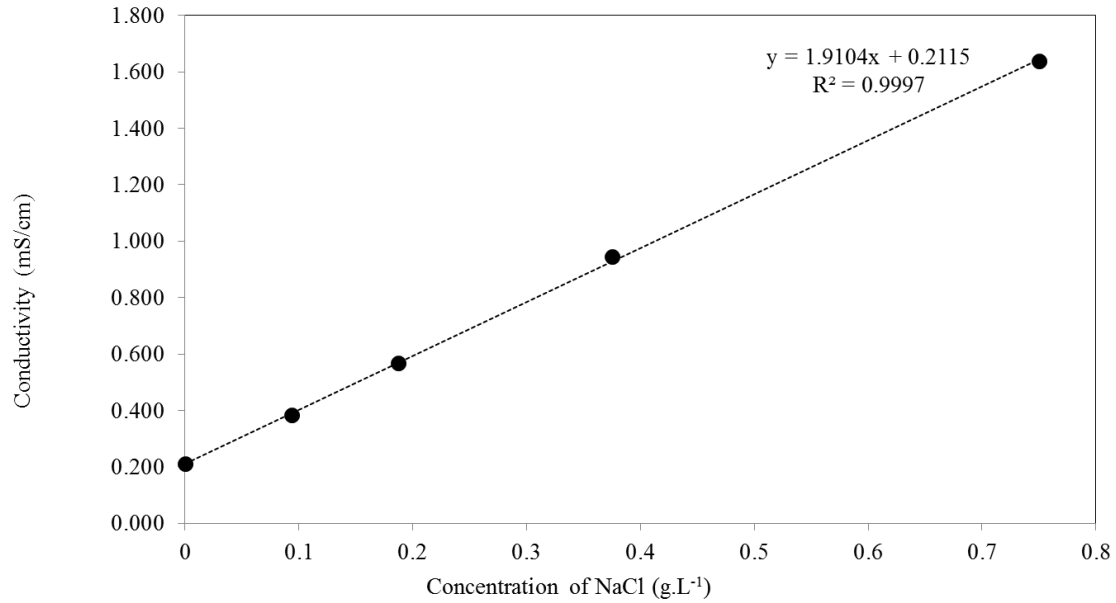


Figure II-20 : Conductivity standard curve of NaCl.

II.5.1.4. Set-up

In this study, the RTD was performed by measuring the conductivity. 10 mL of the tracer solution were injected with a Dirac pulse injection in the feed of the reactor, and the variations of concentrations in the permeate side were measured with a conductivity probe (Figure II-21). The data were acquired via a monitoring software (AcquiChimie) connected to a computer, and the acquisition frequency was set to 0.008 Hz (1 measurement every 2 min). The whole RTD measurement lasted 48 to 60 h, depending on the cases.

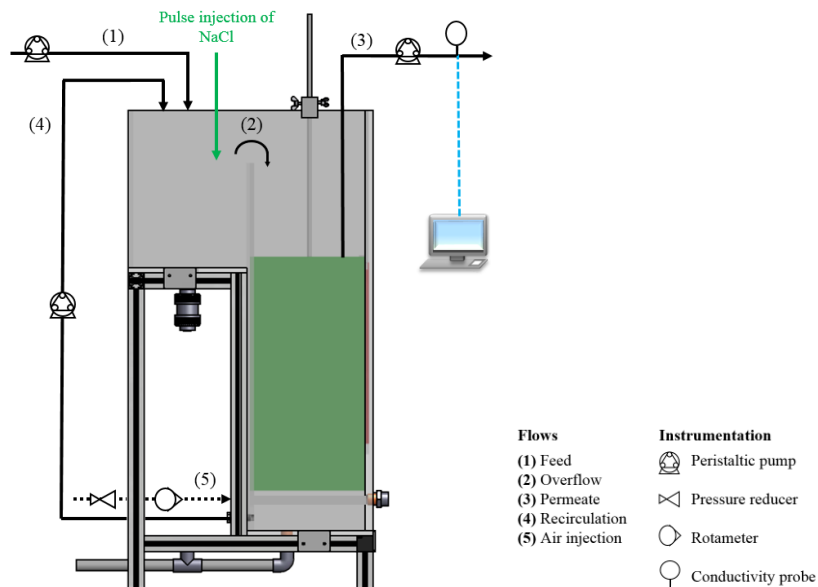


Figure II-21 : Experimental setup for the RTD measurement.

II.5.1.5. Experimental protocol

In this part of the study, the effect of the air flowrate as well as the effect of the QQ media shape were investigated (Figure II-22). The volume fraction of the introduced QQ media was set to 0.45 % v/v and the riser width was set to 15 mm. The permeate flux was constant and set to $15 \text{ L.h}^{-1}.\text{m}^{-2}$, and the recirculation flowrate between the two tanks of the ALMBR was set to 4 L.h^{-1} . Additional RTD measurements were also performed in absence of QQ media under the same three air flowrates.

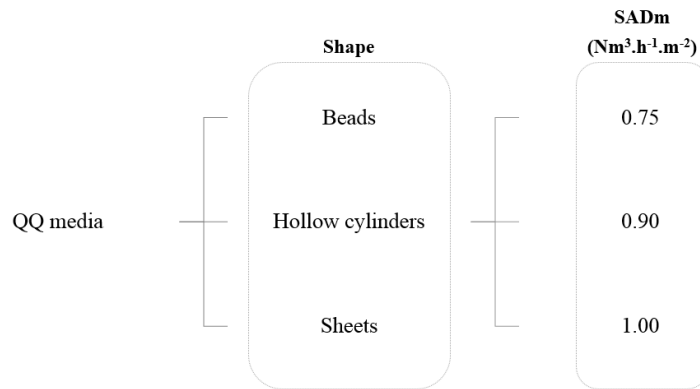


Figure II-22 : Experimental procedure for the study of the RTD in presence of QQ media.

II.5.1.6. Signal analysis for the determination of the RTD function

The conductivity was monitored during the operation and the corresponding concentration $C(t)$ of salt was determined using the standard curve (Figure II-20), and an example of raw curves is presented in Figure II-23.

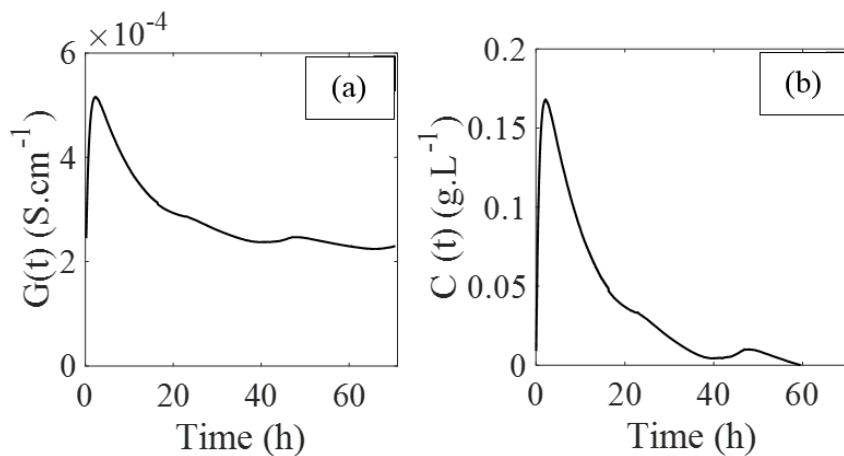


Figure II-23 : Example of (a) Conductivity and (b) concentration curves, obtained in the ALMBR under an air flowrate of $0.75 \text{ Nm}^3.\text{h}^{-1}.\text{m}^{-2}$ with a riser width of 15 mm.

The corrected concentration $C(t)$ was further used to determine the RTD function $E(t)$, according to Equation II-9, where τ is the theoretical hydraulic retention time τ (which represents the ratio of the total volume V (18 L) to the working flowrate (1.5 L.h⁻¹) is worth 12 h, in the case of the studied ALMBR). C_0 is determined as in Equation II-10 and represents the initial amount of salt injected m_0 (in g) distributed in the whole volume of the reactor. The RTD parameters such as the mean residence time and the variance of the RTD function could be further deduced. The details about the RTD parameters are given in Chapter III.

$$E(t) = \frac{C(t)}{\int_0^\infty C(t)dt} = \frac{1}{\tau} \frac{C(t)}{C_0} \quad \text{II-9}$$

$$C_0 = \frac{m_0}{V} \quad \text{II-10}$$

II.5.1.7. *Tracer recovery and repeatability of the measurement*

The first important indicator for the reliability of the RTD measurement is the total recovery of the tracer at the end of the operation. In order to validate the tracer recovery, the Equation II-11 should be verified.

$$\frac{\int_0^\infty C(t)dt}{\tau} = C_0 \quad \text{II-11}$$

The two terms of Equation II-11 were calculated for each experiment and presented in Table II-7, and the discrepancies were quantified.

Table II-7 : Tracer recovery for each experiment.

Experiment		C_0 (g.L ⁻¹)	$\frac{\int_0^\infty C(t)dt}{\tau}$ (g.L ⁻¹)	$ C_0 - \frac{\int_0^\infty C(t)dt}{\tau} $ (g.L ⁻¹)	$ 100 \times \frac{C_0 - \frac{\int_0^\infty C(t)dt}{\tau}}{C_0} $ (%)
QQ media	SADm (Nm ³ .h ⁻¹ .m ⁻²)				
None	0.75	0.20	0.19	0.01	5
Hollow cylinders		0.19	0.15	0.04	21
Sheets		0.16	0.16	0.00	0
Beads		0.20	0.15	0.05	25
None	1.00	0.19	0.16	0.03	16
Hollow cylinders		0.19	0.17	0.02	11
Sheets		0.20	0.19	0.01	5
Beads		0.19	0.20	0.01	5
None	0.90	0.21	0.17	0.03	14
Hollow cylinders		0.18	0.15	0.03	17
Sheets		0.18	0.17	0.01	6
Beads		0.19	0.16	0.03	16

The discrepancies range from 0 to 25 %, which means that the tracer was not totally recovered in all the experiments. The biggest discrepancy is obtained for the experiment conducted in presence of QQ beads under an SADm of 0.75 Nm³.h⁻¹.m⁻², as a 25 % difference was observed between the expected

concentration C_0 and the measured one $\frac{\int_0^\infty c(t)dt}{\tau}$. This difference can be due to the fact that a part of the tracer can be held into dead volumes into the reactor.

The repeatability is another important indicator that sets a confidence range indicating the reliability of the comparison between the different experiments. In order to evaluate the repeatability, some experiments were replicated under the exact same conditions, and one example is presented in Figure II-24 in terms of conductivity. The two curves were obtained in presence of QQ beads under an SADm of $0.90 \text{ Nm}^3 \cdot \text{h}^{-1} \cdot \text{m}^{-2}$, and lasted about 24 h.

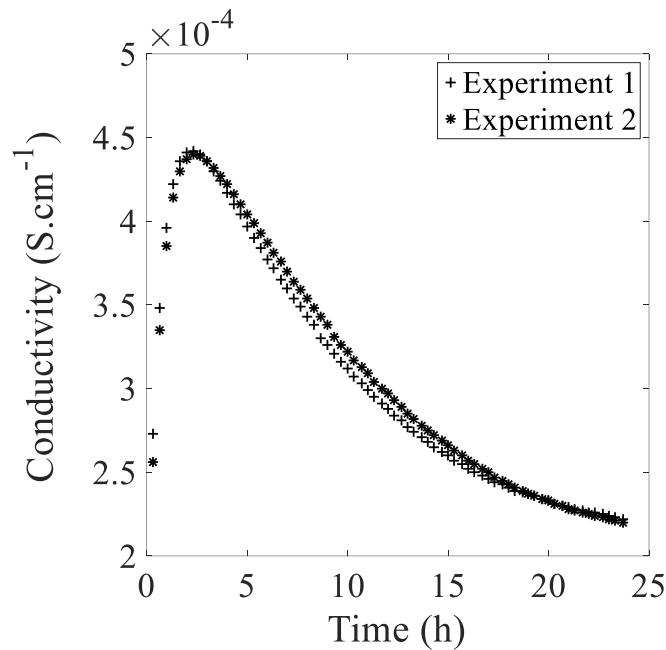


Figure II-24 : Conductivity curves obtained in the ALMBR in presence of QQ beads and under an SADm of $0.90 \text{ Nm}^3 \cdot \text{h}^{-1} \cdot \text{m}^{-2}$.

As it is possible to observe, the two curves seem to be very close, and the discrepancies between them range between 0 and 11 %, with an average gap of 2 % over the investigated time. Therefore, the RTD experiment can be considered as repeatable, and an average gap between two curves of 2 % can be considered as insignificant.

II.5.2. Mixing time measurement

II.5.2.1. Principle and setup

The principle is to determine the time necessary for the bulk in the aerobic tank of the ALMBR to reach a homogeneous concentration. In this study a colorimetric method was chosen together with a camera. The dye Rose Bengal Lactone (Sigma-Aldrich) was selected as a tracer and solutions at $0.4 \text{ g} \cdot \text{L}^{-1}$ were

prepared prior to the experiments and stored at 4°C. The experiment consisted in instantaneously injecting 20 mL of the tracer solution into the aerobic tank of the ALMBR, as the injection point presented in Figure II-25. A 12 bits (4096 gray level) CMOS camera (Basler-Ace Aca1920-155 um) was used for the visualization of the mixing phenomenon. A backlight panel (Phlox-LedW-BL, 400 x 200 mm², 24 V, 2A, Phlox) was set behind the reactor to illuminate the liquid phase through the clear walls of the reactor. The observation window was 97.5 mm-wide and 150 mm-long, and located at the bottom of the aerobic tank (as far as possible from the injection), as presented in Figure II-25. Images were recorded with the camera at a frequency of 10 Hz and then processed with a Matlab (MathWorks, USA) program consisting in measuring the mean intensity of each image (the program was a simplified version of the one used for the mass transfer study, presented in the subsequent). The evolution of the light intensity overtime could be deduced, and the mixing time was finally defined as the time necessary for the intensity to reach 96 % of homogeneity in the bulk.

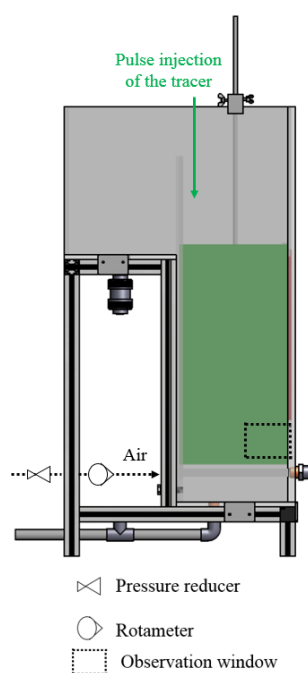


Figure II-25 : Experimental setup for the mixing time measurement.

II.5.2.2. Experimental protocol

As it appears in Figure II-25, the mixing time was only measured in the aerobic tank of the ALMBR. The measurements were performed under the batch mode for the liquid phase (with no feed) and the continuous mode for the gas phase (continuous injection of air). The measurements were conducted under different air flowrates and with/without the addition of QQ media. For each condition, the measurement was replicated 3 times.

II.5.2.3. *Signal analysis for the determination of mixing time*

An example of the raw signal of the light intensity overtime resulting from the image processing is presented in Figure II-26. The red dots represent the experimental data and the continuous blue line is a smoothed curve, used to reduce the noise of the signal. In the selected example, the time to reach 96 % of the final value was found to be 44 s, and the injection time was known to be 15 s after the beginning of the recording. Therefore, the mixing time for this condition was $44 - 15 = 29$ s.

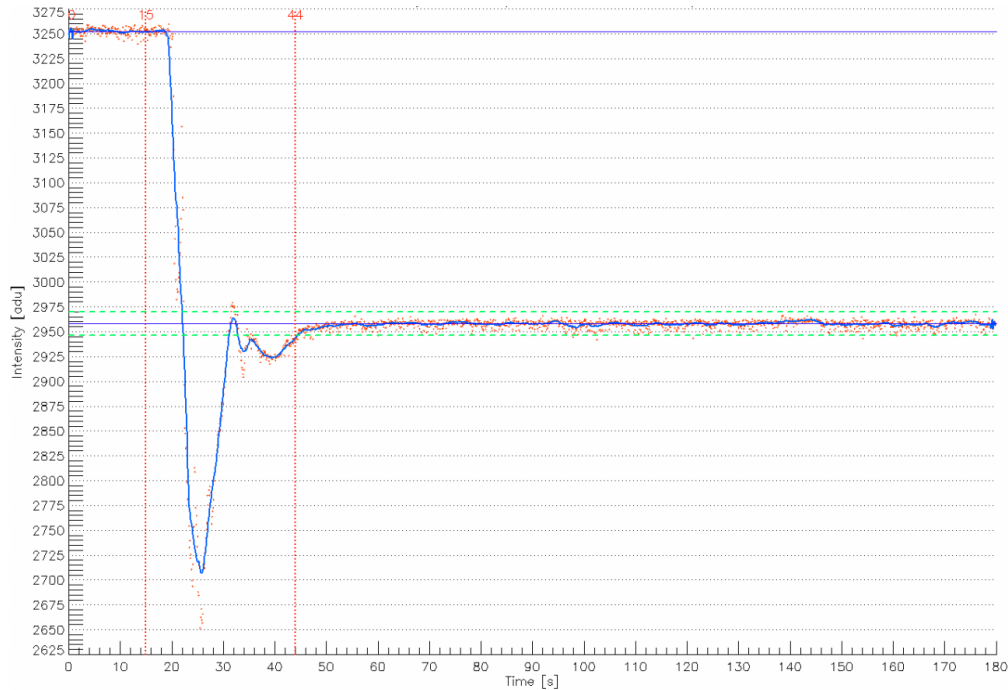


Figure II-26 : Example of raw signal of the light intensity through the aerobic tank of the ALMBR under an air flowrate of $0.90 \text{ Nm}^3 \cdot \text{h}^{-1} \cdot \text{m}^{-2}$.

II.5.2.4. *Repeatability of the measurement*

For each condition, three replicates were conducted and the average was taken as the mixing time. The example with the biggest discrepancies was selected to discuss the repeatability and was obtained in the ALMBR under an air flowrate of $0.35 \text{ Nm}^3 \cdot \text{h}^{-1} \cdot \text{m}^{-2}$.

The results in terms of mixing time for the selected example are presented in Table II-8.

Table II-8 : Mixing time (s) for three replicates.

Replicate 1	Replicate 2	Replicate 3	Average value (s)	Standard deviation (s)	Standard deviation (%)
83	76	45	68	20	30

A variability in the results is observed which is mainly due to the moment in which the tracer is injected with respect to the air-lift motion. Actually, it was visually observed that the tracer could be more or less quickly homogenized depending on the distribution and the motion of bubbles at the injection time. Nevertheless, it is important keeping in mind that the presented example corresponds to the worst case, and that the randomness of the bubbles distribution and motion tends to be attenuated at high air flowrates.

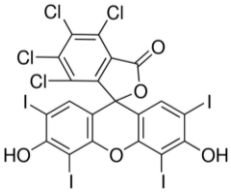
II.6. Characterization of the mass transfer by a tracer technique

The mass transfer of AHLs was more specifically addressed in this study and would have required the detection and quantification of AHLs. For this, several methods exist and were reported in the literature (Appendix A-II-1), among which the biological method relying on the use of the reporter strain *A.tumefaciens* A136 was tested in the present study (Appendix A-II-1). However, this method requires to maintain perfectly sterile conditions, which is hard to achieve at the reactor scale. In addition, the decision was made to study the mass transfer at the global scale, not only at the QQ media scale. Thus, the selection of a mimic molecule (tracer) was preferred.

II.6.1. Selection of the tracer (*Rose Bengal Lactone*)

The Rose Bengal Lactone is light red to pink powder used as a dye molecule, and its main properties are presented in Table II-9. The Rose Bengal Lactone is composed of a lactone group, as the AHLs, which is why it was chosen as a model-molecule to study the mass transfer.

Table II-9 : Physico-chemical properties of the Rose Bengal Lactone.

Chemical formula/Molecular structure	C ₂₀ H ₄ Cl ₄ I ₄ O ₅
	
Molecular weight (g.mol ⁻¹)	973.67
Appearance	Pink powder
Purity	≥ 95 %

II.6.2. Preparation of the solution

The Rose Bengal Lactone was purchased from Sigma-Aldrich. Solutions of Rose at a concentration of 0.4 g.L⁻¹ were prepared by dissolving the proper amount of powder in tap water. In order to help the dissolution, the solutions were sonicated 3 to 4 times for 15 min and shaken between two sonication cycles, until obtaining a clear dark-pink solution.

II.6.3. Calibration curve (spectrophotometry)

In this study, the concentration of the Rose Bengal Lactone was determined using optical methods. As a first step, the spectrum of Rose Bengal Lactone in the visible range was measured in order to determine the wavelength corresponding to the maximum of absorbance and use it for further analysis. For this, a solution of Rose Bengal Lactone was prepared (0.014 g.L^{-1}) and the spectrum was measured using a spectrophotometer (Jasco-V630, Germany). The resulting spectrum is presented in Figure II-27. The wavelength corresponding to the maximal absorbance (λ_{max}) was found to be 548 nm, therefore, all of the measurements in the spectrophotometer were carried out at 548 nm.

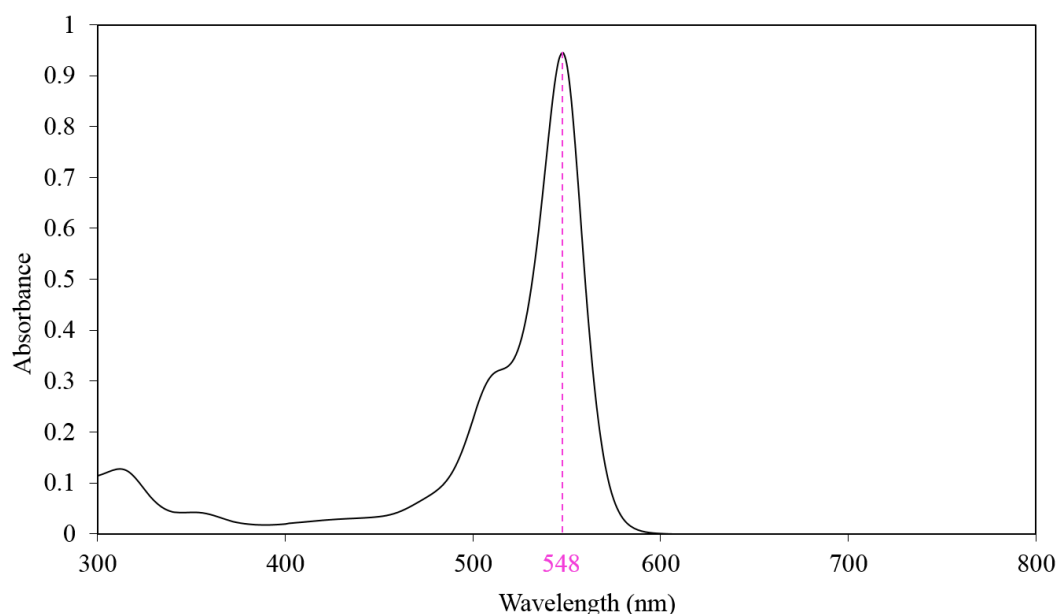


Figure II-27 : Light spectrum of Rose Bengal Lactone.

A calibration curve was determined by measuring the absorbance at 548 nm of several standard solutions that were prepared beforehand by successive dilutions of the mother-solution (0.4 g.L^{-1}). The calibration curve is presented in Figure II-28. The equation of the linear regression was used in the whole study to convert the absorbance into its corresponding value of Rose Bengal Lactone concentration.

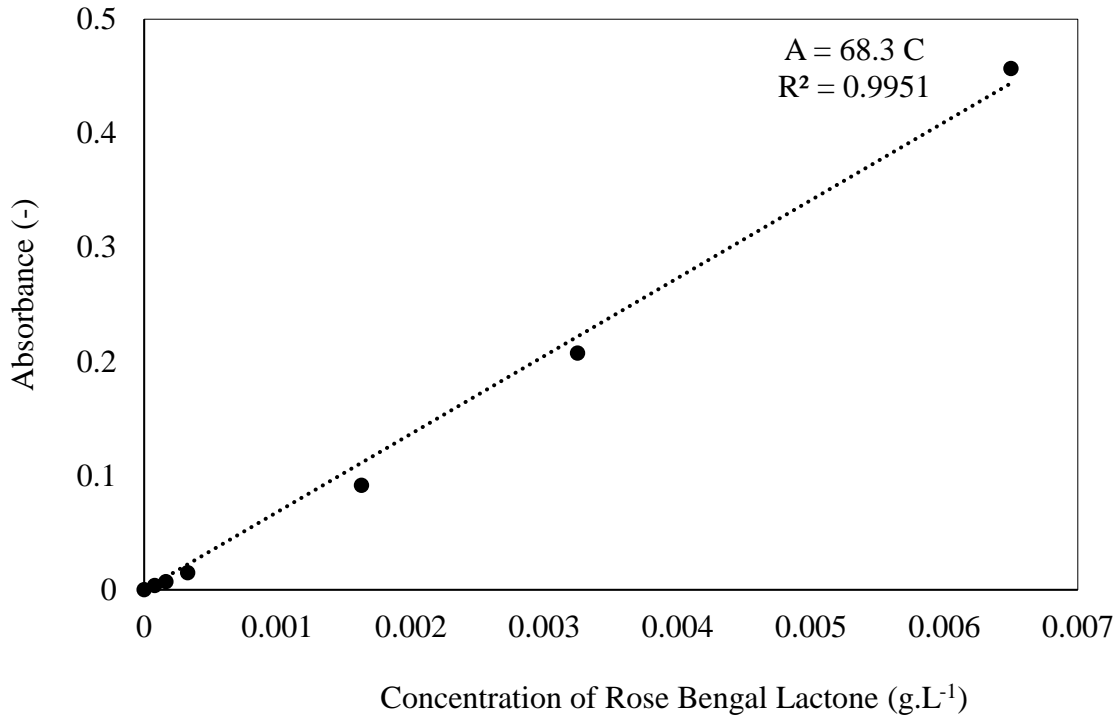


Figure II-28 : Spectrophotometry calibration curve of the Rose Bengal Lactone.

II.6.4. Mass transfer in the jar-tests

II.6.4.1. Principle and setup

The transfer from the liquid phase into the QQ media was performed in jar-tests (Floculateur, Bioblock Scientific) and consisted in suspending the fresh QQ media in a solution of Rose Bengal Lactone (around 0.4 g.L⁻¹) in a solid:liquid ratio of 1:9 and under stirring (90 rpm) at the room temperature (Figure II-29). The total volume of QQ media was 58.5 mL in each beaker and was the same for the three shapes. For the first experiment, two controls with no QQ media (one with water and one with the saturated solution of Rose Bengal Lactone) were added to ensure that the observed decrease of concentration in the liquid phase could only be attributed to a transfer in the QQ media, and not to additional phenomena such as natural degradation, precipitation, ...etc. Samples were collected from the jars every 30 min at first and then spaced out after the first 7 hours. The samples were diluted 100 times before measuring their absorbance by spectrophotometry to deduce their concentration. The experiments lasted 24 h which was found to be the time for the concentration to reach a constant value, indicating a stabilization of the system. After 24 h, the QQ media were collected and drained to be used for the subsequent experiments.

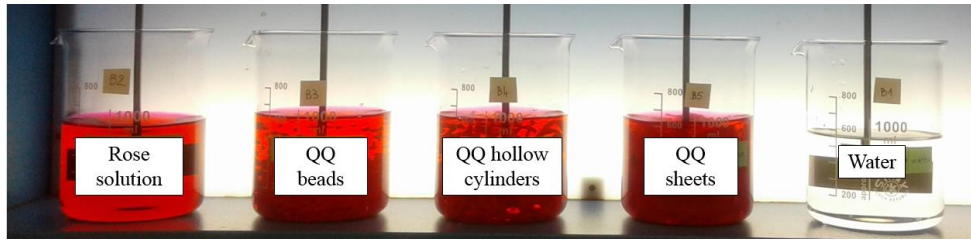


Figure II-29 : Jar-tests experiments for the study of the transfer into the QQ media.

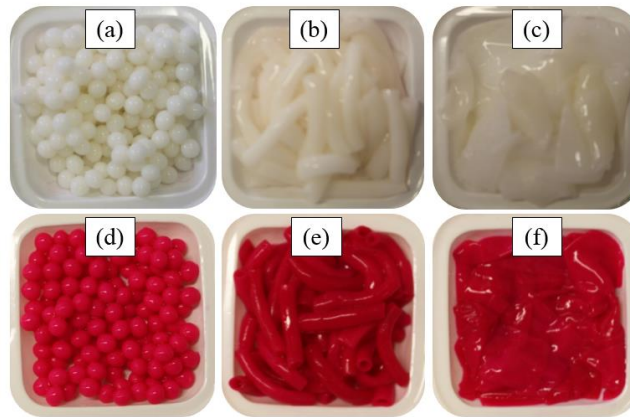


Figure II-30 : Fresh QQ (a) beads (b) hollow cylinders (c) sheets and stained QQ (d) beads (e) hollow cylinders and (f) sheets, after the 24 h jar-test experiment.

II.6.5. Mass transfer in the lab-scale reactor

II.6.5.1. Principle and setup

The mass transfer from the QQ media to the liquid phase was studied in the lab-scale ALMBR by introducing the stained QQ media collected at the end of the jar-test experiment (Figure II-30(d), (e) and (f)) in the aerobic tank of the ALMBR, initially filled with tap water. The experiments were conducted under the batch mode for the liquid phase and the continuous mode for the air injection.

In order to visualize the transfer phenomena in the reactor, a camera technique was developed to measure the absorbance (and thus the concentration of Rose Bengal Lactone in the liquid phase) and consisted in using a 12 bits (4096 gray level) CMOS camera (Basler-Ace Aca1920-155 um) equipped with a green filter (495 to 505 nm). A backlight panel (Phlox-LedW-BL, 400 x 200 mm², 24 V, 2A, Phlox) was set behind the reactor as presented in Figure II-31. The observation window was 97.5 mm-wide and 150 mm-long, and located at the bottom of the reactor (under the membrane) so that the whole depth of the tank could be observed (thanks to the clear baffles) (Figure II-31). The camera technique was preferred to a simple absorbance measurement via a light sensor because of the coexistence of three phases in the reactor: gas, liquid and solid, which can more accurately be taken into account with an image processing.

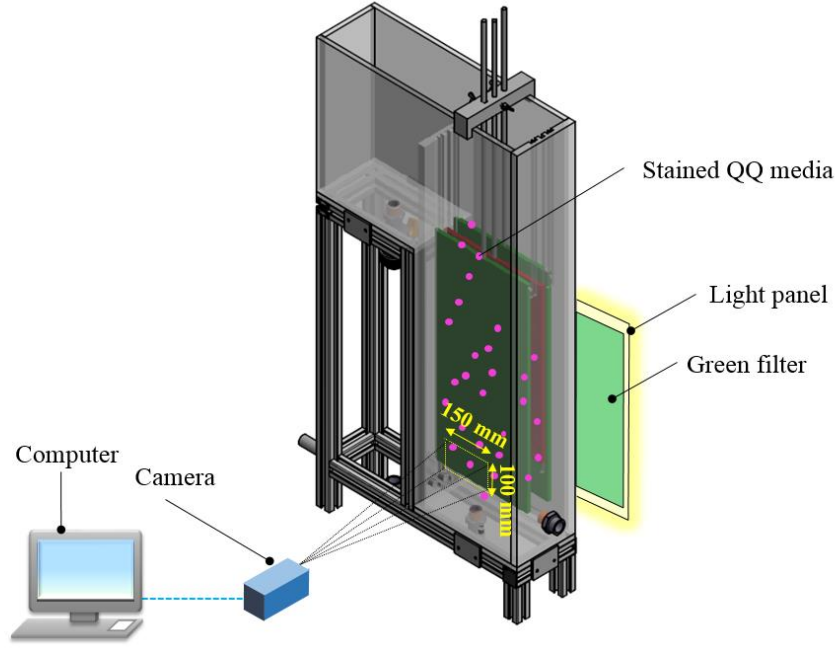


Figure II-31 : Experimental setup for the visualization of the mass transfer in the MBR.

An image was recorded every 10 s (acquisition frequency of 0.1 Hz) and the total acquisition lasted 1 day or more, depending on the cases and on the time necessary to reach the equilibrium of the system. The size of the images was 1000 x 650 pixels² (1 pixel = 150 µm). The software Pylon (Basler, Germany) was used to control the camera as well as to configure all of its settings.

The filter was used to narrow down the range of wavelengths passing through the liquid in the reactor to approach a monochromatic beam (~ 500 nm, for which the absorbance is considerable as presented in Figure II-27) and be able to link the intensity of light to the concentration of Rose Bengal Lactone, according to Beer-Lambert law presented in Equation II-12, where A is the instantaneous absorbance, I is the instantaneous light intensity, I_0 is the light intensity through the blank (water), C is the concentration of Rose Bengal Lactone, l is the optical pathway and ϵ_λ is the molar attenuation coefficient. The latter coefficient was determined via the achievement of a calibration curve which consisted in deducing the absorbance (by image processing) of images of different solutions of known concentrations. The calibration resulted in the curve presented in Figure II-32.

$$A = -\log \left(\frac{I}{I_0} \right) = \epsilon_\lambda \cdot l \cdot C \quad \text{II-12}$$

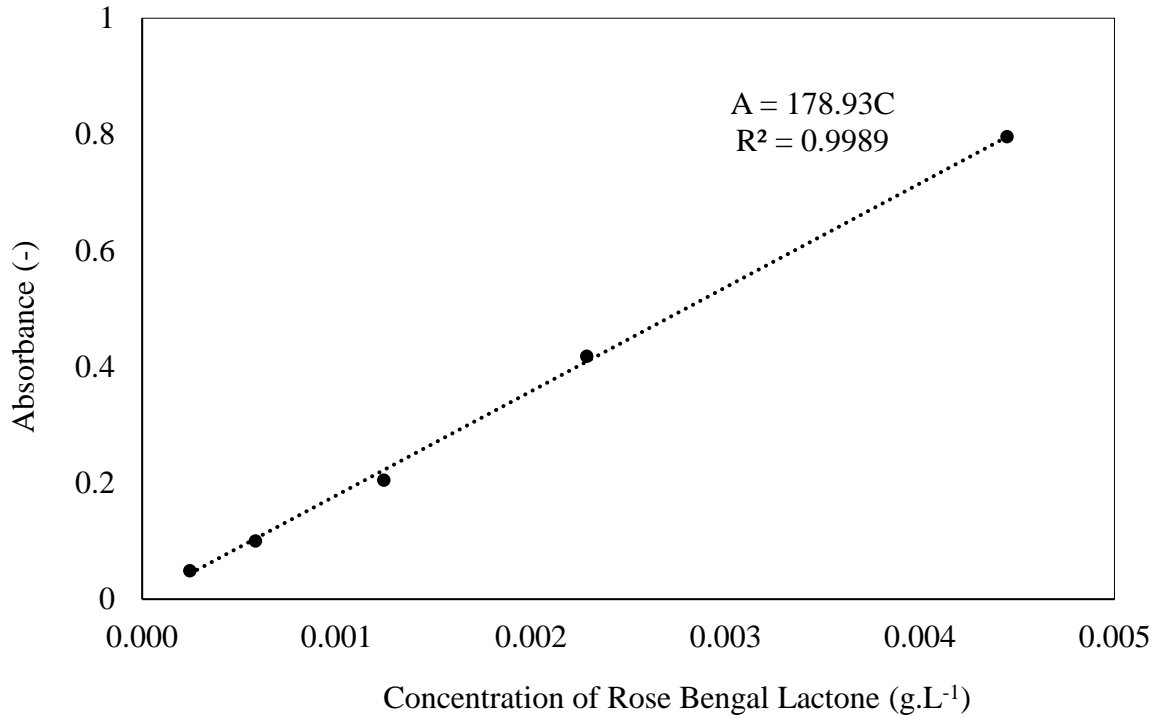


Figure II-32 : Camera calibration curve of the Rose Bengal Lactone.

II.6.5.2. Validation of the camera technique

Standard solutions of Rose Bengal Lactone with known concentrations (Table II-10) were prepared and introduced in the reactor. Using the previously presented camera setup, images of the different solutions were recorded for further processing. In addition, the absorbance of the standard solutions was measured using a spectrophotometer at 500 nm, and the results are presented in Table II-10.

Table II-10 : Spectrophotometer and camera-deduced optical parameters for standard solutions of Rose Bengal Lactone.

Concentration of Rose Bengal Lactone solution C (g.L ⁻¹)	0.0002	0.0006	0.0012	0.0023	0.0044
Spectrophotometer					
Absorbance at 500 nm $A_{spectro}$ (-)	0.0037	0.0088	0.0188	0.0346	0.0673
Optical pathway $l_{spectro}$ (cm)	1.0				
$\frac{A_{spectro}}{l_{spectro}}$ (cm ⁻¹)	0.0037	0.0088	0.0188	0.0346	0.0673
$\epsilon_{500\text{ nm}}$ (L.g ⁻¹ .cm ⁻¹)	15.136				
Camera					
Absorbance at 500 nm A_{camera} (-)	0.0490	0.1000	0.2050	0.4180	0.7960
Optical pathway l_{camera} (cm)	11.6				
$\frac{A_{camera}}{l_{camera}}$ (cm ⁻¹)	0.0042	0.0086	0.0177	0.0360	0.0686
$\epsilon_{500\text{ nm}}$ (L.g ⁻¹ .cm ⁻¹)	15.425				

The absorbances per unit of optical pathway are plotted on the same graph for comparison in Figure II-33. It is possible to observe that the ratios of the absorbance to the optical pathway, are very close for both measurement techniques. Also, the attenuation coefficients $\epsilon_{500\text{ nm}}$ were found to be very close (Table II-10)), with less than 2 % deviation. From this comparison, it is possible to conclude that the camera technique that was specifically developed for the study of the mass transfer in the ALMBR, together with the image processing, allow indeed the measurement of an absorbance which follows Beer-Lambert law. Given these results, the camera was selected as the only measurement technique for the rest of the mass transfer study from the QQ media to the liquid phase in the ALMBR.

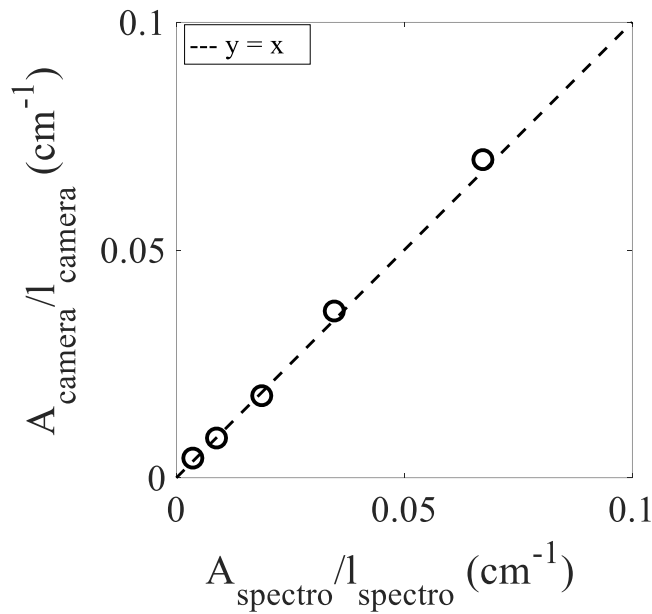


Figure II-33: Comparison of the ratios of the absorbance to the optical pathway obtained by the spectrophotometer and the camera technique.

II.6.5.3. Image processing

The images recorded during the experiments were processed using a Matlab (MathWorks, USA) program. Prior to each experiment (before the addition of the stained QQ media), around 60 images of the blank (tap water) in the reactor were recorded to determine the intensity I_o , as well as 100 images of the dark (turning the light panel off) for further calibration of the sensitivity of the measurement.

After defining the total number of images to process, the acquisition period and the threshold factor of 60 % (used to remove the bubbles or QQ media from the image) were defined. The flowchart in Figure II-34 presents the main steps of the program.

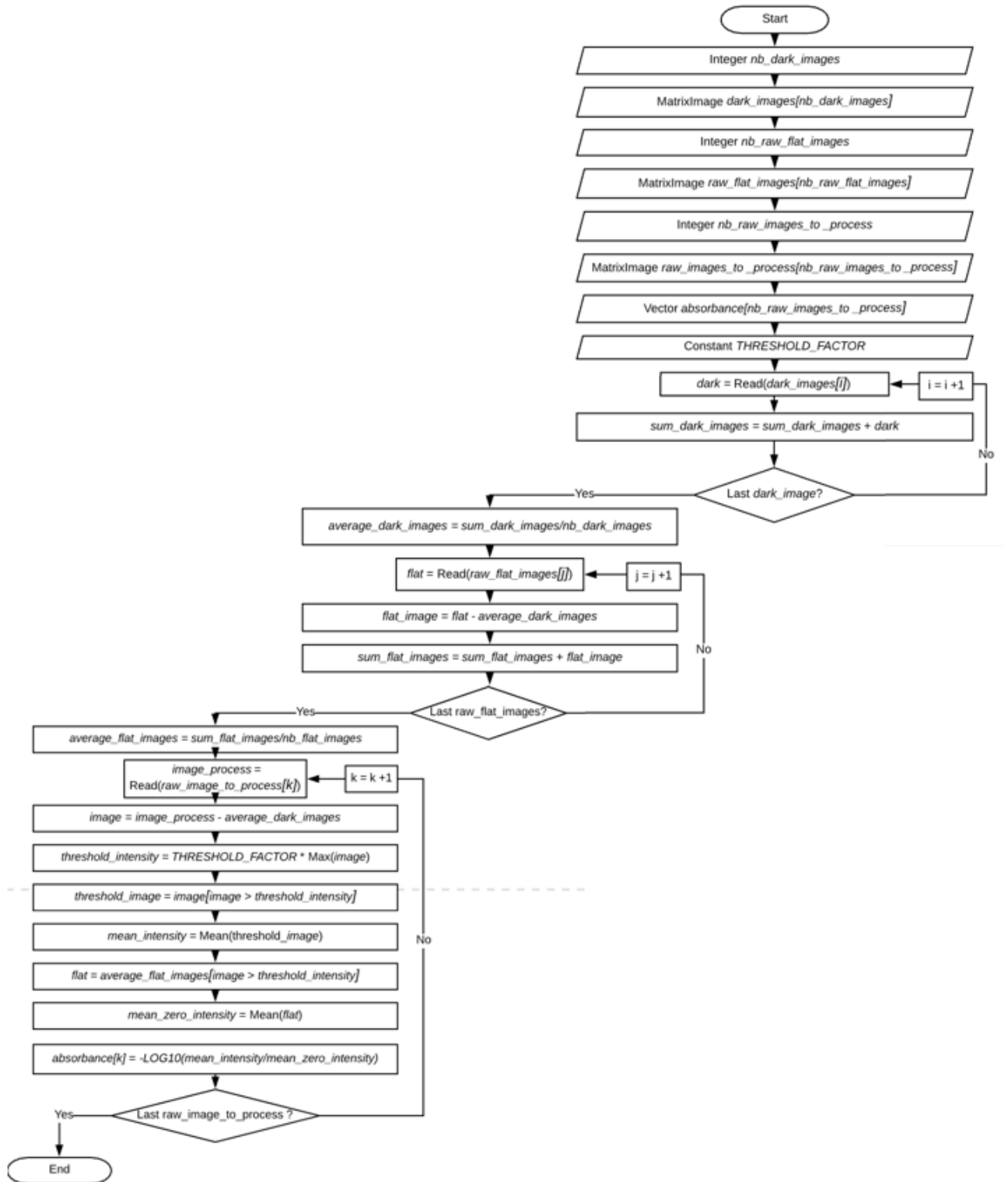


Figure II-34 : Flow chart of the image processing program used for the mass transfer experiments.

The matrices corresponding to the dark images were first summed and then divided by their total number to obtain one average matrix of the dark image. This average dark image was subtracted from the rest of the images to process in order to attenuate the signal noise (especially at the low intensities). The matrices of the raw images of the blank were then processed by subtracting the average matrix of the dark image, resulting in a “flat” matrix. The flat matrices were averaged in one single flat matrix (Figure II-35(a)).

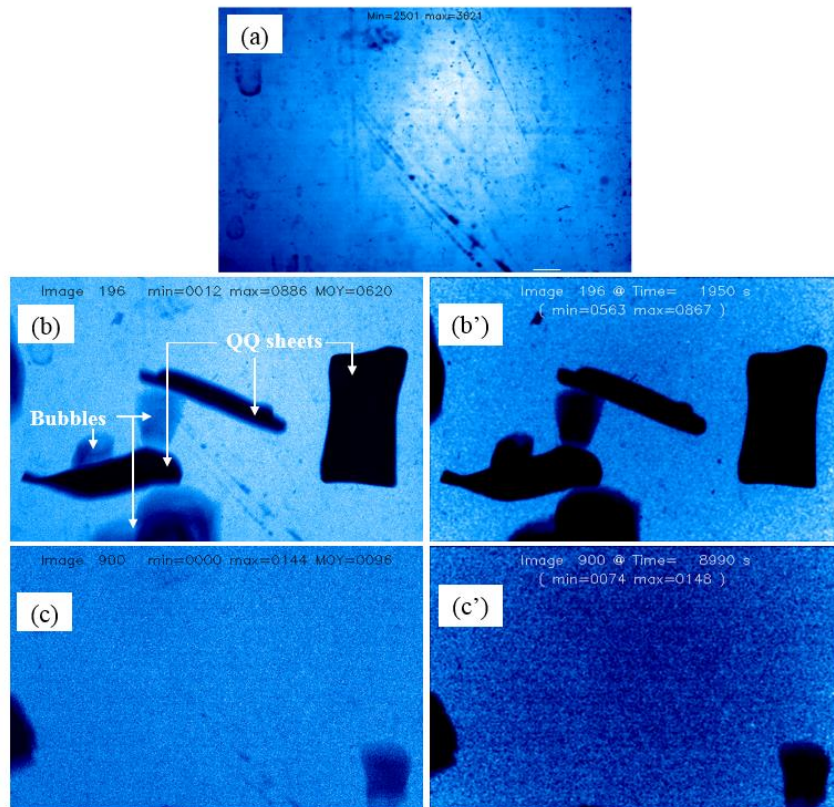


Figure II-35 : Example of images recorded during the mass transfer from the QQ sheets to the liquid under an air flowrate of $0.75 \text{ Nm}^3 \cdot \text{h}^{-1} \cdot \text{m}^{-2}$. (a) Average flat image obtained prior to the experiment. (b) Raw and (b') final processed image obtained at 32.5 min. (c) Raw and (c') final processed image obtained at 32.5 min.

The raw images of the experiment were then processed by subtracting the matrix of the average dark image to each one of them as a first step. Then, the threshold factor was applied in order to remove the objects (bubbles and QQ media) from the image and only keep the pixels corresponding to the liquid phase (having at least an intensity of 60 % of the maximal intensity). After applying the threshold factor, the mean intensity I of the processed image was determined by averaging the remaining pixels, and the intensity I_0 was deduced from averaging the intensities of the corresponding pixels (in the same location) on the flat matrix. Finally, the corresponding absorbance A was determined as in Equation II-12. Two

examples of images before and after processing are presented in Figure II-35 (b; b') and (c; c') at 35.5 and 150 min of operation, respectively. It is possible to observe that on the final processed images (Figure II-35 (b') and (c')) how only the pixels corresponding to the liquid phase are taken into account for the determination of the intensity I .

The intensity, absorbance and concentration curves corresponding to the mass transfer experiment from the QQ sheets to the liquid under an air flowrate of $0.75 \text{ Nm}^3.\text{h}^{-1}.\text{m}^{-2}$ are presented in Figure II-36(a), (b) and (c). In Figure II-36, the points a , b and c indicate the times corresponding to the examples of images presented in Figure II-35. It is possible to see that the mean intensity measured at 32.5 min (corresponding to the image in Figure II-35(b')) is around 850 whereas the intensity reached at 150 min (corresponding to the image in Figure II-35(c')) is around 100.

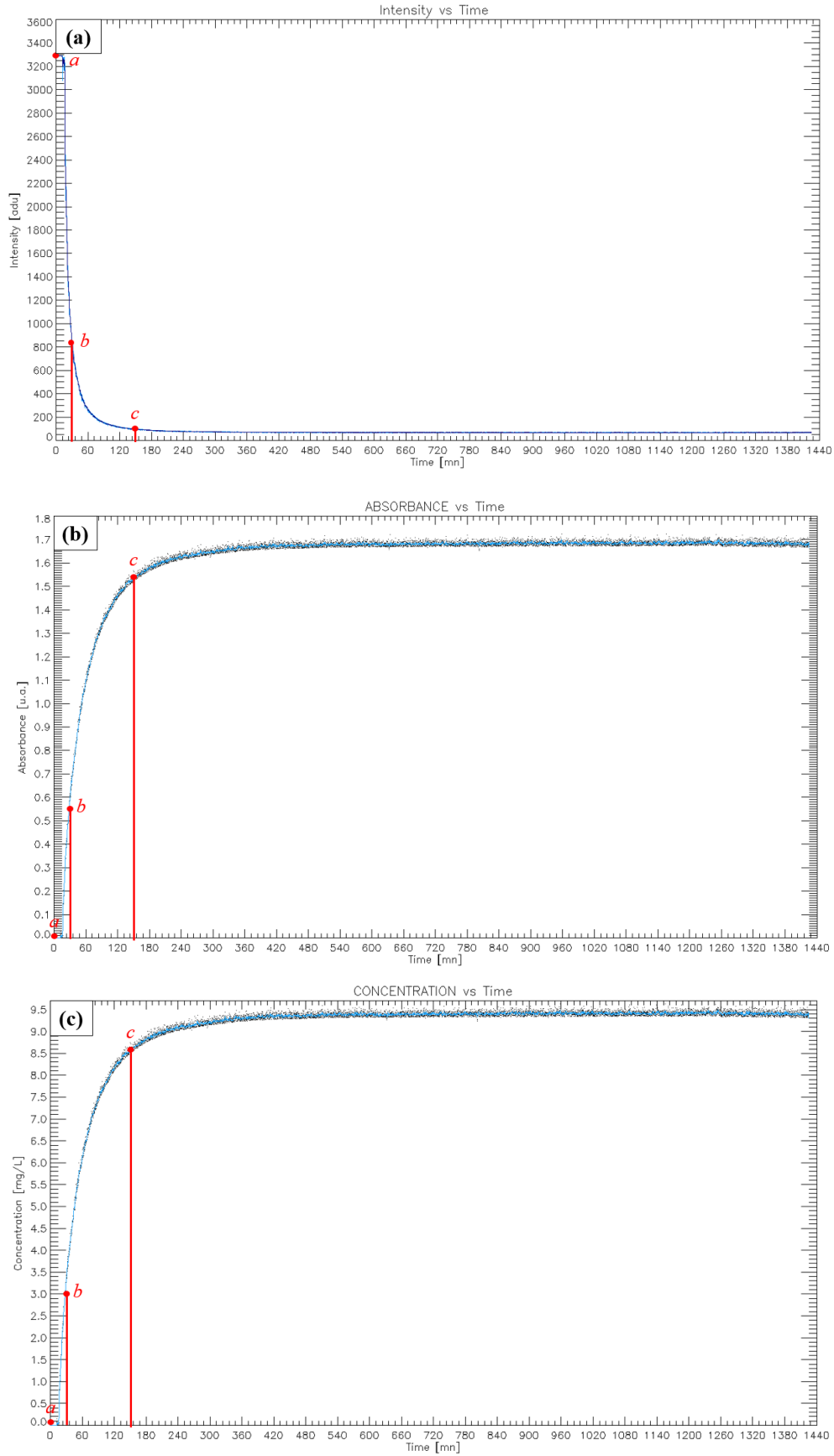


Figure II-36 : Example of (a) intensity (b) absorbance and (c) concentration curves obtained for the mass transfer experiment from the QQ sheets to the liquid under an air flowrate of $0.75 \text{ Nm}^3 \cdot \text{h}^{-1} \cdot \text{m}^{-2}$.

II.6.5.4. *Experimental protocol*

The transfer in the lab-scale ALMBR was studied in the aerobic tank, where the QQ media were introduced, and under the batch mode for the liquid phase (no feed) and the continuous mode for the gas phase (air injection). The QQ media were introduced at the beginning of the experiment in a volume fraction of 0.45 % v/v with respect to the total volume of the aerobic tank (13 L). The air-lift was set to a riser width of 15 mm and the experiment were conducted in absence of membrane, in order to prevent the transfer of tracer from the QQ media to the membrane, and only study the transfer to the liquid. In order to keep the hydrodynamics conditions similar, a plate was introduced to replace the membrane.

Different operating conditions were investigated in order to highlight the effect of the QQ media shape, as well as the effect of the hydrodynamics (three air flowrates) on the transfer from the QQ media to the liquid phase, and the investigated conditions are presented in Figure II-37.

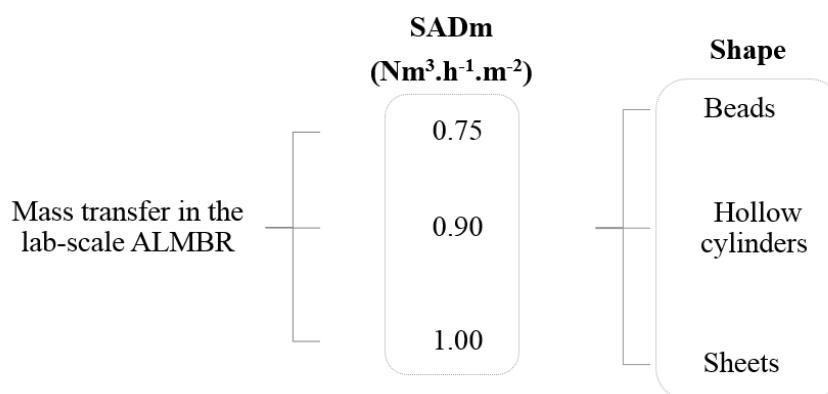


Figure II-37 : Experimental procedure for the study of the mass transfer from the QQ media to the liquid phase of the ALMBR.

II.6.5.5. *Stability of the Rose Bengal Lactone*

The stability of the Rose Bengal Lactone overtime was evaluated by introducing a solution of known concentration in the aerobic tank and measuring the light intensity of the light panel through it with the camera overtime (the light intensity being related to the concentration as in Equation II-12). The Rose Bengal Lactone was found to be sensitive to the strong and long-term exposure to the light panel, as the intensity was found to increase (concentration decrease) overtime. Thus, the strength of the light panel was adjusted with the view to avoid the degradation of Rose Bengal Lactone during the experiment, and be able to draw reliable conclusions on the mass transfer.

II.7. Filtration test for the study of membrane fouling

II.7.1. Principle, setup and experimental protocol

The filtration experiments were conducted in the lab-scale ALMBR in order to assess the membrane fouling under given conditions. As presented in Figure II-38, it consisted in feeding continuously (1.5 L.h^{-1}) the ALMBR with a model suspension and running the reactor with the recirculation between the aerobic tank and the anoxic tank (4 L.h^{-1}) and a permeate flowrate of around 1.5 L.h^{-1} corresponding to 15 LMH (precisely determined for each experiment). The feed was continuously mixed in the feed tank to prevent particles from settling and ensure the homogeneity of the suspension. A pressure sensor (Keller, PR-21Y / $\pm 1 \text{ bar}$) was set on the permeate side in order to measure the permeate pressure and then deduce the TMP (Figure II-38). The permeate was collected in a tank placed on a connected weighing balance (Sartorius, Germany) so that the permeate flowrate (and flux) could be monitored during the operation time. The filtration was run during 3 h, which was observed to be the time necessary to obtain significant membrane fouling. The filtration experiments were conducted under two different aeration conditions (0.75 and $1.00 \text{ Nm}^3.\text{h}^{-1}.\text{m}^{-2}$, in terms of SADm) and with or without the presence of QQ media (beads, hollow cylinders and sheets).

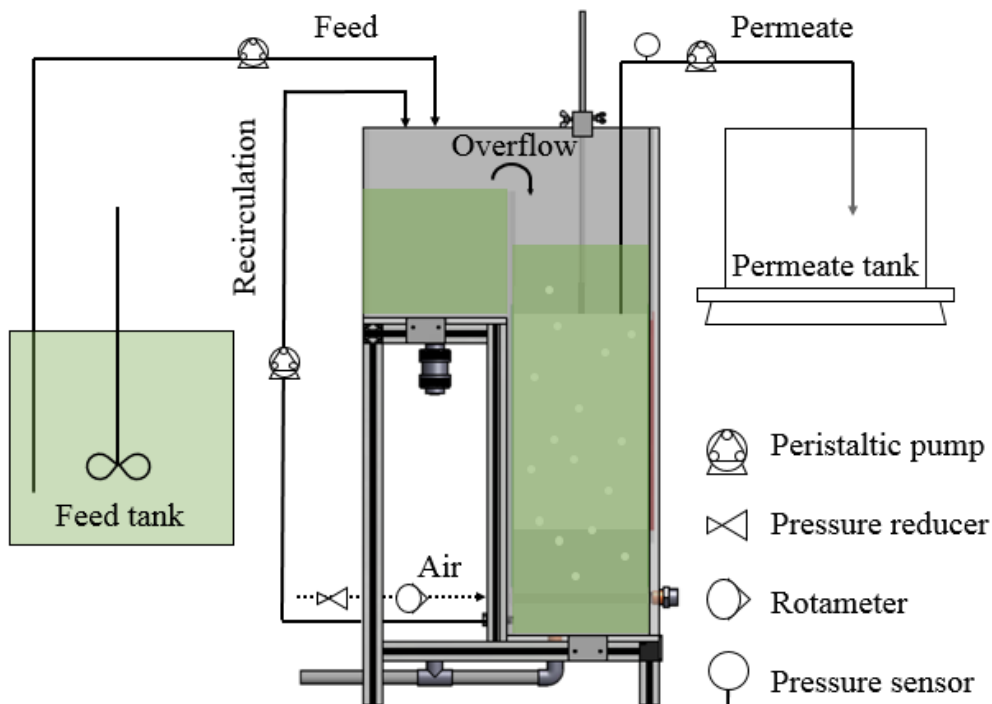


Figure II-38 : Experimental setup for the filtration experiment.

II.7.2. Model suspension (bentonite)

II.7.2.1. Selection of and preparation of the suspension

The filtration tests were performed with a model suspension of bentonite (Roth, Germany) in order to characterize the effect of the addition of QQ media on particles deposition on the surface of the membrane. The use of a model suspension also allowed to easily replicate the experiments by always preparing the same suspension. The bentonite was prepared at the concentration of 1.0 g.L^{-1} according to the following procedure:

- 30 g of bentonite powder were measured and introduced in a 1L-beaker, together with 1 L of deionized water.
- The resulting suspension of 30 g.L^{-1} was magnetically stirred at 250 rpm during 5 to 6 hours until complete homogeneity (complete destruction of massive bentonite aggregates).
- The stirring was stopped and the suspension was then left still overnight so that the biggest particles of the suspension settled to the bottom of the beaker.
- After 24 h, the bentonite particles were correctly hydrated, and only 800 mL of suspension were taken from the upper part of the beaker using a pipette. The suspension was then diluted with deionized water to prepare 24 L of feed at the concentration of 1 g.L^{-1} for the filtration experiment. The concentration was precisely measured with a turbidimeter before starting the experiment, and adjusted if needed.

II.7.2.2. Calibration curve (turbidity)

The turbidity was used to measure the concentration of bentonite and a calibration curve was made prior to the experiments. The curve is presented in Figure II-39. The linear regression obtained as used to convert the turbidity to the corresponding bentonite concentration.

II.7.2.3. Characterization of the suspension (size distribution)

The suspension of bentonite was characterized by measurement its particle size distribution using the Mastersizer 2000 (Malvern, United Kingdom). The size distribution of the feed was determined prior to each experiment to ensure the reproducibility of the operating conditions. An example of size distribution is presented in Figure II-40. The bentonite suspension used to feed the reactor described a monodisperse distribution with an average diameter $d_{4,3}$ ranging from 15 to 20 μm , for all the experiments.

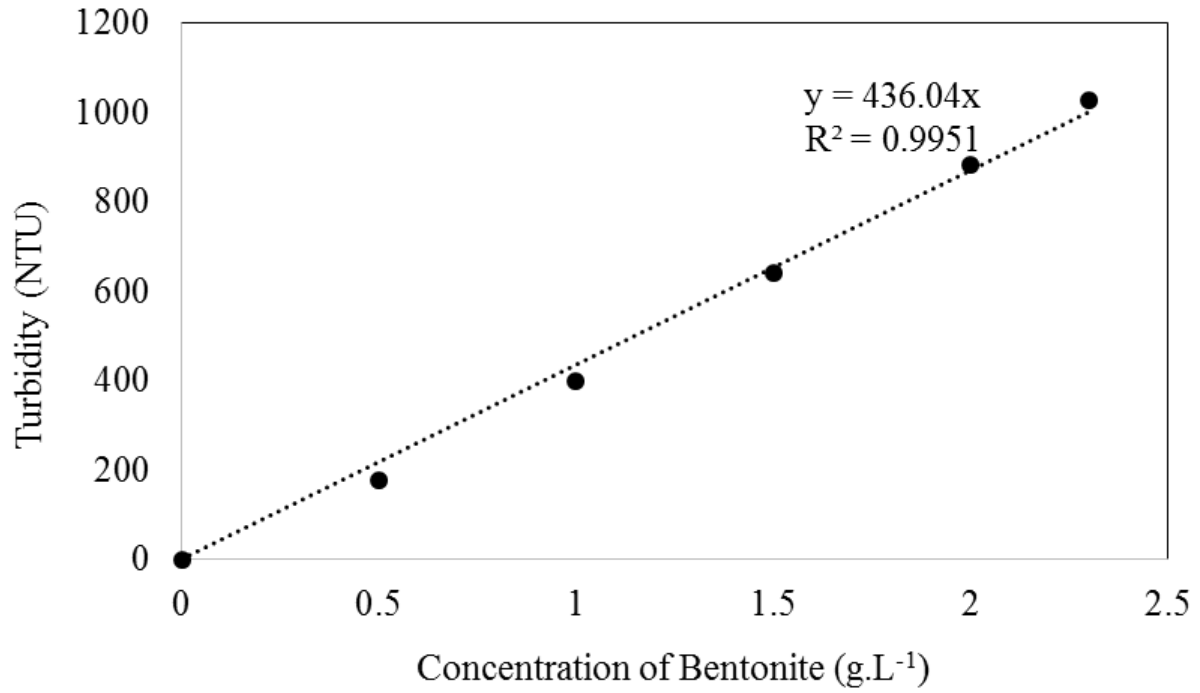
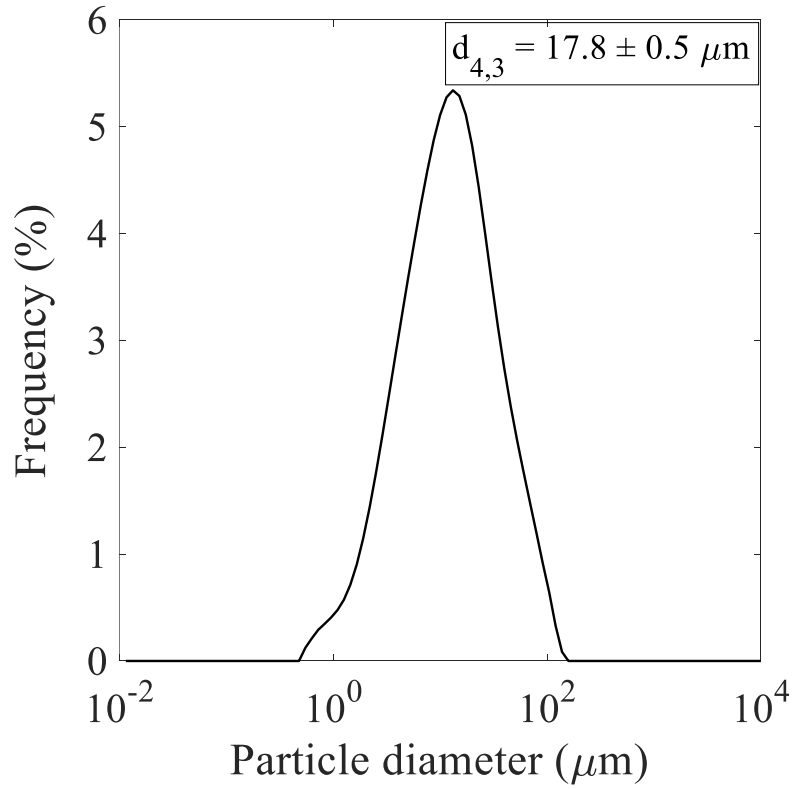


Figure II-39: Turbidity calibration curve for bentonite.

Figure II-40 : Size distribution curve of the bentonite suspension used to feed the ALMBR (for the experiment run under an SADm of 0.75 Nm³.h⁻¹.m⁻²).

II.7.3. Pressure monitoring for the TMP determination

The pressure sensor monitored the permeate pressure P_p overtime, and the data were recorded using a software and a computer. The TMP overtime is expressed as in Equation II-13, where P_i is the mean pressure of the liquid in the membrane tank. The pressure P_i was measured using the same pressure sensor once the permeate pump was turned off (under no suction).

$$TMP(t) = P_i - P_p \quad \text{II-13}$$

II.7.4. Permeability measurement

The permeability of the membrane to water was measured at different stages (before or after the filtration experiment). The measurement consisted in running a filtration with deionized water maintaining a constant volume of water in the tank, and varying the permeate flowrate. In total four different permeate flowrates $Q_{permeate}$ were selected and measured during the experiment to determine the permeate flux J according to Equation II-14 (where A_m is the membrane surface). The permeate flux was then converted from the actual temperature T during the experiment to 20 °C, as in Equations II-15 and II-16, where μ is the viscosity of water. The TMP was also measured and the permeability to water at 20 °C $L_p(20^\circ C)$ could finally be determined according to Equation II-17.

$$J = \frac{Q_{permeate}}{A_m} \quad \text{II-14}$$

$$J(20^\circ C) = J(T) \frac{\mu(T)}{\mu(20^\circ C)} \quad \text{II-15}$$

$$\mu(T) = 1.002 \exp \left(3.056 \frac{20 - T}{T + 105} \right) \quad \text{II-16}$$

$$L_p(20^\circ C) = \frac{J(20^\circ C)}{TMP} \quad \text{II-17}$$

II.7.5. Fouling characterization

In order to evaluate the extent of membrane fouling the permeability was constantly measured during the filtration experiments by monitoring the TMP together with the permeate flux.

In addition, the membrane permeability to water was measured before the experiment ($L_{p,initial}$), after the experiment with the fouled membrane ($L_{p,fouled}$) and then with the cleaned membrane ($L_{p,cleaned}$), in order to deduce the corresponding membrane resistances, via the Equations II-18 to II-20.

In Equations II-18 to II-20, R_m , R_t and R_{irr} are respectively the membrane resistance, the total resistance and the irreversible fouling resistance, in a way that the condition expressed as in Equation II-21 is fulfilled. The Equation II-21 describes the model of resistances-in-series which was used as an additional indicator of fouling extent, and in which R_{rev} is the resistance corresponding to the reversible part of fouling.

$$L_{p,initial} = \frac{1}{\mu R_m} \quad \text{II-18}$$

$$L_{p,fouled} = \frac{1}{\mu R_t} \quad \text{II-19}$$

$$L_{p,cleaned} = \frac{1}{\mu(R_m + R_{irr})} \quad \text{II-20}$$

$$R_t = R_m + R_{rev} + R_{irr} \quad \text{II-21}$$

In the present chapter, the methods used to conduct the experimental approach of this study were presented, in order to better understand how exactly the results of this study were obtained. The next chapter focuses on the hydrodynamics characterization of the ALMBR/QQ-ALMBR using optical techniques.

CHAPTER III.
HYDRODYNAMICS
CHARACTERIZATION OF THE
ALMBR/QQ-ALMBR

RESUME EN FRANCAIS

La caractérisation hydrodynamique du système étudié fait l'objet principal du présent chapitre. Avec l'application du Quorum Quenching (QQ), le bioréacteur à membrane à air-lift étudié devient un réacteur triphasique (gaz, solide, liquide) dont l'hydrodynamique complexe est particulièrement intéressante, du fait de son potentiel de décolmatage de la membrane. Le travail synthétisé dans ce chapitre a été réalisé afin de répondre à trois principales questions scientifiques qui se résument en :

- L'évaluation d'un éventuel impact de l'ajout des particules de QQ (QQ media) sur les paramètres hydrodynamiques des phases gazeuse et liquide (vitesses, rétention gazeuse, contraintes de cisaillement, ...etc.)
- L'étude du comportement intrinsèque des QQ media dans le réacteur étudié sous différentes conditions, principalement en termes de fluidisation.
- L'identification de conditions opératoires optimales assurant un juste compromis entre les deux précédents enjeux, en d'autres termes, le maintien des bénéfices des phases gaz et liquide (pour le décolmatage), et la promotion de la fluidisation des QQ media pour un effet ajouté sur la réduction du colmatage, par d'éventuelles collisions entre les QQ media et la membrane.

Dans cette optique, un état de l'art est d'abord dressé pour présenter les grandeurs physiques habituellement caractérisées dans les études hydrodynamiques de systèmes similaires à celui de cette étude. Quelques résultats tirés d'études pertinentes sont ensuite synthétisés et discutés, permettant de mettre en évidence deux échelles de caractérisation hydrodynamique : l'échelle globale (réacteur) et l'échelle locale (partie réduite ou point du réacteur). En adoptant cette distinction et en s'appuyant sur les matériels et méthodes présentés, les résultats dans ce chapitre permettent de montrer que les QQ media ont peu d'influence sur l'hydrodynamique à l'échelle globale, mais que les modifications à l'échelle locale dans la phase liquide en leur présence sont, elles, bien significatives.

III.1. Introduction

Hydrodynamics covers the in-depth study of the fluid motion in general, and is the subject of wide research in chemical engineering. For a great number of applications, hydrodynamics plays a key-role in the overall efficiency of the processes, as it is involved in determinant factors such as the residence time, the contact time between the different phases of a system, the flowing regime...etc. In the present study, the addressed system is an ALMBR for which the hydrodynamics is particularly interesting to explore, since it was reported to be of crucial importance for the (bio)fouling control. Also, with the application of QQ to the ALMBR, the studied system becomes a three-phase reactor, for which the hydrodynamics is even more complex and essential to investigate, since each of the three phases can be involved in the mitigation of biofouling: the gas phase by creating the driving force for the liquid to flow, the liquid phase by being the carrier of turbulence and shear stress forces, and the solid phase by exerting a mechanical effect on the membrane surface.

For these reasons, the present study focuses on the hydrodynamics by separately characterizing all the phases of the ALMBR/QQ-ALMBR, with the aim to meet the following objectives:

- Characterizing the ALMBRs in terms of hydrodynamics, via the study of the gas and the liquid phases. The confrontation of the results to the literature also served for their validation as well as their reliable use as a reference for comparison with the QQ-ALMBR.
- Characterizing the inherent behavior of the QQ media when introduced in the ALMBR and identifying the optimal conditions for their correct fluidization. Fluidization is a key-phenomenon in this study because it ensures the continuous recirculation of QQ media in the reactor and thus, it increases their chances to exert the expected mechanical washing effect on the membrane [9,13,39,40,51].
- Characterizing the QQ-ALMBRs using the same criteria as for the ALMBR, and assessing their potential effect on the gas and the liquid phases.
- On the basis of the obtained results, identifying the optimal conditions in terms of operating parameters and QQ media shape with the view to finding the right balance between maintaining the benefits of the gas-liquid flow and fostering the mechanical effect of QQ media.

To this end, a background section is first given in this chapter to present the fundamental tools for the hydrodynamics characterization of multiphase reactors, with the distinction between two scales: the global scale and the local scale. In addition, some results reported in the literature about the hydrodynamics of multiphase systems having similarities with the present study (MBR, ALRs, or ALMBRs) are presented for analysis. The selected investigation techniques (mostly optical) of the present study are further presented in the materials and methods section, and the results are discussed at

the two aforementioned scales. The approach consists in conducting experiments in the lab-scale ALMBR, under different operating conditions (aeration, riser width) and in presence or not of QQ media. Camera techniques are developed to characterize the solid and gas phase and give access to the bubble size, the bubble velocity, the QQ media velocity and the QQ media position. For the liquid phase, the PIV is used to measure the liquid velocities as well as the membrane shear stress. At each scale the characterization consists in focusing first on the ALMBR (with no QQ media), to be further able to assess the effect of the addition of QQ media on the different parameters.

III.2. Background

Multiphase reactors are the basis of a wide range of processes for several applications at the industrial scale. Some applications of multiphase reactors can be found in the areas of water treatment, production of chemicals, pesticides, pharmaceuticals, gas and oil refining...etc. In these reactors, the coexistence of the different phases creates favorable conditions for the transport phenomena (momentum, mass and/or heat transfer). In addition to the different possible applications, several types of multiphase reactors can be defined, distinguishing the combination of phases they are based upon (gas-liquid, gas-liquid-solid, liquid-liquid...etc.), or distinguishing their configurations (bubbles columns, airlift reactors, confined reactors, fixed-bed reactors, fluidized-bed reactors...etc.). The importance of characterizing the multiphase systems is twofold: firstly, it allows a better understanding of the interactions between the different phases and the identification of the key-parameters within one process; secondly, using the same characterization tools for different processes allow the comparison of their performances.

With respect to the three-phase ALMBR that is the subject of the present study, the most commonly used analysis tools for gas-liquid or gas-liquid-solid reactors are presented in the following. With this view, the main physical properties, correlations, dimensionless numbers are presented, and categorized depending on whether they provide global or local information about the process. A literature review of hydrodynamics characterization of systems having similarities with the present one is given.

In this study, the reactor consists in a **rectangular internal ALMBR** (Chapter II), but most of the correlations presented in the following were defined for cylindrical ALRs (either draft-tube or external-loop ALRs).

III.2.1. *Characterization of the hydrodynamics at the global-scale*

III.2.1.1. *Aeration*

Aeration intensity is a key-parameter in gas-liquid or gas-liquid-solid (bio)reactors as it was proved to govern the oxygen mass transfer [99–101], the mixing performance [99], the biofouling mitigation in MBRs [102–104], and thus, the overall process efficiency. The aeration is technically achieved by injecting in the reactor a certain amount of air expressed in terms of air flowrate Q_g , that can be directly

measured with a flowmeter. In order to take into account the geometry of the reactors, and to improve the comparison between several processes, the superficial gas velocity U_{gs} (m.s^{-1}) is used in most multiphase reactors and is calculated according to Equation III-1, where S is the cross-section opened to the free passage of air.

$$U_{gs} = \frac{Q_g}{S} \quad \text{III-1}$$

In the specific case of ALRs, the superficial gas velocity in the riser U_{gr} (m.s^{-1}) is defined as in Equation III-2, where A_r is the cross-section of the riser (the only aerated part of the reactor).

$$U_{gr} = \frac{Q_g}{A_r} \quad \text{III-2}$$

In MBRs, the aeration can be characterized in terms of Specific Aeration Demand (SAD), either with respect to the total membrane area A_m ($SADm$ in $\text{Nm}^3.\text{h}^{-1}.\text{m}^{-2}$) (Equation III-3), or to the total permeate flux J in m.s^{-1} ($SADp$ unitless) (Equation III-4) [97].

$$SADm = \frac{Q_g}{A_m} \quad \text{III-3}$$

$$SADp = \frac{Q_g}{JA_m} \quad \text{III-4}$$

III.2.1.2. Global gas-hold up

The global gas hold-up in gas-liquid or gas-liquid-solid reactors represents the volume fraction of air entrapped in the liquid phase and can be deduced from Equation III-5, where V_g is the total volume of gas and V the total working volume of the reactor. The global gas hold-up is an interesting parameter in (bio)reactors, because it can be correlated to the gas-liquid interface area, and to the oxygen transfer phenomenon.

$$\varepsilon_g = \frac{V_g}{V} \quad \text{III-5}$$

The global gas hold-up in ALRs can also be decomposed into a gas hold-up in the riser part and in the down-comer part, as in Equations III-6 and III-7, respectively, where V_{gr} and V_{gd} are the total gas volume in the riser and down-comer, and V_r and V_d are the total volume of the riser and down-comer, respectively. The difference of gas hold-up in the riser and down-comer is of great importance, because it is responsible of generating the driving forces inducing the internal liquid circulation.

$$\varepsilon_{gr} = \frac{V_{gr}}{V_r} \quad \text{III-6}$$

$$\varepsilon_{gd} = \frac{V_{gd}}{V_d} \quad \text{III-7}$$

In ALRs, The gas hold-up in the riser can also be calculated from the correlation proposed by Chisti et al. (1988) [105], that comes from a rearrangement of the correlation proposed by Hills (1976) [106] and links the riser gas hold-up to the gas and liquid superficial velocities in the riser U_{gr} and U_{lr} , respectively, according to Equation III-8. In this equation, the liquid velocity U_{lr} corresponds to the superficial velocity of the liquid flow induced by the air-lift motion. This correlation is only valid for air-water ALRs with $U_{lr} > 0.3 \text{ m.s}^{-1}$. The Equation III-9 further allows the determination of the corresponding gas hold-up in the down-comer.

$$\varepsilon_{gr} = \frac{U_{gr}}{0.24 + 1.35(U_{gr} + U_{lr})^{0.93}} \quad \text{III-8}$$

$$\varepsilon_{gd} = 0.89 \varepsilon_{gr} \quad \text{III-9}$$

A variety of other correlations were reported in the literature, linking the global gas hold-up in ALRs, not only to the superficial gas velocity as in Equation III-8, but also to the geometry and the physico-chemical properties of the fluid. Merchuk et al. (2002) [91] reviewed these correlations distinguishing the two types of ALRs: internal and external. Most of correlations reported for internal ALRs take the form presented in Equation III-10, where μ_{ap} is the effective viscosity of the fluid and a, α, β and γ are constants depending on the geometry and the physico-chemical properties of the liquid.

$$\varepsilon_{gr} = a(U_{gr})^\alpha \left(\frac{A_d}{A_r}\right)^\beta (\mu_{ap})^\gamma \quad \text{III-10}$$

In external loop-ALRs, the Equation III-11 was presented as the general form reported in the literature for the specific case of very low or nil gas recirculation from the riser to the down-comer parts, where α is a constant depending on the friction loss in the loop, and β a constant usually worth 0.6 to 0.7. In this case, the global gas hold-up in the riser only depends on the superficial gas velocity.

$$\varepsilon_{gr} = \alpha(U_{gr})^\beta \quad \text{III-11}$$

In three-phase ALRs (ALRs with calcium alginate beads with a density close to water, loaded at volume fractions up to 30 %) Freitas et al. (1999) [107] proposed the correlation presented in Equation III-12,

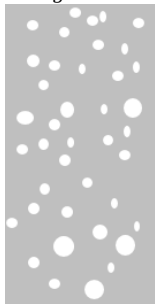


taking into account the solid hold-up ε_{sr} , the solid settling velocity U_{st} , the gas and liquid superficial velocities U_{gr} and U_{lr} . The parameters of the model C and U_{bt} were respectively the distribution factor (indicating the flow pattern, equals 1 when the flow is radially uniform) and the terminal velocity of a single bubble. Both parameters were optimized to fit to experimental data obtained in two configurations of ALRs (internal and external-loop), under superficial gas velocities up to 0.5 m.s^{-1} . In the three-phase internal-loop ALR, the increase of the solid hold-up from 0 to 30 % was found to increase the distribution factor from 1.13 to 2.21, indicating enhanced perturbation of the flow. However, in the three-phase external-loop ALR, the flow was perturbed when the solid hold-up varied from 0 to 10 %, and was more uniform when the solid hold-up was over 10 % (C approaching the value of 1).

$$\varepsilon_{gr} = \frac{U_{gr}}{C \left[U_{gr} + U_{lr} \left(1 + \frac{\varepsilon_{sr}}{1 - \varepsilon_{gr} - \varepsilon_{sr}} \right) - \varepsilon_{sr} U_{st} \right] + U_{bt}} \quad \text{III-12}$$

III.2.1.3. Distribution of the gas phase and flowing regimes

A lot of parameters can affect the distribution of the gas phase in multiphase reactors such as the geometry of the reactor, the gas and the liquid superficial velocities, and the physico-chemical properties etc. As an example, in confined reactors where the bubble size can be in the range of the reactor dimension, three different gas-liquid flowing regimes were proposed on the basis of the values of the global gas hold-up, as presented in Table III-1. For low gas hold-up, the gas phase is completely dispersed in the liquid in the form of bubbles with more or less uniform size distribution. Under the intermediate gas hold-up, the flow consists in an alternation of big bubbles and liquid slugs. Finally, for the high gas hold-up, the gas phase becomes continuous and flows into the liquid channel that surrounds it.

Table III-1: Gas-liquid flowing regimes in confined environments.

Flowing regime	Bubbly flow	Slug flow	Annular flow
Global gas hold-up (%)	$\varepsilon_g < 20$	$20 < \varepsilon_g < 90$	$\varepsilon_g > 90$
Schematic representation			

In MBRs, the bubbly and slug flows are the most reported regimes. Based on image observations, Wicaksana et al. (2006) [108] have demonstrated that the number of bubbles also varied with the

aeration intensity in a non-confined tank with hollow fibers under the bubbly flow. This result was further confirmed by Pollet et al. (2009) [103] in a more compact hollow fiber module, where the increase of the air flowrate was also found to generate more heterogeneous populations of bubbles. The characterization of the bubbles in terms of size and shape will be more deeply discussed in the next section, since it is part of the local hydrodynamics characterization.

III.2.1.4. *Liquid circulation*

The liquid circulation is of great importance in multiphase reactors because it rules the prevailing flow regime, the mixing performance, the heat and mass transfer phenomena, and also the global gas hold-up in the case of ALRs (as showed by Equation III-8). The liquid circulation in multiphase reactors can either be ensured by forced convection (using pumps) or can be induced by the injection of air. Indeed, in the case of ALRs, the injection of air generates a difference of densities in the bulk between the riser and down-comer parts, which induces the circulation of liquid.

In order to characterize the liquid circulation in ALRs, a great number of studies focused on demonstrating the interdependence of the liquid velocity in the riser U_{lr} or V_{lr} (superficial or linear depending on the authors, with $V_{lr} = U_{lr}/(1-\varepsilon_{gr})$ where ε_{gr} represents the gas hold-up) to various parameters related to the geometry, the liquid properties and to the superficial gas velocity. As an example, Bello et al. (1984) [109] proposed, via an energy balance approach, a correlation to predict the liquid velocity in the riser, according to Equation III-13, where α depends on the type of reactor (it is worth 1.55 for external-loop ALRs and 0.66 for draft-tube ALRs), and β takes values around 0.75.

$$V_{lr} = \alpha \left(\frac{A_d}{A_r} \right)^\beta (U_{gr})^{1/3} \quad \text{III-13}$$

The latter correlation was found to correctly predict the liquid velocity in the riser in the two types of ALRs tested: draft-tube ALR under superficial gas velocities ranging from 1.37 to 8.60 m.s⁻¹; and external loop-ALR under superficial gas velocities comprised between 0.014 and 0.086 m.s⁻¹.

However, Chisti et al. (1988) [105] further proposed a more universal model (applicable to a wider range of cylindrical ALRs) with the general form presented in Equation III-14, where h_D is the total liquid height, g is the gravitational acceleration, K_T and K_B are the frictional loss coefficients at the top and the bottom connecting sections of the ALR, respectively.

$$U_{lr} = \left[\frac{2gh_D(\varepsilon_{gr} - \varepsilon_{gd})}{\frac{K_T}{(1 - \varepsilon_{gr})^2} + K_B \left(\frac{A_r}{A_d} \right)^2 \frac{1}{(1 - \varepsilon_{gd})^2}} \right]^{0.5} \quad \text{III-14}$$

From this general correlation, two particular cases were distinguished for split-cylinder or concentric-tube ALRs with Equation III-15, and for external-loop ALRs with Equation III-16.

$$U_{lr} = \left[\frac{2gh_D(\varepsilon_{gr} - \varepsilon_{gd})}{K_B \left(\frac{A_r}{A_d}\right)^2 \frac{1}{(1 - \varepsilon_{gd})^2}} \right]^{0.5} \quad \text{III-15}$$

$$U_{lr} = \left[\frac{2gh_D(\varepsilon_{gr} - \varepsilon_{gd})}{K_B \left(\frac{1}{(1 - \varepsilon_{gr})^2} + \left(\frac{A_r}{A_d}\right)^2 \frac{1}{(1 - \varepsilon_{gd})^2} \right)} \right]^{0.5} \quad \text{III-16}$$

For different types of internal-loop ALRs, the frictional loss coefficient K_B was found to depend on the geometry, according to Equation III-17, where A_b is the free area available for the liquid flow between the riser and the down-comer, as described in Chapter I.

$$K_B = 11.402 \left(\frac{A_d}{A_b} \right)^{0.789} \quad \text{III-17}$$

The model of Chisti et al. (1988) [105] was applied to several experimental data from a wide range of ALRs, and was demonstrated to predict well the liquid velocity in the riser with a $\pm 30\%$ deviation.

For the application to MBRs, Prieske et al. (2008) [110] proposed a modification of the model of Chisti et al. (1988) [105] in a ALMBR equipped with several plates in the riser to mimic the presence of a flat-sheet membrane module, as presented in Figure III-1.

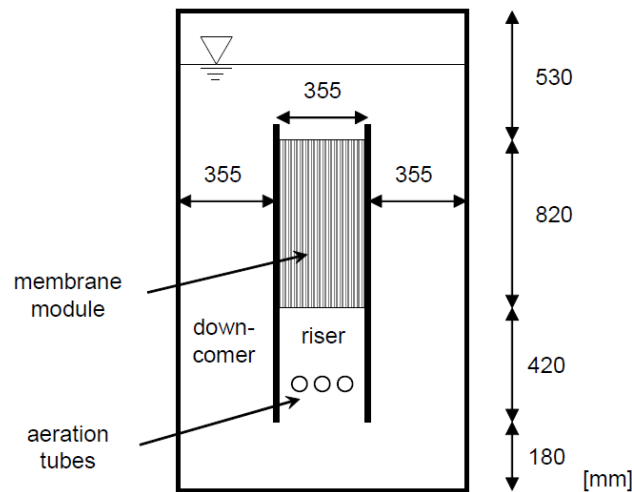


Figure III-1: Experimental setup of ALMBR studied by Prieske et al. (2008) [110].

In their model, Prieske et al. (2008) [110] took into account the pressure loss in the liquid flow in the riser, due to the presence of the membrane module in it, which resulted in the addition of a term to the model of Chisti et al. (1988) according to Equation III-18, where K_{MM} is a resistance coefficient traducing the effect of the membrane module in the riser, A_{MM} is the free area for the liquid flow between the membrane plates, l_{MM} is the height of the membrane module, d_{MM} is the distance between the membrane plates, and T is the depth of the membrane module. The coefficient K_B is defined as in the model of Chisti et al. (1988), and represents the frictional loss coefficient at the bottom sections of the ALR.

$$U_{lr} = \left[\frac{2gh_D(\varepsilon_{gr} - \varepsilon_{gd})}{K_B \left(\frac{A_r}{A_d}\right)^2 \frac{1}{(1 - \varepsilon_{gd})^2} + K_{MM} \frac{1}{2} \left(\frac{A_r}{(1 - \varepsilon_{gr})A_{MM}}\right)^2 \frac{l_{MM}(d_{MM} + T)}{d_{MM}T}} \right]^{0.5} \quad \text{III-18}$$

The resistance coefficient of the membrane module K_{MM} can be determined either by the Equation III-19 or the Equation III-20 [110], where Re_{MM} is the Reynolds number inside the membrane module deduced from Equation III-21 (ν_l is the kinematic viscosity of the liquid). In order to apply Equation III-19 or Equation III-20, Re_{MM} should be between 2.3×10^3 and 10^5 , or between 2×10^4 and 2×10^6 , respectively.

$$K_{MM} = (100Re_{MM})^{-0.25} \quad \text{III-19}$$

$$K_{MM} = 0.0054 + \frac{0.3964}{Re_{MM}^{0.3}} \quad \text{III-20}$$

$$Re_{MM} = \frac{U_{lr} A_r D_h}{(1 - \varepsilon_{gr}) A_{MM} \nu_l} \quad \text{III-21}$$

Among the presented models, the model of Prieske et al. (2008) [110] could be relevant for the application to the ALMBR with flat-sheet membrane modules as in the present study, with the difference that the studied ALMBR comprises one single flat-sheet membrane.

III.2.1.5. Liquid flow regime

The liquid flow regime can be characterized by calculating the Reynolds number on the basis of the liquid velocity. For a liquid flowing between two parallel plates for example, a Reynolds number relative to the liquid velocity U_l can be determined as in Equation III-22, where D_h is the hydraulic diameter defined as in Equation III-23 (where A and P are respectively the wetted area and perimeter of the cross-section of the flow).

$$Re_l = \frac{\rho_l U_l D_h}{\mu_l} \quad \text{III-22}$$

$$D_h = \frac{4 A}{P} \quad \text{III-23}$$

In the case of ALRs, where gas and liquid are the two phases present in the riser, the mix velocity U_{mr} can be defined as in Equation III-24, and the corresponding mix-Reynolds number can be determined via Equation III-25.

$$U_{mr} = U_{lr} + U_{gr} \quad \text{III-24}$$

$$Re_m = \frac{\rho_l U_{mr} D_h}{\mu_l} \quad \text{III-25}$$

The values of Reynolds that delimit the different flowing regimes vary with the geometry and different values were reported in the literature. However, the value of 2000 is the most commonly used as a reference below which the flow can be considered as laminar.

III.2.1.6. Global solid hold-up

Similarly to the gas hold-up, the solid hold-up in multiphase reactors (including a solid phase) is defined as the total volume of solid V_s entrapped in the total working volume V , as in Equation III-26.

$$\varepsilon_s = \frac{V_s}{V} \quad \text{III-26}$$

The total solid hold-up in the specific case of ALRs can be decomposed in a solid hold-up in the riser ε_{sr} and a solid hold-up in the down-comer ε_{sd} . Based on a force balance (gravity forces = friction forces), Heijnen et al. (1997) [111] proposed a hydrodynamic model defining the pressure difference per unit of height $\frac{\Delta P}{gh_d}$ as in Equation III-27. This model offers a complete representation of the fluid dynamics in a three-phase ALR from a macroscopic perspective and actually reveals that the presence

of solid particles may lower the liquid circulation in the ALR, if $\varepsilon_{sr} > \varepsilon_{sd}$ (which happens when $\rho_s > \rho_l$ and thus, when the solid rising velocity is lower than the liquid one).

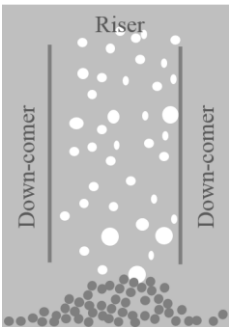
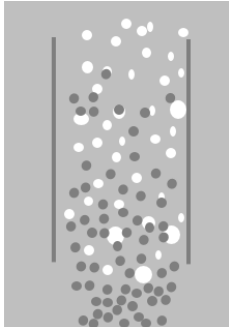
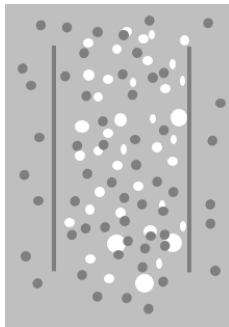
$$\frac{\Delta P}{gh_d} = (\varepsilon_{gr} - \varepsilon_{gd}) - (\varepsilon_{sr} - \varepsilon_{sd})(\rho_s - \rho_l) \quad \text{III-27}$$

III.2.1.7. Fluidization regime

When particles are added to ALRs, different flowing behaviors for the solid phase can be observed depending on the operating conditions. In a draft-tube ALR with a conical bottom, Fan et al. (1984) [112] defined three different regimes of fluidization based on their experimental observations, using spherical particles having a diameter of 2 to 4 mm, and a density of 2500 to 3700 kg.m⁻³. Our interpretation of what was reported by Fan et al. (1984) is schematically represented in Table III-2. Three main flowing regimes for the solid particles are observable: the packed bed regime where the particles are settled at the bottom of the reactor and slowly carried by the increasing liquid flow to form a spout under the riser part; the fluidized bed regime where all the particles migrate to the riser part; and the circulated bed regime where the particles overpass the riser and are recirculated to the down-comer. Fan et al. (1984) [112] proposed domains of superficial gas and liquid velocities to delimit the three regimes, however these are specific to their conical geometry and particles properties, and cannot be used as universal values. Nevertheless, these regimes can still be used qualitatively to characterize three-phase ALRs.

It is worth mentioning that the circulated bed regime is the most valuable for application to (bio)chemical reactors (also in the present study) as it offers optimal contact efficiency, however it requires higher energy consumption.

Table III-2: Fluidization regimes for solid particles in three-phase ALRs based on the observations of Fan et al. (1984) [112] (*the white circles represent bubbles and the dark ones represent solid particles*).

Flowing regime	Packed bed	Fluidized bed	Circulated bed
	Gas and/or liquid velocity increase →		
Schematic representation			

III.2.1.8. Minimum (or critical) fluidization velocity

The fluidization of solid particles in three-phase systems, and particularly in three-phase ALRs, is ensured by the driving force transported by the liquid circulation. The minimum fluidization velocity refers the critical amount of energy needed to counterbalance the gravity or buoyancy forces naturally exerted on the particles. The minimum fluidization velocity can be measured experimentally using visualization techniques, and two values can be determined whether the experiment is conducted under increasing or decreasing velocity, corresponding respectively to the minimum fluidization velocity to generate or maintain the complete suspension of particles. These two values were reported to be different as the fluidization phenomenon describes a hysteresis effect [113].

Some correlations were reported in the literature for the prediction of the minimal fluidization velocity in three-phase reactors, knowing the operating conditions and the properties of the three phases. In the literature, the minimal fluidization was defined with respect to either the gas or the liquid phase, since both are interdependent and contribute to the whole hydrodynamics.

Immich and Onken (1992) [114] were one of the first to propose a model based on energy balance to express the minimum fluidization gas velocity U_{gmf} in bubble columns and draft-tube ALRs, according to Equation III-28, where \overline{U}_{lr} and \overline{U}_{sr} are the mean liquid and solid superficial velocities in the riser, ε_{lr} and ε_{sr} are the liquid and solid hold-ups in the riser, ε_l is the total liquid hold-up, $\overline{\rho_r}$ is the mean density in the riser (gas and liquid), and f is the drag coefficient of the particle in free motion (rise or fall depending on its density) in the liquid. This model showed good agreement with experimental data using small glass spheres (0.1 to 0.3 mm), but required the measurement of global parameters such as the hold-ups and the mean superficial velocities during the operation.

$$U_{gmf} = \frac{(\overline{U}_{lr}\varepsilon_{lr} + \overline{U}_{sr}\varepsilon_{sr})A_r}{Vg((\rho_s - \rho_l)\varepsilon_l + \rho_l\varepsilon_l)} f \frac{\overline{\rho_r}}{2} \overline{U}_{lr}^2 \quad \text{III-28}$$

Petrovic et al. (1993) [115] further proposed an empirical correlation on the basis of experiments conducted in a draft-tube ALR with glass spheres (1 to 6 mm, density $> 2500 \text{ kg.m}^{-3}$) under the circulated bed regime (Table III-2), expressed as in Equation III-29, where U_{tp} is the terminal velocity of a single particle in free motion in the liquid, μ_l is the liquid viscosity, σ is the surface tension, and M is the Morton number determined by Equation III-30. The fact that this approach is only based on data that can be known *a priori*, makes it a predictive model.

$$\frac{U_{gmf}}{U_{tp}} = 11.48\varepsilon_s^{1.22} \left(\frac{U_{tp}\mu_l}{\sigma} \right)^{-0.64} M^{0.14} \left(\frac{A_r}{A_d} \right)^{0.32} \quad \text{III-29}$$

$$M = \frac{g(\rho_l - \rho_g)\mu_l^4}{\rho_l^2 \sigma^3} \quad \text{III-30}$$

Concerning the minimum fluidization liquid velocity U_{lmf} , Nakao et al. (2003) [116] measured it in an external-loop ALR loaded with glass spheres and defined it as the velocity induced in the liquid by the injection of gas at the velocity of U_{gmf} . Based on a dimensional analysis, Nakao et al. (2003) [116] proposed the correlation presented in Equation III-31, where D_r is the diameter of the riser part and C_s is the average concentration of solid particles in the reactor.

$$\frac{\rho_l U_{lmf} D_r}{\mu_l} = 8.71 \left(\frac{\rho_l U_{tp} d_p}{\mu_l} \right)^{0.60} \left(\frac{d_p}{D_r} \right)^{-1.13} \left(\frac{\rho_s}{\rho_l} \right)^{1.12} \left(\frac{C_s}{\rho_s} \right)^{0.07} \quad \text{III-31}$$

The presented correlations were all developed for and/or validated with experiments in draft-tube or external-loop ALRs with particles having higher density than water, under continuous gas injection but with no liquid feed. To our best knowledge, no similar studies were carried out in rectangular ALRs, or with particles having a density close to the water density. Still, the few reported studies show the strong dependency of the minimal fluidization velocity (of the gas or the liquid phase) to the particles properties (size, density) and terminal velocity, to the properties of the liquid and gas phases (densities, viscosity, and surface tension) and to the operating conditions (solid holdup, reactor geometry). In a three-phase fluidized bed reactor, Pjontek and Macchi (2014) [117] also showed the importance of the particle shape, by comparing the minimum fluidization velocities obtained with spheres and cylinders (having roughly the same diameter) under the same aeration conditions. These findings are valuable information for the design of process with a view to enhancing the fluidization and reducing the energy consumption.

III.2.2. Characterization of the hydrodynamics at the local-scale

III.2.2.1. Bubble size and shape

The bubbles in multiphase flows can exhibit a variety of sizes and shapes, including in one single system, as their properties can be influenced by a great number of parameters such as: the geometry (confinement), the superficial gas velocity, the properties of the liquid phase and the type of the air diffuser. For this reason, the size and shape of bubbles has been widely investigated subject in all kinds of multiphase reactors: bubbles columns, ALRs, MBRs...etc.

The bubbles are usually axisymmetric and their size can be characterized in terms of equivalent diameter of a sphere having the same volume V_b (volume-equivalent diameter d_e) or the same projected area A_p (circle-equivalent diameter d_a), respectively deduced from Equations III-32 and III-33.

$$d_e = \left(\frac{6V_b}{\pi}\right)^{1/3} \quad \text{III-32}$$

$$d_a = \left(\frac{4A_p}{\pi}\right)^{1/2} \quad \text{III-33}$$

Based on the volume-equivalent diameter d_e , the determination of the dimensionless Eötvös, Morton (Equation III-30) and (bubble-)Reynolds numbers is made possible, in order to quantify the interactions between the viscous forces, interfacial tension, gravity forces and kinetics forces. These numbers are deduced from Equations III-34 and III-35, where $\Delta\rho$ is the difference of densities between the liquid and the gas phases, σ is the gas-liquid interfacial tension and μ_l the dynamic viscosity of the liquid.

$$Eö = \frac{g\Delta\rho d_e^2}{\sigma} \quad \text{III-34}$$

$$Re_b = \frac{\rho_l U_b d_e}{\mu_l} \quad \text{III-35}$$

On the basis of these three dimensionless numbers, Clift et al. (1978) [118] proposed the diagram presented in Figure III-2 for the prediction of the shape of free-rising bubbles in infinite and stationary liquid media. This diagram is only valid for gas-liquid dispersions under the bubbly flow with no interactions between the bubbles and with no wall effect.

Experimentally, the bubble size and shape are often determined by visualization techniques through clear reactors. The variety of sizes and shapes and the order of magnitude that were reported in the literature for different multiphase systems, will be discussed in the following.

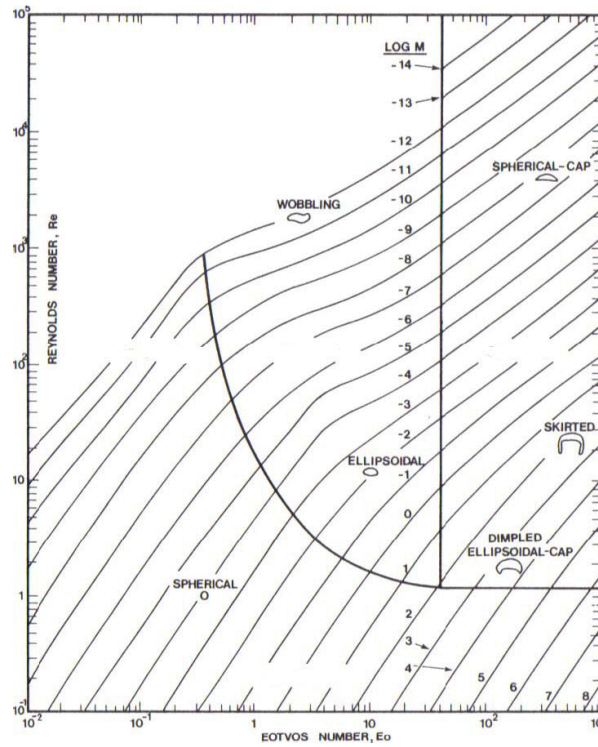


Figure III-2: Shape regimes for bubbles in free motion through infinite and stationary liquid media [118].

III.2.2.2. Bubble velocity

The bubble velocity is also one of the most commonly measured parameters in multiphase flows, usually via visualization techniques similarly to the ones used for the bubble size and shape characterization. Besides, as for the other parameters, some correlations have been reported in the literature for the prediction of bubble velocity.

Davies and Taylor (1950) [119] proposed physical models to link the bubble velocity of large bubbles rising in infinite stationary liquid media or in confined cylindrical channels under the slug-flow regime, according to Equations III-36 and III-37, respectively, where a is the radius of the channel and R_c is the radius of curvature of the bubble (the radius of its spherical top part).

$$U_b = \frac{2}{3} \sqrt{g R_c} \quad \text{III-36}$$

$$U_b = 0.464 \sqrt{g a} \quad \text{III-37}$$

Davies and Taylor (1950) [119] validated these models with experimental data in both configurations (non-confined and confined environments) with bubbles having a diameter ranging from 1 to 8 cm.

The diagram presented in Figure III-2 proposed by Clift et al. (1978) [118] can also be used as a tool for estimating the bubble terminal velocity U_b that appears in the bubble-Reynolds number (Equation III-35) knowing its volume-equivalent diameter, the properties of the liquid and gas phases, and keeping in mind that it only concerns rising bubbles in infinite and stationary liquid media. In addition, Clift et al. (1978) [118] gathered a great number of experimental data for the specific case of air bubbles rising in water, distinguishing the cases of pure water and contaminated water, as presented in Figure III-3. For bubbles having a volume-equivalent diameter d_e above 1.3 mm in pure water (the highest curve on Figure III-3), Clift et al. (1978) approximate the bubble terminal velocity with Equation III-38.

$$U_b = \left[2.14 \frac{\sigma}{\rho d_e} + 0.505 g d_e \right]^{1/2} \quad \text{III-38}$$

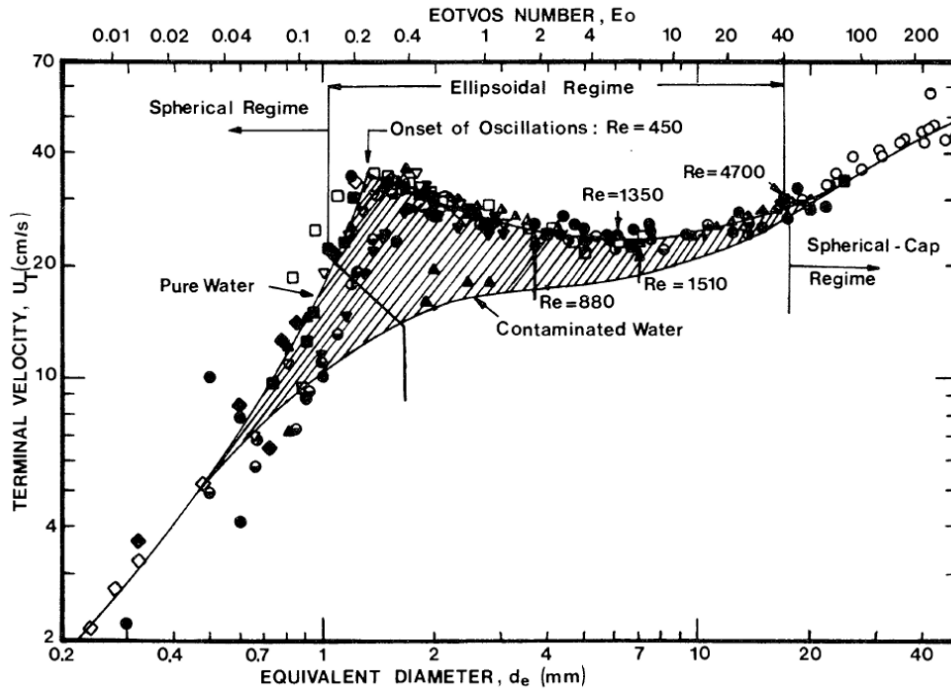


Figure III-3: Terminal velocity for air bubbles rising in stationary water at 20 °C [118].

The presented correlations show that a strong interaction exists between the size and the velocity of a bubble, with different regimes depending on the bubble size (higher or lower than about 1.3 mm). Nevertheless, it is important stressing that these tools are based on a single rising-bubble, whereas most of the multiphase systems encountered in reality deal with bubbles swarms with non-negligible bubble-bubble interactions. Therefore, their application to the characterization of ALRs, MBRs or ALMBRs, is

to be taken carefully. The characterization of bubbles in non-stationary liquid addressed in some experimental studies will be discussed in the following.

III.2.2.3. *Liquid velocity field*

The local velocity of the liquid U_l can be decomposed in an average liquid velocity \bar{U}_l and a fluctuation u_l' , according to the Reynolds theory represented by Equation III-39.

$$U_l = \bar{U}_l + u_l' \quad \text{III-39}$$

The local liquid velocity can be experimentally measured by advanced techniques, among which Laser-Doppler Anemometry and PIV are the most used ones, as reviewed by Jensen (2004) [120]. These techniques allow obtaining a velocity field, which means a distribution of velocity in a given region of the liquid phase.

Some authors have investigated the local velocity in MBRs equipped with hollow fibers. As an example, Yeo et al. (2006) [121] characterized by PIV the liquid flow in a 3x3 hollow fiber module under two different liquid circulation flowrates. As it is possible to observe in Figure III-4, the velocity inside the module is much lower than the velocity outside of it, indicating the difficulty of the liquid to circulate in between the fibers and the pressure loss in the fibers. Even though this was a very specific case, this study actually demonstrated the benefit of characterizing the liquid flow at the local-scale which allows identifying the non-uniformities in a multiphase system, and thus, the non-reliability of the average liquid velocity as a single physical parameter for the characterization of the liquid flow. Furthermore, the determination of the liquid velocity field gives access to the local turbulence phenomena, as well as, to the local shear stress on the membrane, in the case of MBRs that are phenomena which can have an effect on fouling control.

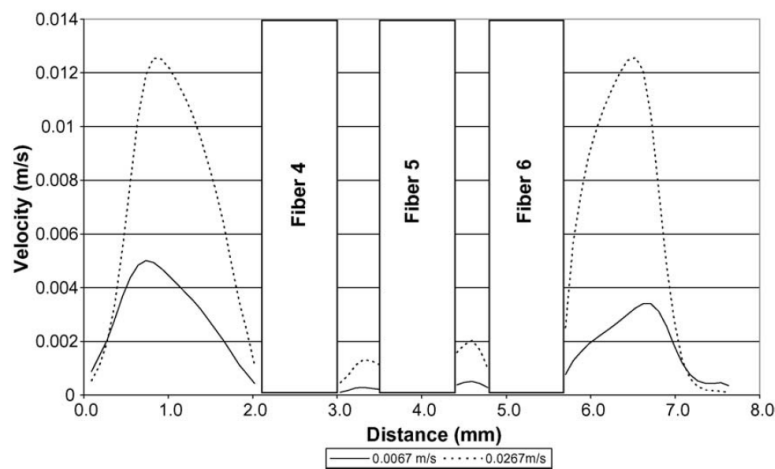


Figure III-4: Velocity profiles using PIV in a 3x3 hollow fiber module under two different liquid axial flowrates (0.0067 and 0.0267 m.s^{-1}) [121].

III.2.2.4. Wall shear stress

The wall shear stress τ is defined as the viscosity force induced by the flow on the surface of a wall. It is linked to the liquid flow velocity U_l parallel to the wall and the liquid viscosity μ_l , according to Equation III-40.

$$\tau = \mu_l \left(\frac{\partial U_l(x)}{\partial x} \right)_{x_{wall}} \quad \text{III-40}$$

The wall shear stress is highly valuable information when studying aerated MBRs because the shear stress created by the bubbles circulation is assumed to be involved in the biofouling reduction. For its determination from Equation III-40, the knowledge of the local liquid flow velocity $U_l(x)$ is needed and requires the use of advanced measurement techniques (such as PIV). Also, in the case of MBRs, the membrane shear stress could also be directly measured either by an electrochemical technique [122,123] or using a shear stress meter (piezoelectric sensor) [124].

Using a shear stress meter, Yamanoi and Kageyama (2010) [124] measured the shear stress on the surface of a flat sheet membrane located at 10 mm from the tank wall, defining a riser part in which air bubbles were injected at a superficial gas velocity of 0.03 m.s^{-1} through a glass ball filter diffuser. Figure III-5 shows the shear stress profile obtained by Yamanoi and Kageyama (2010) [124] which displays high fluctuations that were attributed to the passage of bubbles and to the liquid disturbance due to these bubbles.

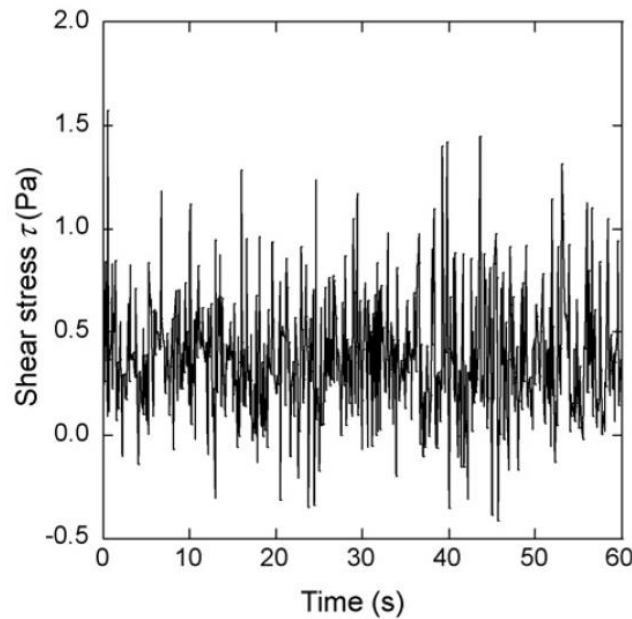


Figure III-5: Example of membrane shear stress profile measured with a shear stress meter located in the middle of the membrane, under an aeration of 4.8 L.min^{-1} [124].

III.2.3. Literature review on the hydrodynamics characterization of multiphase systems

The most relevant studies on the hydrodynamics in ALRs, MBRs or ALMBRs, were selected and gathered in Table III-3 for the analysis of their main results and trends. The importance of the hydrodynamics parameters for fouling mitigation in the case of (AL)MBRs is also highlighted through this literature review.

Table III-3 : Selected studies of the hydrodynamics in Air-Lift Reactors (ALRs) and Air-Lift Membrane Bioreactors (ALMBRs).

Material										Main results							Reference			
Reactor			Aeration			Solid load			Method(s)	At the global scale			At the local scale			Highlights				
Type	V (m ³)	<i>h_d</i> (m)	<i>D_r</i> *(m)	<i>A_r</i> / <i>A_d</i>	<i>U_{gs}</i> (m.s ⁻¹)	<i>U_{gr}</i> (m.s ⁻¹)	<i>d_p</i> (mm)	<i>ρ_s</i> (kg.m ⁻³)		<i>ε_s</i> (%)	<i>ε_{gr}</i> (%)	Flowing regime	<i>U_{ls}</i> (m.s ⁻¹)	<i>U_{lr}</i> (m.s ⁻¹)	<i>d_b</i> (mm)			<i>U_b</i> (m.s ⁻¹)	<i>φ</i> (Pa)	
ALRs																				
Rectangular ALRs	0.65	2.6	n.a.	n.a.	n.a.	0 to 0.045	-	-	-	Tracer method for the measurement of the liquid velocity, difference of level for the gas hold-up	0 to 8	B	n.a.	0 to 0.25	-	-	-	<ul style="list-style-type: none">• A mathematical model was proposed for the prediction of the <i>ε_{gr}</i> and <i>U_{lr}</i>• The model was validated with experimental data from rectangular ALRs at different scales, and good agreement was obtained	[125]	
	0.0047	0.65	n.a.	n.a.	n.a.	0 to 0.02	-	-	-		0 to 5		n.a.	0 to 0.25	-	-	-			
	4.6	5.7	n.a.	n.a.	n.a.	0 to 0.04	-	-	-		0 to 10		n.a.	0 to 0.30	-	-	-			
Rectangular ALR	0.65	2.6	0.25	1	n.a.	0.003 to 0.045	3.76	934	0 to 18	Tracer method for the measurement of the liquid velocity	-	B	n.a.	0.10 to 0.25	-	-	-	<ul style="list-style-type: none">• <i>U_{lr}</i> describes a power law of <i>U_{gr}</i> and then reaches a plateau value for <i>U_{gr}</i> ≥ 0,015 m.s⁻¹• The presence of solid particles has no effect on <i>U_{lr}</i>	[99]	
	0.65	2.6	0.25	1	n.a.	0.003 to 0.045	2.4	870	0 to 16 and 16 to 28		0.5 to 6.5 and 0.5 to 4.5		B	n.a.	-	-	-			-
MBRs																				
Confined FS-membrane cell	n.a.	n.a.	0.005	-	0.01 to 0.07	-	-	-	-	Optical characterization of bubbles + electrochemical method for the membrane shear stress measurement	-	B/S	-	-	14.2 to 16	0.26 to 0.43	-	<ul style="list-style-type: none">• The volume-equivalent diameter of bubbles and their rising velocity increase with the superficial gas velocity• Under low liquid velocity, the average shear stress on the membrane is significantly heightened with the injection of bubbles, which was linked to an improved filtration flux	[123,126]	
	n.a.	n.a.	0.005	-	0.1 to 0.4	-	-	-	-		-		0.075	0.075	-	-	2.8 to 4.3 times the average shear stress without gas			
Cylindrical HF-MBR	0.0036	1	-	-	0 to 0.16	-	-	-	-	Optical characterization of bubbles + difference of pressure method for the gas hold-up	0 to 25	B	-	-	-	-	-	<ul style="list-style-type: none">• The gas hold-up increases with the increase of the gas superficial velocity. The increase is first quick under the low gas superficial velocities (<i>U_{gs}</i> ≤ 0.03 m.s⁻¹), and then tends to be less pronounced. This refers to a sudden change in the flowing regime, from the homogeneous bubbly one to a heterogeneous one.• Bidisperse population of bubbles under high air flowrates (<i>U_{gs}</i> ≥ 0.023 m.s⁻¹). The higher is the air flowrate, the more important is the difference between the two types of bubbles of a population.• Existence of an internal liquid recirculation phenomenon	[103]	
	-	-	0.007 to 0.10	-	-	-	-	-	-		-		-	5 to 50	-	-				
Rectangular HF-MBR	0.08	2.5	-	-	0.06	-	-	-	-	High-speed camera for the characterization of bubbles + PIV for the characterization of the liquid flow	-	B	0.02	-	0.2 to 50 (From 3 to 5 for 66 % of the population)	~ 0.4	-	[127]		

* D_r is the characteristic dimension of the riser part (width for a rectangular ALR, diameter for a cylindrical ALR). **B**: bubbly flow; **S**: Slug-flow. **n.a.**: non-available data.

Table III-3: Continuation.

Material										Main results								Reference	
Reactor					Aeration		Solid load			Method(s)	At the global scale				At the local scale				Highlights
Type	V (m ³)	h _d (m)	D _r *(m)	A _r /A _d	U _{gs} (m.s ⁻¹)	U _{gr} (m.s ⁻¹)	d _p (mm)	ρ _s (kg.m ⁻³)	ε _s (%)		ε _{gr} (%)	Flowing regime	U _{ls} (m.s ⁻¹)	U _{lr} (m.s ⁻¹)	d _b (mm)	U _b (m.s ⁻¹)	φ (Pa)		
ALMBRs																			
Rectangular flat HR-ALMBR	2.4	1.43	-	0.91	-	0.011 to 0.04	-	-	-	Measurement of the liquid velocity with a propeller flow velocity meter	-	n.a.	-	0.26 to 0.45	-	-	-	• The liquid velocity in the riser U _{lr} is not uniformly distributed between the parallel HF plates • The average U _{lr} increases with U _{gr} , and good agreement was found between the experimental data and the predicted values (from Equation III-15) • High values U _{lr} induced a less pronounced fouling rate	[128]
Rectangular flat HF-ALMBR	1.9	1.6	-	0.70	-	0.026 to 0.06	-	-	-		-	n.a.	-	0.43 to 0.57	-	-	-		
Rectangular HF-ALMBR	0.19	1.29	-	1	-	0.008 to 0.032	-	-	-	Measurement of the liquid velocity with a propeller flow velocity meter	-	n.a.	-	0.24 to 0.44	-	-	-	• An empirical model was defined to determine the average rising velocity of activated sludge • A correlation was established between the increasing rate of the membrane filtration resistance and the aeration intensity, the filtration flux and the sludge concentration	[129]
Rectangular HF-ALMBR	0.04	2.1	_____	0.85	0.0016 to 0.007 (into the HF modules)	_____	-	-	-	-	Optical probe for the gas hold-up and bubbles velocity measurements	0.7 to 2.1	B	_____	-	-	0.5 to 0.55	-	[104]
					0.0016 to 0.007 (into + in between the HF - modules)							-					-	-	
Rectangular FS-ALMBR	0.20	1.7	0.35	0.5	-	0.005 to 0.03	-	-	-	Optical analysis of the gas hold-up	0.5 to 2.0	B	-	0.2 to 0.35	2 to 3	-	-	• The mathematical model expressed by the Equations III-18 to III-21 was developed to predict the average liquid velocity in the riser	[110]
Rectangular flat HF-ALMBR	1.25	1	n.a.	n.a.	0.0052	n.a.	-	-	-	CFD simulation for the determination of the gas hold-up, and the shear stress induced on the membrane + PIV for the validation of the calculated liquid velocity	0 to 1.0	-	-	- 0.05 to 0.15	-	-	0.16 to 0.80 (surface distribution)	• The shear stress is not evenly distributed on the membrane module surface, it reaches its highest value in the bubble wakes at the bottom of the module (close to the bubbles generation) • The same trend was observed for the gas hold-up distribution inside the filtration module	[130]
Rectangular FS-ALMBR	0.03	0.4	0.007	0.15	-	n.a.	-	-	-	CFD simulation for the determination of the gas hold-up, the liquid velocity and the membrane shear stress + PIV for the validation of the liquid velocity	0 to 25	n.a.	-	0 to 1	-	-	0 to 3	• The average membrane shear stress is heightened in presence of baffles (air-lift configuration) • The presence of baffles and their location were optimized to obtain maximal membrane shear stress • The effectiveness of baffles was found to be particularly prominent at lower aeration intensities	[131]
					-	0 to 0.003	-	-	-		-	n.a.	-	-	-	-	0 to 0.6 (average membrane shear stress)		
Rectangular FS-ALMBR	0.01	0.4	-	0.17	-	0 to 0.004	-	-	-	CFD simulation for the determination of the gas hold-up, the liquid velocity and the membrane shear stress + PIV for the validation of the liquid velocity	-		-			0 to 2 (average membrane shear stress)	• The baffled MBR had an average membrane surface shear 74% higher than the unbaffled one • MBR with smaller width would promote higher shear on membrane surface	[132]	
			-	0.13 to 1.25	-	n.a.	-	-	-		-	0.75 to 0.25	-						
Rectangular FS-ALMBR	0.03	0.7	n.a.	n.a.	-	0.002 to 0.026	-	-	-	CFD simulation + optical method for the bubbles characterization	1 to 1.0	n.a.	-	-	1.7 to 2.4	-	-	• The level of water above the membrane was varied in order to study its effect on the liquid flow • With the highest water level, the shear stress spreads over a large part of the membrane surface, whereas it is only restricted to certain parts under lower water level	[93]
						0.016	-	-	-		-	n.a.	-	0 to 1.1	-	-	5 to 15 (surface distribution)		

*D_r is the characteristic dimension of the riser part (width for a rectangular ALR, diameter for a cylindrical ALR). **B**: bubbly flow; **S**: Slug-flow. **n.a.**: non-available data.

In **ALRs**, it appears first when globally observing the studies reported in Table III-3, that the characterization of the hydrodynamics is mostly conducted at the global scale. As a matter of fact, the measurements and models developed are specifically based on global parameters such as the global gas hold-up and the average liquid circulation velocity (in the riser and/or the down-comer). The studies reported in Table III-3 were conducted in rectangular ALRs with different sizes (from about 0.005 to 5 m³), in non-confined configuration and under the bubbly regime for the gas-liquid flow. The superficial gas velocity in the riser U_{gr} was varying in similar ranges (up to 0.05 m.s⁻¹) for all the studies.

In all the reported studies in ALRs, the average liquid velocity in the riser and the global gas hold-up were found to increase with the increase of the superficial gas velocity. The three-phase ALRs were much less investigated and the few studies that were reported focused on predicting the minimum fluidization velocity (III.2.1.8) for the particles, but their impact on the gas and liquid phases was not fully explored. In addition, the authors didn't work in similar experimental ranges and didn't use the same parameters to characterize the liquid phase behavior. Couvert et al. (2004) [99] provided clues in that way by characterizing the gas and liquid phases in presence or not of polymer particles (with densities of 870 and 934 kg.m⁻³). They concluded that, for superficial gas velocity in the range 0 to 0.05 m.s⁻¹, when solid particles were fluidized under the circulated bed regime with a solid hold-up up to 16 %, neither the average liquid velocity in the riser U_{lr} nor the gas hold-up ε_{gr} in the riser were affected. On the other hand, for a solid hold-up greater than 16 %, the presence of particles was found to hinder the increase of ε_{gr} with the superficial gas velocity U_{gr} , which was attributed to the fact that the particles reduce the space available for the free passage of bubbles leading to their coalescence. The author underlined that the presence or not of a plateau value would depend on several parameters, especially on the gas-liquid separator. However, Freitas et al. (1998) [133] reported a different trend working with heavier calcium alginate particles (1016 and 1038 kg.m⁻³) and higher superficial gas velocity in the range of 0 to 0.5 m.s⁻¹, in a draft-tube ALR (60 L). They showed that the interstitial liquid velocity in the riser increased with the superficial gas velocity and with the solid loading up to 30 %.

In **MBRs**, the air injection (sparging) is of crucial importance because it is involved in the biofouling control as well as it is a source of oxygen for biomass. For this reason, the hydrodynamics characterization in MBRs was widely investigated. In the studies reported in Table III-3, it appears that the characterization of the hydrodynamics was investigated at both the global and local scales, and for different geometries of reactors and membranes.

In order to identify the mechanisms involved in the air-mediated biofouling control, the bubble size was one of the most investigated parameters in MBRs, and considerable scattering in the results was observed indicating the strong influence of the geometry on this parameter. As an example, Ducom et al. (2001, 2002) [123,126] investigated the gas-liquid flow in a 5 mm (confined) space along a flat-sheet membrane and the average bubble size (volume-equivalent diameter) obtained under an superficial gas

velocity U_{gs} of 0.01 to 0.07 m.s⁻¹ ranged between 14 and 16 mm, which refers to a relatively homogeneous population. However, under similar ranges of superficial gas velocity (from 0.007 to 0.1 m.s⁻¹), much different results were obtained in terms of bubble size in non-confined environments [103,127]. Pollet et al. (2009) [103] obtained, in a cylindrical hollow-fiber module, bubble sizes from 5 to 50 mm, and the presence of a bidisperse population of bubbles was particularly observed under high air flowrates ($U_{gs} \geq 0.023$ m.s⁻¹). In a rectangular hollow-fiber MBR, Liu et al. (2010) [127] also obtained a wide distribution of bubbles size going from 0.2 to 50 mm for a superficial gas velocity of 0.06 m.s⁻¹. These studies indicate that heterogeneous population of bubbles are most likely to be generated in non-confined configurations. Concerning the local membrane shear stress, Ducom et al. (2001, 2002) [123,126] quantified the contribution of the gas phase on it. The membrane shear stress induced by the gas-liquid flow was approximately 2 to 5 times greater than that of the sole liquid flow (with the same liquid flowrate), which was actually linked to an improved filtration flux.

For **ALMBRs**, the studies gathered in Table III-3 concerned more specifically rectangular reactors with either FS or HF as filtration modules. Similarly to simple ALRs, the global gas hold-up in all the studies was found to increase with the superficial gas velocity. Concerning the average liquid velocity in the riser part, it was found to increase with the superficial gas velocity in all the studies, which is also the same trend as in simple ALRs. However, Liu et al. (2000) [128] showed that in the case of an ALMBR packed with 11 parallel HF plates in the riser, the liquid velocity was not evenly distributed between the plates and that the velocity in the middle of the module (around 0.4 m.s⁻¹) was 18 to 23 % higher than the velocity on the sides.

Another key-parameter for ALMBRs is the membrane shear stress. It was quantified in a great number of studies performed on ALMBRs and in addition to describing considerable fluctuations in time (Figure III-5), CFD simulations proved that it was not uniformly distributed on the membrane surface, with either HF or FS membranes [93,130–132]. The order of magnitude of membrane shear stress obtained in the selected studies varied from 10⁻¹ to 10 Pa, depending on the cases, but the comparison is made difficult as the superficial gas velocities in the riser were not mentioned in all the studies. However, these studies brought valuable information concerning the parameters influencing the membrane shear stress. In addition to the gas and liquid properties and velocities, the geometry was found to play an important role. As an example, Yan et al. (2015, 2016) [131,132] performed the CFD simulation of a rectangular ALMBR with one single FS membrane to investigate the effect of the presence of baffles and their position on the membrane shear stress. They demonstrated that the average membrane shear stress in presence of baffles (air-lift configuration) was 74 % higher than that obtained without baffles [132]. This result is in accordance with another study conducted by Prieske et al. (2010) [95] determining the maximum shear stress for different widths of inter-membrane space (using flat-sheets) and showing that for the same bubble size, the maximum membrane shear stress induced in a 3 mm space was higher than the ones induced in 5 and 7 mm spaces. Besides, the membrane shear stress was also found to

depend on the level of water above the membrane as demonstrated by Khalili-Garakani et al. (2009) [93]. Indeed, they showed that lowering the level of water above the membrane from 12 to 4 cm leads to a decrease of the membrane shear stress, and thus, a heightened probability of fouling. This observation was correlated with the fact that bubbles tend to accumulate in the down-comer when the liquid level is reduced, creating a stronger liquid circulation in the air-lift.

In sum, this literature review allowed being aware of the existing tools for the hydrodynamics characterization and of their application to ALRs, MBRs and ALMBRs. First, it appears that the ALRs are usually characterized at the global scale, unlike MBRs and ALMBRs, where the complex combination of global and local phenomena is involved in the fouling mitigation, as reviewed by Böhm et al. (2012) [94]. Even though some authors attached importance in correlating these hydrodynamics parameters to an improvement of the filtration flux, the exact mechanisms by which the fouling is mitigated still need to be fully explored, and a deeper investigation of the relationships between the hydrodynamics and the phenomena taking place in the vicinity of the membrane (such as the microbial growth, the biofilm formation, the pore clogging, the cake compressibility) should be the subject to future research. Finally, this literature review also revealed that the addition of solid particles as a fouling mitigation technique was not assessed from a hydrodynamics perspective. Yet, several fouling control methods that consisted in the addition of solid particles were recently developed (among which QQ and GAC particles [134]), but to our best knowledge, the potential impact of these particles on the hydrodynamics was not analyzed.

III.3. Material and methods

III.3.1. *ALMBR/QQ-ALMBR operation*

The lab-scale ALMBR used in this study had a total working volume of 18 L and was composed of an anoxic tank (5 L) and an aerobic membrane tank (13 L). Figure III-6 presents the experimental setup with its main elements as well as the observation windows that were chosen for visualization. With the purpose of studying the hydrodynamics and the effect of the addition of QQ media on it, the **aerobic tank was the only part of the reactor considered in this study**. A plastic plate with a length of 315 mm, a width of 225 mm and a thickness of 7 mm was introduced in the aerobic tank to mimic the presence of the flat-sheet membrane. On both sides of the central membrane mimic, two baffles were set at a distance D_r to create an air-lift configuration (Figure III-6). Three different shapes of QQ media were used. The ALMBR/QQ-ALMBR were operated under the batch mode for the liquid phase (no feed and no permeate suction) and under the continuous mode for the gas phase (air injection). The liquid height in the aerobic (air-lift) tank of the reactor was set to 0.585 m. More details about the ALMBR operation as well as the QQ media properties are available in Chapter II.

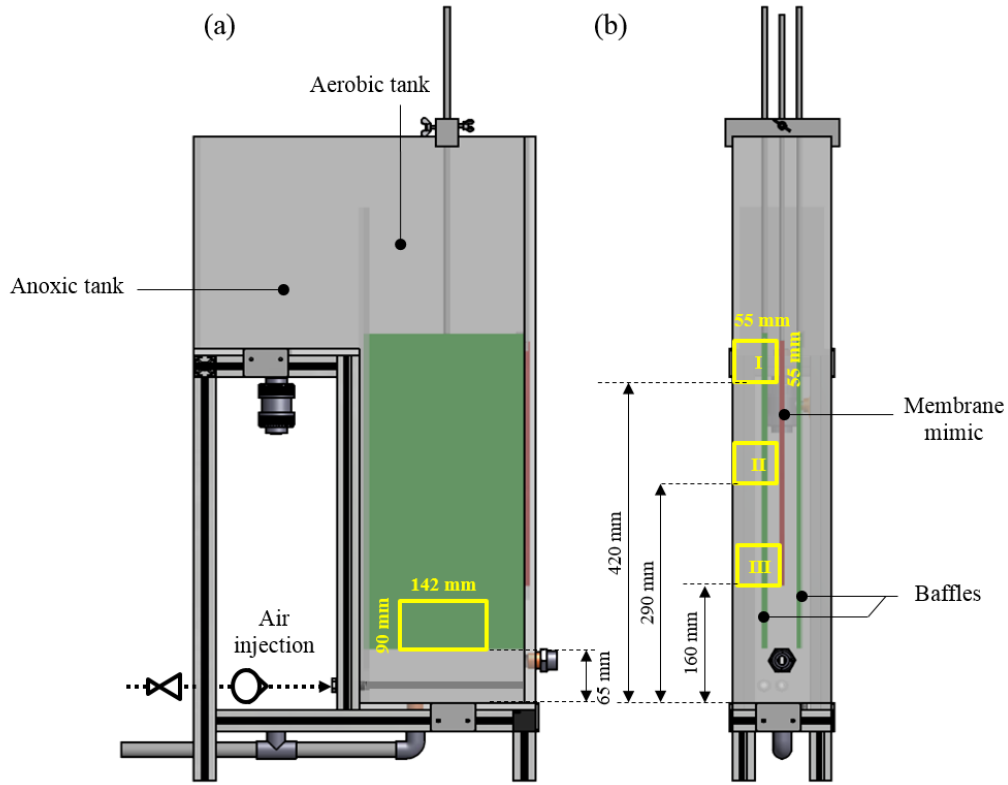


Figure III-6 : Experimental setup and observation windows for (a) the assessment of the fluidization of QQ media (b) the PIV and camera measurements.

III.3.2. Gas hold-up measurement

The gas hold-up in the riser part, which corresponds to the fraction of air trapped in the space between the membrane and the baffle, was experimentally determined by measuring the height of the free surface at the top of the reactor. For this to be achieved, several pictures of the free surface were captured and then, the height of several points of the water-air interface was measured to determine one average height for each image. The gas hold-up was obtained from the difference of the water height without bubbling and the average height with bubbling multiplied by the reactor cross-section (corresponding to the average volume of air trapped in the reactor) , and divided by the volume of liquid in the riser compartment to obtain the gas hold-up in the riser.

III.3.3. Assessment of the fluidization of QQ media

The fluidization of the QQ media was visually determined under different operating conditions. For this to be achieved, QQ media were introduced at different volume fractions in the aerobic tank, and images were recorded in the observation window presented in Figure III-6(a). The QQ media were counted in the images, and given the total number of QQ media introduced, a fluidization rate was defined as the ratio of the QQ media in suspension N_{FM} to the total number of QQ media introduced N_{TM} , according

to Equation III-41. The fluidization rate was determined under decreasing air flowrates. More details about the method are available in Chapter II.

$$\text{Fluidization rate (\%)} = \frac{N_{FM}}{N_{TM}} \times 100 \quad \text{III-41}$$

III.3.4. Camera for the characterization of gas and solid phases

The camera technique was used in order to characterize both of the gas phase and the solid phase. The experimental setup consisted in a Complementary Metal-Oxide-Semiconductor (CMOS) camera (acA1920 - 155 μm , 1920 x 1200 pixels², 164 fps, Basler) with a 105 mm lens (Micro-NIKKOR, 105 mm, Nikon). A backlight panel (Phlox-LedW-BL, 400 x 200 mm², 24 V, 2A, Phlox) was set up against the back of the aerobic tank in order to illuminate the reactor (Figure III-7). The acquisition of pictures was set to 200 Hz and lasted 15 s. The focus was made on the median plane in the middle of the reactor, orthogonally to the camera. The images were acquired using the appropriate software (pylon Viewer 64-bit) and then processed using a Matlab (MathWorks, USA) program to determine the size and velocity of the bubbles, as well as the position and the velocity of the QQ media in the riser. For the QQ media position, the minimal horizontal distance was more specifically determined as a criterion for discussion, as showed in Figure III-8. More details about the image processing are given in Chapter II.

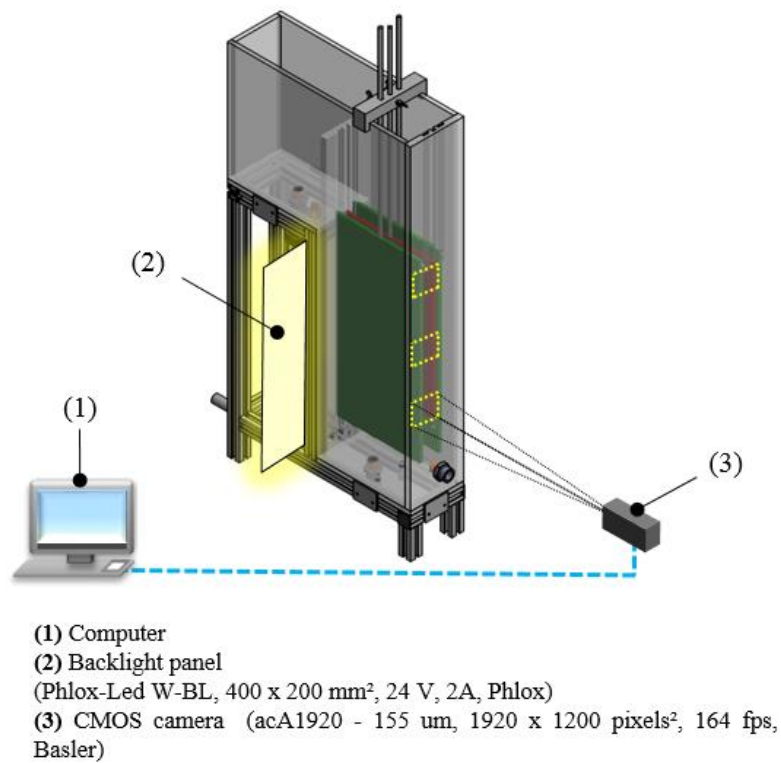


Figure III-7 : Camera setup for the characterization of the hydrodynamics of the reactor.

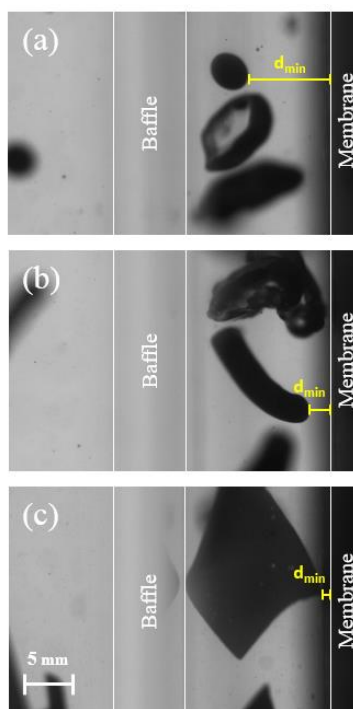


Figure III-8 : Definition of the minimal horizontal distance to the membrane to characterize the QQ media position in the riser. The images were recorded in window II (Figure III-6(b)) with a riser width of 15 mm, under an SADm of $1.00 \text{ Nm}^3 \cdot \text{h}^{-1} \cdot \text{m}^2$, in presence 0.45 % v/v of (a) QQ beads (b) QQ hollow cylinders and (c) QQ sheets.

III.3.5. *PIV for the characterization of the liquid phase*

In this study, the PIV measurements were performed with silver-coated hollow glass spheres (Dantec Dynamics, Denmark) as a tracer, with a density of 1.4 g/cm^3 , a size distribution ranging from 10 to 30 μm and an average diameter of 15 μm . The middle vertical plane of the reactor was illuminated with a laser sheet (Nd:YAG unit laser source, DualPower 200-15, class 4, Dantec Dynamics, Denmark) and a CMOS camera (FlowSense EO 4M, 2048 x 2048 pixels² (1 pixel = 27 μm), 20.4 fps, Dantec Dynamics, Denmark) was placed orthogonally to the laser sheet and a 105 mm lens (Micro-NIKKOR, 105 mm, Nikon) was mounted on it (Figure III-9). The software DynamicStudio (2015a, Dantec Dynamics, Denmark) was used for the control and synchronization of the camera and the laser, for the settings configuration (acquisition frequency, time Δt between two consecutive frames of a pair of images), as well as, for the image processing. The time Δt depended on the aeration conditions, and ranged between 0.5 and 5.0 ms in the investigated range of air flowrates. The acquisition was set to 10 pairs of images per second for 25 s. In order to focus on the liquid phase, the possible effect of bubbles was attenuated by averaging the 250 images to get one time-averaged velocity field as presented in Figure III-10. From the time-averaged velocity field, a Matlab (MathWorks, USA) program was used to deduce an average liquid velocity in the riser for the global characterization of the liquid phase, as well the horizontal profiles of vertical velocities in each areas for the local characterization of the liquid phase (Figure

III-10). The membrane shear stress was also deduced from the velocity vectors in the vicinity of the membrane. More details about the PIV setup and settings, and the data processing are given in Chapter II.

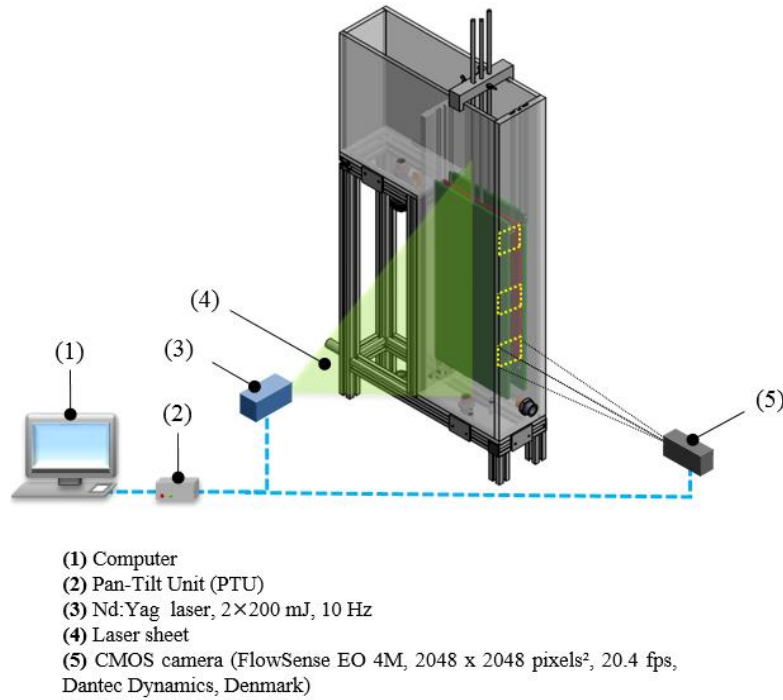


Figure III-9 : PIV setup for the characterization of the hydrodynamics of the reactor.

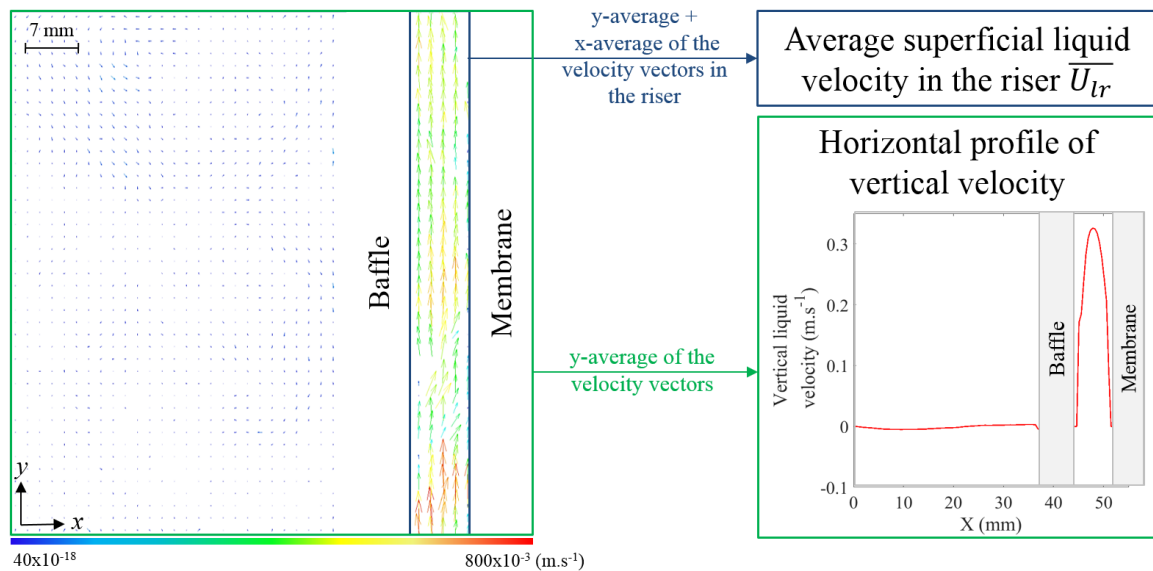


Figure III-10 : Example of determination of the liquid superficial velocity in the riser and the velocity profile, from a time-averaged velocity field recorded in the ALMBR at the top of the membrane (window I) with $D_r = 7$ mm and under an air flowrate of $1.0 \text{ Nm}^3 \cdot \text{h}^{-1} \cdot \text{m}^2$.

III.3.6. *Experimental procedure*

In order to characterize all the phases of the ALMBR/QQ-ALMBR at both the global and local scales, different operating parameters were varied. All the operating conditions are gathered in Table III-4. First, the experiments were performed under different air flowrates ranging from 0.30 to 1.00 $\text{Nm}^3 \cdot \text{h}^{-1} \cdot \text{m}^{-2}$ (Table III-4) that have been selected on the basis of the recommendations for industrial flat-sheet MBRs. The effect of the air flowrate on the three phases was assessed. Also, the effect of the geometry of the riser was evaluated by investigating two riser widths $D_r = 7$ and 15 mm, as the literature review revealed the importance of the parameter. Additionally, in order to characterize the behavior of the solid phase, the different shapes of QQ media were introduced in different amounts corresponding to different total number of particles and different volume fractions, as presented in Table III-4.

Table III-4: Operating parameters for the ALMBR/QQ-ALMBR.

Operating	
Air-lift	
Distance between the membrane mimic and the baffle D_r (mm)	[7 ; 15]
Total riser width $2D_r$ (mm)	[14 ; 30]
Total down-comer width $2D_d$ (mm)	[80 ; 64]
Total riser cross sectional area A_r (m^2)	[0.00294 ; 0.0063]
Total down-comer cross sectional area A_d (m^2)	[0.0168 ; 0.01344]
A_r/A_d ratio (-)	[0.175 ; 0.469]
Liquid height h_D (m)	0.585
Aeration	
SADm ($\text{Nm}^3 \cdot \text{h}^{-1} \cdot \text{m}^{-2}$)	0.30 to 1.00
Superficial gas velocity in the riser ($\text{m} \cdot \text{s}^{-1}$)	
- For $D_r = 7$ mm	0.0028 to 0.0094
- For $D_r = 15$ mm	0.0013 to 0.0044
QQ media	
Volume fraction (% v/v)	[0.06 ; 0.10 ; 0.45]
Total number (N_{TM}) of:	
Beads	[347 ; 578 ; 2600]
Hollow cylinders	[39 ; 65 ; 298]
Sheets	[78 ; 130 ; 585]

III.4. Results and discussion

In the following the results will be presented and categorized into two main parts: the global characterization and the local characterization of the reactor. In each of these two parts, the two-phase ALMBR (with no qq) will be presented first, and then the case of the three-phase qq-ALMBR will be discussed, in order to assess the effect of the addition of qq media on the different aspects of the ALMBR.

III.4.1. Global characterization of the hydrodynamics of the ALMBR/qq-ALMBR

III.4.1.1. Global characterization of the hydrodynamics of the ALMBR

III.4.1.1.1. Gas hold-up in the riser of the ALMBR

The gas hold-up in the riser part was measured for the two riser configurations under several air flowrates. The results are presented in Figure III-11. The results range between 5.5 ± 0.7 % and 9.5 ± 0.9 % when D_r is 7 mm, and between 0.8 ± 0.4 % and 3.0 ± 0.5 % when D_r is 15 mm. The order of magnitude of these results is consistent with the study of Yan et al. (2015) [131] conducted in a similar rectangular FS-ALMBR, with $D_r = 7$ mm, $h_d = 0.4$ m and $A_r/A_d = 0.15$. In these conditions, the simulated gas hold-up distribution in the riser ranged approximately between 0 and 25 %.

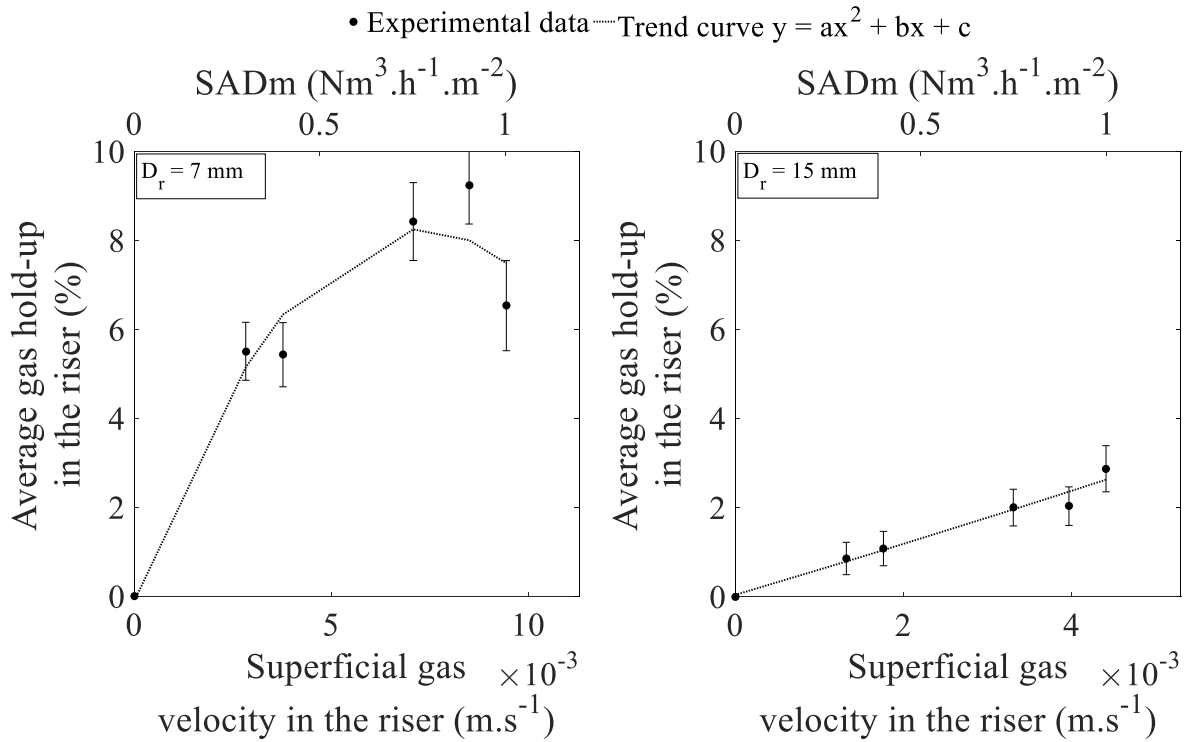


Figure III-11: Average gas hold-up in the riser of the ALMBR for two riser widths.

The gas hold-up values obtained for the lowest riser width $D_r = 7$ mm (corresponding to the lowest A_r/A_d ratio) are 2 to 6 times greater than the values obtained at $D_r = 15$ mm. This result is consistent with the expectations and can be attributed to the fact that when the riser width increases, the corresponding liquid volume in the riser increases consequently, whereas the total volume of air entrapped in remains the same (when keeping the same liquid height).

For the lowest riser width $D_r = 7$ mm, the experimental data were correctly fitted ($R^2 > 0.93$) with a 2nd order polynomial trend curve as it is possible to be observed in Figure III-11, while for $D_r = 15$ mm a linear correlation is suitable. The correlation parameters are presented in Table III-5. The polynomial model is consistent with the correlation reported by Freitas et al. (1998) [133] for an internal-loop draft-tube ALR with a A_r/A_d ratio of 0.19 and under superficial gas velocities comprised between 0 and 0.5 m.s⁻¹.

Table III-5: Correlation ($y = ax^2 + bx + c$) parameters for the average gas hold-up in the ALMBR presented in Figure III-11.

$D_r = 7$ mm				$D_r = 15$ mm			
a	b	c	R ²	a	b	c	R ²
-158987	2306	0	0.93	0	610	0	0.95

Concerning the effect of the air flowrate, it can be noticed that when the riser width is set to 15 mm, the average gas hold-up increases with the superficial gas velocity, which is the typical trend observed and reported in the literature on air-lift reactors (Table III-3). However, for the lowest riser width ($D_r = 7$ mm), the average gas hold-up seems to have reached a maximum value around 10 % for a critical superficial gas velocity comprised between 0.0085 and 0.0094 m.s⁻¹. This phenomenon can be explained by the fact that above this critical superficial gas velocity, the amount of gas in the riser becomes so important that the interactions between the bubbles are enhanced, leading to coalescence and thus, to the formation of bigger bubbles with higher rising velocities. Therefore, the residence time of bubbles in the riser is reduced decreasing the gas hold-up.

Based on visual observations, the gas-liquid flow in the riser was found to describe a bubbly flow regime, and the order of magnitude obtained for the gas hold-up is consistent with this observation, according to the ranges presented in Table III-1. The characterization of the bubbles *per se* will be discussed in the local characterization part.

Consequently, in this study, due to the low gas hold up in the selected experimental conditions, the average liquid velocity could be considered to be about equal to the superficial liquid velocity.

III.4.1.1.2. Average liquid velocity in the riser

The average vertical liquid velocities for the two riser widths and at the three windows are presented in Table III-6. The standard deviation of data, shows that the greater the air flowrate is, the wider is the dispersion. This means that non-uniform velocity fields tend to be induced at higher air flowrates, with up to ± 50 % of dispersion from the mean value for the vertical velocity.

Table III-6: Average liquid velocities in the riser under different operating conditions.

D_r (mm)	7					15				
$SADm$ (Nm ³ .h ⁻¹ .m ⁻²)	0.03	0.40	0.75	0.90	1.00	0.30	0.40	0.75	0.90	1.00
U_{gr} (m.s ⁻¹)	0.0028	0.0038	0.0071	0.0085	0.0094	0.0013	0.0018	0.0033	0.0040	0.0044
U_{lr} (m.s ⁻¹) in:										
Window I	0.009 \pm 0.006	0.09 \pm 0.04	0.20 \pm 0.07	0.25 \pm 0.07	0.26 \pm 0.07	0.010 \pm 0.005	0.011 \pm 0.007	0.09 \pm 0.05	0.15 \pm 0.08	0.2 \pm 0.1
Window II	0.05 \pm 0.03	0.07 \pm 0.04	0.19 \pm 0.09	0.2 \pm 0.1	0.2 \pm 0.1	0.009 \pm 0.008	0.02 \pm 0.01	0.15 \pm 0.07	0.2 \pm 0.1	0.2 \pm 0.1
Window III	0.06 \pm 0.03	0.04 \pm 0.03	0.17 \pm 0.08	0.18 \pm 0.09	0.18 \pm 0.09	0.02 \pm 0.01	0.02 \pm 0.02	0.14 \pm 0.08	0.17 \pm 0.09	0.2 \pm 0.1
The riser (\overline{U}_{lr})	0.04 \pm 0.04	0.07 \pm 0.07	0.19 \pm 0.14	0.2 \pm 0.2	0.2 \pm 0.2	0.01 \pm 0.01	0.02 \pm 0.02	0.1 \pm 0.2	0.2 \pm 0.2	0.2 \pm 0.2

When analyzing the vertical flow at different positions (Table III-6), it appears that when D_r was set to 7 mm, the average vertical velocity increases with the height under the same air flowrate. On the other hand, when D_r was set to 15 mm, the liquid flow reaches a maximal vertical velocity at the middle window (window II), before slowing down again at the top. The average vertical liquid velocities recorded in the middle and the top windows are on average 15 % and 30 % greater than the ones recorded at the bottom window, respectively, when D_r equals 7 mm. When D_r is 15 mm, the average vertical liquid velocities are on average 13 % greater in the middle and 5 % lower in the top window, compared to the velocities recorded at the bottom. The analysis of the average vertical liquid velocities at different heights of the reactor reveals that the liquid phase describes a non-uniform flow in the riser part, since considerable space variations were found. These space variations can be attributed to the non-uniform distribution of the gas phase in the riser, as it was reported by Yan et al. (2015) [131] via the simulation of the gas hold-up in the riser.

In the present case, the gas-hold up was measured globally, which makes its space-distribution impossible to determine, however, it can be assumed that the non-uniform liquid velocities can also be correlated to the existence of a heterogeneous population of bubbles. It is worth mentioning that these space variations depict different trends depending on the riser width, since the middle area is the one with higher velocities when D_r is 15 mm, whereas, the liquid velocity keeps on increasing along the membrane height when D_r is 7 mm.

Even though space variations were identified, a global (space-averaged) liquid velocity in the riser $\overline{U_{lr}}$ was deduced from the values at each observation area, in order to study its relationship to the other parameters of the air-lift (superficial gas velocity and gas hold-up), according the approach and correlations presented in the background section (III.2.1). The values of the average liquid velocities in the riser are gathered in Table III-6, for each air flowrates and for the two riser widths, and are also represented as a function of the superficial gas velocity in Figure III-12.

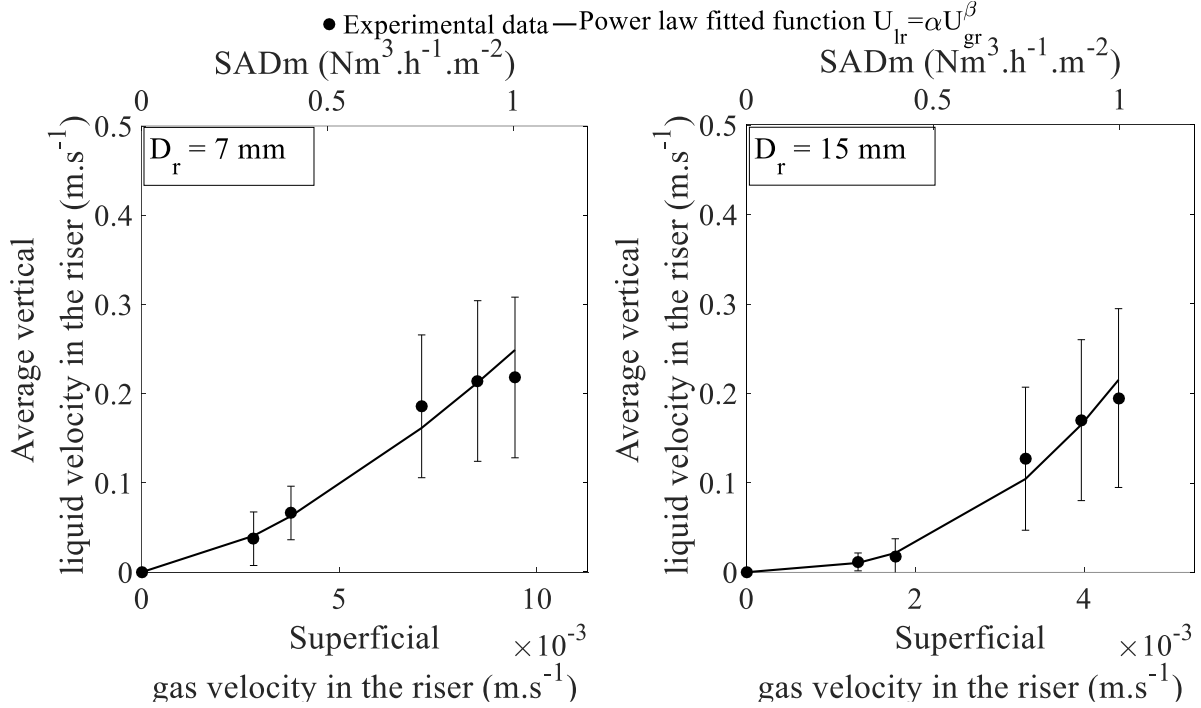


Figure III-12: Average liquid velocity in the riser of the ALMBR for two riser widths.

It is possible to notice that the average liquid velocity increases with the superficial gas velocity (and thus with air flowrate), ranging between 0.04 and 0.20 m.s⁻¹ when D_r was set to 7 mm, and between 0.01 and 0.20 m.s⁻¹ when D_r was set to 15 mm. The results are in accordance with the studies about ALRs reported in Table III-3, in terms of order of magnitude, as well as, in terms of the increase described by the liquid velocity with the air flowrate. In the present case, the average liquid velocity was, more specifically, found to be correctly fitted ($R^2 > 0.98$) by a power law function according to Equation III-42. This kind of behavior was also reported by Couvert et al. (2004) [99] in a rectangular ALR operated under superficial gas velocities ranging from 0 to 0.015 m.s⁻¹, as well as by Freitas et al. (1998) [133] in an internal draft-tube ALR under a wider range of superficial gas velocities (0 to 0.5 m.s⁻¹). The parameters of the correlation corresponding to Equation III-42 are presented in Table III-7.

$$\overline{U_{lr}} = \alpha U_{gr}^{\beta} \quad \text{III-42}$$

Table III-7: Correlation (Equation III-42) parameters for the average liquid velocity in the ALMBR presented in Figure III-12.

$D_r = 7 \text{ mm}$			$D_r = 15 \text{ mm}$		
α	β	R^2	α	β	R^2
273.45	1.5018	0.98	180974	2.5152	0.98

Various models were proposed in the literature to link the liquid velocity in the riser to the gas hold-up for different geometries of ALRs, as reviewed in the background part (III.2.1.4). The model of Prieske et al. (2008) [110] adapted from ALRs to ALMBRs was selected as the most relevant one to compare the experimental velocities obtained in this study, to the predicted ones calculated with Equations III-18 to III-21. The parameters of the model were calculated (Table III-8), as well as the resulting velocities.

Table III-8: Parameters and results of the model of Prieske et al. (2008) [110] calculated for the two riser widths of the present study.

D_r (m)							0.007							0.015						
Experimental data																				
U_{gr} (m.s ⁻¹)	0	0.0028	0.0038	0.0071	0.0085	0.0094	0	0.0013	0.0018	0.0033	0.0040	0.0044								
ε_{gr} (%)	0	5.5	5.4	8.4	9.2	6.5	0	0.9	1.1	2.0	2.0	2.9								
U_{lr} (m.s ⁻¹)	0	0.04	0.07	0.19	0.21	0.22	0	0.01	0.02	0.13	0.17	0.19								
Parameters of the model																				
A_r (m ²)	0.00294						0.0063													
A_d (m ²)	0.0168						0.0134													
A_r/A_d (-)	0.175						0.468													
A_b (m ²)	0.0273						0.0273													
K_B (Equation III-17)	7.77						6.50													
h_d (m)	0.585						0.585													
l_{MM} (m)	0.315						0.315													
A_{MM} (m ²)	0.0015						0.0032													
d_{MM} (m)	0.007						0.015													
D_h (m)	0.014						0.030													
T (m)	0.21						0.21													
ν_l (m ² .s ⁻¹)	1.0037×10^{-6}						1.0037×10^{-6}													
Results of the model																				
Re_{MM} (-)	0	12865	12763	16400	17292	14182	0	11257	12734	17748	17906	21612								
K_{MM} (-)	Inf	0.0297	0.0298	0.0279	0.0276	0.0290	Inf	0.0307	0.0298	0.0274	0.0273	0.0261								
U_{lr} (m.s ⁻¹)	0	0.44	0.43	0.54	0.56	0.47	0	0.19	0.21	0.29	0.29	0.35								

The comparison of the experimental data to the calculated data is presented in Figure III-13. The model was applied, using the experimental values of the average gas hold-up in the riser, and considering the gas hold-up in the down-comer part as nil ($\varepsilon_{gd} = 0$), based on the experimental observations.

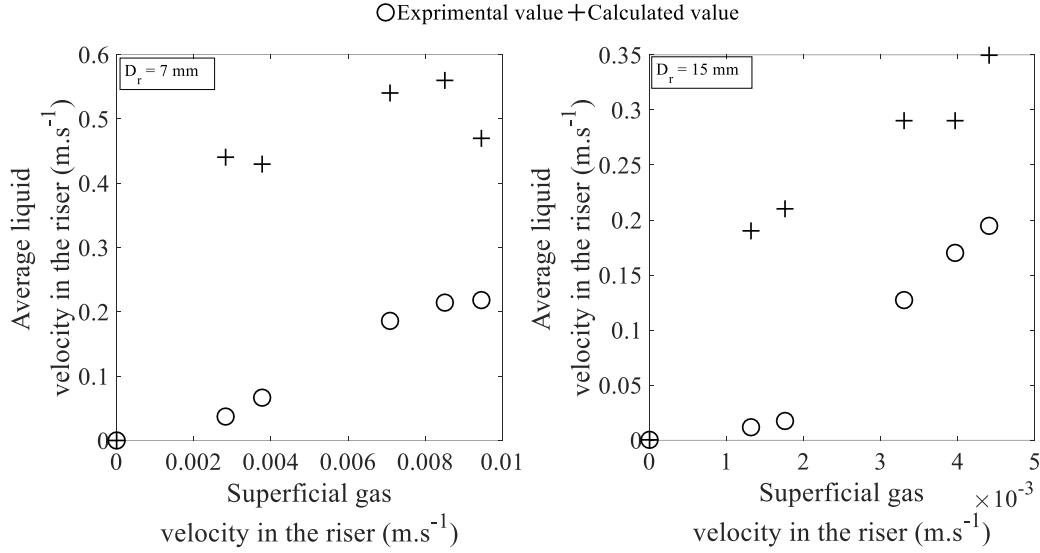


Figure III-13: Comparison of the experimental average liquid velocities in the riser and the calculated ones by the model of Prieske et al. (2008) [110], for the two riser widths.

From Figure III-13, it appears that the values obtained by the model of Prieske are higher than the experimental values, which means that the model overestimates the average liquid velocity, in both configurations of riser. Although, it is important to keep in mind that the experimental liquid velocity in the riser is an average value, and that space-variations in the liquid flow can exist. These results are still in good agreement with the literature in terms of trends.

III.4.1.1.3. Liquid flow regime in the riser

Based on the measured gas and liquid velocities in the riser, the Reynolds numbers were calculated according to the Equations III-22 and III-25, and gathered in Table III-9. Based on the usual threshold value of 2000 [103], it can be concluded that the two lowest air flowrates of the investigated range (0.30 and 0.40 Nm³.h⁻¹.m⁻²) lead to a laminar flow whatever is the distance D_r , whereas the higher air flowrates (from 0.75 to 1.00 Nm³.h⁻¹.m⁻²) induce a global behavior closer to a turbulent flow in the riser. Besides, it is also possible to notice that there is no much difference in the Reynolds numbers whether they are based on the liquid velocity in the riser (Re_l) or the mix velocity in the riser (Re_m). This result is understandable given that the superficial gas velocities are 9 to 44 times lower than the liquid ones, which is in accordance with the ratios u_{tr}/u_{gr} found in the literature for ALRs (Table III-3).

Table III-9: Reynolds numbers based on the superficial velocities in the riser, for the two riser widths and the different air flowrates.

D_r (mm)	7					15				
$SADm$ (Nm ³ .h ⁻¹ .m ⁻²)	0.30	0.40	0.75	0.90	1.00	0.30	0.40	0.75	0.90	1.00
U_{gr} (m.s ⁻¹)	0.0028	0.0038	0.0071	0.0085	0.0094	0.0013	0.0018	0.0033	0.0040	0.0044
U_{lr} (m.s ⁻¹)	0.0375	0.0664	0.1859	0.2143	0.2182	0.0115	0.0174	0.1270	0.1701	0.1948
U_{lr}/U_{gr} (-)	13	17	26	25	23	9	10	38	43	44
Re_l (Equation III-22)	500	900	2600	3000	3000	300	500	3800	5100	5800
Re_m (Equation III-25)	600	900	2700	3100	3200	400	600	3900	5200	6000

III.4.1.2. Global characterization of the hydrodynamics of the QQ-ALMBR

III.4.1.2.1. Fluidization of the QQ media

The fluidization rates were determined for the three shapes of QQ media introduced at volume fractions of 0.06, 0.10 and 0.45 % v/v.

Firstly, no fluidization was observed when the riser width was set to 7 mm under the selected range of air flowrates (from 0 to 1.35 Nm³.h⁻¹.m⁻²), for the three shapes of QQ media. When D_r was 7 mm, the QQ media were observed to settle in the bottom of the reactor, where the liquid circulation induced some slight motion of the bed of particles, describing the typical packed bed regime (Table III-2), but was not strong enough to lift the particles and drag them to the riser. In contrast, when D_r was 15 mm, QQ media fluidization could be achieved under SADm higher than 0.50 Nm³.h⁻¹.m⁻².

This observation can be explained by determining the average liquid velocity in the down-comer U_{ld} . Based on a mass balance between the riser and the down-comer, and assuming the total conservation of the liquid flowrate, the average liquid velocity in the down-comer can be deduced from Equation III-43. The values are presented in Table III-10.

$$U_{ld}A_d = U_{lr}A_r \quad \text{III-43}$$

Table III-10 : Average liquid velocities in the riser and the down-comer for the two riser widths and under different air flowrates.

D_r (mm)	7					15				
$SADm$ (Nm ³ .h ⁻¹ .m ⁻²)	0.30	0.40	0.75	0.90	1.00	0.30	0.40	0.75	0.90	1.00
U_{gr} (m.s ⁻¹)	0.0028	0.0038	0.0071	0.0085	0.0094	0.0013	0.0018	0.0033	0.0040	0.0044
U_{lr} (m.s ⁻¹)	0.0375	0.0664	0.1859	0.2143	0.2182	0.0115	0.0174	0.1270	0.1701	0.1948
U_{ld} (m.s ⁻¹)	0.0066	0.0116	0.0325	0.0375	0.0382	0.0054	0.0082	0.0594	0.0796	0.0912

It appears that the average liquid velocity in the down-comer is lower for $D_r = 7$ mm than for $D_r = 15$ mm, for SADm higher than $0.75 \text{ Nm}^3 \cdot \text{h}^{-1} \cdot \text{m}^{-2}$. These results confirm that the liquid flow in the down-comer in the investigated range of air flowrates is not strong enough when $D_r = 7$ mm to drag the QQ media into the riser.

The liquid velocities presented in Table III-10 were obtained in absence of QQ media but were used to illustrate the observed results in terms of fluidization. However, with the liquid velocities obtained in presence of QQ media with a riser width of 15 mm (presented in the following), the same conclusions can be drawn.

The fluidization rate obtained for $D_r = 15$ mm are presented in Figure III-14. The error bars in Figure III-14 are due to the fact that the fluidization rate was determined from a relatively limited number of pictures (around 10) that presented heterogeneous behaviors (the reliability of the fluidization rate determination is explained in Chapter II).

It is worth mentioning that the fluidization rate was based on the assumption that the QQ media are uniformly distributed in the reactor, which is not exact. In their study of a three-phase draft-tube ALR with calcium alginate beads (2.15 mm , $1048 \text{ kg} \cdot \text{m}^{-3}$), added at a volume fraction of 7 % and more, Klein et al. (2003) [135] observed that the solid distribution increased from the top to the bottom of the riser. In our case, the measurement was performed at the bottom which means that the fluidization rates are potentially overestimated.

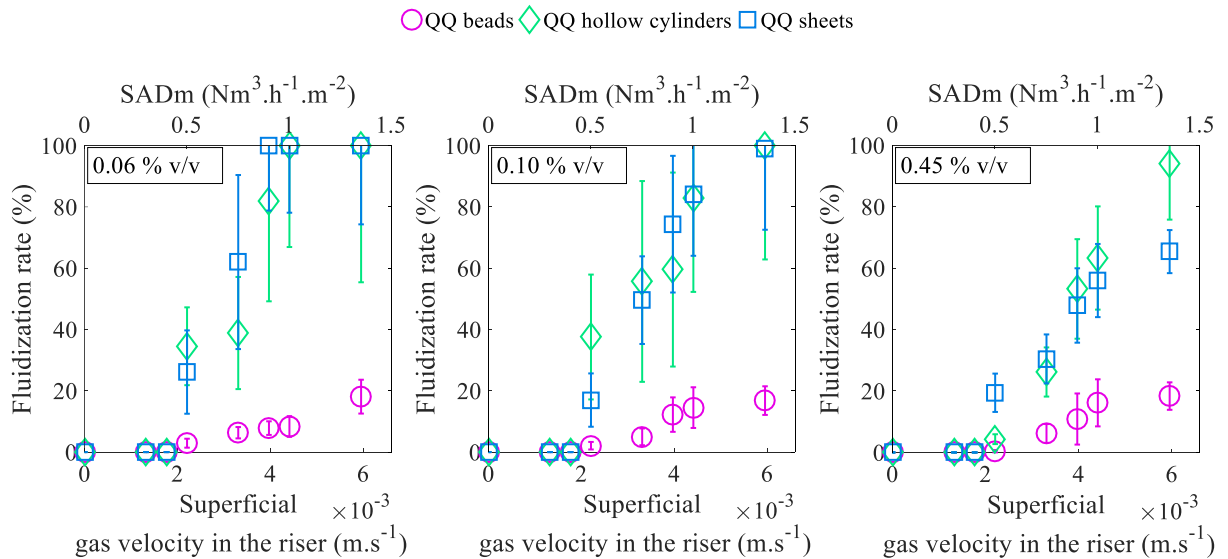


Figure III-14: Fluidization rate of the QQ media introduced at different volume fractions and measured under different air flowrates with a riser width (D_r) of 15 mm.

For all the shapes and volume fractions, the fluidization rate increases with the aeration flowrate, which is consistent with the fluidization regimes in three-phase ALRs, presented in the background part (III.2.1.7). The volume fraction of QQ media introduced has no significant effect on this trend; however, it appears that the greater volume fraction (0.45 % v/v) induces lower fluidization rates in comparison to the other volume fractions, for a same air flowrate. As an example, under a superficial gas velocity of 0.033 m.s^{-1} , 62 % of the sheets are fluidized when they are introduced at 0.06 % v/v, whereas only 50 and 30 % of them are fluidized when they are introduced at 0.10 and 0.45 % v/v, respectively, under the same air flowrate. This observation can be attributed to a density effect, which means that the particle-particle interactions are no longer negligible, and that some QQ media may be prevented from rising because of the presence of other QQ media in the surroundings.

Concerning the different shapes, the beads appear in Figure III-14 to reach lower fluidization rates than the hollow cylinders and sheets. This result can be linked to the morphological properties of the QQ media, and more specifically to their projected areas. The projected areas A_p were calculated and the corresponding terminal falling velocities U_{tp} were determined using the approach of Heywood for non-spherical particles (detailed calculations in Appendix A-III-1) and gathered in Table III-11. It appears that the terminal falling velocity decreases with the projected area, thus this supports the fact that the higher is the projected area, the easier it is to maintain the particle in suspension, which actuarially explains the better fluidization behavior obtained for the hollow cylinders and sheets.

Table III-11: Projected areas A_p and calculated terminal falling velocities U_{tp} for the three shapes of QQ media (*the hollow cylinders and sheets were considered to fall horizontally*).

QQ media	Beads	Hollow cylinders	Sheets
$A_p \text{ (} 10^{-6} \text{ m}^2 \text{)}$	9.6	94.5	200
$U_{tp} \text{ (} 10^{-2} \text{ m.s}^{-1} \text{)}$	5.8	5.0	2.0

For the three shapes of QQ media and the three tested volume fractions, it appears in Figure III-14 that it exists a minimum fluidization gas velocity below which all the QQ media would settle down in the reactor. The ranges of superficial gas velocities including the experimental minimum fluidization gas velocity (experimental U_{gmf}) were gathered in Table III-12 for comparison with the minimum fluidization velocity (calculated U_{gmf}) calculated using the model of Petrovic (Equation III-29).

Table III-12: Experimental and calculated minimum fluidization gas velocities for the three shapes of QQ media at different volume fractions (*the model of Petrovic is based on a total fluidization of particles, whereas the experimental values of the present work correspond to a partial fluidization*).

QQ media Volume fraction (% v/v)	Beads			Hollow cylinders			Sheets		
	0.06	0.10	0.45	0.06	0.10	0.45	0.06	0.10	0.45
Experimental U_{gmf} (10^{-2} m.s^{-1})	2.2 to 3.3			1.8 to 2.2					
Calculated U_{gmf} (10^{-5} m.s^{-1}) (Equation III-29)	7.4	14	86	6.9	13	81	5.0	9.4	58

From Table III-12, it appears that the calculated minimum fluidization velocity are 30 to 460 times lower than the ones measured experimentally, depending on the cases. This significant difference can be explained by the difference in the reactor geometries, since the model of Petrovic was defined and validated in a cylindrical draft-tube ALR in which the air was injected at the very bottom (thus below the particles bed) of the reactor through a centered perforated plate. On the other hand, in the present study the air diffuser was located above the bed of particles, which explains why a higher superficial gas velocity is needed to achieve effective fluidization.

In conclusion, the study of the fluidization behavior of the QQ media in the ALMBR revealed that in the configuration of the present study, no fluidization occurred when the riser width was set to 7 mm. Knowing that the inter-membrane distance in industrial flat-sheet membrane modules is 7 mm, this result is key-information, and the improvement of the fluidization in these conditions should be addressed in future research. In particular, some complementary experiments were conducted in the present work and showed that the height of the baffles could play an important role in the fluidization (more details available in Appendix A-III-2). When the riser width was set to 15 mm, it was found that the higher is the air flowrate the greater is the fluidization rate of QQ media. The QQ hollow cylinders and sheets were found to have the most favorable shapes for fluidization, compared to QQ beads, for a given volume fraction. Therefore, the mechanical washing effect of the QQ hollow cylinders and sheets can be expected to be more important than beads, since better fluidization leads to a greater probability of collisions between the QQ media and the membrane surface. The volume fraction was found to play a considerable role, and more specifically, the fluidization rate was greater at low volume fractions. However, with the view to reducing biofouling in MBRs via the mechanical effect of the QQ media in suspension, the number of fluidized QQ media may be a more important parameter to consider than their fluidization rate. The inherent behavior of the QQ media was necessary to investigate in order to further understand their effect on the hydrodynamics of the ALMBR.

III.4.1.2.2. Gas hold-up in the riser of the QQ-ALMBR

In order to assess the effect of the addition of QQ media, the gas hold-up in the riser part was measured as previously described in presence of 0.45 % v/v of beads, with a riser width of 15 mm. The results are presented in Figure III-15.

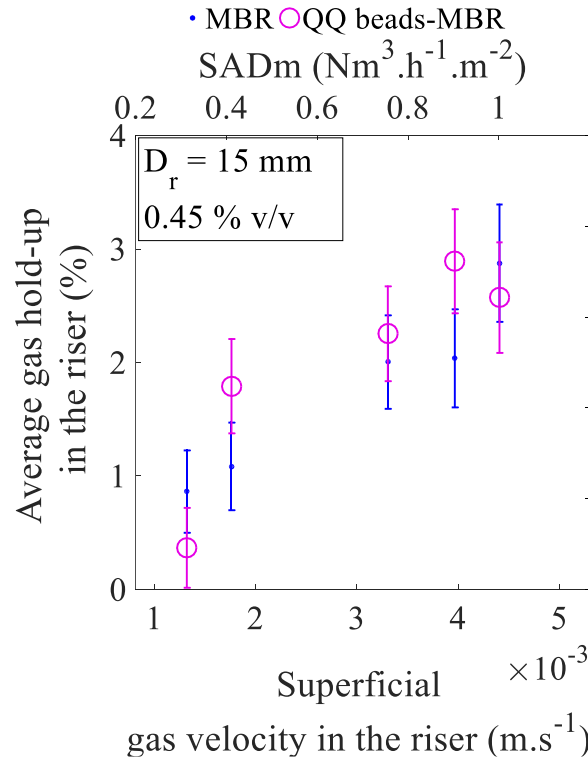


Figure III-15: Average gas hold-up in the riser of the QQ-ALMBR for a riser width of 15 mm and in presence of QQ beads at 0.45 % v/v.

The increase of the air flowrate from 0.30 to 0.90 Nm³.h⁻¹.m⁻² leads to an increase of the gas hold-up in presence or not of QQ beads. The average gas hold-up values obtained in presence of QQ beads are on average 38 % different (higher or lower) from the ones obtained in absence of QQ media, which can be considered insignificant, given the relative experimental error of 35 % (on average). Thus, the addition of QQ media with a volume fraction of 0.45 % v/v can be considered as having no effect, neither on the gas hold-up in the riser, nor on its increase with the air flowrate.

This finding is in accordance with the literature. As an example, Couvert et al. (2004) [99] found that the gas hold-up in the riser of a rectangular ALR, was not affected when polymer particles (with a density of 870 kg.m⁻³) were added in a volume fraction ≤ 12 %. Besides, Lu et al. (1995) [136] showed that the addition of 2 mm-alginate beads similarly to the present study (with a density of 1030 kg.m⁻³), in a volume fraction of 5 % or more could lead to a decrease of approximately 7 % of the gas hold-up in the riser of an internal-loop ALR. The same finding was reported by Freitas et al. (1998) [133] in an

internal draft-tube ALR with 2 mm-calcium alginate beads (with densities of 1016 and 1038 kg.m⁻³) added at volume fractions higher than 5 %.

Therefore, no significant effect on the global gas hold-up in the riser is observed, under the investigated range of air flowrates and volume fractions.

III.4.1.2.3. Average liquid velocity in the riser of the QQ-ALMBR

The average liquid velocity in the riser was measured under the different air flowrates when QQ media were added to the ALMBR at different volume fractions (0.06, 0.10 and 0.45 % v/v). The results are presented in Figure III-16. The average liquid velocities in the riser in presence of QQ media, are up to 30 % lower than the ones obtained in the ALMBR, which can be considered as insignificant, considering the standard deviation of about 50 %. However, it appears that when QQ media are added to the reactor, the average liquid velocity in the riser globally increases with the superficial gas velocity, but this increase seems to be slowed down compared to what was found in the ALMBR in presence of QQ sheets at volume fractions of 0.10 and 0.45 % v/v. From these results, it can be assumed that the liquid flow in the riser can possibly be slowed down in presence of QQ sheets introduced at volume fractions of 0.10 % v/v or more. In their investigation of a three-phase internal-loop ALR loaded with alginate particles, Lu et al. (1995) also reported a decrease of the average liquid velocity in the riser when spherical particles were loaded at a volume fraction of 5 % or more. However, in their case, this decrease was linked to a decrease of the gas hold-up in the riser, which indirectly reduced the liquid circulation.

When comparing the results obtained for the three different shapes, it seems that the discrepancies are mostly identifiable when the QQ media are introduced at a volume fraction of 0.10 or 0.45 % v/v. Indeed, it appears that the lowest average liquid velocities are induced in presence of QQ sheets. This observation may be linked to the fact that the QQ sheets have the greatest projected area, as it was previously demonstrated, representing thus bigger “obstacles” for the liquid flow in the riser, and inducing an increased charge loss.

In conclusion, a noticeable slowdown of the liquid flow in the riser part is obtained when QQ sheets are added at a volume fraction of 0.10 % v/v or more. Concerning the QQ beads and hollow cylinders, it is hard to conclude considering that the average liquid velocities in their presence are very close to the ones obtained in the ALMBR.

- MBR (blue dot) QQ Beads-MBR (pink circle) QQ Hollow cylinders-MBR (green diamond) QQ Sheets-MBR (blue square)

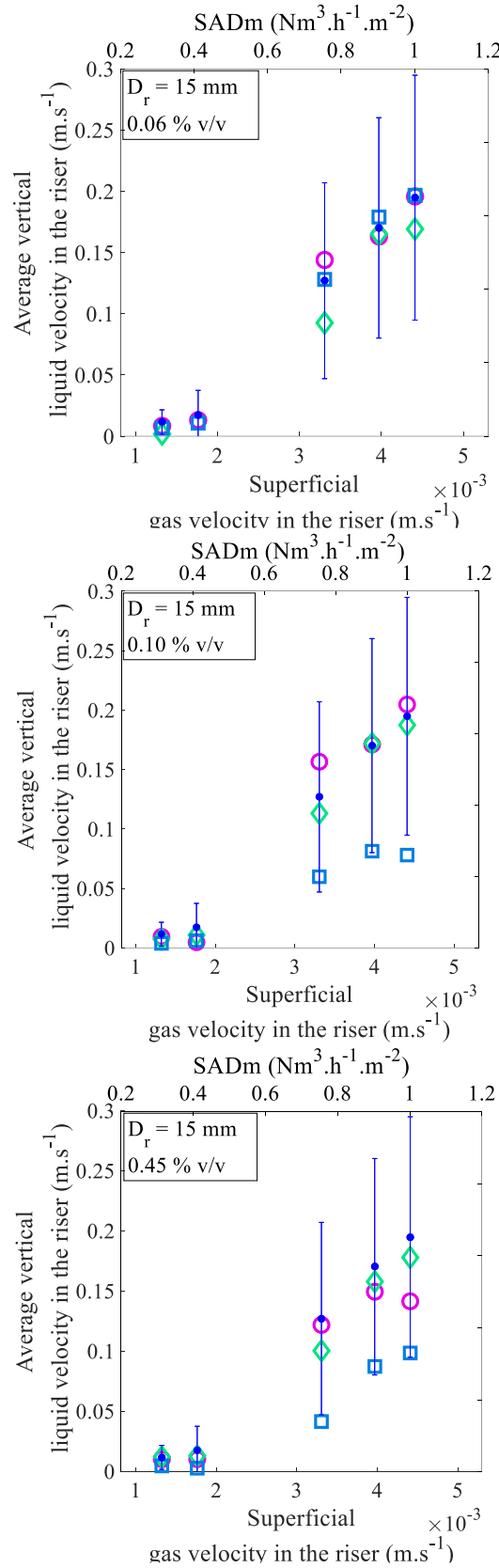


Figure III-16 : Average vertical liquid velocity in the riser of the QQ-ALMBRs for a riser width of 15 mm and for different volume fractions of QQ media (*the error bars were not represented for the data from the QQ-ALMBRs not to clutter the plot, but were about 50 % on average*).

III.4.1.3. Concluding remarks on the global characterization of the ALMBR/ QQ-ALMBR

The ALMBR and the QQ-ALMBR were characterized at the global scale in the same way for comparison, and the inherent behavior of the QQ media at the global scale was studied, coming to the following main conclusions:

- The measurement of the global gas hold-up and the average liquid velocity in the riser were reliable tools to characterize the two phases of the ALMBR at the global scale, as the obtained results were in good accordance with the literature. Similarly to what was reported in the literature, the gas hold-up as well as the average liquid velocity in the riser were found to increase with the superficial gas velocity, and to range respectively from 0 to 10 % and from 0 to 0.20 m.s⁻¹, under the investigated conditions. The determination of the Reynolds number allowed seeing that the turbulent flow tends to be favored under air flowrates higher than 0.75 Nm³.h⁻¹.m⁻².
- The fluidization of the QQ media was studied under different conditions, and no fluidization of QQ media occurred when the riser width was 7 mm. This result together with the comparison of the experimental critical superficial gas velocity to the theoretical value, are of great importance since they highlight that the geometry of the considered system is not optimal for fluidization. For a riser width of 15 mm, the QQ media were found to fluidize for the high flowrates of the investigated range (> 0.5 Nm³.h⁻¹.m⁻²), and the QQ sheets and hollow cylinders exhibited better fluidization properties than the QQ beads, owing to their bigger projected area.
- The characterization of the QQ-ALMBR revealed that the addition of QQ media did not dramatically impair the gas and liquid phases at the global scale, under the investigated conditions. The gas hold-up in presence of QQ media was not considerably affected, and the most noticeable effect was obtained in presence of QQ sheets at a volume fraction of 0.45 % v/v with an overall slowdown on the liquid flow in the riser.

III.4.2. Local characterization of the hydrodynamics of the ALMBR/QQ-ALMBR

III.4.2.1. Local characterization of the ALMBR

III.4.2.1.1. Bubble size in the ALMBR

The bubble size in terms of circle-equivalent diameter as previously explained (Equation III-33) was measured for both riser configurations and under air flowrates ranging between 0.30 and 1.00 $\text{Nm}^3\cdot\text{h}^{-1}\cdot\text{m}^{-2}$. The results are presented in Figure III-17. The bubbles in the investigated conditions roughly ranged between 4 and 10 mm, which is in accordance, in terms of order of magnitude, with what was reported by Khalili-Garakani et al. (2009) [93] in a similar rectangular ALR equipped with a flat-sheet membrane with a 7 mm-space with the membrane and the baffles, and a liquid height of 0.5 to 0.58 m (Table III-3).

It can be noticed from Figure III-17 that the average bubble size describes random variations with the increase of the air flowrate, and the variations (up to 40 % from the lowest to the highest air flowrate) are lower than the standard deviations (± 60 % on average) to the mean values. Hence, the effect of the air flowrate on the average bubble size is not significant in the investigated conditions. This result is in accordance with the literature. As an example, Prieske et al. (2008) showed that the average bubble size in an ALMBR equipped with flat-sheet membranes in the riser (Table III-3), ranged between 2 and 3 mm, for a wide range of superficial gas velocities (up to $0.03 \text{ m}\cdot\text{s}^{-1}$) [110]. In the same way, Khalili-Garakani et al. (2009) proved that the increase of the superficial gas velocity from 0.0026 to $0.026 \text{ m}\cdot\text{s}^{-1}$, had a more considerable effect on the number of bubbles rather than on their size (from 1.6 to 2.6 mm) [93].

When observing the results obtained at the three different windows for the two riser widths, again the variations are random along the height for a same air flowrate. In our configuration, the liquid height is relatively low (0.585 m) and the variations of pressure insignificant, so the impact of the expansion of bubbles is negligible.

On the other hand, the comparison of the results obtained for the two different riser widths (7 and 15 mm), reveals that the geometry of the ALMBR has a significant influence, since it is possible to notice that the greatest riser width (also corresponding to the greatest ratio of the riser surface to the down-comer surface (A_r/A_d)) gives rise to bigger bubbles (Figure III-17). Besides, when comparing the error bars obtained in the two configurations, it seems that when the riser is 15 mm-wide, greater deviations to the mean value are obtained. These results indicate that the geometrical characteristics of the ALMBR have a strong influence on the bubbles, not only on their average size but also on their distribution, which is actually visible on the example of images presented in Figure III-18.

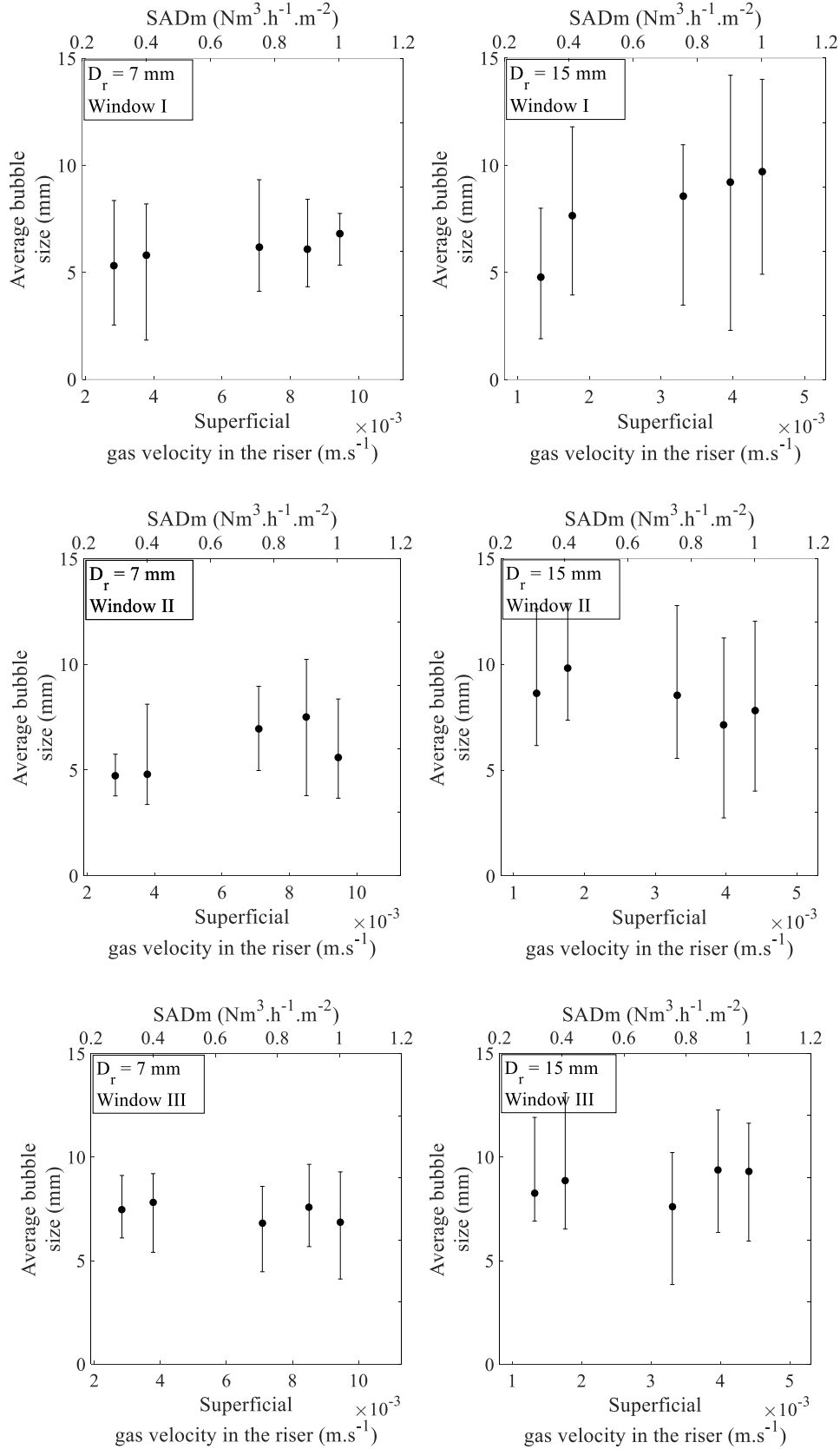


Figure III-17 : Average bubble size in terms of circle equivalent-diameter obtained in the ALMBR for the two riser widths and under different air flowrates.

Lastly, based on the range of bubble sizes that was obtained in the present work (from 4 to 10 mm), the Eötvös and Morton numbers could be calculated according to Equations III-34 and III-30, and were found to be from 2 to 13 and around 2.5×10^{-11} , respectively. Based on these two numbers, the theoretical shapes of the bubbles could be deduced from the diagram of Clift (Figure III-2) and were found to be in the area of the ellipsoidal/wobbling bubbles regime, which is not totally in accordance with the visual observations, since spherical and ellipsoidal caps could also be observed (Figure III-18).

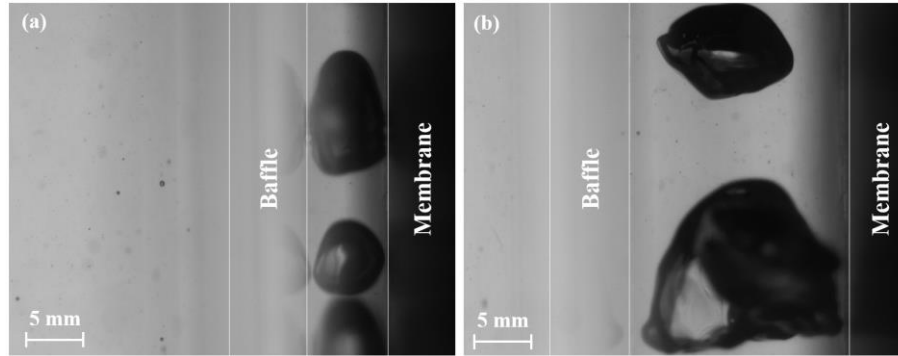

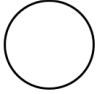


Figure III-18: Example of images recorded at window I under an air flowrate of $1.0 \text{ Nm}^3 \cdot \text{h}^{-1} \cdot \text{m}^{-2}$ and with a riser width of (a) 7 mm and (b) 15 mm.

The circle-equivalent diameter that was determined does not take into account their real shapes and their volume, which can generate considerable error, as it is possible to see in the example presented in Table III-13. This example actually reveals that bubbles having the same projected areas, can have different volumes, and thus different velocities. Hence, it might be interesting to perform complementary observations from the front of the reactor to have more accurate information about the bubbles shape and volume.

Table III-13: Theoretical example of a spherical bubble and a spherical cap having the same projected area but different volumes.

Type of bubble	Spherical cap	Spherical
		
Diameter	d_1	d_2
Projected surface area	$A_p = \frac{1}{2} \frac{\pi d_1^2}{4}$	$A_p = \frac{\pi d_2^2}{4}$
Mathematical relationship between the diameters	$d_1^3 = 2\sqrt{2}d_2^3$	
Volume	$V_1 = \frac{1}{2} \frac{\pi d_1^3}{6}$	$V_2 = \frac{\pi d_2^3}{6}$
Mathematical relationship between the volumes	$V_1 = \sqrt{2}V_2$	

III.4.2.1.2. Bubble velocity in the ALMBR

The average bubble velocities were determined for the same bubbles that were previously used for the bubble size determination, and the values from the three windows were averaged to deduce one mean bubble velocity for each flowrate and riser width. The results are presented in Figure III-19.

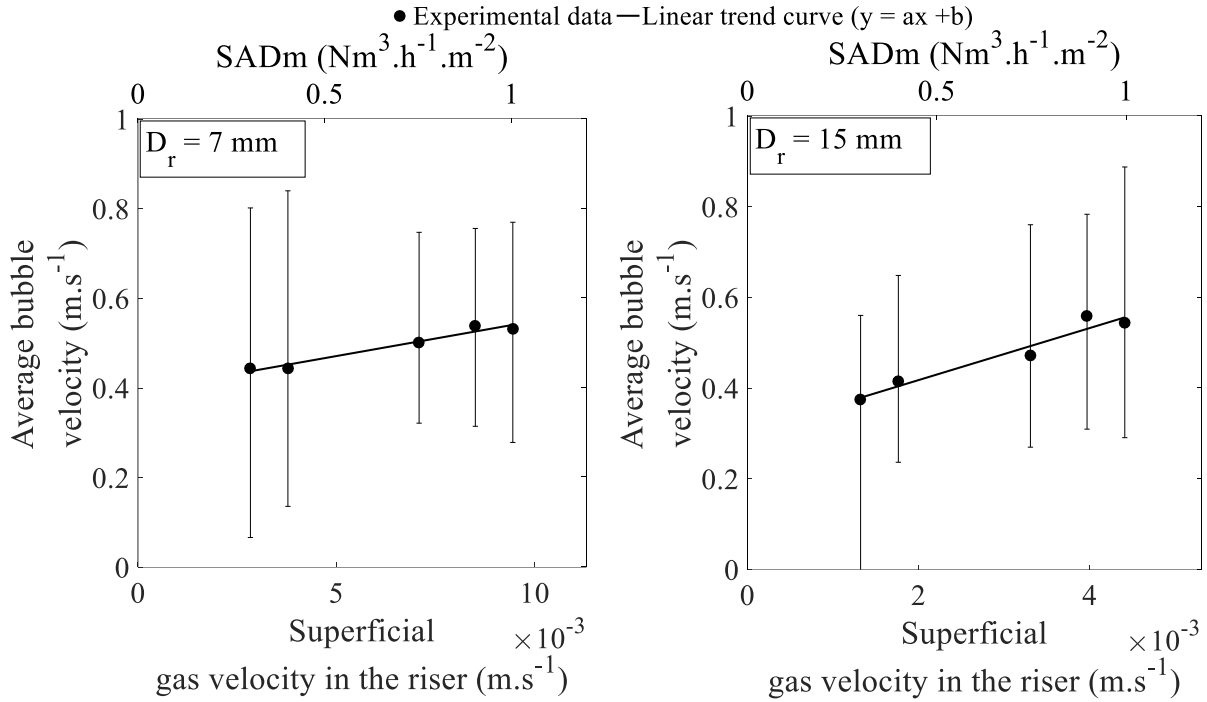


Figure III-19: Average bubble velocity in the ALMBR for the two riser widths and under different air flowrates.

In the investigated range of flowrates, the average bubble velocities ranged approximately from 0.44 ± 0.37 to 0.54 ± 0.22 m.s⁻¹ when the distance between the membrane and the baffle was 7 mm; and from 0.37 ± 0.37 to 0.56 ± 0.25 m.s⁻¹ when the baffle was 15 mm away from the membrane. This order of magnitude is in accordance with a study conducted by Ducom et al. (2001) [126] reporting a range of velocities going from 0.26 to 0.43 m.s⁻¹ for bubbles rising in a 5 mm space between a FS membrane surface and the wall (Table III-3).

From Figure III-19, it appears that the average bubble velocity increases with the superficial gas velocity, for both riser configurations. This observation is in accordance with the work of Ojha and Al Dahhan [137] where the mean bubble velocity was found to increase from 0.81 to 1.22 m.s⁻¹ when the superficial gas velocity increased from 0.003 to 0.028 m.s⁻¹ in a split-column ALR. In the present case, the increase can be described, as a first approximation, by a linear trend with the correlation parameters indicated in Table III-14. The linear correlation ($y = ax + b$) correctly fits to the experimental data ($R^2 > 0.95$) but is only valid in the investigated range of air flowrates.

Table III-14 : Correlation parameters for the liner trend curve ($y = ax + b$) presented in Figure III-19.

$D_r = 7 \text{ mm}$			$D_r = 15 \text{ mm}$		
a	b	R²	a	b	R²
15.655	0.3932	0.96	57.401	0.3032	0.95

When comparing the results obtained for the two riser widths, it appears that the increase of the average bubble velocity with the air flowrate is more pronounced when the riser is set to 15 mm, than when it is set to 7 mm. However, no much difference was obtained in terms of order of magnitude for the bubble velocities in the two configurations (Figure III-19). Although, it was previously demonstrated that the riser width had significant influence on the bubble size. This indicates that, in the investigated range of SADm, the riser geometry plays an important role in the bubble size but, a less important role in the bubble velocity.

The bubble slip velocities U_{bs} in the riser (representing the relative bubble velocity with respect to the liquid flow) could be deduced from these experimental data, via the Equation III-44, where \overline{U}_b is the absolute bubble velocity and \overline{U}_{lr} the average liquid velocity in the riser (presented in III.4.1.1.2).

$$\overline{U}_{bs} = \overline{U}_b - \overline{U}_{lr} \quad \text{III-44}$$

The results are gathered in Table III-15 and compared with the theoretical terminal velocities U_{bt} calculated with the model of Clift and taking the average equivalent diameters previously obtained (Equation III-38).

Table III-15: Average bubble size, slip velocities and calculated terminal velocities for the two riser widths and under different air flowrates.

D_r (mm)	7					15				
SADm (Nm³.h⁻¹.m⁻²)	0.30	0.40	0.75	0.90	1.00	0.30	0.40	0.75	0.90	1.00
U_{gr} (m.s ⁻¹)	0.0028	0.0038	0.0071	0.0085	0.0094	0.0013	0.0018	0.0033	0.0040	0.0044
\overline{U}_{lr} (m.s ⁻¹)	0.04	0.07	0.19	0.21	0.22	0.01	0.02	0.13	0.17	0.20
\overline{U}_b (m.s ⁻¹)	0.44	0.44	0.52	0.54	0.53	0.37	0.41	0.41	0.56	0.55
\overline{U}_{bs} (m.s ⁻¹) (Equation III-44)	0.40	0.37	0.31	0.34	0.33	0.36	0.39	0.37	0.36	0.34
d_e (mm) (Equation III-38)	5.84	6.14	6.65	7.06	6.42	7.22	8.78	8.24	8.57	8.94
U_{bt} (m.s ⁻¹) (Equation III-38)	0.24	0.24	0.24	0.24	0.24	0.24	0.25	0.25	0.25	0.25

First, it is possible to notice that the experimental bubble slip velocities are on average 1.5 times greater than the corresponding calculated theoretical bubble terminal velocities. The non-equality of the experimental bubble slip velocities and the terminal bubble velocities were expected, as the hypotheses of the theory of Clift are not fulfilled in the studied case (free rising of a single bubble in stationary water, with no wall effect).

It can be concluded from these findings that the increase of the absolute bubble velocity with the air flowrate that was previously observed (Figure III-19) is indirectly due to the increase of the liquid velocity, rather than to a direct increase of the size (and thus the slip velocity) of the bubble itself. Also, the more pronounced increase of the average bubble velocity that was obtained for a riser width of 15 mm, which also corresponds to the configuration with the more pronounced increase of the average liquid velocity in the riser with the air flowrate. Therefore, these results reveal the importance of the vertical liquid flow in the riser and its inter-dependency to the gas phase. Unlike the bubble size, the bubble velocity is strongly influenced by the air flowrate, but not significantly by the riser geometry (Table III-15).

III.4.2.1.3. Liquid flow profile in the ALMBR

The liquid flow profiles were deduced as previously explained in the three observation windows, for both riser configurations and under the different investigated air flowrates. The results are presented in Figure III-20.

It is possible to notice that all the resulting profiles describe similar aspects, with a pronounced maximum in the riser part and a relatively less pronounced minimum in the down-comer part, which is actually consistent with the liquid circulation due to the air-lift configuration. The effect of the operating parameters on the liquid flow profile will be discussed in the subsequent, taking into account two main criteria: the global aspect of the profile (width and shape) and the maximal liquid velocity reached in the riser.

From Figure III-20, it appears that the increase of the air flowrate seems to have an influence on the profile shape. When D_r is 15 mm, the profiles appear to be flat-shaped at the low air flowrates, and has a curvier shape at the high air flowrates of the investigated range. When D_r is 7 mm, the global shape of the profiles seems to remain unchanged when the air flowrate increases. These results indicate that the high air flowrates promote space-fluctuations in the local liquid velocity. On the other hand, the maximal vertical velocities reached in the riser seems to be substantially dependent on the air flowrate. As an example, a 3-fold increase in the air flowrate (from 0.30 to 0.90 Nm³.h⁻¹.m⁻²) leads to an average 10-fold increase of the maximal velocity when D_r is 7 mm, and to an average 14-fold increase when D_r is 15 mm. Therefore, the general trend is that the maximal liquid velocities in the riser increases with the air flowrate.

— SADm = 0.3 ($\text{Nm}^3 \cdot \text{h}^{-1} \cdot \text{m}^{-2}$) — SADm = 0.4 ($\text{Nm}^3 \cdot \text{h}^{-1} \cdot \text{m}^{-2}$) — SADm = 0.75 ($\text{Nm}^3 \cdot \text{h}^{-1} \cdot \text{m}^{-2}$) — SADm = 0.9 ($\text{Nm}^3 \cdot \text{h}^{-1} \cdot \text{m}^{-2}$) — SADm = 1.0 ($\text{Nm}^3 \cdot \text{h}^{-1} \cdot \text{m}^{-2}$)

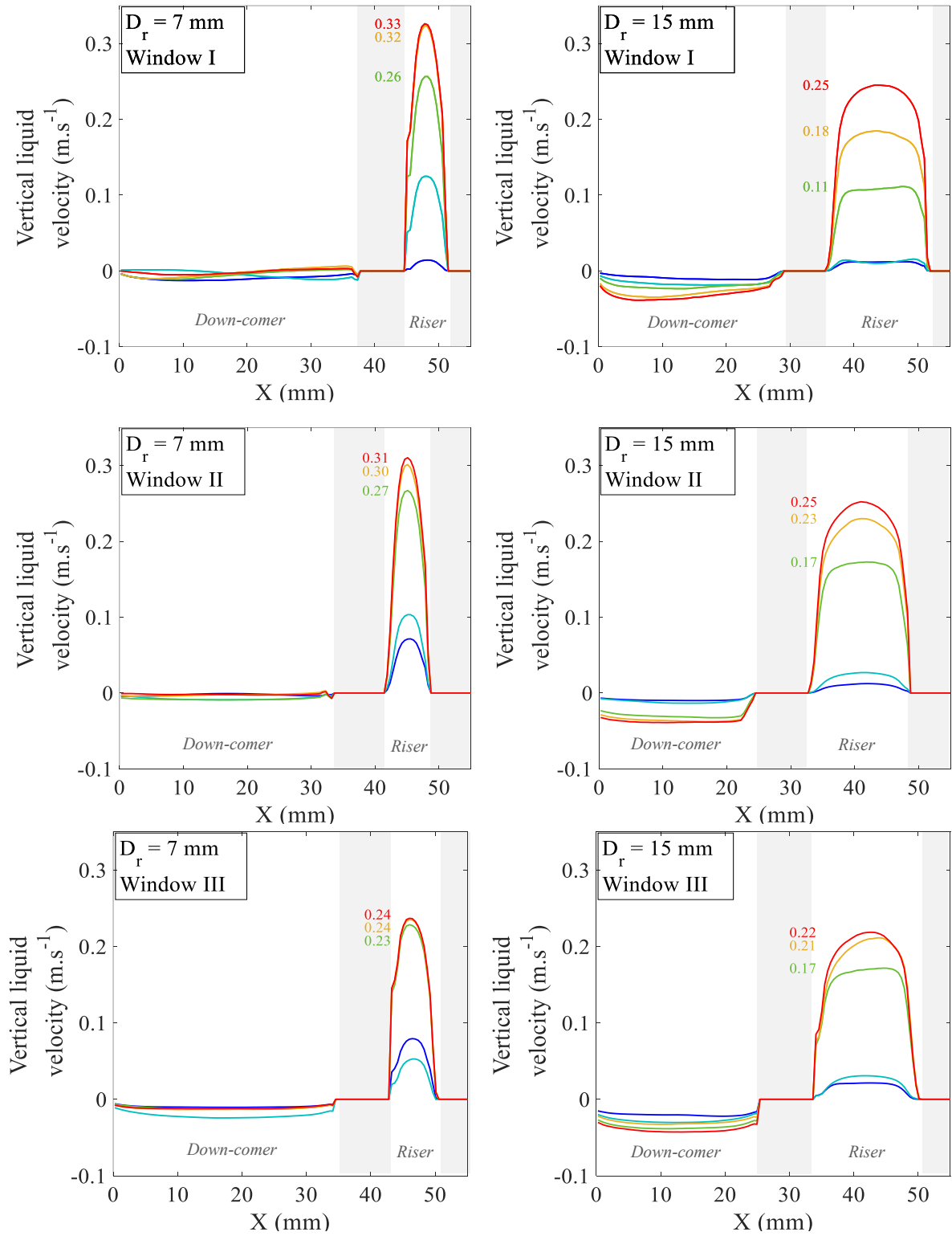


Figure III-20 : Experimental horizontal profiles of vertical velocity in the two configurations of ALMBR, under different air flowrates.

The observation of the two columns of plots in Figure III-20, reveals that the riser width has a substantial effect on the global aspect of the profiles. It appears that when the riser width is 7 mm, more sharp-shaped profiles are obtained, compared to the flat-shaped profiles that are obtained when D_r is 15 mm. Besides, the riser geometry also appears to play a major role in the maximum liquid velocity, for the same air flowrate. As an example, when the air flowrate is set to $0.75 \text{ Nm}^3 \cdot \text{h}^{-1} \cdot \text{m}^{-2}$, the maximal velocity reached at the top of the reactor (window I) is around $0.26 \text{ m} \cdot \text{s}^{-1}$ when D_r is 7 mm, whereas, it only reaches $0.11 \text{ m} \cdot \text{s}^{-1}$ when D_r is 15 mm. Thus, it can be concluded that the more confined riser configuration ($D_r = 7 \text{ mm}$) generates greater local velocities for the same air flowrates. In addition to that, it is also possible to identify in Figure III-20 an effect of the riser geometry on the way the maximal liquid velocity increases with the air flowrate. From these results, it can be concluded that the riser geometry also governs the relationship between the air flowrate and its resulting liquid flow profile, as the wider configuration ($D_r = 15 \text{ mm}$) appears to make the effect of the air flowrate more pronounced.

Finally, when observing the liquid flow profiles at the different observation windows, it seems that no significant difference in the global profile aspect is obtained at the different heights. Also, the maximal liquid velocities evolve randomly with the height for the two riser configurations, depending in the cases, which makes hard to clearly conclude about the evolution of the liquid profile along the height. However, it appears that the effect of the air flowrate is more and more visible with the height. As an example, when D_r is 7 mm and the air flowrate is increased from 0.75 to $1.00 \text{ Nm}^3 \cdot \text{h}^{-1} \cdot \text{m}^{-2}$, the maximal velocity is increased by 27 % at the top of the reactor (window I) (from 0.26 to $0.33 \text{ m} \cdot \text{s}^{-1}$), whereas it is only increased by 6.3 % at the bottom of the reactor (window III). These results show that the interactions between the gas and liquid phases are not uniformly distributed along the height of the reactor.

When comparing the maximal liquid velocities reached in the riser with the bubble velocity (presented in Table III-15), it appears that the gap is less pronounced than that between the bubble velocity and the average liquid velocity in the riser, which is consistent since it actually indicates that the bubbles are driven by the local velocity rather than the global one.

In sum, it can be concluded from these results that the liquid flow profile is strongly dependent on the air flowrate. This was already revealed by the investigation of the average superficial velocities, but the local investigation helped confirming and better understanding how the velocity field can be affected. The liquid flow profile was also found to depend on the geometry of the ALMBR. Finally, the observations at different locations of the ALMBR confirmed the non-uniformities in the liquid velocities, which can be linked to a non-uniform space-distribution of the gas phase in the riser. This latter hypothesis would need deeper research though, for example, by measuring a local gas hold-up rather than a global one.

III.4.2.1.4. Membrane shear stress in the ALMBR

The local membrane shear stress was deduced from the velocity field in the vicinity ($40\ \mu\text{m}$) of the membrane surface, for the different investigated conditions. A representative example of the raw result recorded on a total period of 25 s is presented in Figure III-21.

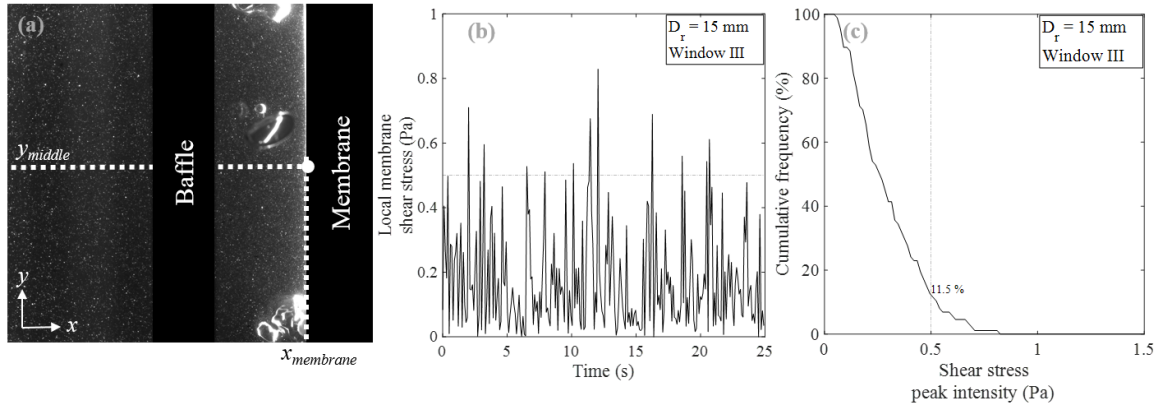


Figure III-21 : (a) PIV image, (b) shear stress evolution at the local point ($x_{membrane}, y_{middle}$) and (c) its derived shear stress peak distribution, taken at the bottom of the reactor (window III) under an SADm of $0.90\text{ Nm}^3\cdot\text{h}^{-1}\cdot\text{m}^{-2}$ and with a riser width of 15 mm.

It appears that the local membrane shear stress is a succession of sharp peaks with considerable fluctuations. This kind of profile is in accordance with what was reported in the literature (Figure III-5), where the variability of the intensity of the peaks was attributed to the passage of bubbles [124]. Also, the instantaneous values of the local membrane shear stress ranged between 0 and 1.5 Pa, which is consistent with the order of magnitude reported by the few studies focusing on similar systems (Table III-3). In the study of an ALMBR equipped with a flat-sheet membrane, Yamanoi and Kageyama (2010) [124] took into account both the average membrane shear stress and the shear stress standard deviation, because both parameters could be involved in the scouring of the membrane. This indicates that both the shear stress peak number (fluctuation **frequency**) and magnitude (fluctuation **intensity**) can be key-factors for biofouling mitigation. Therefore, in order to take into account both of these factors at the same time, a peak size distribution is proposed to support the discussion of results. The peak size distribution is presented in terms of cumulative frequency of number of peaks versus the intensity of peaks, as it appears in Figure III-21(c). As an example, when the MBR is run with an SADm of $0.90\text{ Nm}^3\cdot\text{h}^{-1}\cdot\text{m}^{-2}$, 11.5 % of the shear stress peaks induced have at least an intensity of 0.5 Pa (Figure III-21(b) and (c)). In order to identify the main parameters involved in shear stress peak distribution, an arbitrary criterion was defined as the cumulative frequency of the peaks having at least an intensity of 0.5 Pa.

The arbitrary value of 0.5 Pa was selected for the discussion, however with any another value of shear stress (between 0 and 1.0 Pa), the same global observations and conclusions can be deduced from the experimental data.

The cumulative distributions of the local shear stress were determined for the two riser widths, at the three observation windows and under the three highest air flowrates (0.75, 0.90 and 1.00 Nm³.h⁻¹.m⁻²) of the range. The results are presented in Figure III-22.

The increase of the air flowrate induces in most cases, an overall shift of the distribution curves towards the right indicating the increasing frequency of high shear stress peaks. As an example, at the bottom of the reactor (window III) for a riser width of 15 mm, the frequency of shear stress peaks having an intensity of 0.5 Pa or more, when the air flowrate is set to 0.75, 0.90 and 1.00, are respectively equal to 0%, 11.5 % and 16.7 %. This observation is consistent with the previous results demonstrating the effect of the air flowrate on the bubble velocity and the average liquid velocity. Besides, it is also in accordance with what was reported by Ducom et al. (2001) [126] in the characterization of the gas-liquid flow in 5 mm-wide rectangular channel along a flat-sheet membrane (Table III-3), where the average shear stress was significantly (up to 4 times) heightened with the injection of air bubbles leading to an improvement of the filtration flux by 15 % on average.

In addition, it can be noticed that the proportion of stress peaks having at least an intensity of 0.5 Pa increases, in some cases, along with the height in the reactor. As an example, when the riser width is set to 15 mm and under an air flowrate of 1.00 Nm³.h⁻¹.m⁻², 52 % of the shear stress peaks have at least an intensity of 0.5 Pa at the top of the reactor (window I), whereas this same proportion only reaches 29 % and 17 % at the middle (window II) and the bottom (window III) of the reactor, respectively. This result indicates that higher shear stress is generated at the top of the membrane, which is in accordance with the study of Khalili-Garakani et al. (2009) [93] showing that the highest shear stress values, as well as gas hold-up values, were recorded at the top of the membrane in a similar ALMBR configuration. Given the link that has been made in the literature between the membrane shear stress and the improved filtration flux, this finding indicates that in the present case, the filtration could be potentially more efficient at the top of the membrane.

Finally, the riser width seems to have a significant effect on the membrane shear stress, since the proportion of peaks having at least an intensity of 0.5 Pa is, in most cases, much greater when D_r is set to 7 mm, than when it is 15 mm. As an example, this proportion reaches 76 % at the top of the membrane (window I) under an air flowrate of 1.00 Nm³.h⁻¹.m⁻² when D_r is 7 mm, when it only reaches 52 % under the same conditions when D_r is 15 mm. This observation is consistent with the previous results, as the riser geometry was identified as a key-parameter governing both of the bubble size and the liquid velocity in the riser.

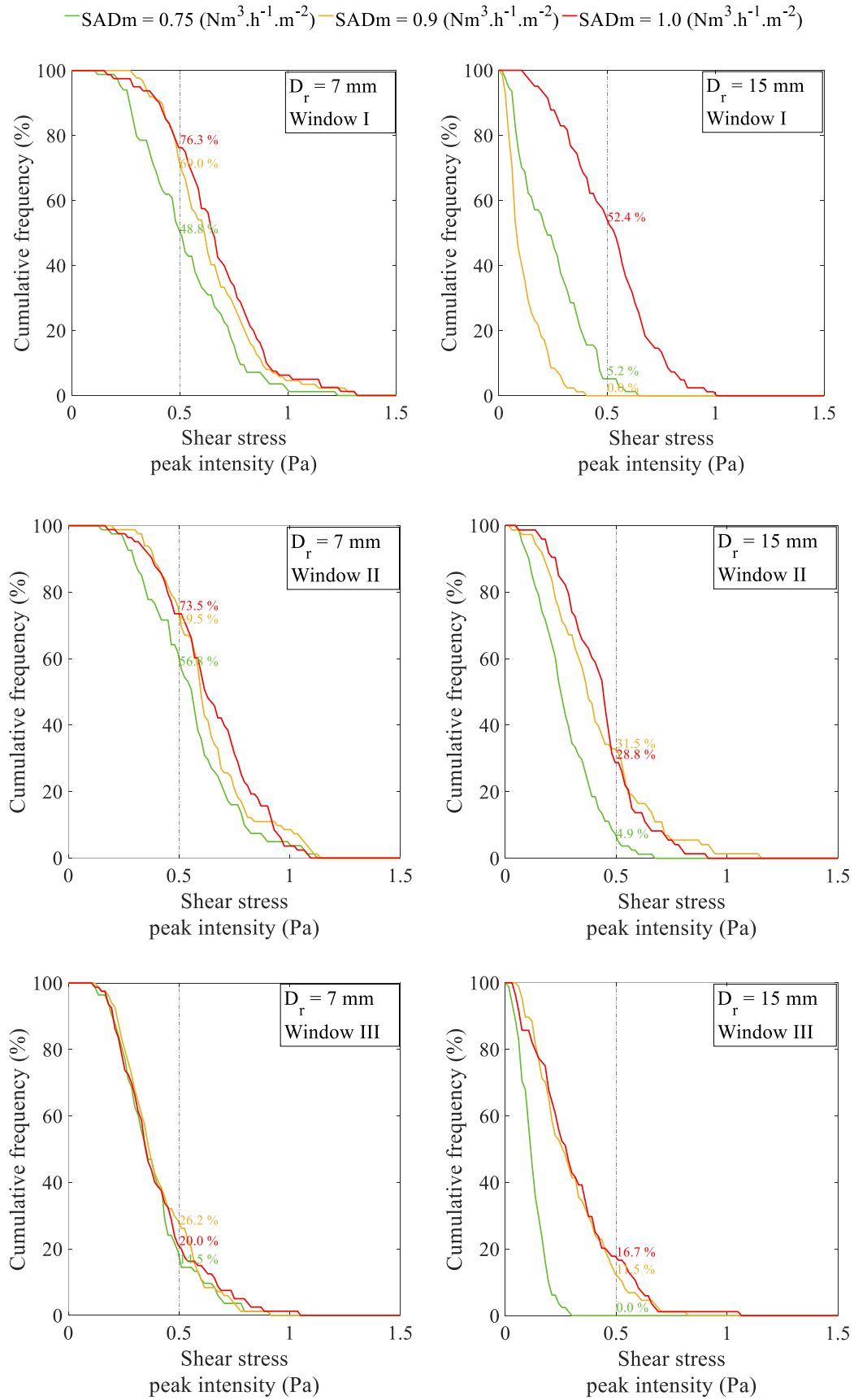


Figure III-22 : Cumulative distribution of local membrane shear stress peak in the ALMBR under different air flowrates and in different observation windows.

To sum up, the analysis of the membrane shear stress leads to the following main conclusions: first, the results are in good accordance with the literature, not only in terms of order of magnitude and space-distribution, but also in terms of their relationships to the investigated parameters (the riser width and the air flowrate). These results, put together with the previous ones, indicate that the increase of the air flowrate could enhance shear stress on the membrane, not via the production of bigger air bubbles, but via the production of a greater number of bubbles, that may accumulate in the top of the reactor, creating more intense pressure on the membrane surface. Finally, from the present findings, it can be retained that enhanced membrane shear stress, and thus enhanced filtration efficiency, is most likely to occur at the top of the membrane, under high air flowrate and small riser width, when considering the present two phase ALMBR.

III.4.2.2. Local characterization of the QQ-ALMBR

The local hydrodynamics of the QQ-ALMBR is discussed in the following, first, for a better understanding of the inherent properties of the solid phase (QQ media) at the local scale in the considered conditions, and then, for the determination of their effect on the gas and liquid phases at the local-scale.

III.4.2.2.1. QQ media position with respect to the membrane

The position of media was determined for each of the three QQ media when they were added at a volume fraction of 0.45 % v/v and for a riser width of 15 mm, at the window II and under the three highest air flowrates of the range (0.75, 0.90 and 1.00 Nm³.h⁻¹.m⁻²). These conditions were selected to ensure significant fluidization of the QQ media. The results are presented in Figure III-23. The discussion is based on the criterion of the minimal horizontal distance to the membrane, as well as on the error bars which correspond to the scattering of the results. In other words, the error bars cover the range of minimal horizontal distances that can result from the rise of QQ media. Thus, the size of the error bars actually indicates the fluctuations described by the QQ media when rising.

From Figure III-23, it appears that the average minimal distance between the QQ media and the membrane surface increases with the air flowrate for both the beads and sheets. However, for the QQ hollow cylinders it seems that the minimal distance reaches its highest value at the intermediate air flowrate of the investigated range (0.90 Nm³.h⁻¹.m⁻²). For the specific case of QQ beads, it also appears that the dispersion of the results is reduced when the air flowrate increases, which indicates that the QQ beads tend to describe fluctuations under low air flowrates, and a straighter trajectory under high air flowrates.

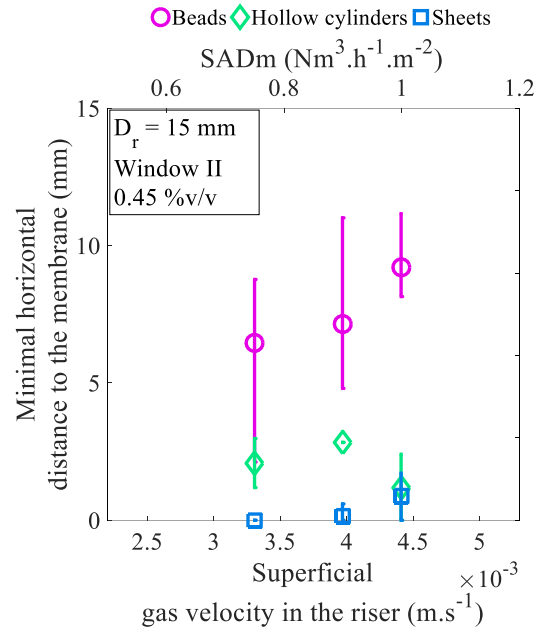


Figure III-23 : Average minimal distance to the membrane of QQ media at a volume fraction of 0.45 % v/v with a riser width of 15 mm and under different air flowrates.

Concerning the different QQ media shapes, noticeable discrepancies can be observed in Figure III-23. Among the three shapes on QQ media, the sheets tend to rise very close to the membrane, with average minimal distances to the membrane surface lower than 0.9 mm. The hollow cylinders rise at a slightly greater average distance from the membrane, comprised between 1.2 and 2.8 mm away from the membrane surface. Lastly, the QQ beads have the greater average minimal distance to the membrane when rising, with values ranging from 6.4 to about 9.2 mm. Again, the deviations to the average values reveal interesting insights in the difference between three shapes of QQ media. It appears that important deviations are obtained in presence of QQ beads, which means that the beads describe more important horizontal fluctuations when rising in the riser, compared to the two other shapes. This finding can be attributed to the different projected surfaces of the QQ media and their spatial conformation (and potential deformation) when rising. Considering that the beads have the smallest projected surface, it seems plausible that they are more sensitive to the local variations of the velocity in the liquid flow. These observations confirm the preliminary results of Lee et al. (2016) [12] showing, via a visualization technique, that the number of collisions between the QQ media and the membrane surface was greater with cylinders than beads, in a batch-type ALMBR with a riser width of 10 mm.

These results are of great interest from the perspective of the biofouling mitigation. In the case of a direct mechanical action of the QQ media exerted on the membrane to mitigate biofouling, it can be assumed that, in the investigated configuration of QQ-ALMBR, the sheets would be the more advantageous shape, owing to their propensity to rise very close to the membrane. However, in the case of additional (indirect) mechanisms involved in the biofouling mitigation, such as enhanced membrane

shear stress due the presence of QQ media, the question of the most favorable shape of QQ media is still open and needs to be linked to the characterization of the gas and liquid phases in presence of QQ media. Finally, it is worth mentioning that the investigated ALMBR is only equipped with one single flat-sheet membrane located in the riser, when the industrial filtration modules are in reality composed of several flat-sheet membranes, which means that, in that case, the position of the rising QQ media should be studied in the inter-membrane space, with respect to the two surrounding membrane surfaces.

III.4.2.2.2. QQ media velocity

The rising velocity of media in the riser part was experimentally measured following the same procedure as for the determination of the bubble velocity. The results come from the processing of images that were recorded at the middle height of the reactor (window II), and about 10 QQ media were processed for each condition to determine the average particle velocity. Figure III-24 presents the average rising velocity for the three shapes of QQ media, under different air flowrates for which the fluidization phenomenon was observed to be significant. The order of magnitude of the average QQ media velocity ranged roughly between 0.20 and 0.45 m.s^{-1} , in the investigated range of air flowrates.

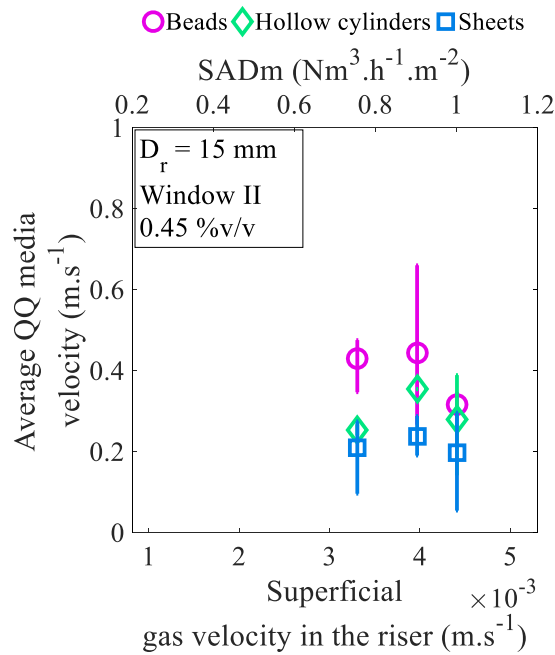


Figure III-24: Average media velocity in the riser part under different air flowrates.

It appears that the air flowrate (in the investigated range) has no significant effect on the average QQ media velocity, considering the standard deviation of the results. When comparing the three shapes, it appears that the beads have higher average rising velocity compared to the two other shapes. The average

velocities for the beads range between 0.31 and 0.44 m.s⁻¹, which is 1.5 to 2 times greater than the velocities reached by the QQ hollow cylinders and sheets.

On the other hand, the average rising velocities were compared to the average liquid velocities in the riser as well as to the bubble velocities, under the same conditions as it is presented in Table III-16.

Table III-16 : Comparison of the average QQ media velocities to the average liquid velocity and the bubble velocity obtained in the riser ($D_r = 15$ mm) under the same conditions.

SADm (Nm³.h⁻¹.m⁻²)	0.75	0.90	1.00
U_{gr} (m.s⁻¹)	0.0033	0.0040	0.0044
Average QQ media (instantaneous) velocity (m.s⁻¹)			
Beads	0.43	0.44	0.31
Hollow cylinders	0.25	0.35	0.28
Sheets	0.21	0.24	0.20
Average liquid velocity in the riser \overline{U}_{lr} (m.s⁻¹)			
Beads	0.12	0.15	0.14
Hollow cylinders	0.09	0.16	0.18
Sheets	0.04	0.09	0.09
Average bubble velocity in the riser \overline{U}_b (m.s⁻¹)			
Beads	0.52	0.59	0.53
Hollow cylinders	0.57	0.49	0.59
Sheets	0.52	0.65	0.58

The values of the bubble velocities obtained in presence of QQ media are presented in Table III-16 for comparison with the QQ media velocities, but will be more deeply discussed in the following (III.4.2.2.4).

It possible to notice that the QQ media velocities are significantly greater (up to 5 times) than the average liquid velocities in the riser under the same conditions. This observation could be surprising, but is actually due to the fact that the two compared velocities were deduced from two different measurement techniques giving different information. As a matter of fact, the QQ media velocity was measured with the camera technique and is actually an instantaneous velocity reached in one single local point of the riser, whereas the average liquid velocity was obtained by averaging the PIV-velocity fields in both space and time. Hence, it makes sense that the instantaneous rising velocity of QQ media depends on the local and instantaneous liquid velocity and is higher than the global liquid velocity averaged in space and time.

III.4.2.2.3. Bubble size in the QQ-ALMBR

Given the fluidization results, the effect of the QQ media on the bubble size was investigated under the extreme conditions, which are the highest volume fraction (0.45 % v/v) under the three highest air flowrates of the range (0.75, 0.90 and 1.00 Nm³.h⁻¹.m⁻²) and with a riser width of 15 mm. As the bubble size was found not to vary significantly with the height in the ALMBR, a space-averaged (over the

results obtained at the three windows I, II and III) bubble size was determined in the riser of the QQ-ALMBR, and the results are presented in Figure III-25.

Considering the error bars in Figure III-25, the air flowrate appears to have no significant effect on the bubble size in presence of QQ media, as for the ALMBR.

The average bubble size in the three QQ-ALMBRs was up to 12 % different (indifferently lower or higher) from the corresponding bubble size in the ALMBR, which again can be considered as insignificant compared to the error bars. Therefore, it appears that the addition of QQ media to the ALMBR induces no considerable modifications in terms of bubble size. In addition, when observing the different shapes of QQ media, the same conclusion can be drawn since only negligible discrepancies are obtained.

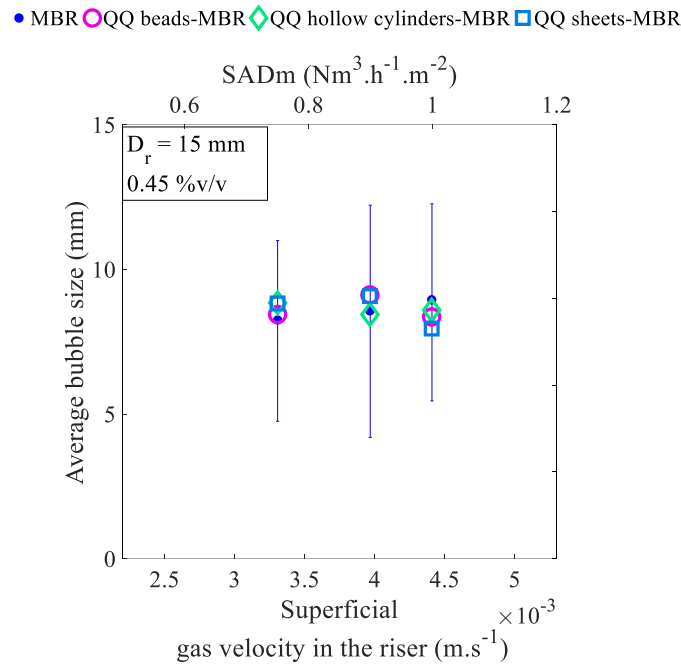


Figure III-25 : Average bubble size obtained in the QQ-ALMBR for a riser width of 15 mm, a volume fraction of 0.45 % v/v and under different air flowrates (*the error bars were not represented for the data from the QQ-ALMBRs not to clutter the plot*).

III.4.2.2.4. Bubble velocity in the QQ-ALMBR

The bubble velocity in presence of QQ media was determined under the same operating conditions as for the bubble size. The results are presented in Figure III-26. It appears that the bubble velocities in the QQ-ALMBRs are up to 16 % different from the bubble velocity obtained in the ALMBR, which can be considered as non-significant, given the standard deviation obtained in the measurement of the bubble velocity. Also, the discrepancies between the three different shapes of QQ media are not substantial.

These observations put together mean that, under the investigated conditions, the addition of QQ media has no effect on the bubble size and velocity in the ALMBR. This result is of great importance and indicates that the effect of the bubbles on biofouling mitigation can be preserved with the addition of QQ media.

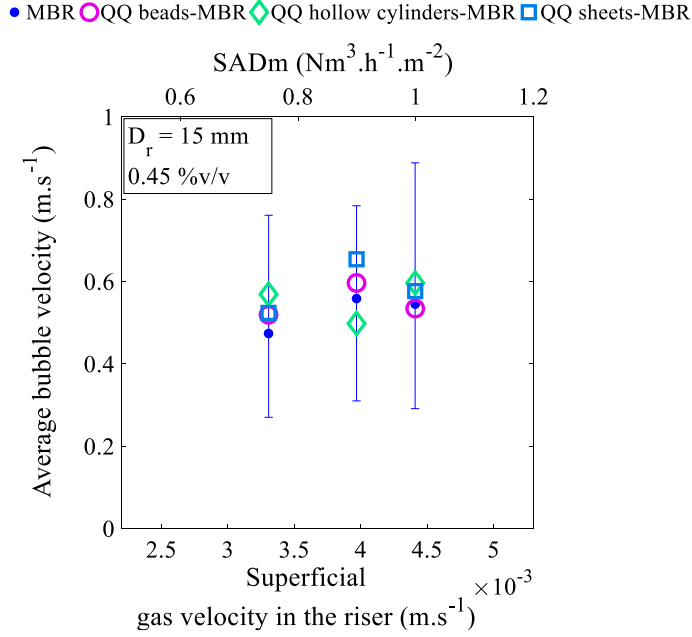


Figure III-26 : Average bubble velocity obtained in the QQ-ALMBR for a riser width of 15 mm, a volume fraction of 0.45 % v/v and under different air flowrates (*the error bars were not represented for the data from the QQ-ALMBRs not to clutter the plot*).

III.4.2.2.5. Liquid flow profile in the QQ-ALMBR

As it was previously done for the ALMBR, the velocity profiles were determined in presence of 0.45 % v/v of QQ media, under the three higher air flowrates of the investigated range (0.75, 0.90 and 1.00 $\text{Nm}^3.\text{h}^{-1}.\text{m}^{-2}$) and at different heights of the reactor (windows I, II and III). The results are presented in Figure III-27. The same global behavior is observed and consists in a profile with a maximum in the riser part and a less pronounced minimum in the down-comer part, which indicates that the air-lift configuration is effectively maintained with the addition of QQ media.

The increase of the air flowrate, in presence of QQ media, has no clear effect on the global shape of the profile of the liquid flow. The maximal velocity reached in the riser in presence of QQ media is globally the same as in the ALMBR: an increase in the air flowrate induces an increase of the maximum.

With the addition of QQ media, the global shape of the liquid flow profiles seems to be significantly modified. As an example, at the bottom of the reactor (window III) under an air flowrate of 1.00 $\text{Nm}^3.\text{h}^{-1}.\text{m}^{-2}$, the profiles in presence of QQ media appears to be asymmetrical in comparison to the

profile obtained in the ALMBR. This observation indicates that the space-distribution of the liquid velocities is modified, most likely because of the presence of QQ media in the flow that have an effect on the local velocities. In addition, the maximal velocity reached in the riser seems to be considerably reduced in presence of QQ media, with up to a 70 % decrease in the worst case (in the presence of QQ sheets, at the top of the reactor (window I) under an air flowrate of $1.00 \text{ Nm}^3 \cdot \text{h}^{-1} \cdot \text{m}^{-2}$). This observation indicates that the addition of QQ media to the ALMBR tends to slow down the liquid flow, mainly the QQ sheets, because are obstacles that can provoke a loss of the kinetic energy transported by the liquid flow.

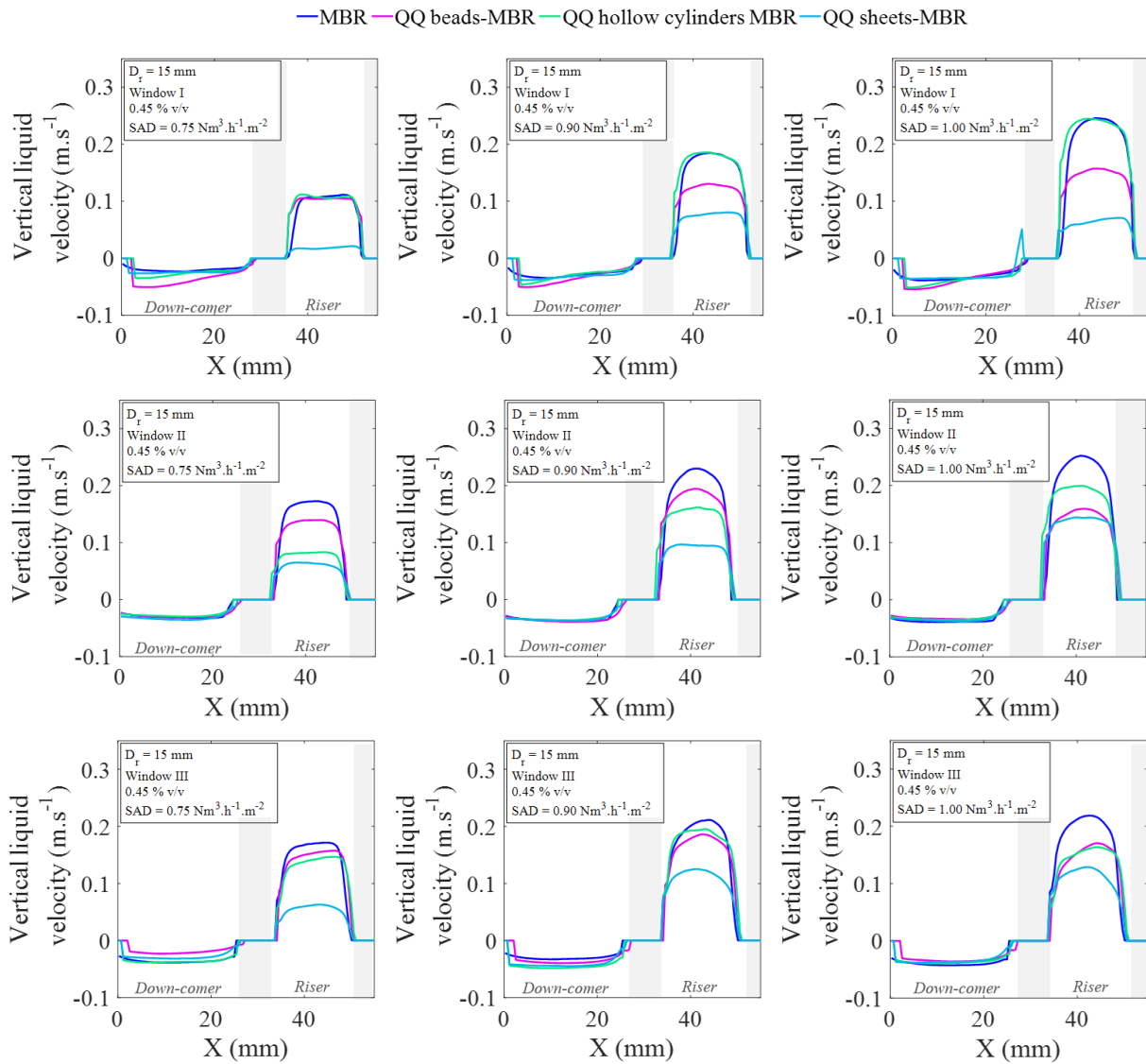


Figure III-27: Experimental horizontal profiles of vertical velocity, in the QQ-ALMBRs in presence of 0.45 % v/v of QQ media, with a riser width of 15 mm and under different air flowrates.

In presence of QQ media, the flow profiles describe some different behaviors at the different observation windows in terms of shape and maximal velocity, which proves that the liquid flow in the QQ-ALMBR is not uniformly space-distributed in the riser. When hollow cylinders are added, it appears that the liquid flow profile at the top of the reactor (window I) is very close to the profile obtained in the ALMBR, under the three investigated air flowrates (Figure III-27). The QQ media do not globally affect the liquid flow profile in the riser, but rather affects it locally, which can be explained by the heterogeneous distribution of the fluidized media in the riser. In all the investigated cases, the profiles obtained in presence of QQ sheets appear to be the lowest ones.

From all these results, it can be concluded that the addition of QQ media definitely generates a slowing down and local modifications of the liquid flow in the riser part. Indeed, the maximal vertical liquid velocity reached in the riser is reduced in average by 16, 19 and 58 % in presence of QQ hollow cylinders, beads and sheets respectively. Therefore, it seems that the QQ hollow cylinders induce the less significant effect on the liquid flow with only 16 % in average. On the other hand, the QQ sheets appear to induce the more severe effect on the liquid flow. These results complement considerably the conclusions that have been drawn concerning the effect of the QQ media on the global scale, and confirm that the decrease that was observed in the average liquid velocity is actually due to local modifications of the liquid velocity field due to the presence of QQ media.

III.4.2.2.6. Membrane shear stress in the QQ-ALMBR

The membrane shear stress in the QQ-ALMBRs was studied in terms of shear stress peaks distribution for three different air flowrates under which the QQ media fluidize significantly (0.75 , 0.90 and $1.00 \text{ Nm}^3 \cdot \text{h}^{-1} \cdot \text{m}^{-2}$) and for a riser width of 15 mm . The results are gathered in Figure III-28, and the proportions of peaks having at least an intensity of 0.5 Pa are considered as a criterion for comparison and discussion.

As it was mentioned previously, the proportions of more intense shear stress peaks increased in the ALMBR when the air flowrate increased, since the distribution curves tended to be shifted to the right as the air flowrate increased. When QQ media are added to the ALMBR, the latter behavior was only strictly maintained for QQ hollow cylinders, whereas the QQ beads and sheets induce random evolution of this criterion. As an example, in presence of QQ hollow cylinders, the proportion of peaks having at least an intensity of 0.5 Pa at the top of the membrane (window I) is 7.9 , 17.1 and 29.3% , when the air flowrate is set to 0.75 , 0.90 and $1.00 \text{ Nm}^3 \cdot \text{h}^{-1} \cdot \text{m}^{-2}$, respectively.

If the evolution of the shear stress peak distribution increases with the height in the ALMBR, this trend is not maintained in presence of QQ media. As an example, in presence of QQ beads and under an air flowrate of $0.90 \text{ Nm}^3 \cdot \text{h}^{-1} \cdot \text{m}^{-2}$, about 17% of the peaks have at least an intensity of 0.5 Pa at the bottom and the middle of the membrane, (windows III and II), whereas the proportion of these peaks only reaches 9% at the top of the membrane (window I).

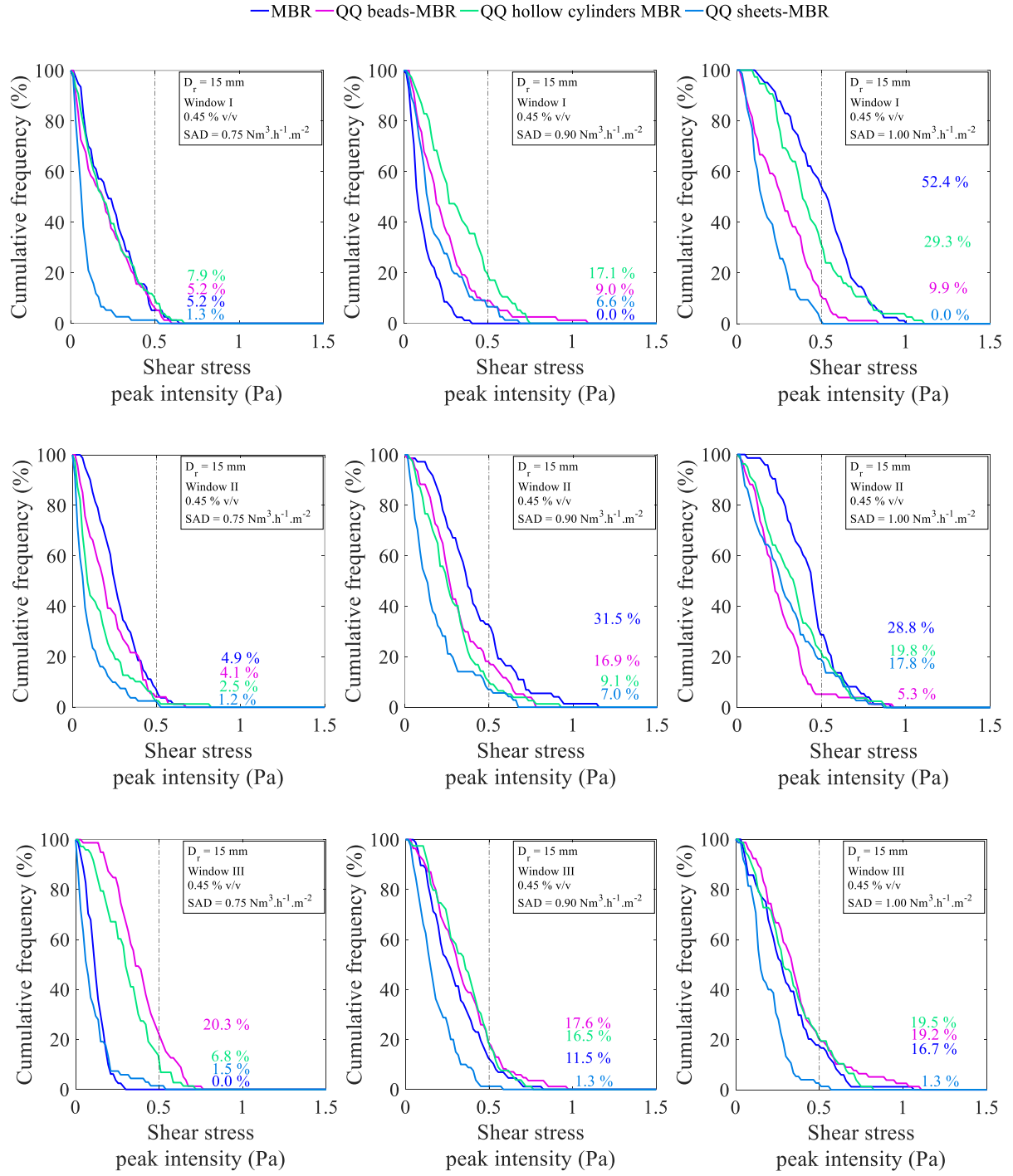


Figure III-28: Cumulative distribution of local membrane shear stress peak in the QQ-ALMBRs with a volume fraction of QQ media of 0.45 % v/v, under different air flowrates and in different observation windows.

Concerning the addition of QQ media, it can be drawn from the observation of the curves that it generates random effect on the shear stress peak distribution, since the curves are indifferently located above or below the distribution curve of the ALMBR, depending on the different conditions. It can be noticed that the distribution curves obtained at the middle of the membrane (window II) in presence of QQ media are always lower than the ones without any QQ media, which means that the stress peaks in this area of the membrane have lower intensity when QQ media are added. However, under some other conditions the QQ media can give rise to more intense stress peaks, for example, at the top of the membrane (window I) under an air flowrate of $0.90 \text{ Nm}^3 \cdot \text{h}^{-1} \cdot \text{m}^{-2}$, the proportion of the peaks greater than or equal to 0.5 Pa which was 0 % in the ALMBR, is increased to 7, 9 or 17 % in presence of QQ sheets, beads or hollow cylinders, respectively.

Finally, regarding the effect of the different QQ media shapes on the membrane shear stress, it can be perceived from the results that their addition does not globally increase the proportion of high intensity shear peak on the membrane. The QQ sheets are the media that induce the lower shear stress peak distribution in comparison to the ALMBR, in most cases, even though they were found to rise very close to the membrane surface. The presence of QQ beads and hollow cylinders seems to result in higher shear stress distribution at the bottom of the membrane (window III), which means that their effect on the biofouling mitigation can be considerable there. However, in the middle of the membrane (window II), the shear stress distributions induced in presence of QQ media are always lower than the ones obtained in the ALMBR. These results confirm the importance of the local characterization of the hydrodynamics, and actually show that the addition of QQ media can have multiple effects on the membrane shear stress (either increase it or decrease it) depending on the location. It is worth keeping in mind that these results were calculated in one single local point of the membrane, therefore, it could be of great interest to take them to the next step by analyzing the totality of the membrane surface, since considerable non-uniformities were reported in the literature [93,130,132].

III.4.2.3. Concluding remarks on the local characterization of the ALMBR/QQ-ALMBR

The characterization of the ALMBR and the QQ-ALMBRs at the local scale allowed drawing the following main conclusions:

- In the ALMBR, the bubbles were characterized and their size was found to be strongly dependent on the riser geometry, whereas, their velocity was mostly influenced by the aeration conditions. For a riser width D_r of 7 mm, the average bubble size was about 5 to 7 mm, whereas for the riser width D_r of 15, the average bubble size was about 8 to 10 mm.
- The study of the liquid velocity fields in the ALMBR revealed non-uniformities, confirming the importance of characterizing this kind of systems locally. Overall, the maximal liquid velocity reached

in the riser was up to 1.5 times greater than the average liquid velocity in the riser (up to about 0.2 m.s^{-1}). Furthermore, the liquid flow profile was found to be strongly influenced by the aeration as well as the geometry of the reactor.

- The membrane shear stress in the ALMBR was assessed on the basis of an original approach, consisting in considering the number and the intensity of the shear stress peaks. The obtained trends in terms of membrane shear stress were consistent with the literature, and in the specific case of this study, enhanced membrane shear stress tends to be induced under high air flowrates, at the top of the membrane for a riser width of 7 mm.

- The study of the QQ media position revealed interesting features about the QQ media. The sheets were found to rise very closely to the membrane surface compared to the other two shapes. Also, the QQ beads were demonstrated to rise “far” from the membrane but describing more fluctuations.

- The addition of QQ media appeared to have no significant effect on the bubble size and velocity. However, the effect of the liquid flow was considerable as the maximum liquid velocities reached in the riser were significantly reduced in presence of QQ media, with up to a 70 % decrease in presence of QQ sheets for example.

On the basis of the membrane shear stress, the effect of QQ media was not clearly identifiable, since the high membrane shear stress peaks could be even favored or reduced in presence of QQ media, depending on the conditions. Thus, deeper research would be needed to determine accurately the effect of the QQ media on the membrane surface.

III.5. Conclusions and perspectives

In this chapter, a literature review on multiphase systems was first presented allowing the selection of relevant tools for the hydrodynamics characterization, as well as, the determination of the state-of-the-art concerning ALRs and MBRs. The hydrodynamics characterization of the ALMBR and the QQ-ALMBRs was then performed, distinguishing two scales: the global scale and the local scale. The obtained results were presented, discussed and confronted to the literature, and the following key-conclusions can be retained:

- The ALMBR chosen for this study was characterized and found to be in good accordance with the literature concerning the air-lift configuration, which allowed its use as a reliable reference to determine the effect of the addition of QQ media on it.
- The fluidization of QQ media was found to be strongly affected by the air flowrate and the reactor geometry. In the present case, the ALMBR was not fully suitable for optimal fluidization and some improvements should be made. In particular, no fluidization was observed for a riser width of 7 mm. For the riser width of 15 mm, the fluidization was observed for $SADm$ higher than $0.5 \text{ Nm}^3 \cdot \text{h}^{-1} \cdot \text{m}^{-2}$. Above this value, the fluidization rates were up to 100 %, and were always greater for the sheets and hollow cylinders than for the beads.
- Given the fluidization features of the QQ media, their effect on the ALMBR was assessed at both of the aforementioned scales. At the global scale, the effect of QQ media was found to be insignificant since the total gas hold-up was not impaired and the average liquid velocity in the riser was only slightly affected in presence of QQ sheets, under some specific conditions. At the local scale, however, the presence of QQ media was found to have a significant effect on the liquid velocities in the riser. More precisely, the presence of QQ sheets could induce up to 70 % slowdown of the liquid flow in the riser.
- Making the distinction between the global and local scales was actually relevant, because it allowed concluding about the effect of QQ media on the ALMBR.

**CHAPTER IV. MIXING AND
CIRCULATION
PERFORMANCE OF THE
ALMBR/QQ-ALMBR**

RESUME EN FRANCAIS

Le présent chapitre traite des performances de mélange et d'écoulement des bioréacteurs à membrane à air-lift, avec application ou non de Quorum Quenching (QQ). Le mélange est un processus physique dont de nombreux procédés sont le siège. Il consiste à réduire les hétérogénéités spatiales rencontrées dans des fluides en termes de concentrations, températures, ou autres propriétés. Le mélange est ainsi un facteur-clé qui peut être déterminant pour les performances d'un procédé. Dans le cas particulier des bioréacteurs à membrane, il a été montré que la biodégradation, le colmatage ainsi que la consommation d'énergie sont fortement liés aux performances de mélange. Ainsi, le premier objectif de ce chapitre est de caractériser le bioréacteur à membrane à air-lift, qui a été récemment développé et présenté comme étant prometteur pour la réduction du colmatage. Dans un second temps, il s'agira d'identifier un éventuel effet causé par l'introduction de particules supports de QQ sur le mélange.

En vue de répondre à ces deux principaux objectifs, le présent chapitre s'articule autour de plusieurs parties qui sont complémentaires. En premier lieu, une partie bibliographique présente les fondamentaux des différentes techniques de caractérisation du mélange dans les réacteurs multiphasiques. Une synthèse de résultats pertinents tirés de la littérature a également été effectuée et a permis de choisir une démarche expérimentale pour cette étude, en distinguant les performances de mélange à **deux échelles de temps** : à court terme et à long terme. Cette distinction, qui est essentielle dans l'étude des performances biologiques, se définit par rapport au temps de séjour du réacteur : le mélange à court-terme renvoie à l'homogénéisation du réacteur sur un temps négligeable devant le temps de séjour du réacteur, alors que le mélange à long-terme concerne l'homogénéité (ou non) du volume réactionnel durant l'opération sur **un ou plusieurs** temps de séjour. L'intérêt d'opérer cette distinction est de caractériser et modéliser le réacteur (réacteur parfaitement agité, piston, combiné ...) pour pouvoir ensuite, en déduire l'impact de l'ajout des particules supports de QQ à long terme.

La caractérisation du mélange à court-terme concernait la partie aérée du réacteur et s'est basée sur une technique de traceur. Le temps de mélange de la partie aérobie, défini comme le temps nécessaire pour un colorant injecté pour s'homogénéiser, a été mesuré par une technique optique (caméra et panneau lumineux). La caractérisation du mélange à long-terme a été réalisée avec des mesures de distribution de temps de séjour et en mesurant une conductivité. Les principaux résultats concernant le mélange à court terme, ont montré que le temps de mélange dans le bioréacteur à membrane à air-lift était relativement court, de l'ordre de 30 s (toujours < à 80 s dans cette étude) et que l'aération avait peu d'effet sur ce temps, au-delà d'un certain seuil de débit. L'ajout de particules de QQ s'est révélé avoir peu d'influence sur ces performances de mélange à court terme. Le réacteur considéré peut donc être assimilé à un réacteur agité, en présence ou non de particules de QQ. En revanche, à long terme, l'ajout de particules de QQ s'est traduit par une altération du mélange global, notamment, par l'apparition de volumes morts et par une perturbation de la recirculation entre les deux compartiments du réacteur.

IV.1. Introduction

The study of the mixing performance in reactors is of great interest in chemical engineering, and has been, over the years, one of the key-subjects of investigation in fundamental research as well as in various industrial processes. Mixing is a physical phenomenon (or process) which aims to reduce the heterogeneities in fluids, by lowering the space-gradients of concentration, temperature, or other properties. Mixing takes place in a wide range of processes and plays a key-role in their overall performance. In the case of MBRs, the mixing performance can be crucial for the biodegradation efficiency, the biofouling and the energy consumption.

In this chapter, the mixing performance of an Air-Lift Membrane Bioreactor (ALMBR) will be more specifically addressed. ALMBRs are a combination of a membrane bioreactor together with an air-lift motion, leading to enhanced circulation and mixing performances. On a hydrodynamics level this specific configuration is of particular interest since it creates more complex flowing behavior in the reactor. With the development of Quorum Quenching (QQ) as a biofouling mitigation technique and the implementation of QQ media to the MBR, the hydrodynamics could be even more complex.

For these reasons, the mixing and circulation performance of the ALMBR/QQ-ALMBR is developed in this work, with a double-objective:

- Characterizing the ALMBR in terms of mixing. The ALMBRs were recently developed and presented as favorable technique for fouling control. Thus, the present study aims to better understand the mixing performance in such specific configuration, and to use it as a reliable reference for further comparison with the QQ-ALMBR.
- Assessing the effect of the implementation of QQ media in ALMBRs, in terms of mixing. Since the ALMBR is expected to have excellent mixing and flowing features, the potential impact of the addition of QQ media has to be determined.

With this view, the present chapter includes a background section, where the fundamentals of the techniques used to characterize the mixing performance are presented. Some results reported in the literature are also discussed. On this basis, the experimental approach is then developed distinguishing two time-scales: the short-term and the long-term mixing performance. The experiments conducted consist in tracer techniques in both cases. For the short-term mixing performance, a dye is injected in the aerobic part of the reactor under different aeration conditions, and a camera is used to visualize and measure the mixing time (time necessary to reach the complete homogeneity of the bulk). The Residence Time Distribution is measured to characterize the long-term mixing performance of the ALMBR/QQ-ALMBR. The experiments consist in using NaCl as a tracer, and are conducted under different operating conditions (aeration, different shapes of QQ media).

IV.2. Background

Given the importance of the mixing performance for a wide range of processes at the industrial scale, research has come up with different characterization tools that can be subcategorized into different types (experimental, numerical, local, global...). In the present study, the selected characterization techniques are presented in the following based on the literature and distinguishing two different cases, depending on whether the techniques provide information about the mixing performance at the **short-term** (during a time negligible compared to the residence time of the reactor) or at the **long-term** process operation (during a time corresponding, a least, to the residence time of the reactor).

IV.2.1. Characterization of the short-term mixing performance

In order to characterize the **short-term** mixing performance, the **mixing time** was defined as the key-parameter to analyze. In this section, mixing time will be defined, and the main techniques for its measurement will be mentioned. Relevant results from the literature will be presented for discussion.

IV.2.2. Definition of mixing time and measurement techniques

The mixing time was first defined by Kramers et al. (1953) [138] as the time needed to obtain a certain degree of uniformity of concentration in a reactor (usually 95 to 99 % of uniformity in the bulk of the reactor). Mixing time is a global parameter giving information about the macromixing performance of a reactor. It is a key-parameter, and its comparison with other characteristic times of a process (reaction time, mass transfer time, residence time) is of particular interest to determine the limiting mechanism of the whole process.

Over the last decades, several measurement methods were reported and consisted all in the injection of a small amount of tracer in a local point of the reactor and the monitoring of its concentration in the bulk overtime. The mixing time being finally deduced from the time interval between the disturbance and its stabilization. Among the measurement techniques, colorimetry, conductivity, pH, thermography, fluorescence spectrometry, can be cited as the most reported experimental techniques, as reviewed by Ascanio (2015) [139].

IV.2.2.1. Literature review on the short-term mixing performance in multiphase systems

Even though mixing time was originally defined to characterize mechanically stirred single phase (liquid) reactors, the principle was further extended to complex multiphase systems, having common features with the process studied in the present work (ALMBR/QQ-ALMBR). Relevant studies about multiphase systems were gathered in Table IV-1 in order to analyze their main results.

Table IV-1 : Summary of studies characterizing the short-term mixing performance in multiphase reactors.

Reactor				Measurement technique	Main results		Reference		
Type	Total working volume (m ³)	Air supply* (Nm ³ .h ⁻¹)	Superficial gas velocity (m.s ⁻¹)		Mixing time t _m (s)	Circulation time t _c (s)		Highlights	
ALRs									
Double draft-tube ALR	2.42x10 ⁻⁵	0.05	1.4×10 ⁻³	Conductivity with sodium chloride as a tracer	83.8	24.1	<ul style="list-style-type: none">The mixing and circulation times decrease with the increasing air flowrateThe concentric double draft tube geometry offers better mixing performance than the conventional concentric ALR	[140]	
		0.06	1.7×10 ⁻³		75.7	20.2			
		0.07	1.9×10 ⁻³		74.4	16.8			
Draft-tube ALR	2.42x10 ⁻⁵	0.05	9.9×10 ⁻⁴		162.1	29.0			
		0.06	1.1×10 ⁻³		143.5	27.4			
		0.07	1.2×10 ⁻³		131.7	26.1			
2D rectangular ALR	2.4x10 ⁻³	0.02	5.0×10 ⁻³	Image analysis with blue ink as a tracer	141	32.8	<ul style="list-style-type: none">The mixing and circulation times decrease with the increasing air flowrate	[141]	
		0.04	1.0×10 ⁻²		93	17.6			
		0.06	1.5×10 ⁻²		78	11.6			
Draft-tube ALR	6.0x10 ⁻²	0.1 to 5.22	0.002 to 0.09	pH measurement with hydrochloric acid as a tracer	230 to 100	44 to 28	<ul style="list-style-type: none">The mixing time decreases with the increasing air flowrateThe circulation time describes a minimum with the increasing air flowrate	[142]	
Split-cylinder ALR	6.0x10 ⁻²	0.1 to 5.22	0.002 to 0.1		170 to 85	47 to 20			<ul style="list-style-type: none">The experimental data were found to be correctly fitted by correlations based on the Peclet (or Bodenstein) and Froude numbers, indicating the dependency of the mixing and circulation times on hydrodynamics
Draft-tube ALR	8.0x10 ⁻³	0.48 to 2.41	0.02 to 0.1	Visual monitoring of an acid-base reaction in presence of color indicator	40 to 20	20 to 10	<ul style="list-style-type: none">The mixing and circulation times decrease with the increasing air flowrateThe mixing and circulation times increase with increasing viscosity owing to the enhanced internal friction losses leading to less efficient overall mixing performance	[143]	
MBRs									
Rectangular submerged HF-MBR	4.0x10 ⁻²	1.70	8.4×10 ⁻³	Conductivity with sodium chloride as a tracer	480	-	<ul style="list-style-type: none">The mixing time was found to be constant into the investigated range of air flowrates	[144]	
		5.10	2.5×10 ⁻²		480				
ALMBRs									
Single tubular riser airlift-MBR	4.8x10 ⁻²	0.16	0.014	pH measurement with hydrochloric acid as a tracer	-	55	<ul style="list-style-type: none">The circulation time decreases with the increasing air flowrateThe use of 2 risers instead of a single one, keeping the same superficial air velocity, results in reduced circulation time	[145]	
		0.33	0.028		-	42			
		0.65	0.054		-	33			
Double tubular riser airlift-MBR	4.8x10 ⁻²	0.32	0.014		-	36			<ul style="list-style-type: none">The overall mixing performance is enhanced with the increasing number of risers in the multi-tubular riser-airlift MBR configuration
		0.66	0.028		-	30			
		1.3	0.054		-	23			

* Total air supply in the aerated part of the reactor: riser part for ALRs/ALMBRs and membrane tank for MBRs; n.a.: not available data.

Based on this selection of studies, it is first possible to notice that the measurement of mixing time was more widely used as a characterization tool for ALRs, rather than MBRs, which will be explained in the following by the precise analysis of the studies.

For the **ALRs**, all the experimental data were obtained under the batch mode for the liquid phase (no liquid feed) and the continuous mode for the gas phase (continuous air injection). In the specific case of ALRs, the circulation time t_c was another characteristic time that was measured and defined as the time needed for the liquid to achieve a complete loop from the riser to the down-comer part. A dimensionless mixing time was also defined as the ratio of the mixing time t_m to the circulation time t_c , as in Equation IV-2. This dimensionless time represents the number of loops needed for the liquid phase to obtain complete uniformity in the bulk.

$$\theta_m = \frac{t_m}{t_c} \quad \text{IV-2}$$

The references [140–143] in Table IV-1 report ALRs with working volume ranging from 2.4×10^{-5} to $6.0 \times 10^{-2} \text{ m}^3$, and under superficial gas velocities going from 10^{-3} to 10^{-1} m.s^{-1} . The mixing times reported ranged between 70 and 170 s (Table IV-1). In all the cases, it can be retained that both the mixing and circulation times vary with the operating conditions, among which, the geometry of the reactor, the aeration intensity, the viscosity of the fluid are the most important ones. In this variety of ALRs and operating conditions, and using different measurement techniques (Table IV-1), the short-term mixing performance in ALRs was found to be enhanced with increasing air flowrate [140–143], with decreasing viscosity [143], and with decreasing $\frac{A_r}{A_d}$ ratio [140,142].

Bando et al. (1998) [146] proposed a correlation to describe the effect of the aeration on the mixing time in draft-tube ALRs, following the general form presented in Equation IV-3, where U_{gs} is the superficial gas velocity in the riser part (in m.s^{-1}), and K is a constant depending on the sparger type and the airlift dimensions.

$$t_m = K U_{gs}^{-0.5} \quad \text{IV-3}$$

In addition, Sánchez Mirón et al. (2004), mentioned the existence of a critical air flowrate (around 0.01 m.s^{-1} in terms of superficial gas velocity) in a draft-tube ALR, above which the mixing time was constant and the circulation time slightly increased [142]. This phenomenon was attributed to the creation of microbubbles that tend to accumulate in the down-comer part, affecting the liquid circulation. In this case, the overall mixing performance is ensured by the enhanced local turbulence induced by the large amount of micro-bubbles rather than to the liquid circulation. The impact of the geometry is not obvious though given the great variety of airlift geometries and configurations.

In a rectangular lab-scale submerged HF-**MBR**, Čurlin et al. (2004) conducted a similar tracer method for characterizing the short-term mixing under the continuous mode for both of the liquid and the gas phases [144]. For a working volume of 40 L and liquid residence times ranging from 1.0 to 5.4 h, the mixing time was constant and found to be about 480 s even when the superficial gas velocity was three-fold increased from 8.4×10^{-3} to $2.5 \times 10^{-2} \text{ m.s}^{-1}$ (Table IV-1). This result can be explained by the fact that the investigated range of aeration was already above a certain threshold for which the gas hold-up in the liquid phase was insignificantly affected, giving rise to a constant amount of bubbles that ensure the mixing by creating local turbulence, eventually leading to global homogenization.

Xu and Yu (2008) [145] studied two configurations of **ALMBRs** with a total working volume of 48 L: a single riser ALMBR (with three tubular down-comers) and a double riser ALMBR (with two tubular down-comers) as presented in Figure IV-1 (where A_r and A_d are the riser and down-comer areas, respectively). Based on the circulation time measured under the batch mode (presented in Table IV-1), the short-term mixing performance in an ALMBR was clearly improved with the increase of the aeration as well as with the multiplication of riser parts, which is in accordance with the results obtained in simple ALRs [145].

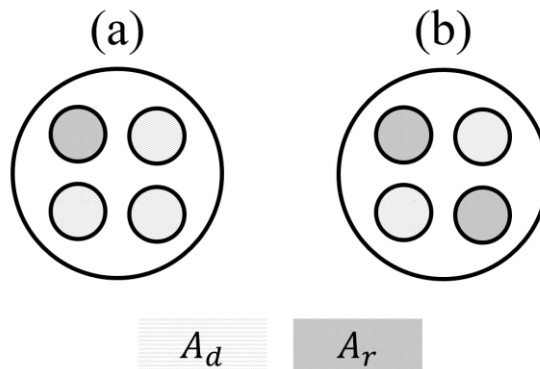


Figure IV-1 : (a) Single tubular riser ALMBR and (b) double tubular riser ALMBR, studied by Xu and Yu (2008) [145].

In sum, it can be concluded that the short-term mixing performance is mostly characterized in ALRs or ALMBRs, rather than in simple MBRs, precisely because of the added value of the airlift configuration to the overall mixing performance, as it is possible to see with the comparison of the mixing times gathered in Table IV-1 (for a the simple MBR, mixing time was 2 to more than 20 times greater than those obtained under the airlift configurations). However, in all the cases the mixing times ranged between 20 and 480 s, which remains negligible compared to the residence times. Lastly, these studies highlight the high dependency of the short-term mixing behavior on parameters such as the aeration intensity, the geometry, and the physical properties of the fluids.

IV.2.3. Characterization of the long-term mixing performance

The Residence Time Distribution (RTD) was defined as an effective tool for the characterization of the long-term mixing and circulation performance of reactors. It allows in particular characterizing the degree of homogeneity of the whole volume of the reactor, during a long time, worth several times the residence time. In the following, the RTD will be presented, from its measurement to its actual analysis in order to deduce some characteristic parameters. Relevant studies dealing with RTD in different systems will be then reviewed.

IV.2.3.1. Definition of the RTD and measurement technique

The RTD is a method used in chemical engineering to characterize the mixing and the flowing behaviors in non-ideal reactors. The principle was first introduced by MacMullin and Weber in 1935, but was further more deeply developed by Danckwerts in 1953. The RTD is based on the determination of a probability function describing the age distribution of the fluid elements circulating in the reactor. The RTD is a global method based on a stimulus-response experiment. It usually consists in injecting a certain amount of non-reactive tracer in the feed of the reactor and measuring its concentration in the output over time. The analysis of the signal and its deviation from the ideal flow patterns can reveal some dysfunctions that may take place in real reactors, such as dead volumes, channeling of fluid, or recycling of fluid.

IV.2.3.2. Quantitative analysis of the signal and RTD function

The aforementioned probability function describing the age distribution of a fluid passing through a vessel (reactor) is noted E and is expressed in units of time^{-1} . The distribution function is normalized, which means the area under its curve is unity (Equation IV-4). Given a specific time t_1 , it is then possible to identify the fraction of fluid younger or older than the age t_1 by the Equations IV-5 and IV-6, respectively.

$$\int_0^{\infty} E \, dt = 1 \quad \text{IV-4}$$

$$\int_0^{t_1} E \, dt \quad \text{IV-5}$$

$$\int_{t_1}^{\infty} E \, dt = 1 - \int_0^{t_1} E \, dt \quad \text{IV-6}$$

In practice, two types of stimuli are usually used to obtain the RTD function: the pulse injection and the step injection [147]. In the case of a pulse injection (case considered in the present study because more commonly reported in the literature), the distribution function is deduced from the monitored response

of the system in terms of concentration of tracer $C(t)$, as described by Equation IV-7, where τ is the hydraulic retention time (or theoretical residence time, defined as the ratio of the total volume of the reactor to the fluid flowrate passing through it) and C_0 is the theoretical tracer concentration in the reactor if it was uniformly distributed in the reactor (defined as the total amount of tracer introduced in the reactor divided by its volume).

$$E(t) = \frac{C(t)}{\int_0^\infty C(t)dt} = \frac{1}{\tau} \frac{C(t)}{C_0} \quad \text{IV-7}$$

The RTD curve can also be used in its normalized form described by the Equation IV-8, where θ is the normalized time (defined as the ratio of time to the theoretical residence time τ)

$$E(\theta) = \tau E(t) \quad \text{IV-8}$$

A set of parameters can be deduced from the RTD curve and used as indicators of the flowing and mixing performances of the considered reactor. Among these parameters, the first and second moments of the RTD function indicate, respectively, the mean residence time μ and the variance σ^2 of the distribution (Equations IV-9 and IV-10).

$$\mu = \frac{\int_0^\infty tC(t)dt}{\int_0^\infty C(t)dt} \quad \text{IV-9}$$

$$\sigma^2 = \frac{\int_0^\infty (t - \mu)^2 C(t)dt}{\int_0^\infty C(t)dt} \quad \text{IV-10}$$

IV.2.3.3. *Usual flow patterns for reactors modelling*

Since most of real reactors are non-ideal, the modelling approach consists in describing their behavior based on well-defined ideal flow patterns. The comparison of the experimental and theoretical RTD curves $E(t)$ allows to conclude about how representative is the selected model. Two main modelling approaches are usually adopted for this:

- The **compartment model** which consists in using a combination of the ideal reactors in different ways (in series, in parallel, with/without recycling flow, with/without dysfunctions...).
- The **dispersion model** which consists in assessing the deviation of the real reactor from the ideal plug-flow.

Some of the models usually used are presented in the following. These few models were selected because they were used to describe either MBRs or ALRs in the literature, as it will be reviewed in the following.

- *Model of completely mixed reactor with dead zones and short-circuiting*

This model was introduced by Cholette and Cloutier in 1959 and assumes the existence of a dead zone volume and a short-circuiting flowrate. Both of these dysfunctions are recurring defects in real reactors. The dead volumes (dead zones) are stagnant regions of the reactor where very low or no mixing occurs, which can reduce the effective reaction volume. The short-circuiting phenomenon refers to the fact that a portion of the fluid entering the reactor is directly transported out of it before actually taking part to the reaction.

In this model, these two dysfunctions are evaluated with two indexes: m (the dead zone index) and n (the short-circuiting rate), respectively deduced from Equations IV-11 and IV-12. The theoretical RTD curve of the model is expressed according to Equation IV-13, where $\delta(t)$ is the Dirac function which is worth 1 when $t = 0$ and 0 otherwise.

$$m = \frac{\mu}{\tau} \quad \text{IV-11}$$

$$\sigma^2 = m^2 \tau^2 \left(\frac{2}{n} - 1 \right) \quad \text{IV-12}$$

$$E(\theta) = \frac{n^2}{m} \exp\left(-\frac{n}{m}\theta\right) + (1 - n)\delta(t)\tau \quad \text{IV-13}$$

In the case of the ALMBR/QQ-ALMBR that are considered in this study, the presence of dead volumes is a plausible hypothesis, and will be investigated in the following. However, the presence of short-circuiting is less likely to take place, given the fact that the outlet (permeate) of the reactor passes through the membrane.

- *Tanks-in-series model*

This model is based on the assumption that the reactor can be divided into a number N of stirred tanks-in-series. The number N can be deduced from the first and second moments of the experimental RTD distribution as described by Equation IV-14. Based on this number, the normalized theoretical RTD curve is defined as in Equation IV-15.

$$N = \frac{\mu^2}{\sigma^2} \quad \text{IV-14}$$

$$E(\theta) = N \frac{(N\theta)^{N-1}}{(N-1)!} e^{-N\theta} \quad \text{IV-15}$$

- *Model of two tanks-in-series with different volumes*

The model is based on two stirred tanks-in-series with different volumes V_1 and V_2 . With the condition that the mean residence time μ equals the theoretical hydraulic retention time τ , a theoretical RTD curve can be defined as in Equation IV-16, where α is the ratio of the volume of the first tank to the volume of the second tank, and is deduced from Equation IV-17.

$$E(\theta) = \frac{1 + \alpha}{1 - \alpha} [\exp(-(1 + \alpha)\theta) - \exp(-(1 + \frac{1}{\alpha})\theta)] \quad \text{IV-16}$$

$$\sigma^2 = \frac{1 + \alpha^2}{(1 + \alpha)^2} \quad \text{IV-17}$$

- *Tanks-in-series with back-mixing model*

This model is based on the existence of a back-mixing flow, which refers to the fact that a portion of fluid in each tank is internally recirculated instead of being transported out of it. In practice, this model is particularly suitable to describe real reactors with an actual internal recirculation such as bubble columns, or air-lift reactors. This model is built on two parameters: the number N of tanks-in-series and the back-mixing rate R . Given the number of tanks N , the back-mixing rate R can be determined using Equation IV-18. The theoretical RTD curve is then described by Equations IV-19 to IV-22.

$$\sigma^2 = \frac{N(1 + 2R) - 2R(1 + R)[1 - (\frac{R}{1 + R})^N]}{N^2} \quad \text{IV-18}$$

$$w = \sqrt{1 + R} \quad \text{IV-19}$$

$$r_i = 1 + \frac{2(1 - w \cos \psi_i)}{w^2 - 1} \quad \text{IV-20}$$

$$\psi_i(N + 1) + 2 \arctan \frac{\sin \psi_i}{w - \cos \psi_i} = i\pi \quad \text{IV-21}$$

$$E(\theta) = 2N \frac{w^{N+1}}{w^2 - 1} \sum_{i=1}^N (-1)^{i+1} \frac{\sin^2 \psi_i}{(1 + Nr_i)} \exp(-N\theta r_i) \quad \text{IV-22}$$

- *Dispersion model*

This model usually applies to turbulent flow in pipes, long tubes, long channels or packed beds [147]. It consists in assuming that a longitudinal diffusion-like process is superimposed to the pure plug-flow. In order to characterize the spread in the reactor, a dimensionless number $\frac{D}{uL}$ is defined as the ratio of the dispersion coefficient D ($\text{m}^2.\text{s}^{-1}$) to the product of the fluid velocity u ($\text{m}.\text{s}^{-1}$) in the reactor by the total length L (m) of the reactor. The dispersion number $\frac{D}{uL}$ is deduced from Equation IV-23. When the dispersion number tends to 0, the dispersion phenomenon is negligible and the reactor behaves as a perfect plug-flow. In opposition, when the number tends to infinite the extent of dispersion is very high, and the overall reactor is closer to a completely mixed flow. The theoretical RTD curve is then given by Equation IV-24.

$$\frac{\sigma^2}{\mu^4} = 2 \frac{D}{uL} - 2\left(\frac{D}{uL}\right)^2(1 - e^{-\frac{uL}{D}}) \quad \text{IV-23}$$

$$E(\theta) = \frac{1}{\sqrt{4\pi\left(\frac{D}{uL}\right)}} \exp\left[-\frac{(1 - \theta)^2}{4\theta\left(\frac{D}{uL}\right)}\right] \quad \text{IV-24}$$

IV.2.3.4. Literature review on the long-term mixing performance in multiphase systems

Some studies have investigated the long-term mixing performance of multiphase systems similar to the reactor of the present study, and were gathered in Table IV-2 for the analysis of their main conclusions (in terms of RTD and model parameters). It is first important to notice that the RTD was much more used as a characterization tool for the long-term mixing performance of MBRs, rather than for ALRs. In all the cases presented in Table IV-2, the RTD measurement was performed under the continuous feeding mode. The measurement technique, the sampling point, as well as the main results are indicated in Table IV-2 for all the studies.

Table IV-2 : Summary of studies on the long-term mixing performance in multiphase reactors.

Reactor			RTD measurement			Main results					Reference	
Volume (m ³)	Configuration	Air supply* (Nm ³ .h ⁻¹)	Theoretical hydraulic residence time τ (h)	Technique	Sampling point	RTD and model parameters						
						Mean residence time μ (h)	Time to reach the peak t_p (h)	Effective volume V_{eff} (m ³)	Number of tank-in-series N	Dispersion Number $\frac{D}{uL}$		
MBRs												
0.006	Submerged HF-MBR (aerobic membrane tank)	-	0.75	Pulse input of Lithium chloride as a tracer	Lead membrane	0.57	0.015	0.005	1.1	3.5	• Variations in the membrane position (different sampling points) induce different performance during the beginning of the operation that tend to be attenuated overtime • In both cases, the rectors were close to completely mixed flows	[148]
0.006		-	0.75		Tail membrane	0.53	0.053	0.004	1.14	2.45		
2.36	Side-stream HF-MBR (anoxic + aerobic + membrane tank)	3	5.9		Permeate	5.9	1.4	2.34	1.6	0.74	• The MBR describes a relatively well-mixed flow • Deviations of the experimental RTD curve were although observed in comparison to the perfectly mixed tanks-in-series model and were explained by the existence of a recirculation flow in the MBR	
75	Submerged HF-MBR (anoxic + aerobic membrane tank)	250	6.05	Pulse input of Lithium chloride as a tracer	Permeate	6.91	3.03	85.7	1.47	0.78	• The two MBRs are relatively well-mixed and their available volumes are effectively used • The aeration in both cases create conditions approaching the well-mixed flow • The presence of humps on the experimental RTD curves is attributed to the existence of a relatively important recycling flow in addition to the through-flow	[149]
73.5	Side-stream FS-MBR (anoxic + aerobic + membrane)	300	5.97	Pulse input of Lithium chloride as a tracer	Permeate	5.41	1.49	67.1	1.45	0.81		
1244	Side-stream FS-MBR (anoxic + aerobic + membrane tank)	992	27.5	Pulse input of Lithium chloride as a tracer	Permeate	31.3	3.63	n.a.	1.1	2.8	• Both of the FS-MBR and the HF-MBR are closer to completely mixed flows • Both of the MBRs describe great deviation from the plug-flow reactor based on their large amount of dispersion • The HF-MBR is more energy efficient than the FS-MBR • The compartment model is deficient to predict the behavior of the typical complex flows in MBRs	[150]
471	Side-stream HF-MBR (anoxic + aerobic + membrane tank)	918	10.3		Permeate	10.3	0.75	n.a.	1.2	1.5		
ALRs												
0.0019	Cylindrical external loop ALR	0 to 450	0.04 to 0.1	Pulse input of methyl-orange as a tracer	Down-comer and Riser	-	-	-	30 to 105	n.a.	• 30 to 105 (depending on the hydrodynamics conditions) equally sized perfectly stirred tanks were necessary to describe the ALR behavior • The ALR as a whole was found to be correctly modeled by the plug-flow reactor with axial dispersion	[151]

*Total air supply in the aerated part of the reactor: riser part for ALRs and membrane tank for MBRs; **n.a.**: not available data.

The RTD profiles in MBRs and ALRs are usually quite different, as it is possible to notice in Figure IV-2. The main difference can mainly be explained by the way the measurement is performed. A schematic illustration is proposed in Figure IV-3, and shows the differences in the injection and detection of tracers for MBRs (or ALMBRs) and ALRs.

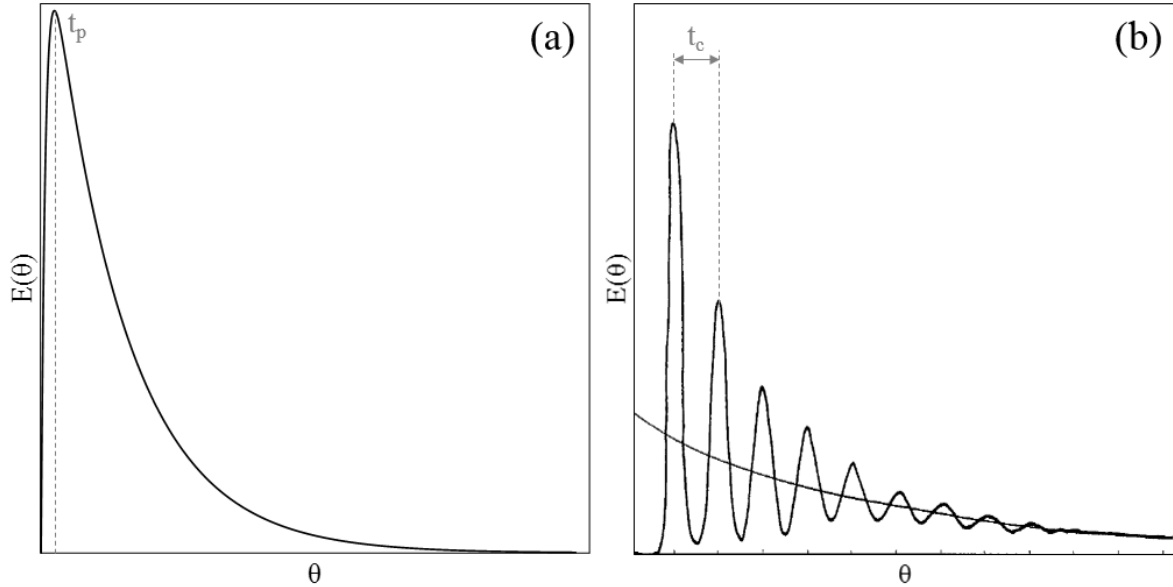


Figure IV-2 : Typical RTD profiles obtained as a response to a pulse injection in (a) MBRs, (b) ALRs [151].

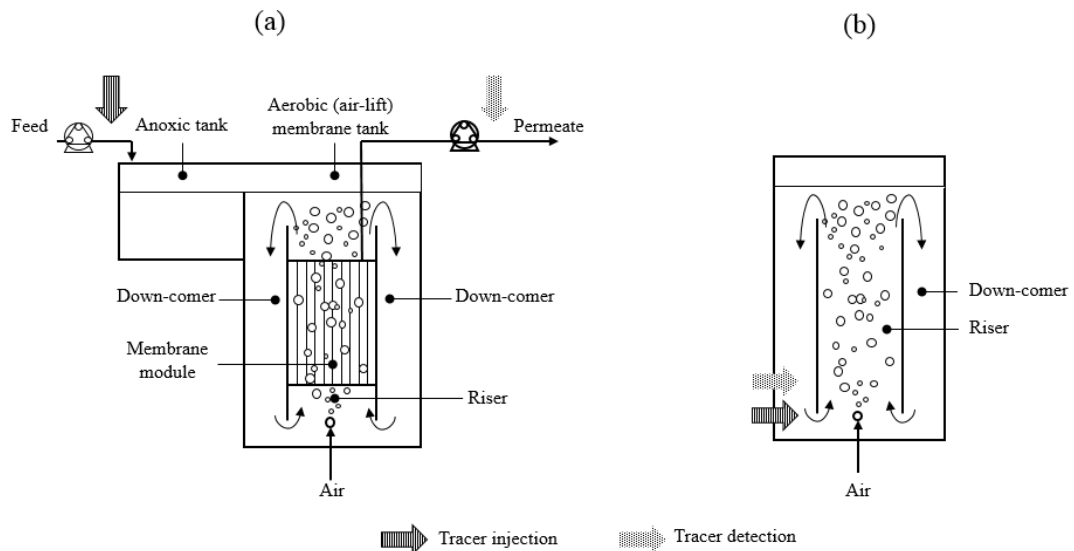


Figure IV-3 : RTD measurement in the case of (a) an MBR or an ALMBR (as in the present study) and (b) an ALR.

For **MBRs**, the typical RTD response to a pulse perturbation was reported to describe a more or less quick increase until reaching a peak, followed by a slow decrease towards the baseline, as presented in Figure IV-2(a).

In these studies, the time to reach the peak t_p (Figure IV-2(a)) was 2 to 50 times smaller than the theoretical hydraulic residence time τ (knowing that the total RTD measurement usually lasts at least 3τ , in order to allow the total tracer recovery), which confirms the similar shapes (early peak) of RTD curves reported for MBRs. In all these studies, the mean residence time μ was deduced to be compared to the theoretical hydraulic residence time τ , according to Equation IV-9. In all the cases, some discrepancies between the experimental and theoretical times were recorded.

Wang et al. (2009) [148] studied a bench-scale MBR (0.006 m^3) with two submerged HF modules placed in series in the direction of the flow (the lead membrane being the closest to the outlet). By measuring the tracer response from the two membranes, differences were observed at the beginning of the experiment and attributed to a short-circuiting from the inlet to the outlet. However, after 10 minutes of operations these differences were attenuated.

Wang et al. (2009) [148] also investigated a pilot-scale side-stream MBR (2.36 m^3), composed of an anoxic tank, an aerobic tank and a membrane tank. The tracer was in the anoxic tank and detected in the permeate. The presence of humps in the obtained RTD curve in the pilot-scale MBR was attributed to the existence of internal recirculation flow in the MBR, which means that a part of the tracer was internally recycled before leaving the reactor. For the different scales and types of MBRs investigated, Wang et al. (2009) [148] came to the conclusion that the considered reactors could be reasonably modeled by the completely mixed flow.

Wang et al. (2008) [149] studied pilot-plant HF and FS-MBR having a volume of 75 and 73.5 m^3 , respectively. The HF-MBR was composed of an anoxic tank and an aerobic membrane tank, whereas the FS-MBR comprised an anoxic tank, an aerobic tank and a membrane tank. For both MBRs, the tracer was injected in the feed of the reactors (anoxic tank) and its concentration measured in the permeate side. In the two cases, it was concluded that the reactors were relatively well-mixed. Even though the presence of humps at the beginning of the RTD curves were attributed to an internal recirculation phenomenon in both reactors, the overall behavior on the long-term was close to the completely mixed flow.

In most of these studies [148,149] (Table IV-2), the mean residence time was found to be lower than the theoretical residence time, which was attributed to the existence of dead volumes in the reactors, and further confirmed via the calculation of the effective volume of the reactor V_{eff} . This volume corresponds to the result of the subtraction of the dead volumes from the total volume, and was found

to be lower than the real volume (the dead volume represented 1 to 33 % of the working volume in these studies).

However, Brannock et al. (2010) [150] obtained for a side stream FS-MBR (1244 m³) with three compartments, experimental mean residence times that were higher than the theoretical hydraulic times, which was attributed to the existence of internal recycling phenomena.

Concerning the modeling of the flowing behavior in the MBRs presented in Table IV-2, both of the number of tanks-in-series and de dispersion number were calculated as model parameters, according to Equations IV-14 and IV-23, respectively. Based on these parameters, all the RTD studies conducted in MBRs concluded that the overall flowing behavior was much closer to a completely mixed reactor, rather than to a plug-flow. However, some deviations from the perfectly mixed flow were obtained and explained by the existence of dysfunctions. The reported studies investigated different operating conditions Table IV-2 in order to identify the optimal conditions allowing to minimize these discrepancies. Pollet et al. (2009) [103] showed in a cylindrical HF-MBR, that different behaviors can coexist: a plug-flow zone at the bottom of the MBR where the air is injected and the hollow fibers are still, and a completely mixed zone at the top of the MBR, where the coalescence of bubbles and the hollow fibers motion favor the mixing. Therefore, these results highlight the fact that the operating conditions as well as the membrane geometry and/or configuration, have significant impact on the overall long-term mixing and flowing performances of MBRs.

Concerning the **ALRs** in terms of long-term mixing performance, Gavrilescu and Tudose (1996) [151] conducted a similar experimental approach in a cylindrical external loop-ALR. The shape of the RTD profile was quite different from the one obtained in MBRs, and described a succession of peaks, of which the decreasing intensity was explained by the axial dispersion (Figure IV-2(b)). On the basis of the model parameters (N and $\frac{D}{uL}$), it was concluded in this study that the overall flowing behavior was closer to a plug-flow with axial dispersion, than to a completely mixed-flow. Also, the time between two peaks was pointed out as the circulation time.

To our best knowledge, no study characterizing the long-term mixing performance of ALMBRs via RTD analysis was reported in the literature to date. Thus, in the specific case of ALMBRs, it is still unknown whether the global flowing performance is closer to the completely mixed-flow or to the plug-flow.

In conclusion, these studies helped identifying the most frequently used models to describe the considered multiphase reactors:

- For MBRs, the completely mixed-flow was preferred over plug-flow in all the studies, whether the considered MBRs comprised several compartments or not.

- For ALRs, the plug-flow with dispersion was more relevant to describe the liquid flow in the recirculation loop characteristic of ALRs.

Also, the observed discrepancies between the experimental and the theoretical residence times were attributed to the presence of dysfunctions such as dead volumes and internal recycling. Lastly, concerning the effect of the operating conditions, Wang et al. (2009) [148] varied the air flowrate in a bench-scale HF-MBR (0.006 m^3) from 3.0 to $6.0 \text{ Nm}^3\cdot\text{h}^{-1}\cdot\text{m}^{-2}$ in terms of SADm, and obtained no significant difference in the RTD curves. The RTD curves obtained for the highest air flowrate reached its peak slightly (a few minutes over a 250 min experiment) earlier than that of the lowest air flowrate, which was attributed to enhance turbulence and hence, slightly quicker dispersion of the tracer molecules in the reactor.

IV.3. Materials and methods

IV.3.1. QQ-ALMBR operation

The considered ALMBR consisted in a reactor with a total volume of 18 L, comprising two tanks: an anoxic tank (mechanically stirred at 188 rpm) with a volume of 5 L, and an aerobic tank with a volume of 13 L, as presented in Chapter II. A flat sheet membrane was used as a filtration module and introduced in the aerobic tank, with two baffles on each side of it. The baffles were located 15 mm away from the membrane surface creating the air-lift configuration (with $D_r = 15 \text{ mm}$). Three different shapes (beads, hollow cylinders and sheets) of QQ media were used and introduced in the aerobic tank, under the exact same volume fraction of 0.45 % v/v, with respect to the volume of the aerobic tank. The ALMBR/QQ-ALMBR was run under the continuous mode (at a permeate flux of $15 \text{ L}\cdot\text{h}^{-1}\cdot\text{m}^{-2}$), and the rest of the operating conditions are gathered in Table IV-3. More details about the ALMBR operation and the QQ media properties are given in Chapter II.

Table IV-3 : Operating conditions for the ALMBR/QQ-ALMBR.

Air-lift	
Distance between the membrane and the baffle D_r (mm)	15
Total riser width $2D_r$ (mm)	30
Total down-comer width $2D_d$ (mm)	64
Total riser cross sectional area A_r (m ²)	0.0063
Total down-comer cross sectional area A_d (m ²)	0.01344
A_r/A_d ratio (-)	0.469
Liquid height h_D (m)	0.585
Superficial gas velocity in the riser (m.s ⁻¹)	0.0015 to 0.0051
MBR	
Feed flow (L.h ⁻¹)	1.5
Recirculation flow (L.h ⁻¹)	4.0
Filtration flux (LMH)	15
Theoretical residence time τ (h)	12
SADm (Nm ³ .h ⁻¹ .m ²)	0.35 to 1.15
QQ media	
Volume fraction (% v/v)	0.45
Total number (N_{TM}) of:	
Beads	2600
Hollow cylinders	298
Sheets	585

IV.3.2. *Mixing time measurement*

The mixing time was experimentally measured using a colorimetric method, together with image processing. A volume of 20 mL of a Rose Bengal Lactone (Sigma-Aldrich) solution at 0.4 g.L⁻¹ was injected at the top of the aerobic tank. A camera and a light panel were used for image acquisition, at the bottom of the aerobic tank (the observation window was selected to be as far as possible from the injection) (Figure IV-4(b)). Similarly to what was reported in the literature, the measurements were performed under the batch mode for the liquid phase (with no feed) and the continuous mode for the gas phase (continuous injection of air). The mixing time was only measured in the aerobic tank of the ALMBR, where a complex three-phase air-lift configuration takes place. The measurements were conducted under different air flowrates and with/without the addition of QQ media. Once the images were recorded, a Matlab (MathWorks, USA) program was used to process them and deduce the evolution of the light intensity overtime. Finally, the mixing time was defined as the time needed to reach 96 % of homogeneity (in terms of light intensity) in the bulk. More details about the experimental setup and the image/data processing are available in Chapter II.

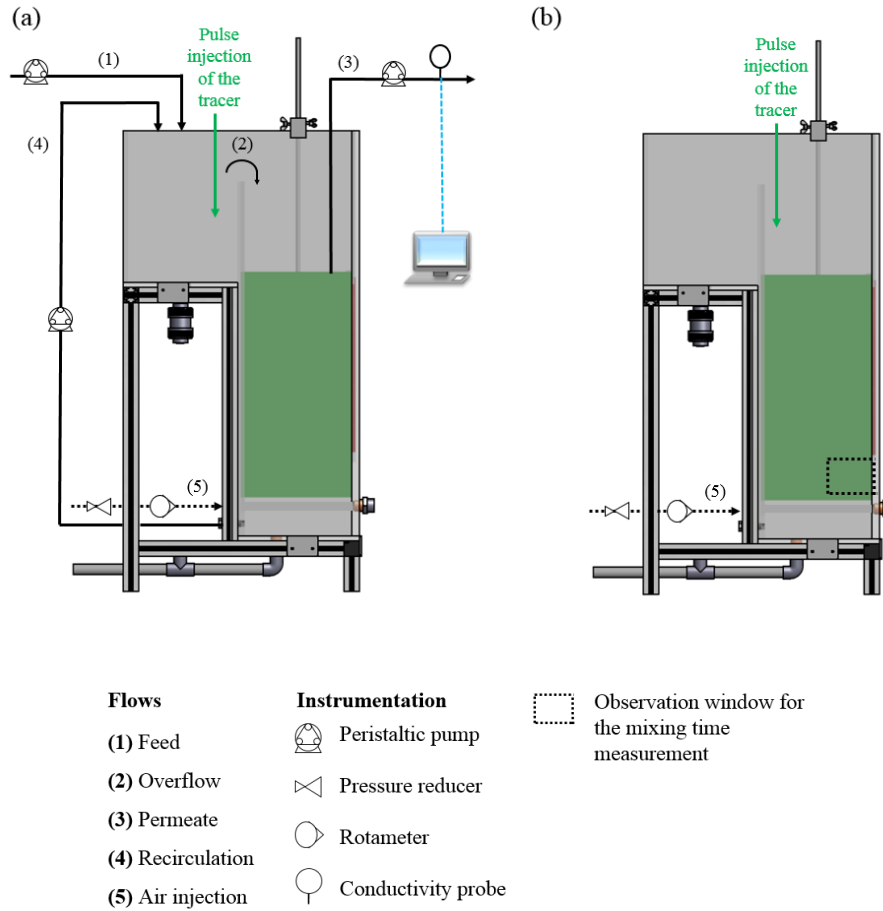


Figure IV-4 : Experimental setup for (a) the RTD measurement (b) the mixing time measurement.

IV.3.3. *RTD measurement*

In order to determine the RTD in the ALMBR/QQ-ALMBR, a conductivity method was used with a saturated salt solution (NaCl at 360 g.L^{-1}) as a tracer. 10 mL of the tracer solution were injected with a Dirac pulse injection in the feed of the reactor, and the variations of concentrations in the reactor were measured with a conductivity probe located in the permeate pipe (Figure IV-4(a)). The data were acquired via a monitoring software (AcquiChimie) connected to a computer. The whole RTD measurement lasted about 48 h for each condition. More details about the experimental setup and the signal analysis are given in Chapter II.

IV.3.4. Experimental procedure

The measurements were performed under different air flowrates in order to highlight the effect of the aeration on the mixing performance. For the mixing time measurement, the air flowrates varied from 0.35 to 1.15 $\text{Nm}^3\cdot\text{h}^{-1}\cdot\text{m}^{-2}$, in terms of SADm. For the RTD measurement three air flowrates were investigated: 0.75, 0.90 and 1.00 $\text{Nm}^3\cdot\text{h}^{-1}\cdot\text{m}^{-2}$, in terms of SADm. These conditions were selected because they were proved to be favorable for the QQ media fluidization (Chapter III). The same measurements were performed with and without QQ media, in order to identify their effect on the mixing performance.

IV.4. Results and discussion

IV.4.1. Characterization of the short-term mixing performance of the ALMBR/QQ-ALMBR

IV.4.1.1. Mixing time in the ALMBR: effect of the aeration

The mixing times obtained under different air flowrates are presented in Figure IV-5. The mixing times ranged between 61 and 23 s in the investigated range of air flowrates.

It can be noticed that the mixing time globally decreases with the air flowrate, which is a logical result, as the increase of aeration was clearly reported in the literature to promote mixing. The model proposed by Brando et al. (1998) [146] was tested according to Equation IV-3 and adjusting the constant K . However, the decrease of the experimental data does not exactly follow the power law proposed by Bando et al. (1998) [146], which can be attributed to the fact that the present ALMBR is rectangular, whereas, the correlation was defined for cylindrical draft-tube ALRs.

When observing the obtained experimental data, it actually appears that the mixing time is sensitive to the modification of aeration increase in the low range of air flowrates, whereas it seems to reach a constant value (around 27 s) in the higher range of air flowrates. Consequently, the existence of a critical air flowrate (comprised between 0.55 and 0.65 $\text{Nm}^3\cdot\text{h}^{-1}\cdot\text{m}^{-2}$ in terms of SADm, and between 0.0024 and 0.0029 $\text{m}\cdot\text{s}^{-1}$ in terms of superficial gas velocity in the riser) can be assumed, which is in accordance with what was reported by Sánchez Mirón et al. (2004) [142] and Freitas et al. (1998) [133] in draft-tube ALRs.

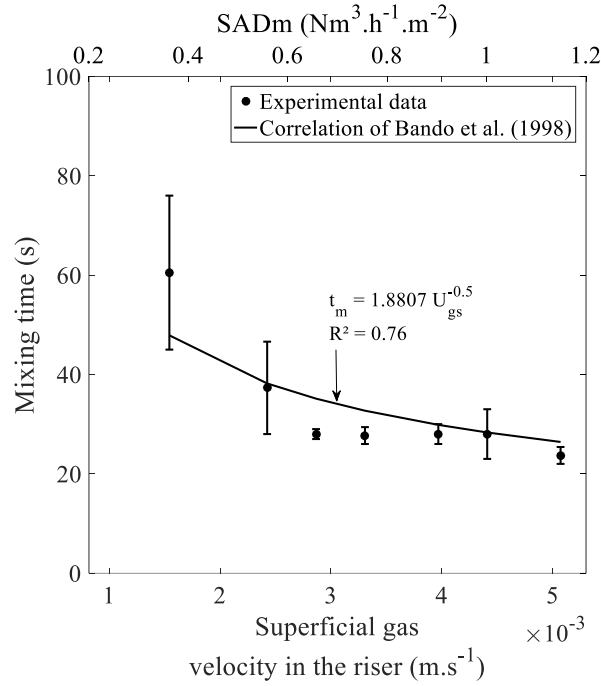


Figure IV-5 : Mixing time in the ALMBR under different air flowrates.

In addition to being in good agreement with order of magnitude and trend reported in the literature for the characterization of ALRs, MBRs and ALMBRs (Table IV-1), these findings indicate that within the investigated operating conditions, the short-term mixing performance of an ALMBR can be optimal for the critical air flowrate that has been identified. From the perspective of the MBR process, this is key-information because it indicates that very short-time (compared to the total residence time of the reactor) is needed for the bulk of the aerobic tank to be uniform. Also, reducing the heterogeneities in the membrane (aerobic) tank ensures a uniform filtration performance over the global membrane surface. Finally, running the process under the critical air flowrate can imply considerable energy savings for an optimal mixing performance.

IV.4.1.2. *Mixing and circulation times in the QQ-ALMBR*

IV.4.1.3. *III.4.1.2.1. Effect of the aeration*

The mixing times in presence of QQ media were measured under three different flowrates of the high range, for which the mixing in the ALMBR was demonstrated to be unaffected. Also, a circulation time could be measured in presence of QQ media, by visually tracking one single QQ particle at the time in the airlift and measuring the time needed for it to achieve a complete loop. The results are gathered in

Table IV-4. It is possible to notice that the increase of the air flowrate from 0.75 to 1.00 Nm³.h⁻¹.m⁻², induces lower mixing and circulation times in presence of QQ media in the ALMBR, whereas it did not significantly affect the mixing time in the ALMBR (around 27 s above 0.55 Nm³.h⁻¹.m⁻²). The observation of the dimensionless times indicates that 3 to 4 loops in total are necessary to reach the

complete homogeneity of the bulk, depending on the operating conditions, which is consistent with the results reported in the literature (Table IV-1).

As a simplified approach, the circulation time was measured by tracking QQ media, making the assumption that the QQ media circulate at the same velocity as the liquid in the ALMBR. The comparison of the QQ media velocity and the liquid velocity will be more deeply discussed in Chapter VI.

Table IV-4 : Average mixing and circulation times measured in the QQ-ALMBR.

	QQ beads			QQ hollow cylinders			QQ sheets		
SADm (Nm ³ .h ⁻¹ .m ⁻²)	0.75	0.90	1.00	0.75	0.90	1.00	0.75	0.90	1.00
Mixing time t_m (s)	27.0	26.0	22.0	22.7	19.3	18.7	23.3	29.0	23.3
Circulation time t_c (s)	9.8	8.5	7.2	9.1	8.2	7.2	10.8	9.6	7.1
Dimensionless time θ_m (-) (from Equation IV-2)	3	4	4	3	3	3	3	4	4

IV.4.1.4. Effect of the addition of QQ media

In order to highlight the effect of the addition of QQ media, the mixing times obtained in the ALMBR and the QQ-ALMBR are presented in Figure IV-6. The results reveal that the addition of QQ media induces similar or slightly lower mixing times, compared to the ones obtained in the ALMBR. As an example, when the air flowrate is set to 0.75 Nm³.h⁻¹.m⁻², the mixing times are up to 18 % lower in the QQ-ALMBR than in the ALMBR. When the air flowrate is increased by 33 % and reaches 1.00 Nm³.h⁻¹.m⁻², the mixing times in the QQ-ALMBR are about 15 to 35 % lower than in the ALMBR. In addition, it can be noticed that the mixing times obtained in presence of QQ hollow cylinders are always lower than the ones with the two other shapes.

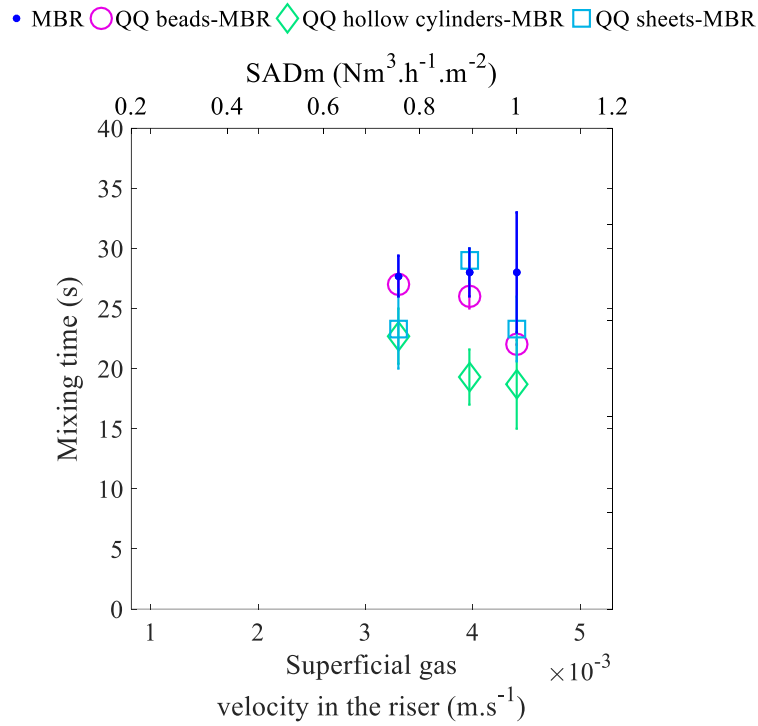


Figure IV-6 : Mixing time in the QQ-ALMBR under different air flowrates.

The reduction of the mixing time in presence of QQ media under high air flowrates can be explained by the creation of secondary circulation phenomena by the suspended QQ media. The QQ media improve the overall mixing, especially under high air flowrates, by enhancing the axial dispersion, which is one of the main mechanisms involved in the short-term mixing.

From the process perspective, the main conclusions to keep in mind are that the addition of QQ media does definitely not affect the optimal mixing time of 27 ± 5 s that was previously identified in the ALMBR, under the critical air flowrate comprised between 0.55 and 0.65 $\text{Nm}^3.\text{h}^{-1}.\text{m}^{-2}$. Besides, it is possible to improve the short-term mixing performance of the ALMBR by adding QQ media under higher air flowrate. For the MBR process, that means that the mixed liquor can be considered as instantaneously and uniformly distributed in the reactor, providing uniform biodegradation efficiency, and preventing heterogeneities that could, for example, induce localized fouling and thus, non-uniform membrane performance.

IV.4.1.5. Concluding remarks on the short-term mixing performance of the ALMBR/QQ-ALMBR

The characterization of the short-term mixing performance of the ALMBR/QQ-ALMBR allowed drawing the following key-conclusions:

- The measurement of the mixing and circulation times was relevant to characterize the short-term mixing performance, and the results and trends were in good accordance with the expectations and the literature.
- In all the investigated cases (different aeration intensities, presence or not of QQ media) the mixing times were found to be lower than 80 s, which is 540 times smaller than the total (anoxic + aerobic) hydraulic residence time ($\tau = 12$ h) of the reactor when it operates under its continuous mode. Therefore, given this result, and according to usual bio-kinetics, it is largely reasonable to consider the aerobic part of the ALMBR as a completely mixed reactor at the long-term operation.
- The short-term mixing performance can still be slightly improved by adding QQ media (especially QQ hollow cylinders) and by increasing the air flowrate. This can be correlated with the results previously obtained (Chapter III), indicating that the increase of the air flowrate results in an increase of the fluidization rate of QQ media. The QQ media being more significantly fluidized create local vortices in their passage improving the overall mixing [133]. In these conditions, the energy consumption at the process-scale would be heightened, but could possibly be balanced by other benefits of the QQ media, in particular fouling mitigation.
- These results suggest that the mixing time could be reduced with QQ media and by increasing the aeration (up to the crucial air flowrate), however, It would be interesting to compare the mixing time to other characteristic times of the process (such as mass transfer time, biodegradation reaction time, QQ enzymatic reaction time, microbial growth time) in order to assess whether the improvement of the short-term mixing could be beneficial for the whole process or not (further discussed in Chapter VI).

IV.4.2. Characterization of the long-term mixing performance of the ALMBR/QQ-ALMBR

IV.4.2.1. RTD analysis of the ALMBR

The whole RTD measurement lasted about 72 h, whereas the theoretical residence time (τ) under the continuous operation mode was worth 12 h, which results in a total duration of 6τ for the RTD experiment. The normalized RTD curves $E(\theta)$ are presented in Figure IV-7.

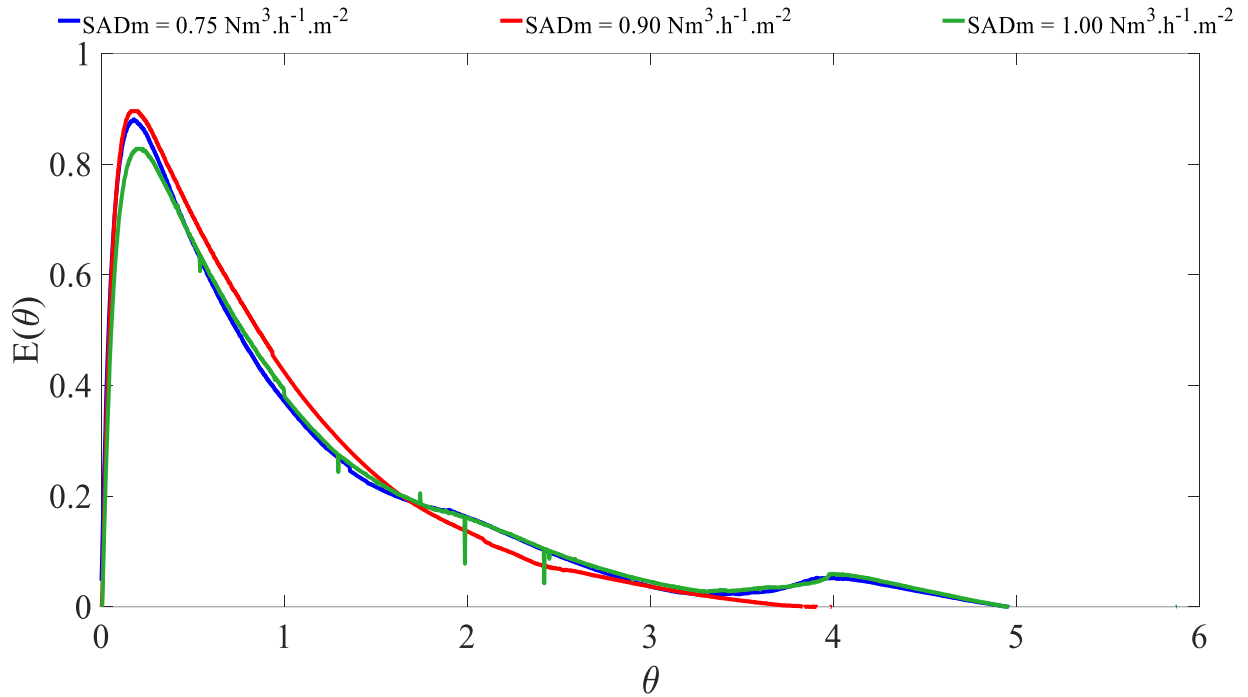


Figure IV-7: Experimental RTD curves obtained in the ALMBR under different air flowrates.

All the RTD curves obtained in the ALMBR describe the same overall shape, characterized by a quick increase in the first hours of the operation until reaching a peak (maximum), followed by a slow decrease towards the baseline. The global shape of the RTD curves is very similar to the typical RTD profiles reported in Table IV-2 for MBRs with several compartments as in our case (anoxic, aerobic), under the continuous mode, and with either hollow fibers or flat sheet membranes (Figure IV-2(a)). These typical “left-skewed” RTD curves were presented as reasonably good flow in the literature, although a more careful analysis of the RTD parameters could reveal some dysfunctions.

In some curves, it is possible to notice the presence of 2θ-periodic waves (1 day-periodic waves) which could be attributed to the temperature variations (day/night) which have an influence on the conductivity of water but was unavoidable given that the experimental setup did not allow the temperature control.

IV.4.2.1.1. RTD parameters of the ALMBR

Several criteria can be selected for the RTD analysis: on the one hand, the previously defined RTD parameters (IV.2.3.2) which are the commonly used tools for the RTD analysis; and on the other hand, more specific criteria that were selected in keeping with the obtained profiles of the present study. All the criteria are gathered in Table IV-5 and will be further analyzed to identify the effect of the operating conditions on the long-term mixing performance of the ALMBR/QQ-ALMBR.

Table IV-5 : Qualitative and quantitative criteria for the RTD analysis.

Category	Parameter	Meaning
General observation of the RTD curves		Shape
		Position
Common RTD parameters	μ	Mean residence time (Equation IV-9): represents the mean of the distribution
	σ^2	Variance (Equation IV-10): indicates the spread of the distribution
Specific RTD parameters	t_p	Time by which the maximum (the peak) is reached
	f_p	Fraction of material younger than the age t_p , defined as follows: $f_p = \int_0^{t_p} E(t)dt = \int_0^{\theta_p} E(\theta)d\theta$
	t_{50}	Time to recover 50 % of the tracer

The RTD parameters deduced from the experiments are presented in Table IV-6.

Table IV-6 : RTD parameters calculated from the experimental results for the ALMBR.

RTD parameters	SADm (Nm ³ .h ⁻¹ .m ⁻²)		
	0.75	0.90	1.00
μ (h)	12.1	10.6	12.6
σ^2 (h ²)	113.3	73.0	117.0
t_p (h)	2.1	2.2	2.5
f_p (%)	11.9	12.0	12.6
t_{50} (h)	8.3	8.5	8.5

For the three air flowrates, the mean residence time μ was found to be worth 11.8 h on average, corresponding to an average deviation of ± 6 % from the theoretical residence time of the reactor ($\tau = 12$ h). The deviation can be considered acceptable when comparing to the studies that have been reported in MBRs (Table IV-2) reporting a discrepancy ranging between 0 and 24 % between the experimental and theoretical residence times. When observing the variance σ^2 , the values range approximately between 70 and 120 h² which is relatively high, indicating that the dispersion around the mean residence time is not negligible and thus, that the considered MBR does not have a perfectly ideal behavior. Concerning, the time to reach the maximum t_p , it is on average 2.3 h corresponding to less than 1/5th of the theoretical residence time τ , which is comprised in the range that has been identified in the literature, where t_p was found to be 2 to 50 times smaller than the theoretical residence time (Table IV-2). At this time t_p , around 12 % of the total amount of the tracer is released, whereas 50 % of the tracer need 8.3 to 8.5 h (t_{50}) to be released, under the three flowrates.

The effect of the air flowrate on the RTD parameters of the ALMBR will be further discussed in III.4.2.1.3, after application of the RTD models.

As a conclusion, the RTD parameters are globally consistent with the trends reported in the studies presented in Table IV-2 [148–150], for various MBRs (multi-compartment or not) at different scales (from 0.006 to 1244 m³). This result is actually key-information at several levels: firstly, it validates the RTD measurement technique and its reliability to describe the long-term mixing performance of the ALMBR. Also, it reveals the correct operation of the considered ALMBR. Lastly, it demonstrates the relevance of selecting the RTD parameters as tools for further RTD analysis, since it can indicate phenomena such the homogeneity of the mixing and lateness/earliness of mixing.

IV.4.2.1.2. Modelling of the ALMBR

IV.4.2.1.2.1. Application of the usual models

The ALMBR, as it was presented in the material and methods section, is composed of two tanks in series with different volumes and a recirculation (recycling) flow from the second tank to the first one. Thus, on the basis of the geometry of the ALMBR, the relevance of some of the usual models presented in the IV.2.3.3 was examined. The detailed application of the usual models is reported in Appendix A-IV-1, but the resulting curves for the different models are presented in Figure IV-8.

The tanks-in-series model was tested (red curves in Figure IV-8) but was found not to be suitable because it is based on the succession of two identical tanks, when the considered ALMBR is actually composed of different compartments in series (anoxic tank and aerobic tank) of different volumes with a recirculation between the two compartments.

In order to take into account the recirculation from the aerobic tank to the anoxic tank, the model of two tanks-in-series with back-mixing was applied (pink curve in Figure IV-8), but again found to be non-adequate to describe the ALMBR, since it is based on the hypothesis of two identical tanks-in-series.

The model of two tanks-in-series with different volumes was evaluated for the ALMBR under an SADm of 0.75 Nm³.h⁻¹.m⁻² (for which the condition $\mu = \tau$ to apply the model was verified) (green curve in Figure IV-8). In this case the model was not accurate to describe the ALMBR either because the ratio of volumes α was calculated according to the Equation IV-17 and found to be 3.5 (indicating that the first tank is 3.5 times greater than the second one), which is not in accordance with the actual geometry of the ALMBR.

Finally, the model of completely mixed reactor with dead zones and short-circuiting was applied by determining the two parameters of the model m and n , using Equations 11. Using these parameters, the theoretical RTD functions were determined (blue curves in Figure IV-8). It appears that this model is not suitable either to describe the behavior of the ALMBR

In conclusion, the application of the usual models reveals that neither of them is completely adequate to correctly model the behavior of the ALMBR under the three considered air flowrates. This finding can be explained by the fact that the models are relatively simple models taking into account one

phenomenon at the time (dysfunction, recycling flow, tanks-in-series), when the ALMBR addressed in the present study is in reality a more complex combination of all of these phenomena. Additionally, the dispersion model was also tried and did not result in a good model of the ALMBR which is, besides, in accordance with what was reported in the literature about MBRs being closer to completely mixed reactors. Therefore, it is possible to conclude that a more complete model is needed in order to describe the flowing behavior of the ALMBR.

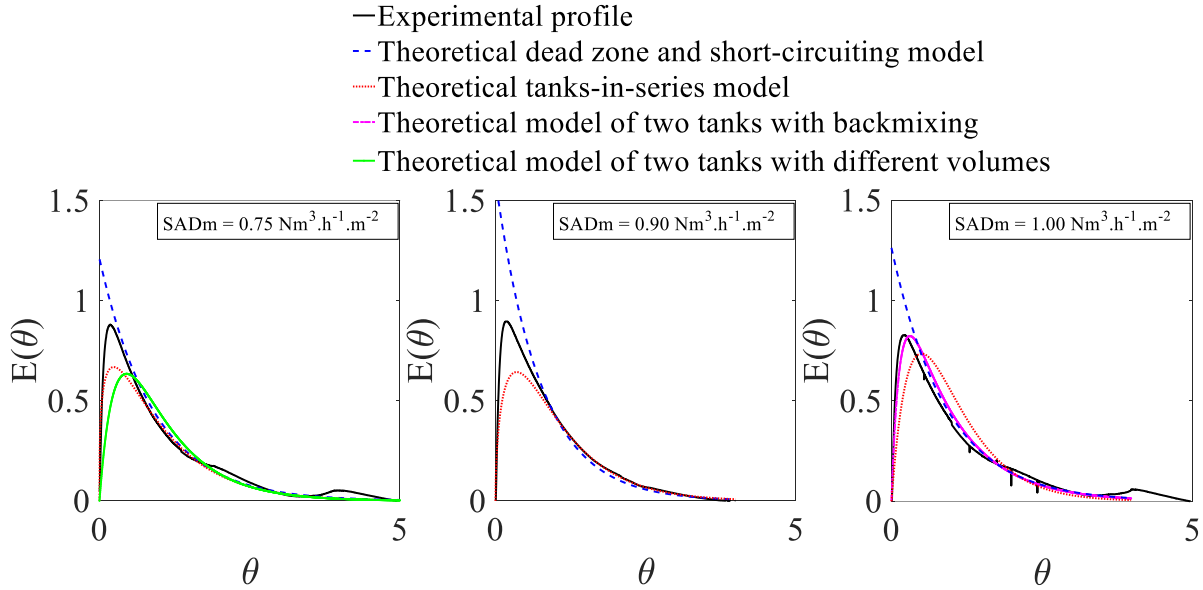


Figure IV-8 : Usual models applied to the ALMBR under different air flowrates.

IV.4.2.1.2.2. Development and application of a specific model for the ALMBR

In order to better describe the MBR, a specific model was defined based on the real geometry of the reactor, taking into account the two compartments (anoxic and aerobic tanks) of the ALMBR and considering them as two stirred reactors in series with different volumes. This assumption was made on the basis of:

- The short-term mixing performance in which it was demonstrated that less than 80 s were necessary to mix the bulk in the aerobic tank, which is very small (540 times smaller) compared to the theoretical hydraulic time ($\tau = 12$ h) of the ALMBR.
- The analysis of the literature, since the studies reported in Table IV-2 concluded that the considered MBRs were completely mixed reactors [148–150].

Therefore, the model is based on a first tank of 5 L, corresponding to the mechanically stirred anoxic tank, and a second tank of 13 L, corresponding to the membrane tank, as described in Figure IV-9. Because the mixing in the membrane tank is actually ensured by aeration (not mechanical) creating a

particular configuration, and that the QQ media are only added in it, dysfunctions such as dead volumes can potentially be taken into account in the stirred tank model, as described in Figure IV-9.

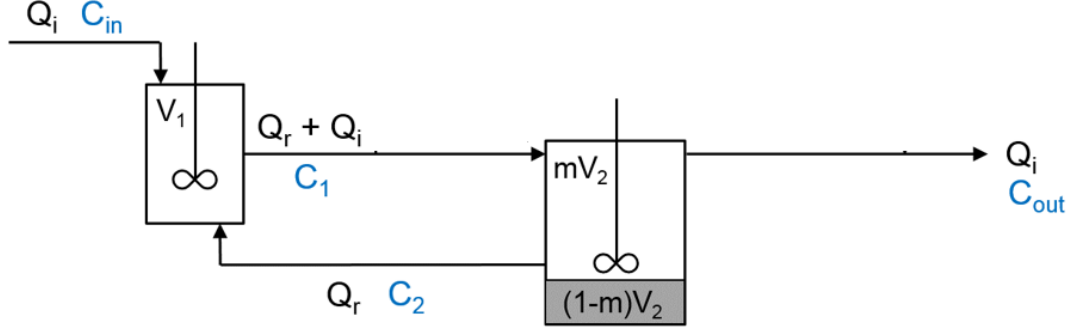


Figure IV-9 : Scheme of the modelling of the reactor as two stirred tanks-in-series with different volumes, with a recirculation between the two tanks and potential dead zones.

In Figure IV-9, C_{in} , C_1 , C_2 and C_{out} are the concentrations of tracer in the feed, in the first tank, in the second tank, and in the permeate, respectively. V_1 , V_2 are the total volumes of the first and second tanks, respectively. The parameter m indicates the fractions of the effective volume in the second tank. The determination of this parameter indicates the extent of the dysfunctions in the MBR.

In order to deduce the theoretical RTD function corresponding to this specific model, the mass balance in each tank has to be written first according to Equations IV-25 and IV-26.

$$\frac{dC_1 V_1}{dt} = Q_r C_2 - (Q_r + Q_i) C_1 + Q_i C_{in} \quad \text{IV-25}$$

$$\frac{dC_2 (mV_2)}{dt} = (Q_r + Q_i) (C_1 - C_2) \quad \text{IV-26}$$

Since the volume of each tank is kept constant during the operation, the only varying parameter (overtime) is the concentration, which leads to the Equations IV-27 and IV-28.

$$\frac{dC_1}{dt} = \frac{1}{V_1} [Q_r C_2 - (Q_r + Q_i) C_1 + Q_i C_{in}] \quad \text{IV-27}$$

$$\frac{dC_2}{dt} = \frac{1}{mV_2} [(Q_r + Q_i) (C_1 - C_2)] \quad \text{IV-28}$$

The time step Δt with which the measurements were done was constant and relatively small (2 min) with respect to the total duration of the experiment, therefore, allowing the discretization of the previous equations to obtain Equations IV-29 and IV-30.

$$\frac{\Delta C_1}{\Delta t} = \frac{C_1(t + \Delta t) - C_1(t)}{\Delta t} = \frac{1}{V_1} [Q_r C_2(t) - (Q_r + Q_i) C_1(t) + Q_i C_{in}(t)] \quad \text{IV-29}$$

$$\frac{\Delta C_2}{\Delta t} = \frac{C_2(t + \Delta t) - C_2(t)}{\Delta t} = \frac{1}{mV_2} [(Q_r + Q_i)(C_1(t) - C_2(t))] \quad \text{IV-30}$$

Therefore, the concentrations in the two tanks are respectively expressed as in Equations IV-31 and IV-32.

$$C_1(t + \Delta t) = C_1(t) + \frac{\Delta t}{V_1} [Q_r C_2(t) - (Q_r + Q_i) C_1(t) + Q_i C_{in}(t)] \quad \text{IV-31}$$

$$C_2(t + \Delta t) = C_2(t) + \frac{\Delta t}{mV_2} [(Q_r + Q_i)(C_1(t) - C_2(t))] \quad \text{IV-32}$$

Finally, the concentration in the permeate side $C_{out}(t)$ is supposed to be equal to the one from the second tank $C_2(t)$ (Equation IV-33).

$$C_{out}(t) = C_2(t) \quad \text{IV-33}$$

A theoretical RTD function $E_{th}(t)$ can then be deduced according the Equation IV-34.

$$E_{th}(t) = \frac{C_{out}(t)}{\frac{1}{\tau} \int_0^\infty C_{out}(t) dt} \quad \text{IV-34}$$

This theoretical RTD function was compared to the experimental RTD profiles obtained under the three investigated air flowrates in Figure IV-10.

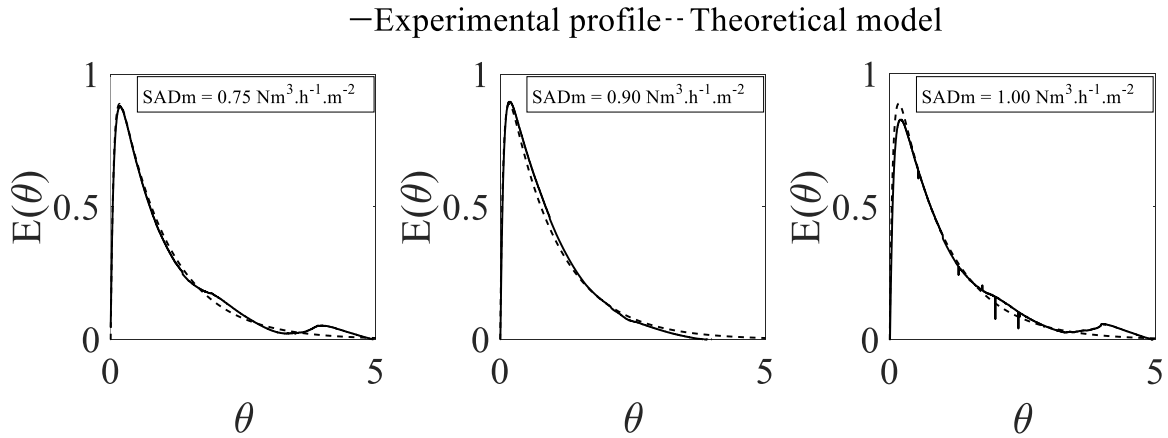


Figure IV-10 : Specific theoretical model with $m = 1$ applied to the ALMBR under different air flowrates.

It seems that the specific model correctly describes the circulation performance of the MBR for the three considered air flowrates, since the visual comparison indicates minimal discrepancies between the experimental and the theoretical profiles (Figure IV-10). These discrepancies were quantified by calculating the average vertical gap between the two profiles as in Equation IV-35, where p is the number of experimental points (more details available in Appendix A-IV-2). This average gap was further used as the criterion to minimize by adjusting the parameter m of the model, and thus quantifying the potential dead volumes in the ALMBR.

$$\text{Average } |E_{th}(\theta) - E_{exp}(\theta)| = \frac{\sum_{i=1}^p |E_{th}(\theta_i) - E_{exp}(\theta_i)|}{p} \quad \text{IV-35}$$

The optimized parameters are gathered in Table IV-7. The parameter m was found to equal 1, which refers to no significant dead zones in the aerobic tank of the ALMBR under the three air flowrates.

Table IV-7 : Optimized m parameter for the specific theoretical model applied to the ALMBR under different air flowrates.

Specific model parameters	SADm ($\text{Nm}^3 \cdot \text{h}^{-1} \cdot \text{m}^{-2}$)		
	0.75	0.90	1.00
m	1	1	1
Average $ E_{th}(\theta) - E_{exp}(\theta) $	0.015	0.014	0.017

In sum, the definition of a specific model, based on the real geometry and operation of the reactor turned out to be indispensable for the ALMBR modelling. The model based on two completely stirred reactors in series was found to give a good description of the MBR behavior, since insignificant discrepancies were observed between the experimental and theoretical RTD profiles. For the three investigated

flowrates, no significant dysfunctions (dead volumes) were identified, which corroborates the fact that the aerobic tank can be considered as a stirred reactor at the long-term level.

IV.4.2.1.3. Effect of the air flowrate on the long-term mixing performance of the ALMBR

After characterizing the long-term mixing performance of the ALMBR via the RTD analysis and the development of a specific model, the effect of the air flowrate will be here discussed.

Firstly, from the general observation of the RTD profiles (Figure IV-7), it is possible to notice that the shape of the curves is quite similar whatever is the air flowrate, indicating no significant effect of the air flowrate (in the studied range) on the overall behavior in the reactor. Also, the three curves are quite close one to each other and only slight discrepancies (less than 5 % on average) can be noticed, which is not significant, considering the confidence range defined in the reproducibility of the measurement technique (2 % on average in Chapter II).

When observing the RTD parameters determined in the ALMBR for the three air flowrates (Table IV-6), it appears that the mean residence time μ was found to be close to the theoretical hydraulic retention time τ under the SADm of 0.75 and 1.00 $\text{Nm}^3\cdot\text{h}^{-1}\cdot\text{m}^{-2}$, reaching respectively 12.1 and 12.6 h. Under the SADm of 0.90 $\text{Nm}^3\cdot\text{h}^{-1}\cdot\text{m}^{-2}$, the mean residence time μ was lower and only worth 10.6 h. Under the SADm of 0.90 $\text{Nm}^3\cdot\text{h}^{-1}\cdot\text{m}^{-2}$, a relatively lower variance σ^2 is obtained though compared to the two other air flowrates, indicating a slightly tighter distribution around the mean residence time. In addition, no substantial discrepancies are noticed in the specific RTD parameters, since under the three considered air flowrates, the time to reach the peak t_p is around 2.3 ± 0.2 h, the fraction of fluid f_p released at that time is around 12.2 ± 0.4 %, and the time t_{50} necessary for 50 % of the fluid to leave the reactor is around 8.4 ± 0.1 h, indicating that the circulation performance in the ALMBR under the investigated range of air flowrates, does not depend on the aeration intensity.

Concerning the specific model that was developed and applied to the ALMBR under the three air flowrates, it appears that a slightly greater difference between the theoretical and experimental functions (Table IV-7) was obtained under the air flowrate of 1.00 $\text{Nm}^3\cdot\text{h}^{-1}\cdot\text{m}^{-2}$, and may be attributed to experimental errors.

In conclusion, the air flowrate, in the selected range, has minimal effect on the RTD in terms of shape and position of the curves, as well as in terms of specific RTD parameters (t_p , f_p , and t_{50}) and modelling of the reactor performance. As a matter of fact, the experimental study about the RTD of a bench-scale HF-MBR conducted by Wang et al. (2009) [148] reported little impact of the air flowrate of the overall flow behavior, which is in good accordance with the observations in the present study. Besides, these observations are consistent with the mixing time results, confirming that, above 0.75 $\text{Nm}^3\cdot\text{h}^{-1}\cdot\text{m}^{-2}$, the air flowrate makes no much difference in the overall mixing performance of the ALMBR, at both the short-term and long-term levels.

IV.4.2.2. *RTD analysis of the QQ-ALMBR*

IV.4.2.2.1. *RTD parameters of the QQ-ALMBR*

The RTD curves obtained in presence of QQ media are presented in Figure IV-11 for different air flowrates. The global shape is the same as the one obtained in the simple ALMBR, which was itself comparable to what was reported in the literature for MBRs (studies presented in Table IV-2). The same RTD parameters as for the ALMBR were deduced from the RTD curves and gathered in Table IV-8.

In Figure IV-11, it seems that the shape is globally unaffected in presence of QQ beads and QQ hollow cylinders in comparison to the ALMBR. However, in presence of QQ sheets, it appears that the shape of the RTD profiles is substantially modified, since more rounded (less sharp) peaks are obtained under the three air flowrates. Also, in terms of position, again the more significant effect is noticed in presence of QQ sheets, with RTD profiles that are shifted to the right compared to the ones obtained in the ALMBR, which refers to a delay in the release of tracer in the permeate, and thus a less efficient mixing.

Table IV-8 : RTD parameters calculated for the ALMBR/QQ-ALMBR.

RTD parameters	SADm (Nm ³ .h ⁻¹ .m ⁻²)											
	0.75	0.90	1.00	0.75	0.90	1.00	0.75	0.90	1.00	0.75	0.90	1.00
	ALMBR			QQ beads- ALMBR			QQ hollow cylinders- ALMBR			QQ sheets- ALMBR		
μ (h)	12.1	10.6	12.6	9.6	11.4	15.1	9.3	11.6	11.5	10.3	12.6	14.3
σ^2 (h ²)	113.3	73.0	117.0	54.4	89.9	136.0	45.3	54.4	84.6	54.5	85.2	142.5
t_p (h)	2.1	2.2	2.5	2.3	2.4	2.2	2.3	2.2	2.5	4.4	4.3	4.0
f_p (%)	11.9	12.0	12.6	12.6	11.8	9.6	14.3	11.5	11.8	20.6	20.0	17.1
t_{50} (h)	8.3	8.5	8.5	7.6	8.5	10.2	7.4	8.7	9.0	8.6	9.1	10.0

In all the cases, the mean residence time μ was not exactly equal to the theoretical residence time τ , with up to 25 % deviation, which is acceptable when comparing to the literature, where differences up to 30 % between the theoretical and experimental residence time were found and attributed to dysfunctions in the reactor (Table IV-2). The variances σ^2 ranged approximately between 50 and 150 h², which is the same order of magnitude of the ones obtained in the ALMBR. Concerning the time to reach the peak t_p , depending on the considered case, it represented 1/5th to 1/3rd of the theoretical residence time, which is again in accordance with the literature (Table IV-2). At the time t_p , 12 to 20 % of the tracer was released depending on the cases, and the time t_{50} needed for 50 % of the tracer ranged between 7 and 10 h under the different conditions, which represents about half to 5/6th of the theoretical residence time.

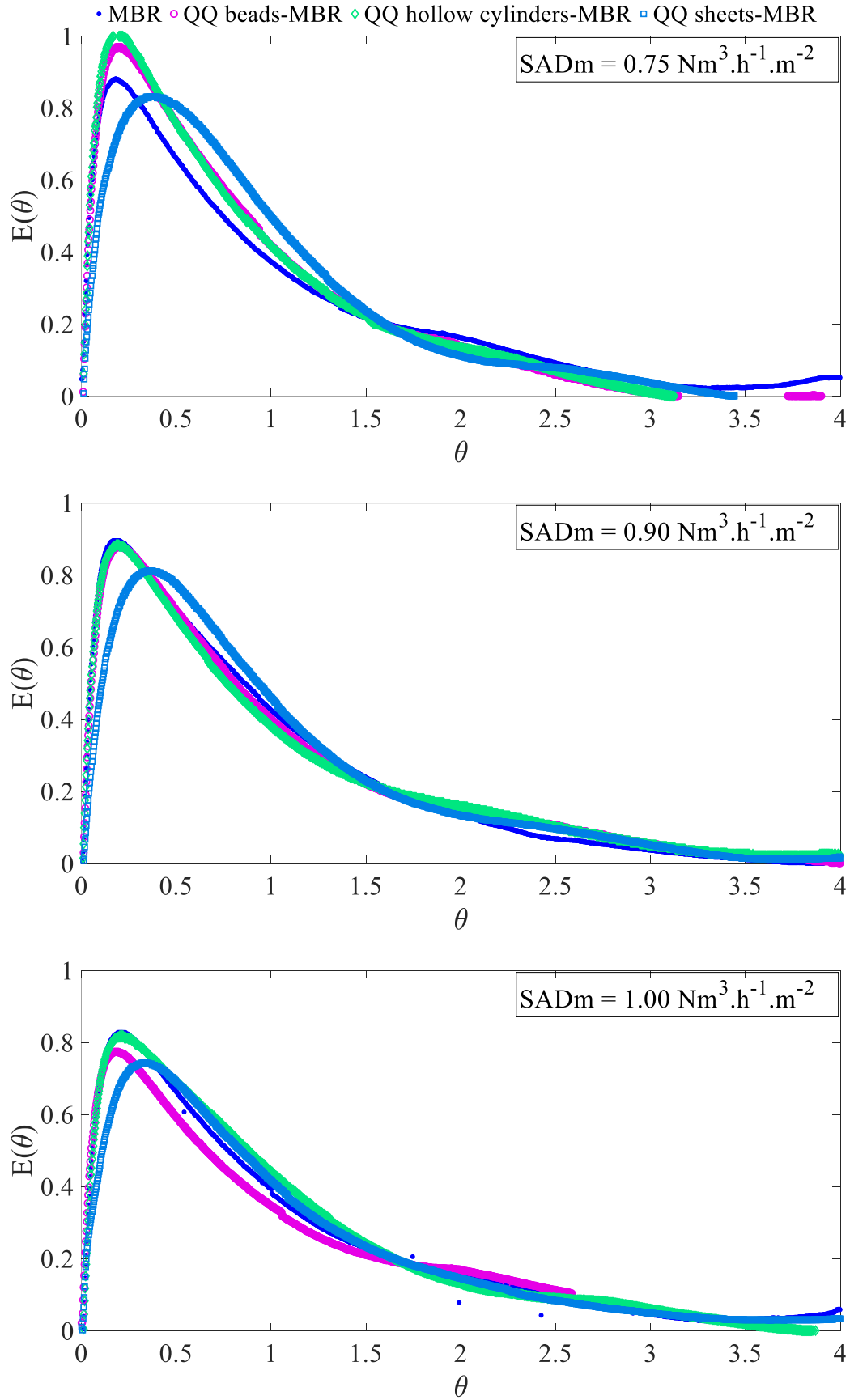


Figure IV-11 : Experimental RTD curves obtained in the ALMBR/ QQ-ALMBRs under different air flowrates.

Concerning the RTD parameters, it can be seen that the mean residence time is affected in presence of QQ media (Table IV-8), but in different ways depending on the aeration conditions and the QQ media shape. As an example, the mean residence time appears to be reduced in presence of QQ media under the lower SADm of $0.75 \text{ Nm}^3 \cdot \text{h}^{-1} \cdot \text{m}^{-2}$, whereas, it is increased in presence of QQ media under the SADm of $0.90 \text{ Nm}^3 \cdot \text{h}^{-1} \cdot \text{m}^{-2}$. The variance is modified as well in presence of QQ media, describing different trends depending on the air flowrate and the shape of the QQ media. The observation of the peak reveals that the time to reach it was almost kept unchanged when QQ beads and QQ hollow cylinders were added to the ALMBR, with approximately a $\pm 10 \%$ variation. In contrast, when QQ sheets were implemented into the ALMBR, the time to reach the peak was significantly affected with up to a two-fold increase under the SADm of 0.75 and $0.90 \text{ Nm}^3 \cdot \text{h}^{-1} \cdot \text{m}^{-2}$, which again highlights the lateness of mixing induced by the QQ sheets. When this time t_p is reached in presence of QQ media in the ALMBR, the fraction of tracer f_p that is released is also affected in different ways depending on the air flowrate and the shape of the QQ media. In presence of QQ sheets, this fraction seems to be always greater than in the ALMBR. Lastly, the time t_{50} is also modified when QQ media are added in the MBR. These results indicate that the presence of QQ media seems to modify the mixing and flowing performances of the ALMBR, but to different extents depending on the operating conditions and the QQ media shape.

In conclusion, the RTD parameters reveal the non-ideality of the considered QQ-ALMBRs, in terms of mixing and flowing behavior, considering the deviation to the theoretical hydraulic residence time. The dysfunctions leading to the non-ideality of the QQ-ALMBR will be determined more accurately thanks to reactor modeling, but these parameters suggest already that the QQ media may slow down the global homogenization in the ALMBR, in particular with the QQ sheets.

IV.4.2.2.2. *Modelling of the QQ-ALMBR*

- *Application of the theoretical specific model with $m = 1$*

The specific model previously obtained was applied first applied to the QQ-ALMBRs with the same parameter ($m = 1$) as for the ALMBR, since it was demonstrated to correctly describe the mixing and flowing behavior of the ALMBR (Figure IV-12). When visually comparing the theoretical and experimental RTD curves, it seems that discrepancies are obtained in some cases. These discrepancies were quantified in terms of average value of $|E_{th}(\theta) - E_{exp}(\theta)|$ and gathered in Table IV-9, where $E_{th}(\theta)$ is be the theoretical specific model applied with $m = 1$.

Table IV-9: Discrepancies between the experimental RTD curve and the specific theoretical model applied to the QQ-ALMBRs under different air flowrates (with $m = 1$).

Specific model parameters	SADm (Nm ³ .h ⁻¹ .m ⁻²)											
	0.75	0.90	1.00	0.75	0.90	1.00	0.75	0.90	1.00	0.75	0.90	1.00
	ALMBR			QQ beads-ALMBR			QQ hollow cylinders-ALMBR			QQ sheets-ALMBR		
Average $ E_{th}(\theta) - E_{exp}(\theta) $	0.015	0.014	0.017	0.032	0.015	0.041	0.034	0.013	0.023	0.053	0.039	0.026

It appears that the deviation between experimental and theoretical RTD functions is, in some cases, more than 3 times greater than the one obtained in the ALMBR, which makes it non-negligible. In particular, it seems that the biggest gaps between the model and the experiment is obtained in presence of QQ sheets. Also, when looking at the curves (Figure IV-12), it seems that the biggest discrepancies are noticed under the highest SADm of the considered range (1.00 Nm³.h⁻¹.m⁻²).

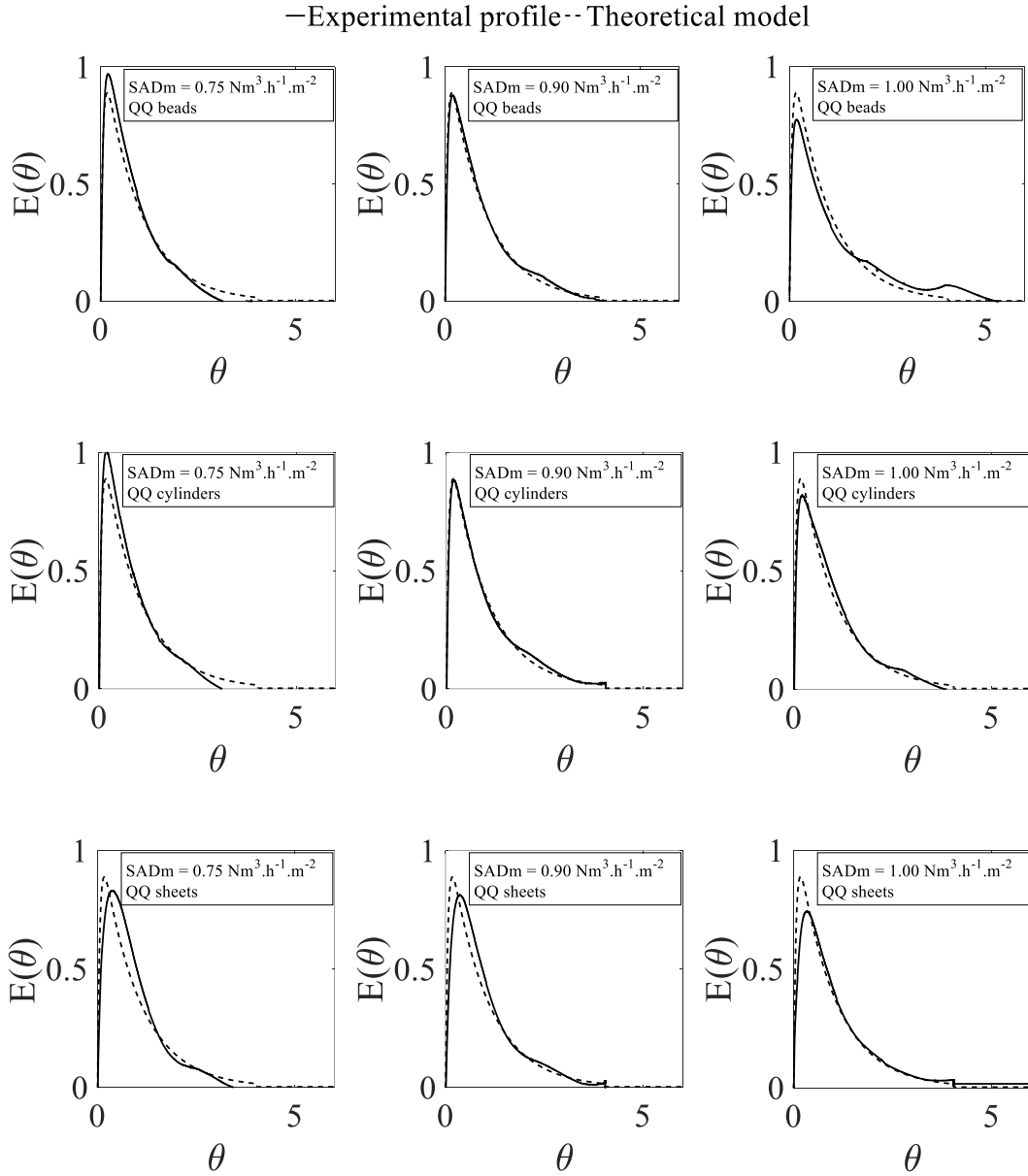


Figure IV-12 : Specific theoretical model applied to the QQ-ALMBRs under different air flowrates ad without dead zones ($m = 1$).

It can be concluded that the direct application of the theoretical specific model that was relevant for the ALMBR (with $m = 1$) is not suitable to describe the behavior of the mixing and flowing performances of the QQ-ALMBRs. This result can be assumed to be due to the induction of some dysfunctions by the addition of QQ media, under the investigated operating conditions. Knowing that the QQ media (QQ sheets in particular) were found to slow down to liquid flow in the riser (Chapter III), it can be assumed that some dead zones (or zones with very slow exchange) can be created with the addition of QQ media. Thus, the specific model needs to be adjusted by varying the parameter m , with the aim to identify and quantifying the physical modifications in the reactor resulting from the addition of QQ media.

- *Adjustment of the theoretical specific model with optimized parameters*

Minimal discrepancies between experimental and theoretical curves were obtained in the ALMBR and the average values of $|E_{th}(\theta) - E_{exp}(\theta)|$ were below 0.017. Thus, in the case of the QQ-ALMBRs, when the discrepancies were worth more 0.017 (*columns in italics* in Table IV-9), the parameters m the model was varied with a view to minimizing the value of the average $|E_{th}(\theta) - E_{exp}(\theta)|$. The optimized parameters as well as the corresponding values of $|E_{th}(\theta) - E_{exp}(t\theta)|$ are gathered in Table IV-10.

Table IV-10 : Optimized m parameter for the specific theoretical model applied to the QQ-ALMBRs under different air flowrates.

Specific model parameters	SADm (Nm ³ .h ⁻¹ .m ⁻²)											
	0.75	0.90	1.00	0.75	0.90	1.00	0.75	0.90	1.00	0.75	0.90	1.00
	ALMBR			QQ beads-ALMBR			QQ hollow cylinders-ALMBR			QQ sheets-ALMBR		
m	1	1	1	<i>0.84</i>	1	<i>1</i>	<i>0.80</i>	1	<i>1</i>	<i>1</i>	<i>1</i>	<i>1</i>
Average $ E_{th}(\theta) - E_{exp}(\theta) $	0.015	0.014	0.017	<i>0.026</i>	0.015	<i>0.041</i>	<i>0.027</i>	0.013	<i>0.023</i>	<i>0.053</i>	<i>0.039</i>	<i>0.026</i>
m	1	1	1	<i>0.84</i>	1	<i>1</i>	<i>0.80</i>	1	<i>1</i>	<i>0.87</i>	<i>0.97</i>	<i>1</i>
Q_r (L.h⁻¹)	4	4	4	<i>2.2</i>	4	<i>4</i>	<i>2.5</i>	4	<i>1.8</i>	<i>0.14</i>	<i>0.46</i>	<i>1.6</i>
Average $ E_{th}(\theta) - E_{exp}(\theta) $	0.015	0.014	0.017	<i>0.017</i>	0.015	<i>0.041</i>	<i>0.019</i>	0.013	<i>0.015</i>	<i>0.014</i>	<i>0.010</i>	<i>0.018</i>

It appears that the adjustment of the parameter m did only allow the minimization of the gap between the experimental and theoretical RTD functions in two cases.

In the QQ beads-ALMBR, the parameter ($m = 0.84$) under the air flowrate of 0.75 Nm³.h⁻¹.m⁻² was found to reduce the gap by 19 % compared to ($m = 1$) (Table IV-9 and Table IV-10). The optimized value in this case ($m = 0.84$) indicates that the introduction of QQ beads under 0.75 Nm³.h⁻¹.m⁻² induces the creation of 16 % of dead volume in the aerobic tank of the ALMBR.

In presence of QQ hollow cylinders and under the air flowrate of 0.75 Nm³.h⁻¹.m⁻², the same observation can be made. The parameter ($m = 0.80$) was found to reduce the discrepancy by 21 % compared to the parameter ($m = 1$). This result indicates that the presence of hollow cylinders under the air flowrate of 0.75 Nm³.h⁻¹.m⁻² induces dead zones (20 %) in the aerobic tank of the ALMBR.

These results are consistent with the hydrodynamics characterization (Chapter III), as it was demonstrated that the QQ media (in particular beads) are weakly fluidized under the SADm of 0.75 Nm³.h⁻¹.m⁻² and tend to settle to the bottom of the reactor. Therefore, it can be assumed that the bed of QQ media at the bottom entrap part of the liquid preventing it from circulating and correctly homogenizing with the rest of the bulk. In addition, the QQ sheets exhibited the best fluidization behavior, which is consistent with the smaller dead volume proportion obtained (13 %).

In all the other considered cases (Table IV-10), the sole adjustment of the parameter m did not result in any reduced gap between the experimental curves. Therefore, in these cases, the presence of dead volumes (m) is not the only dysfunction explaining the obtained discrepancies. Besides, the adjustment of the parameter m did not allow reducing the gap below 0.017 whatever the considered case.

From these observations, the variation of other parameters was achieved in order to better fit the experimental curves. In particular, the recirculation flowrate Q_r between the aerobic and anoxic tanks was added as a parameter. This parameter was selected because in the presence of QQ sheets, it appears in Figure IV-12 that the peak of experimental RTD curves is shifted to the right compared to the theoretical model, which actually refers to a lateness of mixing. Knowing that the recirculation between the two tanks of the ALMBRs takes important part to the global homogenization (Q_r is 2.6 times higher than the permeate flowrate), this lateness can potentially be due to a weaker recirculation between the two tanks, due to the suction of QQ media in the recycling pipe. Thus, the optimal set of parameters $\{m$ and $Q_r\}$ was determined in the cases where the average gap $|E_{th}(\theta) - E_{exp}(\theta)|$ was still above 0.017 and could not be reduced with the sole adjustment of m (*columns in italics* in the second part of Table IV-10).

The adjustment of Q_r did significantly minimize the discrepancies between the experiment and the theory, indicating that this recirculation flowrate can be varying during the operation. As a matter of fact, the average gaps in presence of QQ beads, hollow cylinders and sheets were around 0.027, 0.021 and 0.039, respectively with $Q_r = 4 \text{ L.h}^{-1}$ (recirculation flowrate selected to run the experiment) and were considerably reduced to 0.022, 0.015 and 0.014 with Q_r ranging between 0.14 and 4 L.h^{-1} (adjusted values to fit the experimental and theoretical curves).

The theoretical curves $E_{th}(\theta)$ were plotted in Figure IV-13 with the optimized set of parameters $\{m$ and $Q_r\}$ calculated in Table IV-10. The reduction of the gap between the experimental and the optimized theoretical curves is considerably noticeable.

To conclude, it can be stated that the theoretical specific model that was developed for the ALMBR without dead zones and with a constant recirculation flowrate ($m = 1$ and $Q_r = 4 \text{ L.h}^{-1}$) did not correctly describe the behavior of the QQ-ALMBRs and that the adjustment of the model via the variation of its parameters was necessary. The consideration of the recirculation flowrate Q_r as a parameter of the model was found to result in minimized discrepancies between the experimental and theoretical RTD functions. These results show that in comparison to the ALMBR, the addition of QQ media generate dysfunctions that not only correspond to dead volumes but also to a lateness of mixing caused by a reduced recirculation between the two tanks of the reactor.

–Experimental profile-- Optimized theoretical model

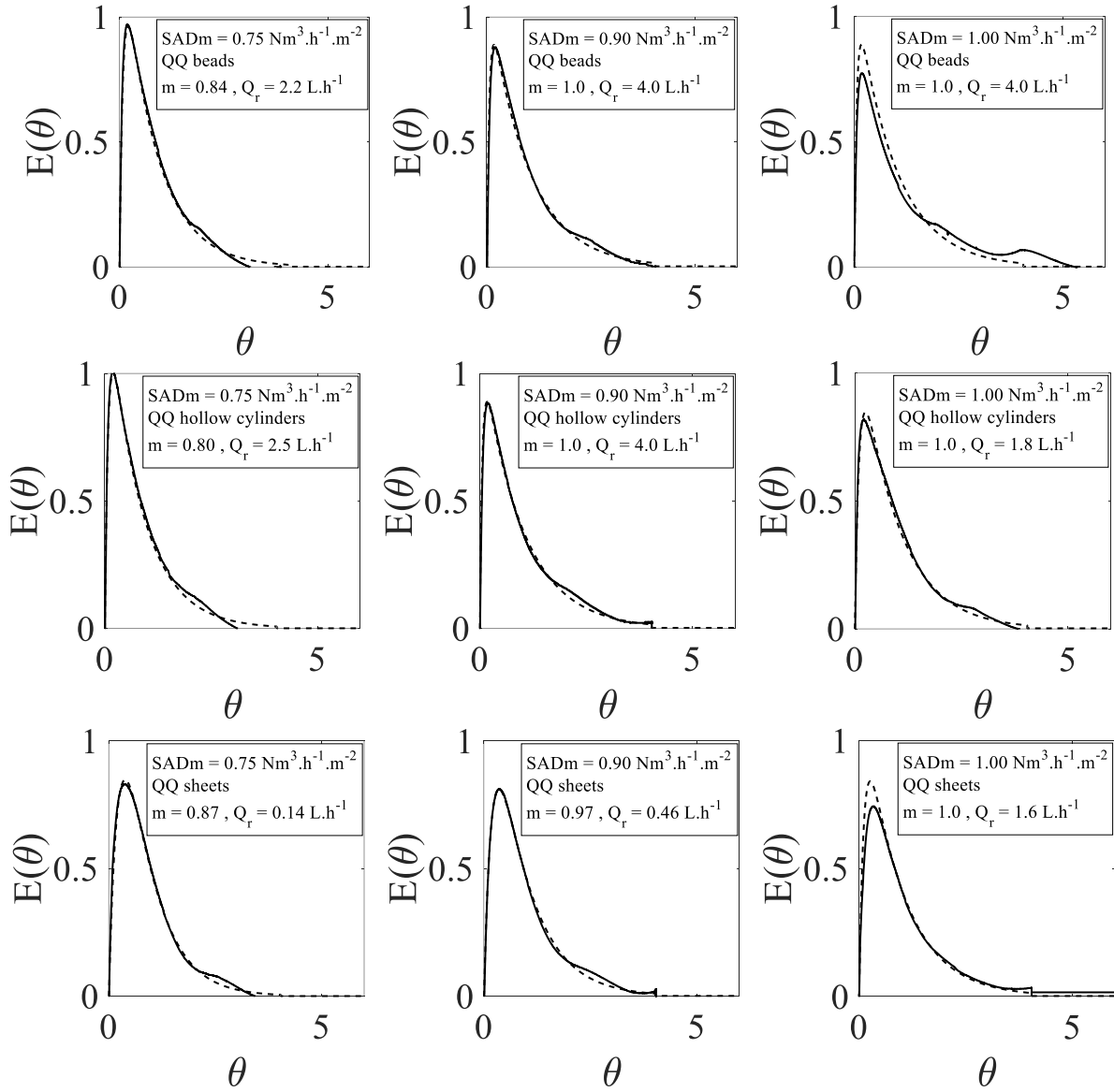


Figure IV-13 : Optimized specific theoretical model applied to the QQ-ALMBRs under different air flowrates and with optimized parameters (m and Q_r).

IV.4.2.2.3. Effect of the QQ media on the long-term mixing performance of the QQ-ALMBR

The analysis of the optimized parameters of the model (Table IV-10) brings more light on how exactly the addition of QQ media affects the mixing and flowing performances. Hence, it appears from the model parameters that the QQ media mostly affect the flowing and mixing behavior by creating dead volumes ($m < 1$), which can be attributed to their density (slightly greater than water) and shape that make them tend to settle down in the reactor rather than being fluidized in the flow. Therefore, depending on the aeration conditions, a more or less substantial part of the QQ media can settle in the bottom of the reactor, entrap a part of the liquid phase, and therefore, create a zone of no or very low exchange

with the rest of the bulk. This dysfunction can be very damaging for the overall performance of the ALMBR, since it leads to a reduction of the effective volume.

The recirculation flowrate Q_r was found to be severely impaired in presence of QQ media, with values ranging from 0.14 to 4 L.h⁻¹ (Table IV-10). As an example, up to 96 % decrease in Q_r was obtained in presence of QQ sheets under 0.75 Nm³.h⁻¹.m⁻². This phenomenon can be attributed to the fact that some QQ media may get sucked into the recirculation flow, which is collected at the bottom of the aerobic tank (Figure IV-4(a)), preventing the liquid from being correctly pumped, and thus affecting the mixing of the overall system.

In conclusion, the addition of QQ media to the ALMBR definitely induces an effect on the long-term mixing performance. The effect of the QQ media was detected via the analysis of the RTD parameters, and the modelling approach allowed identifying with more accuracy this effect and traducing it into physical mechanisms. Hence, it can be retained from this analysis that the presence of QQ media in the aerobic tank mainly affects its long-term mixing via the creation of dead volumes and the reduction of the recirculation flowrate between the two tanks, which may lead to a global loss of efficiency in the ALMBR performance. Moreover, the QQ sheets appear to have the most significant impact on the recirculation flowrate.

IV.4.2.2.4. Effect of the air flowrate on the long-term mixing performance of the QQ-ALMBR

As it was previously demonstrated, the air flowrate was found to have minimal effect on the long-term mixing performance of the ALMBR. However, when looking at the model parameters (Table IV-10) in presence of QQ media, it appears that the air flowrate can play an important role. Actually, it clearly appears that the fraction of dead volume ($1 - m$) is decreased with the increase of the air flowrate in presence of QQ media. As an example, it was found that the highest air flowrate of the tested range (1.00 Nm³.h⁻¹.m⁻²) always results in a 100 % effective volume (no dead zones), whatever is the shape of the QQ media. On the other hand, it also appears that the recirculation flowrate Q_r is globally less affected at high air flowrates. Given that the air flowrate was found to have no effect in the ALMBR (with no QQ media), these observations should be attributed to an indirect effect rather to a direct one. Indeed, as it was demonstrated in Chapter III, the air flowrate has an impact on the fluidization of the QQ media in the aerobic tank. The higher is the aeration, the more the QQ media can be easily set in suspension, preventing them from settling at the bottom of the reactor, where dead zones can be created and QQ media can be sucked into the recirculation flow.

IV.4.2.3. Concluding remarks on the long-term mixing performance of the ALMBR/QQ-ALMBR

The characterization of the long-term mixing performance of the ALMBR/QQ-ALMBR allowed drawing the following key-conclusions:

- The RTD analysis turned out to be a good way to characterize the long-term mixing and circulation performance of the ALMBR, given the good accordance with the literature (Table IV-2) that was obtained in terms of RTD global aspect and parameters. Besides, the application of the same RTD analysis to the QQ-ALMBRs allowed the detection of the dysfunctions induced by the QQ media presence.
- The usual models based on ideal reactors were not appropriate to describe the present ALMBR, because they only take into account one of the components of the considered reactor at a time. A more specific model was necessary to develop and helped better understand the global mixing and flowing behavior of the ALMBR, which was found to operate as two completely stirred tanks-in-series with different volumes and with a recycling flow from the second tank to the first one. In addition, the application of this specific model to the QQ-ALMBRs helped identifying exactly the potential negative effects induced by the addition of QQ media.
- The presence of QQ media was found to impair considerably the mixing performance of the ALMBRs by two physical mechanisms: first by the creation of dead volumes (up to 20 %), probably at the bottom of the reactor where the QQ media tend to settle down due to their density; second by the deterioration of the recirculation between the two tanks of the reactor caused by their tendency to be sucked into the flow.
- The aeration conditions were found to have minimal effect in the ALMBR in the investigated range (from 0.75 to 1.00 Nm³.h⁻¹.m⁻²) referring to optimal mixing conditions. However, in the QQ-ALMBRs, the aeration was found to play a key-role, not directly on the mixing of the bulk, but indirectly by enhancing the QQ media fluidization, and thus minimizing their negative effect on the overall mixing, which is consistent with the fluidization results reported in Chapter III.

IV.5. Conclusions and perspectives

In this chapter, the mixing and circulation performances of the ALMBR/QQ-ALMBR were characterized distinguishing two time-scales: the short-term and the long-term performance. Relevant criteria were selected on the basis of the literature review and applied to discuss the overall mixing performance. The results presented in this chapter, their confrontation to the literature, and their combination one with another, allow drawing the following statements as main conclusions:

- The operation of the ALMBR studied in this work can be considered as comparable to two completely-stirred-tanks-in-series with different volumes and with a recycling flow. Both of the short-term (mixing time) and the long-term mixing (RTD) characterization corroborated that the aerobic membrane-tank could be considered as a completely-stirred reactor.
- The existence of a critical air flowrate (around $0.55 \text{ Nm}^3 \cdot \text{h}^{-1} \cdot \text{m}^{-2}$) was found in the ALMBR. Above this air flowrate, neither the short-term nor the long-term mixing performance was any better, referring to optimal aeration conditions.
- Distinguishing the short-term and long-term mixing performances was found to be relevant, in particular, because it allowed concluding about the effect of QQ media on the ALMBR. As a matter of fact, the QQ media was found to have no negative effect at the short-term operation, but relatively damaging effect at the long-term operation.
- The addition of QQ media was revealed to impair the ALMBR long-term mixing performance. The QQ media affect the long-term mixing, mainly by creating dead volumes and by reducing the recirculation flowrate. In particular, the addition of QQ sheets at a volume fraction of 0.45 % v/v under an SADm of $0.75 \text{ Nm}^3 \cdot \text{h}^{-1} \cdot \text{m}^{-2}$, resulted in a reduction of the recirculation flowrate of 96 % and a dead volume of 13 %. This effect can be critical as the mixing is one of the major mechanisms involved in the MBR biodegradation efficiency, as well as in the membrane fouling tendency.
- The impact of QQ media on the mixing performance was found to be alleviated under high SADm ($> 0.90 \text{ Nm}^3 \cdot \text{h}^{-1} \cdot \text{m}^{-2}$) as the hydrodynamics conditions created are more favorable to their fluidization. It was demonstrated that the QQ media also affect the mixing performance by decreasing the recirculation flowrate between the aerobic tank and the anoxic tank, which is pumped at the bottom of the aerobic tank. The configuration of the ALMBR was one technical constraint of this work and was clearly not optimal for the addition of QQ media. Thus, a different configuration where the QQ media are prevented from being sucked into the recirculation flowrate could be of interest.

CHAPTER V. MASS TRANSFER PHENOMENA INVOLVED IN THE QQ-MBR

RESUME EN FRANÇAIS

Ce chapitre se focalise sur l'étude du transfert de matière mis en jeu dans l'application du Quorum Quenching (QQ) aux Bioréacteurs à Membrane (BRM). Le QQ repose sur une réaction enzymatique entre les molécules signal (AHLs) de communication bactérienne (Quorum Sensing (QS)), et des enzymes capables de les dégrader. Comme dans toute réaction (bio)chimique, l'étude de transfert de matière paraît essentielle car il peut constituer une étape limitante du processus global.

L'étude bibliographique précédemment menée (Chapitre I) a permis non seulement d'identifier l'importance du transfert de matière (par l'évocation des différentes méthodes d'immobilisation de bactéries de QQ ainsi que des différentes bactéries de QQ) mais aussi de mettre en évidence les lacunes existantes sur cet aspect. Dans cette optique, l'objectif de cette partie de l'étude est d'étudier de manière quantitative les phénomènes de transfert de matière en distinguant deux principaux types de transferts : le transfert du liquide vers les « QQ media » et le transfert des « QQ media » vers la phase liquide.

Pour ce faire, une molécule modèle (colorant) a été choisie et des expériences ont été spécifiquement développées. Après une revue des fondamentaux sur le transfert de matière ainsi que des quelques résultats obtenus précédemment sur la mise en évidence de la diffusion d'AHLs dans les « QQ media », les matériels et méthodes utilisés sont présentés avant de discuter les résultats obtenus pour les deux types de transfert.

En ce qui concerne le transfert du colorant de la phase liquide vers les « QQ media », la capacité de charge des QQ media est indépendante de leur forme ainsi que le coefficient de transfert de matière externe. Cependant, le flux de matière transféré est en moyenne 1.3 et 2.1 fois plus élevé pour les feuilles que pour les cylindres creux et les billes, respectivement, car elles développent une surface d'échange plus importante à volume égal.

Dans le cas du transfert de la phase solide (« QQ media ») vers la phase liquide, il ressort de cette analyse que les conditions opératoires (débit d'aération), dans la gamme étudiée, ont peu d'influence sur le transfert. En revanche, l'influence de la forme des supports sur le transfert est très marquée, les feuilles apparaissant les plus performantes en termes de cinétique de transfert et les billes les moins efficaces.

V.1. Introduction

Quorum Quenching (QQ) is based on a biochemical reaction between the signal molecules (AHLs) that are produced for the bacterial communication (Quorum Sensing) and microbial enzymes that have the capacity to degrade these molecules. With the development of the QQ entrapping methods (as reviewed in Chapter I), the mass transfer appeared as one essential question to address and the reasons are mainly twofold: firstly, as in every (bio)chemical reaction, the mass transfer of the reagents is a key-phenomenon to consider as it can be a limiting step. Secondly, the importance of studying the mass transfer involved in QQ is also due to the different entrapping methods that were developed (QQ beads, hollow cylinders or sheets) and to the existing kinds of QQ bacteria: the endo-enzyme-producing bacteria and the exo-enzyme-producing bacteria. From these specificities, two cases of mass transfer can be distinguished: from the mixed liquor towards the inner part of QQ media, in the case of endo-enzyme degradation, and from the QQ media to the mixed liquor in the case of exo-enzyme-mediated QQ.

Even though some attempts were reported in the literature, the mass transfer phenomena involved in QQ are not fully understood yet. Within this scope, the present study aims to contribute to a better understanding of these phenomena. An experimental approach was developed based on the use of a model molecule, in order to quantify the mass transfer at the reactor-scale (not only at the QQ media scale). The following objectives were more specifically addressed:

- Providing a quantitative characterization of the mass transfer of the molecules involved in QQ, from the liquid to the QQ media and *vice versa* via the determination of mass transfer parameters such as the transferred flux, the mass transfer coefficient, the Sherwood number.
- On the basis of these quantitative parameters, discussing the effect of the operating conditions on these mass transfer phenomena.
- Finally, concluding about the effect of the shape of QQ media and bring valuable clues for future research in this area.

For that purpose, this chapter first comprises a literature review on the mass transfer mechanisms involved in QQ. The materials and methods which were specifically developed for the study of the mass transfer are then presented. The selected approach consists in studying the mass transfer in two ways: from the liquid to the QQ media (liquid-solid) and from the QQ media to the liquid (liquid-solid). In both cases, a dye molecule is used to mimic the molecules involved in the QQ reaction (AHLs and QQ enzymes). For the liquid-solid mass transfer, jar-tests experiments putting the fresh QQ media with the dye solution are performed, in order to determine and compare the transferred flux as well as the mass transfer coefficient. For the solid-liquid mass transfer, experiments are conducted in the lab-scale reactor under different hydrodynamics conditions, and the obtained transferred flux is compared for the three

QQ media shape. The choice of this experimental approach is actually the originality of this work, since the mass transfer is studied at the global scale, in opposition to what was reported in the literature (only at the QQ media-scale).

V.2. Background

V.2.1. Mass transfer fundamentals

Mass transfer is the spatial transport of matter under the effect of a driving force. Several mechanisms are distinguishable, depending on the nature of this driving force: the transfer can be induced by a space-gradient of concentration (diffusion from the more concentrated location to the less concentrated location), by a flowing fluid (convective mass transfer), or by another external force such as gravity or an electrical field.

The diffusion mechanism is governed by Fick's law that links the diffusive flux (or rate) N (in $\text{kg.m}^{-2}.\text{s}^{-1}$ or $\text{mol.m}^{-2}.\text{s}^{-1}$) proportionally to the gradient of concentration C , according to Equation V-1, where D is the diffusion coefficient (in $\text{m}^2.\text{s}^{-1}$), and where the minus sign (-) stands for the fact that the transfer occurs from the more concentrated zone to the less concentrated zone. The diffusion coefficient D is specific to the diffusion of one solute in a solvent. When the diffusion is unidirectional, Equation V-1 can be simplified resulting in Equation V-2.

$$N = -D\nabla C \quad \text{V-1}$$

$$N = -D \frac{\partial C}{\partial x} \quad \text{V-2}$$

In order to determine the diffusion coefficient of one specie (solute A) into another (solvent B), some correlations were proposed and are based on the physico-chemical properties of the two species. Among these correlations, the correlations of Stokes-Einstein and Wilke and Chang (1955) [152] are presented in Equations V-3 and V-4, respectively, where k is the Boltzmann constant, T is the temperature (K), μ_s is the viscosity of the solution (Pa.s), r_A is the molecular radius of the solute (m), x is the association parameter (which is worth 2.6 for water and 1 for non-associated solvents), M_B is the molecular weight of the solvent (g.mol^{-1}), and V_A is the molar volume of the solute ($\text{cm}^3.\text{mol}^{-1}$).

$$D_{AB} = \frac{kT}{6\pi\mu_s r_A} \quad \text{V-3}$$

$$D_{AB} = 7.4 \times 10^{-11} \frac{(xM_B)^{0.5}T}{\mu_s V_A^{0.6}} \quad \text{V-4}$$

Concerning the convective mass transfer of one species (solute A) in a fluid from one location (1) to another location (2), a general relation links the transferred flux (or rate) N_A to the gradient of concentrations between ($C_{A1} - C_{A2}$), according to Equation V-5, where k_c is a global mass transfer coefficient characterizing the kinetics of the system (in m.s^{-1}). Unlike the diffusion coefficient, the mass transfer coefficient is not a physical property of the {solute-solvent} system, since it depends on other parameters, such as hydrodynamics.

$$N_A = k_c(C_{A1} - C_{A2}) \quad \text{V-5}$$

As for the diffusion coefficient, the global (convective) mass transfer coefficient can be estimated using correlations, by analogy with heat transfer, involving dimensionless numbers such as the Schmidt number (Sc), the Reynolds number (Re) and the Sherwood number (Sh), defined as in Equations V-6, V-7 and V-8, respectively. The Schmidt number represents the ratio of the momentum diffusivity (with the kinematic viscosity ν) to the mass diffusivity (with the diffusion coefficient D_{AB}). The Reynolds number is characteristic of the flow and is the ratio of the inertia forces (with the density ρ_l of the liquid, the flowing velocity U and a characteristic distance d , at the numerator) to the viscous forces (dynamic viscosity μ_l of the liquid at the denominator). Finally, the Sherwood number characterizes the transfer phenomenon by representing the ratio of the convective mass transfer along a characteristic distance (L) to the diffusive mass transfer.

$$Sc = \frac{\nu}{D_{AB}} \quad \text{V-6}$$

$$Re = \frac{\rho_l U d}{\mu_l} \quad \text{V-7}$$

$$Sh = \frac{k_c L}{D_{AB}} \quad \text{V-8}$$

The general form of the correlations can be expressed as in Equation V-9, where a , b and c are constants that depend on other parameters of the system such as the geometry of the flow (cylindrical, flat plate,...) or the nature of the phases involved in the transfer (gas, liquid, solid) [153].

$$Sh = a Re^b Sc^c \quad \text{V-9}$$

V.2.2. Literature review on mass transfer in QQ-MBRs

A few attempts were made to visualize the mass transfer of AHLs in QQ media, in order to localize their degradation when endo-enzyme-producing bacteria (*Rhodococcus* sp. BH4, for example) are entrapped in QQ media.

Lee et al. (2016) [12] were the first to highlight the existence of a diffusion phenomenon of AHLs into QQ cylinders. Using a fluorescent *E.coli* strain (JB525) which produces a green fluorescent protein in presence of AHLs, the diffusion of a model AHL molecule (C8-HSL) was visualized with Confocal Laser Scanning Microscopy (CLSM). The preparation of sodium alginate cylinders entrapping the *E.coli* JB525 strain allowed highlighting the free diffusion of C8-HSL inside the QQ media (Figure V-1(a)). When cylinders entrapping both the fluorescent strain (*E.coli* JB525) and the QQ bacteria (*Rhodococcus* sp. BH4) were put in contact with a solution of AHLs, the presence of C8-HSL was only observed close to the surface of the cylinders (Figure V-1(b)). This result was attributed to the fact that the QQ bacteria could degrade the AHLs before they reach the center of the QQ media, indicating that the effective region of the QQ media was close to the surface.

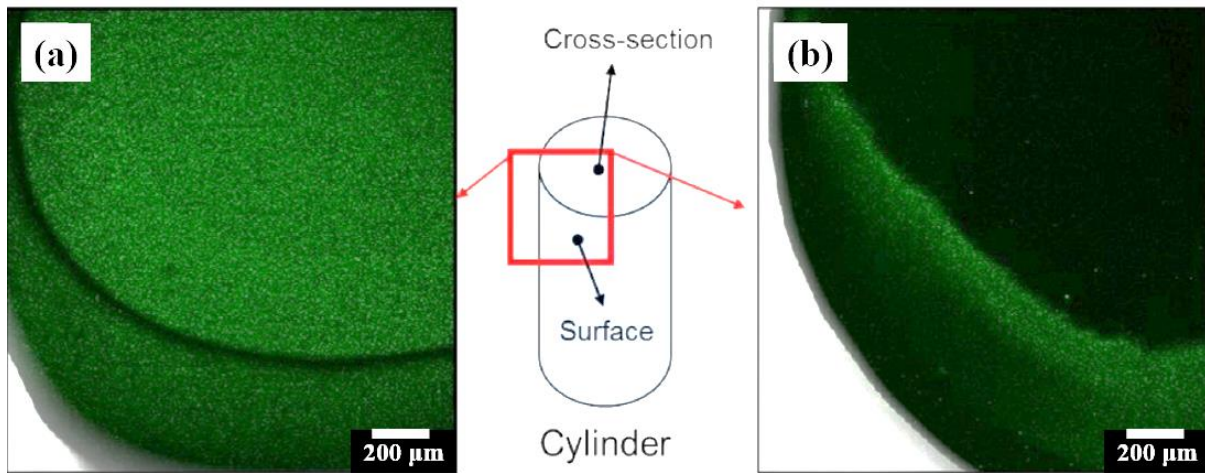


Figure V-1 : CLSM images of cylinders entrapping (a) *E.coli* JB525 and (b) both *E.coli* JB525 and *Rhodococcus* sp. BH4 [12].

Lee et al. (2016) [14] further conducted a similar study with QQ beads that confirmed the free diffusion of AHLs into the QQ beads (Figure V-2(a) and (c)). However, when comparing the two images in Figure V-2(a) and (c), it seems that the fluorescence is higher near the surface than in the center of the beads. This observation indicates the existence of a space-gradient that can be assumed to be due to the limitation of the diffusion of AHLs by the sodium alginate material. When QQ beads were prepared with both entrapped *E.coli* JB525 and *Rhodococcus* sp. BH4, the AHLs concentration remained higher near the surface rather than in the center of QQ media (Figure V-2(b) and (d)), but the thickness of the

zone of high concentration was less than without BH4, revealing the degradation by *Rhodococcus* sp. BH4.. Again, this experiment confirmed that most of the QQ activity of *Rhodococcus* sp. BH4 was localized in the near surface of the QQ media. From these experiments, Lee et al. (2016) [12,14] concluded that the surface of the QQ media was the most effective region and therefore, that QQ media with a thin surface such as QQ hollow cylinders and sheets, should be favored for an optimal QQ activity.

These results provide valuable qualitative information and need to be taken to the next level by conducting a quantitative study, since no physical magnitudes characterizing the mass transfer phenomena (such as mass transfer flux or coefficient) were reported. In addition, these studies mostly focused on the observation of diffusion (with no liquid flow) at the scale of one single QQ medium.

On that basis, the present study aims to characterize and quantify the mass transfer phenomena under specific **hydrodynamics** conditions (with the renewal of liquid film at the QQ surface) at the **global scale** (taking into account several QQ media), and in two ways: from the liquid phase to the QQ media, and *vice versa*.

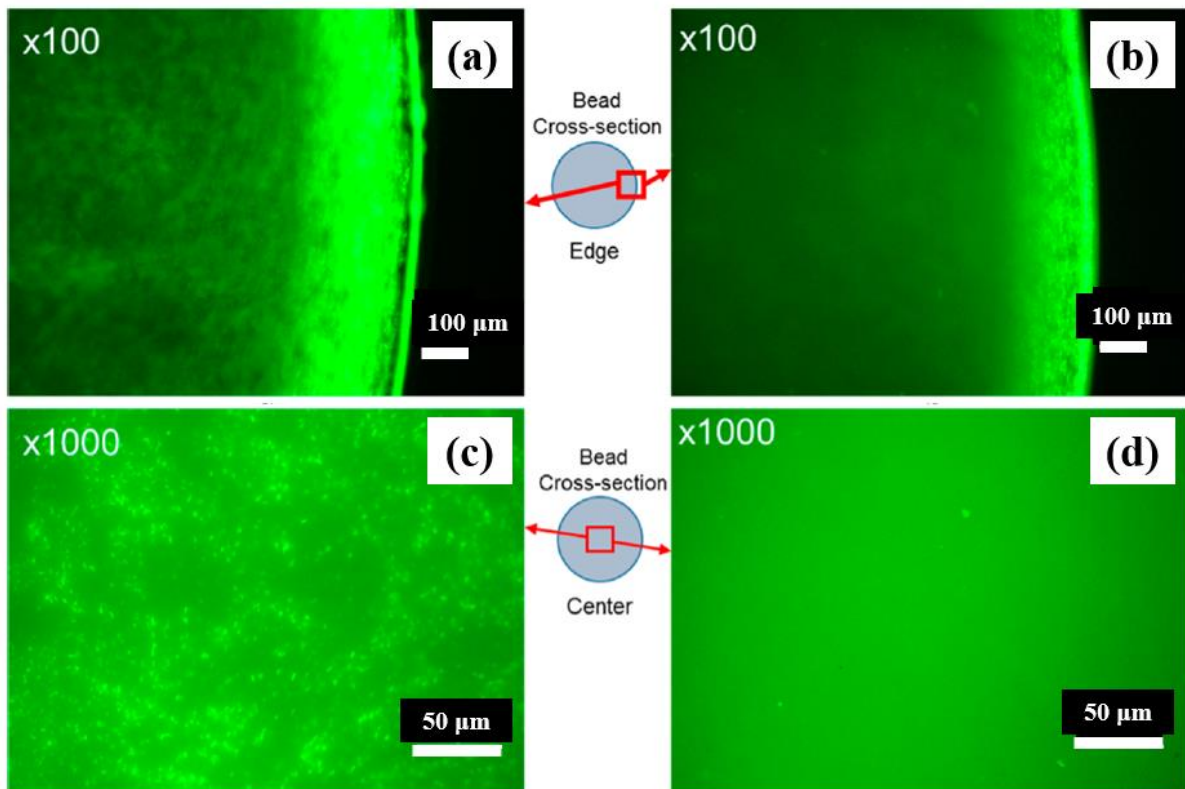


Figure V-2 : CLSM images of the edge of beads entrapping (a) *E. coli* JB525 and (b) both *E. coli* JB525 and *Rhodococcus* sp. BH4. CLSM images of the center of beads entrapping (c) *E. coli* JB525 and (d) both *E. coli* JB525 and *Rhodococcus* sp. BH4 [14].

V.3. Materials and methods

The experimental strategy of this study was to characterize and **quantify** the mass transfer at a global scale (not at the QQ media scale). With this aim, the use of a **mimic molecule** was preferred because the quantification methods of AHLs widely used to date rely on bacterial strains (such as *E.coli* JB525 producing fluorescence in presence of AHLs, or *Agrobacterium tumefaciens* A136 producing a blue color or bioluminescence in presence of a specific substrates in response to AHLs [154]), which would be laborious to apply for the dosage of AHLs in the reactor (big volume, non-sterile conditions). The details of the experimental approach are given in Chapter II and some of the main elements are recalled in the following.

V.3.1. Selection and preparation of the dye solution

The dye used as a tracer for this study was the Rose Bengal Lactone (Sigma-Aldrich), and its main properties were given in Chapter II. This dye was selected to mimic the molecules involved in the QQ reaction (either AHLs that transfer from the liquid to the QQ media, or acylase that transfer from the QQ media to the liquid) and offers the important advantage to be easily detected and quantified.

The Rose Bengal Lactone solutions of Rose Bengal Lactone were prepared, prior to each experiment, by dissolving the proper amount of powder in tap water, at a concentration of about 0.4 g.L^{-1} . In order to help the dissolution, the solutions were sonicated 3 to 4 times for 15 min and shaken between two sonication cycles, until obtaining a clear dark-pink solution. The Rose Bengal Lactone concentration was measured using a spectrophotometer (Jasco-V630, Germany) at 548 nm, as described in Chapter II.

V.3.2. QQ media

The three shapes of QQ media were used in this study (Figure V-3) and their main geometrical properties are recalled in Table V-1. In total, a volume V_s of 58.5 mL of QQ media was used in each experiment.



Figure V-3: Photographs of the QQ (a) beads (b) hollow cylinders and (c) sheets.

Table V-1 : Properties of QQ media.

QQ media	Beads	Hollow cylinders	Sheets
Dimensions (mm)	Diameter: 3.5	Inner diameter: 1.7 Outer diameter: 3.5 Length: 27	Length: 20 Width: 10 Thickness: 0.5
Volume of a particle (mm³)	22.5	198.5	100
Surface of a particle (mm²)	38.5	455.8	400
Total number N_{TM} in 58.5 mL	2600	298	585
Total exchange surface S_s of 58.5 mL (m²)	0.100	0.135	0.234

V.3.3. Jar-test setup and spectrophotometry for the mass transfer study from the liquid to the QQ media

In order to study the kinetics of the mass transfer from the liquid phase to the QQ media, batch experiments were carried out in jar-test (Figure V-4). The mass transfer from the liquid to the media was not directly studied in the lab-scale ALMBR, considering the very small volume of QQ media compared to the liquid volume in the reactor, the variation of the dye concentration in the liquid would not be detectable.

The jar-test allow setting a constant and identical stirring (90 rpm) in the three beakers during the whole experiment, as a consequence two assumptions can be made: firstly, that the liquid phase is uniform in terms of concentrations, and secondly, that identical hydrodynamics conditions are created in the three jars.

Concentrated (around 0.4 g/L) solutions of Rose Bengal Lactone were introduced in 1 L-beakers, together with “fresh” QQ media, in the ratio 9:1 (526 mL of solution with 58.5 mL of QQ media in each jar). The volume of QQ media was identical for the three shapes. The jar-test were performed under stirring (90 rpm), at the room temperature, for 24 h, which was the observed duration for the equilibrium to be reached. Samples of the solution were collected every 30 min in the beginning, and then spaced out, and their concentration was determined by spectrophotometry at 548 nm (more details about the spectrophotometry are available in Chapter II). The experiments were repeated three times for the three shapes of QQ media, in order to determine the mass transfer coefficient from the liquid to the QQ media, via the mass balance on the Rose Bengal Lactone in the solution. Finally, the stained QQ media resulting from the jar-test experiments were used for the subsequent part in order to study the mass transfer from the QQ media to the liquid phase, as explained in the following.

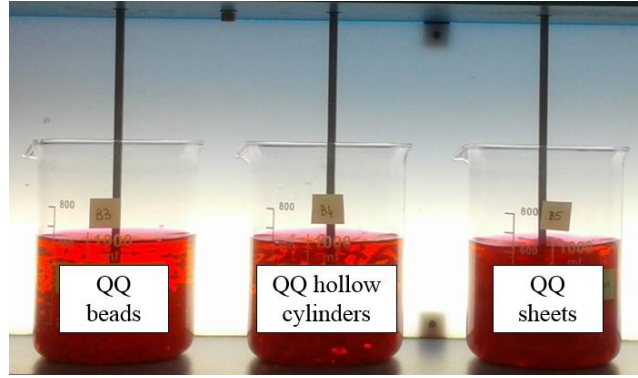


Figure V-4: Jar-test setup for the study of the mass transfer from the liquid phase to the QQ media.

V.3.4. Experimental setup and camera technique for the mass transfer study from the QQ media to the liquid

The kinetics of the mass transfer from the QQ media to the liquid phase was studied in the lab-scale ALMBR under continuous air injection, and under the batch mode for the liquid phase (no feed of the reactor). The stained QQ media, prepared as previously described, were collected at the end of the jar-test experiment and drained before being introduced in the aerobic tank of the ALMBR, as presented in Figure V-5, at a volume fraction of 0.45 % v/v. The initial amount m_0 of Rose Bengal Lactone loaded in the QQ media was deduced from the mass balance between the initial and final conditions of the jar-test operation.

An optical technique was developed to monitor the variations of concentration in the liquid phase overtime, and consisted in recording with a camera (CMOS, Basler-Ace Aca1920-155 um) equipped with a green filter, the intensity of light passing from a light panel (Phlox-LedW-BL, 400 x 200 mm², 24 V, 2A, Phlox) through the bulk. The green filter was used in order to narrow down the range of light wavelengths to around 500 ± 5 nm, for which the absorbance of light was observed to be significant (Figure II-27). Once the QQ media were introduced in the reactor, the camera was set on to record images (0.1 Hz) until reaching the complete stabilization of the system. The images were then processed using a Matlab program, to determine the instantaneous light intensity I , and the absorbance A was finally deduced according to Beer-Lambert law, expressed as in Equation V-10, where I_0 is the light intensity through the blank (water), C is the concentration (in mg.L⁻¹), l is the path length (in cm) and ϵ_λ is the molar attenuation coefficient (in L.mg⁻¹.cm⁻¹). More information about the calibration of the technique, as well as the image processing is available in Chapter II.

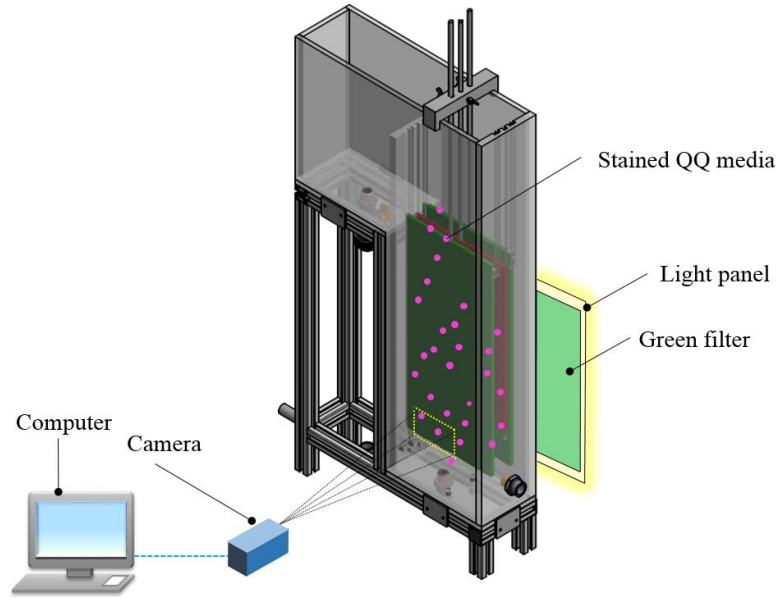


Figure V-5: Experimental setup for the study of the mass transfer from the QQ media to the liquid phase.

$$A = -\log \left(\frac{I}{I_0} \right) = \varepsilon_{\lambda} \cdot l \cdot C \quad \text{V-10}$$

V.4. Theoretical aspects of the mass transfer kinetics

In the following, the theory of the mass transfer governing the phenomena involved in the experiments will be given, for further use in the interpretation of the results.

V.4.1. Liquid-solid mass transfer

In the case of the batch experiment (jar-test) conducted for the study of the mass transfer from the liquid to the QQ media, the overall transfer phenomenon can be considered as an adsorption phenomenon, which is characterized by a succession of steps [155], as illustrated in Figure V-6:

- The external mass transfer through the boundary layer surrounding the QQ media, which is driven by the difference between the homogeneous concentration in the bulk ($C_l(t)$) and the concentration on the surface of the QQ media ($C_s(t)$). This step depends on the hydrodynamics of the system.
- The internal diffusion inside the pores of the QQ media, which can itself involve different mechanisms, depending on whether the diffusion takes place in the volume of the pores, or through the internal boundary layer of the pores [156].

- The adsorption *per se*, which is the attachment of the molecules of solute on the active sites of the sodium alginate material. Unlike the first step, the attachment only depends on the nature of the solute and the solid material.

The last step is very quick in most adsorption systems, therefore, it is generally accepted that the overall phenomenon kinetics is limited by the external transfer step [157]. Thus, studying the overall adsorption kinetics can indeed provide information about the mass transfer mechanisms.

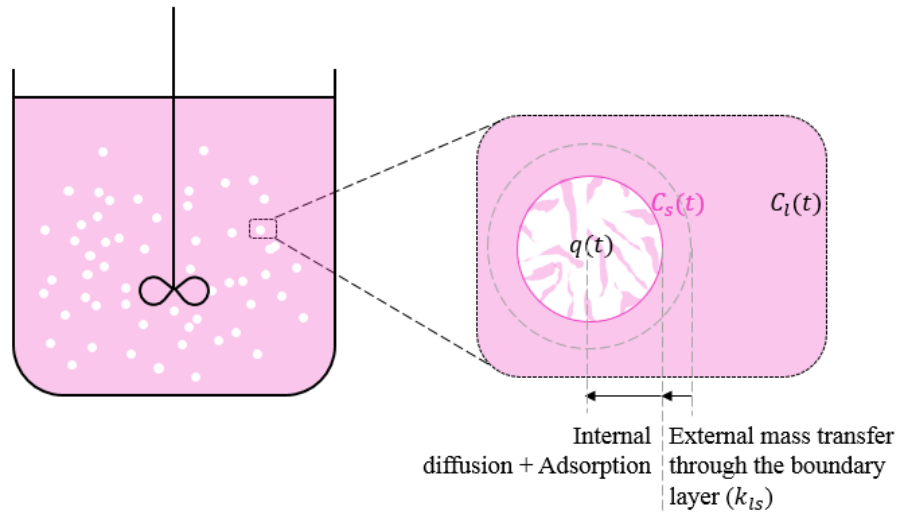


Figure V-6 : Illustrative representation of the transfer of the Rose Bengal Lactone from the liquid solution to the QQ media, in the jar-test experiments.

V.4.1.1. Global adsorption kinetics

Two main mathematical models are proposed in the literature to describe the overall adsorption phenomenon, on the basis of the adsorbed quantity $q(t)$ of solute per mass unit of solid (in mg.g^{-1}).

The pseudo-first order model was proposed by Lagergren in 1898 and is expressed according to Equation V-11, where q_e is the adsorbed quantity reached at the equilibrium, and k_1 is the constant of the pseudo-first order kinetics (in s^{-1}). The determination of this constant requires the linearization of Equation V-11 that results in Equation V-12, where k_1 is the slope of the curve $\ln(q_e - q(t))$ versus time.

$$\frac{dq(t)}{dt} = k_1(q_e - q(t)) \quad \text{V-11}$$

$$\ln(q_e - q(t)) = \ln(q_e) - k_1 t \quad \text{V-12}$$

Another model is the pseudo-second order model which is based on the existence of strong chemical bonds between the solute molecule and the solid. This model is described by the Equation V-13 where k_2 is the constant of the pseudo-second order kinetics (in $\text{g.mg}^{-1}.\text{s}^{-1}$). The linear form presented in Equation V-14 is used to determine the constant k_2 as well as the adsorbed quantity at the equilibrium q_e .

$$\frac{dq(t)}{dt} = k_2(q_e - q(t))^2 \quad \text{V-13}$$

$$\frac{t}{q(t)} = \frac{t}{q_e} + \frac{1}{k_2 q_e^2} \quad \text{V-14}$$

In the present case, the adsorbed quantity $q(t)$ can be deduced from the Equation V-15, where ρ_s and V_s are, respectively, the wet density (in kg.m^{-3}) and the total volume (in m^3) of the solid particles (QQ media), and $C_l(t)$ is the concentration in the bulk (Figure V-6), and V_l is the total liquid volume.

$$q(t) = \frac{C_l(t=0) - C_l(t)}{M_s} V_l = \frac{C_l(t=0) - C_l(t)}{\rho_s V_s} V_l \quad \text{V-15}$$

V.4.1.2. *External mass transfer kinetics*

According to the method proposed by Furusawa and Smith (1973) [155], the external mass transfer step is related to the changes of concentrations overtime by the mass balance expressed in Equation V-16, where k_{ls} is the liquid-solid mass transfer coefficient (in m.s^{-1}), S_s is the total liquid-solid interface (in m^2) and $C_s(t)$ is the concentration at the surface of the solid particles (QQ media) (Figure V-6). A simple method was proposed to deduce k_{ls} , and consists in substituting the Equation V-16 with the corresponding values at the initial conditions (when $t \rightarrow 0$), which results in Equation V-17. Therefore, the liquid-solid external mass transfer coefficient k_{ls} can be deduced from the initial slope $[(\frac{dC_l(t)}{dt})_{t=0}]$ of the curve $C_l(t)$ versus time.

This approach was adopted in the literature to study different systems involving liquid-solid mass transfer, among which some examples are the removal of food dyes using chitosan particles [156,158], or the transfer of ions using ion-exchange resin [159].

$$\frac{V_l dC_l(t)}{dt} = -k_{ls} S_s (C_l(t) - C_s(t)) \quad \text{V-16}$$

$$(\frac{dC_l(t)}{dt})_{t=0} = \frac{-k_{ls} S_s}{V_l} C_l(t=0) \quad \text{V-17}$$

V.4.2. Solid-Liquid mass transfer

In the case of the experiments conducted in the aerated lab-scale ALMBR, the transfer of the Rose Bengal Lactone takes place from the QQ media to the liquid. This kind of configuration (solid-liquid) was much less investigated than the previous one (liquid-solid), especially under similar hydrodynamics conditions. Even though it can be assumed that the transfer from the solid to the liquid is the combination of several mechanisms, as illustrated in Figure V-7, to our best knowledge, no complete model of the whole phenomenon was developed taking into account the involved steps.

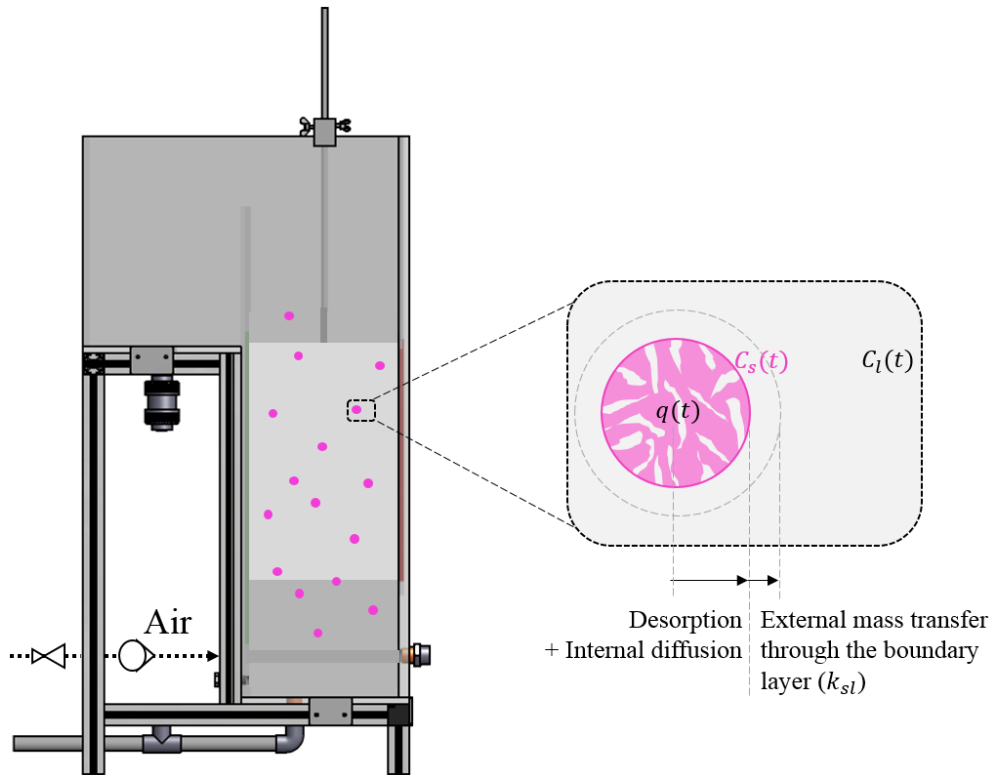


Figure V-7 : Illustrative representation of the transfer of the Rose Bengal Lactone from the QQ media to the liquid, in the aerobic tank of the lab-scale MBR.

Some studies focused on characterizing the solid-liquid mass transfer involved in the dissolution of solid substances in their own solution, using the mass balance presented in Equation V-18 [160]. This approach, similarly to the one developed for the liquid-solid mass transfer (the opposite phenomenon) (Equation V-16), allows the determination of a coefficient k_{sl} for the solid-liquid external mass transfer. The solid-liquid mass transfer coefficient can be deduced from Equation V-19, which corresponds to the very early stage of the operation (when $t \rightarrow 0$) at which the concentration in the liquid is equal to zero and the initial concentration at the surface of the solid $C_s(t = 0)$ can be considered as homogeneous

in the QQ media, and equals the ratio of the initial mass of Rose Bengal Lactone (m_0) to the total volume of QQ media V_S . In practice, k_{sl} is deduced from the initial slope of the curve $C_l(t)$ versus time.

$$\frac{V_l dC_l(t)}{dt} = k_{sl} S_s (C_s(t) - C_l(t)) \quad \text{V-18}$$

$$\left(\frac{dC_l(t)}{dt}\right)_{t=0} = \frac{k_{sl} S_s}{V_l} C_s(t=0) = \frac{k_{sl} S_s m_0}{V_l V_S} \quad \text{V-19}$$

V.5. Results and discussion

V.5.1. Calculation of the diffusion coefficient of the Rose Bengal Lactone

Given the molecular structure of the Rose Bengal Lactone, the dimensions of the molecule could be deduced using a modeling software (PyMOL®) as presented in Figure V-8. The dimensions were used to estimate the diffusion coefficient of Rose Bengal Lactone (specie A) in water (specie B), using the correlations of Stokes-Einstein and Wilke and Chang (Equations V-3 and V-4, respectively).

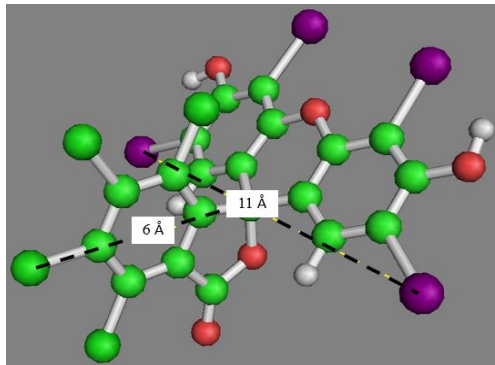


Figure V-8 : 3D-representation of the molecular conformation of the Rose Bengal Lactone.

Table V-2 : Calculated diffusion coefficients for the Rose Bengal Lactone molecule.

Stokes-Einstein (Equation V-3)	Wilke and Chang (Equation V-4)
$k = 1.38 \times 10^{-23} \text{ m}^2 \cdot \text{kg} \cdot \text{s}^{-2} \cdot \text{K}^{-1}$	$\alpha = 2.6$
$r_A = 5.55 \times 10^{-10} \text{ m}$	$M_B = 18 \text{ g} \cdot \text{mol}^{-1}$
	$V_A = 419.54 \text{ cm}^3 \cdot \text{mol}^{-1}$
$D = 3.89 \times 10^{-10} \text{ m}^2 \cdot \text{s}^{-1}$	$D = 3.95 \times 10^{-10} \text{ m}^2 \cdot \text{s}^{-1}$
$D = 3.92 \times 10^{-10} \text{ m}^2 \cdot \text{s}^{-1}$	

The results are presented in Table V-2. The radius of molecule r_A was taken to be half of the largest length of the molecule (Figure V-8) and the molar volume V_A was determined making the assumption that the molecule is a perfect sphere of radius r_A . The two diffusion coefficients are very close to each other with less than 2 % discrepancy. The order of magnitude (10^{-10}) is consistent with the diffusivities of dissolved solids in water. The average value of $3.92 \times 10^{-10} \text{ m}^2 \cdot \text{s}^{-1}$ will be retained for further use.

V.5.2. Liquid-solid mass transfer from the liquid to the QQ media

The jar-test experiments were performed several times in the same conditions. The results are presented in Figure V-9, in terms of the total amount of Rose Bengal Lactone per unit of mass of QQ media ($q(t)$) (defined in Equation V-15).

The curves in Figure V-9 describe a very quick increase in the first hour, and then an overall slowdown until reaching the equilibrium after 24 h. This kind of trend was predictable as it is typical of a mass transfer phenomenon, in which the gradient of concentrations tends to decrease overtime, therefore, slowing down the increase of the total transferred amount.

The final amounts of Rose Bengal Lactone transferred in the QQ media after 24 h are indicated in Table V-3, for the different conditions. The comparison of the three experiments reveals that the jar-test experiment was repeatable, with less than 10 % standard deviation between the three final values of the transferred amount of Rose Bengal Lactone (Table V-3).

Table V-3 : Final amounts (q_e) of Rose Bengal Lactone transferred in the QQ media after 24 h, for three repeated experiments.

	QQ beads	QQ hollow cylinders	QQ sheets
$q_e \text{ (mg} \cdot \text{g}^{-1})$			
Experiment 1	3.01	3.10	3.02
Experiment 2	2.67	2.59	2.81
Experiment 3	2.91	2.89	2.98

The experimental data from Experiment 1 are presented in the following for illustration, but the final results will be presented for the three experiments given the considerable deviations.

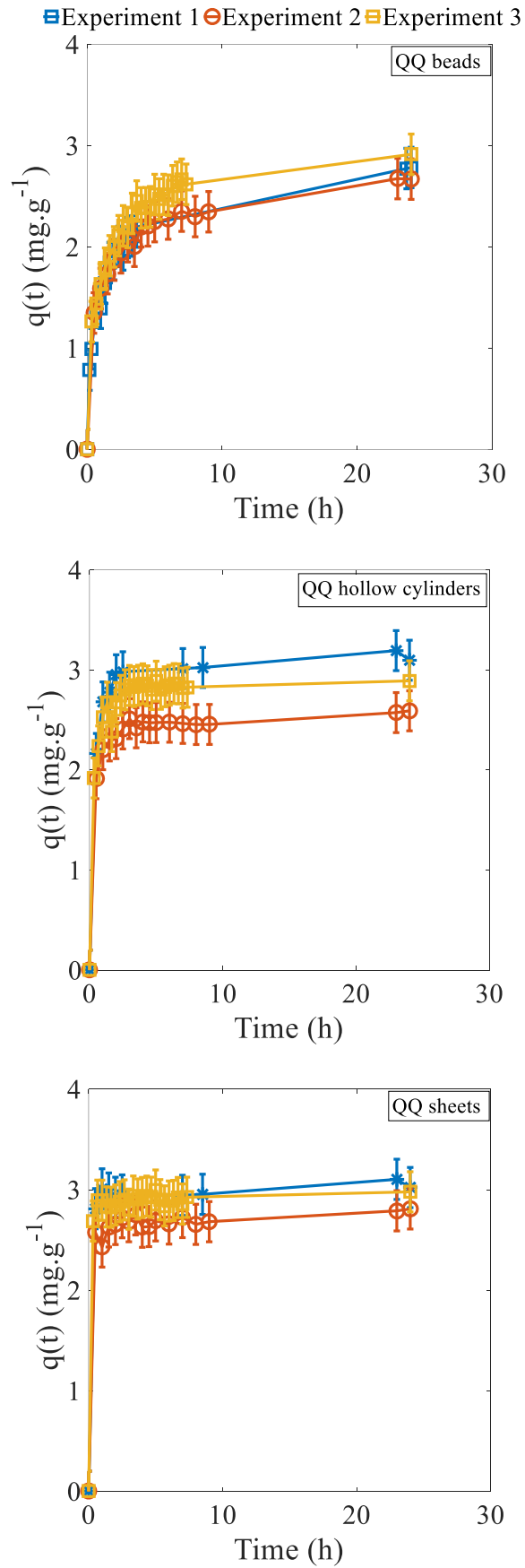


Figure V-9 : Transferred amount of Rose Bengal Lactone in the QQ sheets overtime, for three repeated experiments.

V.5.2.1. Analysis of the adsorption kinetics

The evolution of the transferred amount of Rose Bengal Lactone overtime ($q(t)$) is presented for the three QQ media shapes in Figure V-10. The comparison of the three curves suggests that the global adsorption dynamic is undeniably different for the three shapes of QQ media. In addition, the time to reach 96 % of the final value was 0.5 h and 2 h for QQ sheets and QQ hollow cylinders, respectively, whereas, for QQ beads this time was much greater with about 8.5 h.

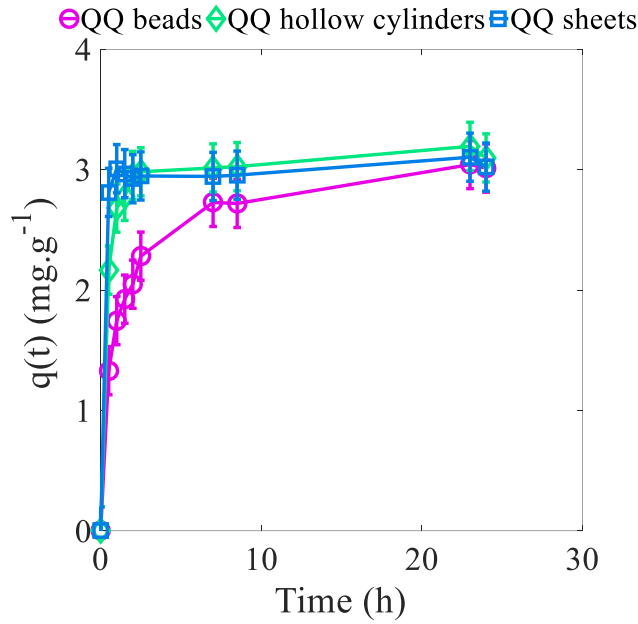


Figure V-10 : Transferred amount of Rose Bengal Lactone in the QQ media overtime (from Experiment 1).

According to the previously presented adsorption theory, the pseudo-first and pseudo-second order models were tested to describe the kinetics of the studied phenomenon. With this view, the variations of $\ln[q_e - q(t)]$ and $\frac{t}{Q}$ overtime were deduced from the experimental data and presented in Figure V-11.

As it possible to notice, the variations of $\ln[q_e - q(t)]$ overtime do not describe a linear trend, in opposition to the variations of $\frac{t}{Q}$, which suggests that the pseudo-second order model could be more appropriate ($R^2 > 0.99$) to describe the adsorption phenomenon. The parameters of the linear correlations ($y = ax + b$) are presented in Table V-4. The parameters of the pseudo-second order adsorption model (k_2 and q_e) are deduced from the correlation parameters a and b , according to the Equations V-20 and V-21 (by equating the linear correlation to Equation V-14). The same approach was conducted for the analysis of the experimental data from the Experiments 2 and 3, and the corresponding pseudo-second order model parameters are presented in Table V-4.

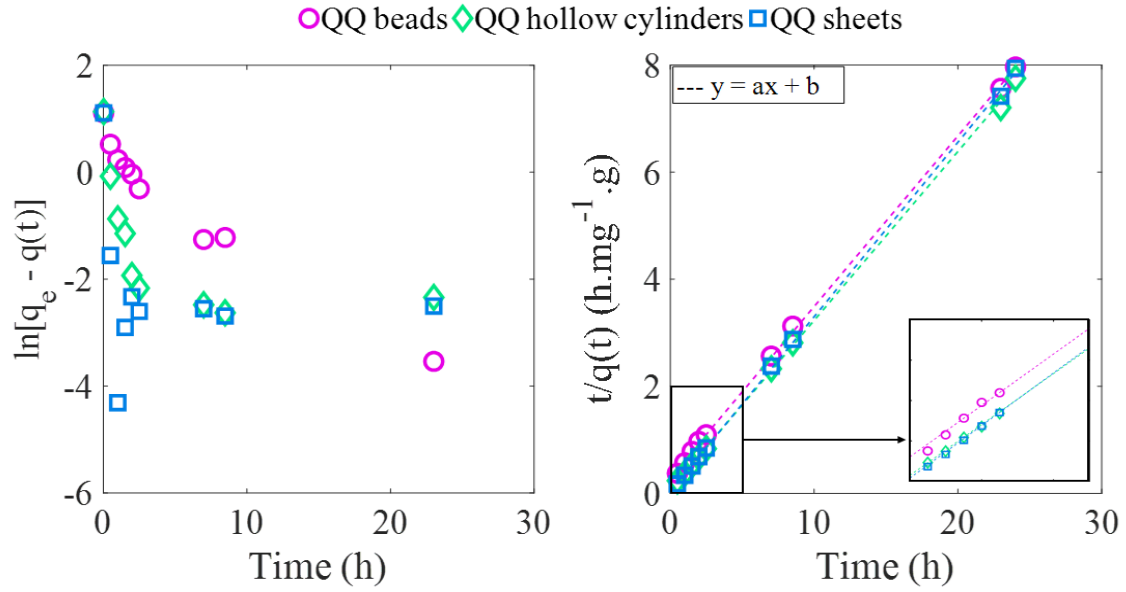


Figure V-11 : Identification of the adsorption model for the experimental data from Experiment 1.

$$q_e(\text{calculated}) = \frac{1}{a} \quad \text{V-20}$$

$$k_2 = \frac{a^2}{b} \quad \text{V-21}$$

Table V-4 : Linear correlation parameters (for Experiment 1) and parameters of the pseudo-second order kinetics model for the adsorption of Rose Bengal Lactone into QQ media.

	QQ beads	QQ hollow cylinders	QQ sheets
Linear correlation parameters ($y = ax + b$) (Experiment 1)			
a (g.mg ⁻¹)	0.3187	0.3157	0.3260
b (h.mg ⁻¹ .g)	0.3015	0.0712	0.0376
R^2	0.9996	0.9995	0.9996
Model parameters (Experiment 1)			
q_e (calculated) (mg.g ⁻¹)	3.14	3.17	3.07
q_e (experimental) (mg.g ⁻¹)	3.0 ± 0.2	3.1 ± 0.2	3.0 ± 0.2
k_2 (g.mg ⁻¹ .h ⁻¹)	0.34	1.40	2.83
k_2 (10 ⁻⁵ g.mg ⁻¹ .s ⁻¹)	9.36	38.89	78.51
$k_2 q_e$ (10 ⁻⁴ s ⁻¹)	2.94	12.33	24.10
Model parameters (Experiment 2)			
q_e (calculated) (mg.g ⁻¹)	2.77	2.60	2.81
q_e (experimental) (mg.g ⁻¹)	2.7 ± 0.2	2.6 ± 0.2	2.8 ± 0.2
k_2 (g.mg ⁻¹ .h ⁻¹)	0.33	1.51	1.77
k_2 (10 ⁻⁵ g.mg ⁻¹ .s ⁻¹)	9.26	41.95	49.22
$k_2 q_e$ (10 ⁻⁴ s ⁻¹)	2.57	10.91	13.83
Model parameters (Experiment 3)			
q_e (calculated) (mg.g ⁻¹)	3.01	2.91	2.98
q_e (experimental) (mg.g ⁻¹)	2.9 ± 0.2	2.9 ± 0.2	3.0 ± 0.2
k_2 (g.mg ⁻¹ .h ⁻¹)	0.35	2.34	3.32
k_2 (10 ⁻⁵ g.mg ⁻¹ .s ⁻¹)	9.60	64.90	92.18
$k_2 q_e$ (10 ⁻⁴ s ⁻¹)	2.89	18.89	27.47

It appears first that the calculated maximal amounts q_e of Rose Bengal Lactone adsorbed at the equilibrium (also representing the adsorption capacities of the QQ media), are very close to the experimental values reached after 24 h (Table V-4), with less than 5 % discrepancies, which confirms that the studied phenomenon reached the stable state at 24 h, even for the QQ beads.

When comparing the final amounts q_e reached for the three shapes in each experiment, very small differences are observed, since the three (experimental) values are less than 5 % different. This finding indicates that the shape of the QQ media has no effect on their adsorption capacities, which is logical since the media are made from the same material.

However, significant differences appear in the pseudo-second-order rate constant of adsorption k_2 (representing the adsorbed flux per unit of mass of QQ media), since it was found to be, respectively, 12 and 24 times greater for the QQ hollow cylinders and sheets, than for the QQ beads (Table V-4). This trend is confirmed by the observation of the adsorption rate index ($q_e k_2$) defined by Wu et al. (2009), which purely reflects the kinetic performance of the system [161]. Thus, considering the same volume of QQ media, the adsorption kinetic performance for QQ sheets is considerably greater than for the QQ hollow cylinders and beads.

Non-negligible differences in the pseudo-second order parameters (k_2 and calculated q_e) can be observed between the three replicated experiments because of the repeatability problem, however the conclusions about the comparison of the three shapes of QQ media remain valid.

In sum, these results put together are of importance because they indicate that the difference observed in the adsorption kinetics between the three QQ media (Figure V-10) cannot be attributed to different adsorption capacities. Knowing that the adsorption phenomenon involves a succession of mechanisms (external mass transfer, internal mass transfer, pore diffusion...), and that the constant k_2 englobes all of these mechanisms, these results prove that the differences between the three shapes of QQ media originate necessarily in, at least, one of the steps.

V.5.2.2. Analysis of the external liquid-solid mass transfer mechanism

According to the theory previously presented (V.4.1.2), the external mass transfer was studied on the basis of the evolution of the concentration in the liquid phase $C_l(t)$, which is presented in Figure V-12. This approach is based on the assumption that the concentration in the liquid $C_l(t)$ is uniform.

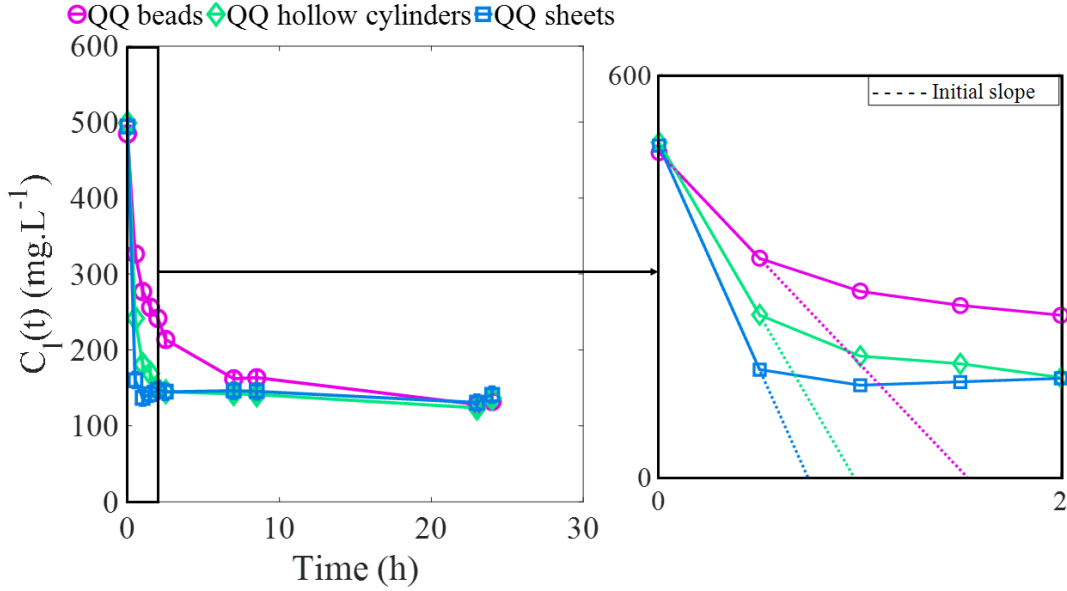


Figure V-12 : Concentration of the Rose Bengal Lactone in the liquid phase overtime for the Experiment 1.

In order to evaluate the external mass transfer coefficient, the initial slopes $(\frac{dC_l(t)}{dt})_{t=0}$ for each curve were determined (Figure V-12), and used to calculate the external mass transfer k_{ls} via Equation V-17, and resulting in Equation V-22. The results are presented in Table V-5.

$$k_{ls} = -\frac{V_l}{S_s C_l(t_0)} \left(\frac{dC_l(t)}{dt} \right)_{t=0} \quad \text{V-22}$$

Table V-5 : External liquid-solid mass transfer parameters for the three QQ media shape (under 90 rpm and solid:liquid ratio of 1:9).

	QQ beads	QQ hollow cylinders	QQ sheets
Experiment 1			
S_s (m ²)	0.100	0.135	0.234
$C_l(t = 0)$ (mg.L ⁻¹)	484	499	495
$(\frac{dC_l(t)}{dt})_{t=0}$ (mg.L ⁻¹ .h ⁻¹)	- 316	- 514	- 668
$k_{ls}S_s$ (10 ⁻⁷ m ³ .s ⁻¹)	0.95	1.51	1.98
k_{ls} (10 ⁻⁶ m.s ⁻¹)	0.95	1.12	0.85
Experiment 2			
S_s (m ²)	0.086	0.115	0.200
$C_l(t = 0)$ (mg.L ⁻¹)	424	409	436
$(\frac{dC_l(t)}{dt})_{t=0}$ (mg.L ⁻¹ .h ⁻¹)	- 320	- 455	- 612
$k_{ls}S_s$ (10 ⁻⁷ m ³ .s ⁻¹)	0.94	1.39	1.75
k_{ls} (10 ⁻⁶ m.s ⁻¹)	1.12	1.21	0.88
Experiment 3			
S_s (m ²)	0.086	0.115	0.200
$C_l(t = 0)$ (mg.L ⁻¹)	506	492	503
$(\frac{dC_l(t)}{dt})_{t=0}$ (mg.L ⁻¹ .h ⁻¹)	- 300	- 456	- 639
$k_{ls}S_s$ (10 ⁻⁷ m ³ .s ⁻¹)	1.14	1.74	2.38
k_{ls} (10 ⁻⁶ m.s ⁻¹)	1.30	1.51	1.19
Average values over the three experiments \pm standard deviation			
$k_{ls}S_s$ (10 ⁻⁷ m ³ .s ⁻¹)	1.0 \pm 0.1	1.5 \pm 0.2	2.0 \pm 0.2
k_{ls} (10 ⁻⁶ m.s ⁻¹)	1.1 \pm 0.2	1.3 \pm 0.2	1.0 \pm 0.2

The product $k_{ls}S_s$, representing the transferred flux, describes the same trend as the adsorption kinetics parameters, since it was found to be greater for QQ sheets than for QQ hollow cylinders and beads. Despite the 30 % uncertainty in the product $k_{ls}S_s$, the differences between the three shapes are significant (on average 50 % between the beads and cylinders, and 33 % between the cylinders and sheets). This result confirms the assumptions that were made in the adsorption analysis indicating that the shape of QQ media induces significant differences in the external mass transfer step of the whole phenomenon. In particular, the external mass transfer is governed by the external surface of the QQ media, which explains the greater flux obtained for the QQ sheets.

In addition, the external mass transfer coefficient k_{ls} was determined for the three shapes (Table V-5). On average, a 18 % difference between the mass transfer coefficients of the QQ beads and hollow cylinders was found, and a 30 % difference between the QQ hollow cylinders and sheets, which can be viewed as insignificant (≤ 30 %). Therefore, the external mass transfer coefficient for the three shapes of QQ media can be considered as similar, which is consistent with the fact that the hydrodynamics conditions created in the jar-test were identical.

V.5.2.3. *Identification of the prevailing mechanism*

With the determination of the external liquid-solid mass transfer coefficient as well as the diffusion coefficient of Rose Bengal in water, the Sherwood number could be determined for each condition according to Equation V-8. In order to take into account the fact that the transfer occurs from all around the QQ media to the center of it, the characteristic length L in Equation V-8 was taken to be the radius for the QQ beads, and half of the thickness for both the QQ hollow cylinders and sheets. The results were obtained taken the average values of k_{ls} from Table V-5, and are presented in Table V-6. According to the literature, the external convective mass transfer step is completely prevailing for $Sh < 0.5$, whereas the diffusion is significantly prevalent for $Sh > 10$ [156].

Table V-6 : Sherwood numbers for the mass transfer of Rose Bengal Lactone from the liquid to the different shapes of QQ media.

	QQ beads	QQ hollow cylinders	QQ sheets
L (10^{-3} m)	1.75	0.45	0.25
D (10^{-10} m ² .s ⁻¹)		3.92	
k_{ls} (10^{-6} m.s ⁻¹)	1.1	1.3	1.0
Sh	4.9	1.5	0.6

In the present case, the Sherwood numbers roughly ranged between 0.5 and 5, which is comprised between 0.5 and 10, and thus, indicates there is no strong predominance of one mechanism over another, under the investigated conditions. This result shows that the internal diffusion as well as the external convection can be considered as two mechanisms of equivalent importance, both governing the overall transport of molecules from the bulk to the QQ media. In addition, when comparing the three shapes of QQ media, the greatest Sherwood number is obtained for the QQ beads, which means that the internal diffusion in this shape is more significant than for the other two shapes.

V.5.2.4. *Concluding remarks on the liquid-solid mass transfer from the liquid to the QQ media*

Two different approaches were adopted to analyze the transfer phenomenon: the adsorption approach and the external mass transfer approach. The analysis of the adsorption phenomenon allowed confirming that the adsorption capacities are the same for the three shapes of QQ media, and that the observed differences in the global adsorption coefficient are due to the mass transfer mechanisms.

The analysis of the external mass transfer mechanism revealed that this step was, indeed, different for the three shapes of QQ media. For the same introduced volume of QQ media, the transferred flux from the liquid to the surface of the QQ sheets was found to be, on average, 1.3 times and 2 times greater than for the QQ hollow cylinders and beads, respectively, because of the greater exchange surface of QQ

sheets (1.7 and 2.3 bigger than that of the hollow cylinders and beads, respectively). However, the external mass transfer coefficient k_{ls} was found to be in the same order of magnitude for the three shapes of QQ media, due to the identical hydrodynamics conditions.

The determination of the Sherwood number also provided clues about the internal diffusion phenomenon in the three shapes of QQ media, which is valuable to explain the observed differences, and the fact that the global transfer phenomenon seems to be less significant for the QQ beads. It appeared that the internal diffusion was more important in presence of QQ beads than for the other two shapes (Table V-6). This can be clearly attributed to a shape effect as illustrated in Figure V-13. As the QQ sheets and hollow cylinders are thin, the internal diffusion is facilitated. On the other hand, the internal polymeric structure of the QQ beads is thicker, which slows down the internal diffusion and consequently, affects the renewal of the concentration at the surface of the QQ media $C_s(t)$ (Figure V-13).

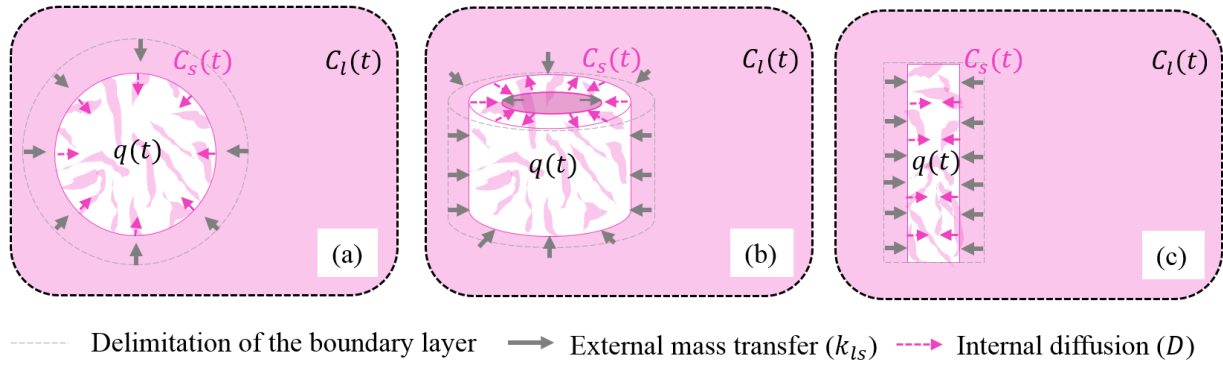


Figure V-13 : Illustrative representation of the liquid-solid mass transfer of the Rose Bengal Lactone from the liquid to the QQ (a) beads (b) hollow cylinders and (c) sheets.

In order to verify this explanation, the concentration $C_s(t)$ was deduced via the discretization of Equation V-16 that results in Equations V-23 and V-24. The evolution of $C_s(t)$ is presented in Figure V-14, and reveals that the concentration at the surface of the QQ beads is indeed higher than for the two other shapes. Considering that the hydrodynamics conditions were identical for the three shapes, this difference confirms the aforementioned effect of the shape.

$$\frac{V_l \Delta C_l(t)}{\Delta t} = -k_{ls} S_s (C_l(t) - C_s(t)) \quad \text{V-23}$$

$$C_s(t) = C_l(t) + \frac{V_l \Delta C_l(t)}{k_{ls} S_s \Delta t} \quad \text{V-24}$$

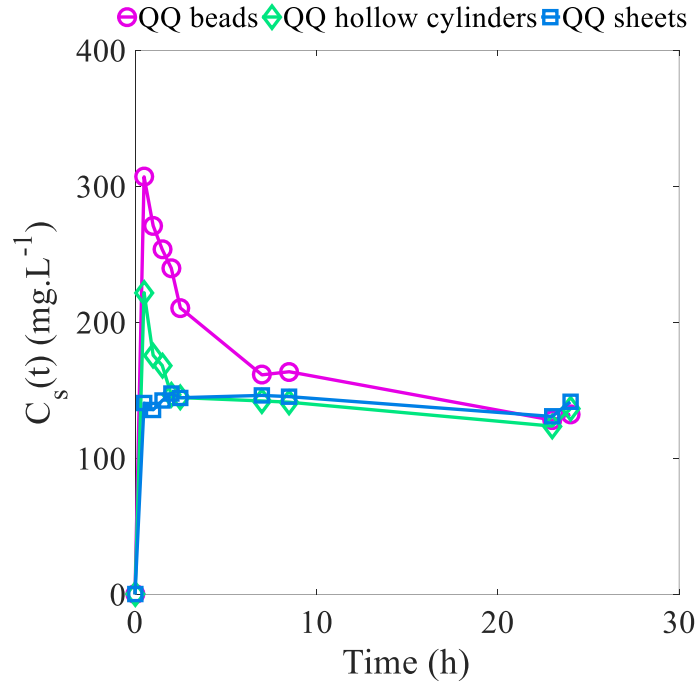


Figure V-14 : Concentration of the Rose Bengal Lactone at the surface of the QQ media overtime.

To conclude, with the perspective to apply QQ for biofouling mitigation by using endo-enzyme producing bacteria (such as *Rhodococcus* sp. BH4), the (external) mass transfer of AHLs from the mixed liquor towards the core of the QQ media could be favored in presence of QQ sheets in terms of transferred flux ($k_{ls}S_s$) rather than with the other two shapes for the same volume of QQ media. The QQ beads seem to be the least favorable shape for the mass transfer: not only their small surface gives rise to the lowest transferred flux ($k_{ls}S_s$) (in comparison to the other shapes), but also their great diameter slows down the internal transfer step. Considering that QQ is based on an enzymatic reaction, further investigation is needed in order to know whether the transferred flux or the transfer kinetics of AHLs (substrate) towards QQ enzymes is the key-parameter to promote with the view to reducing effectively biofilm formation.

V.5.3. Solid-liquid mass transfer from the QQ media to the liquid

In the following the mass transfer from the QQ media to the liquid phase was studied in the ALMBR under different aeration conditions, in order to evaluate how the hydrodynamics and the QQ shape could influence the transfer. However, before analyzing the results, it is worth mentioning that, in the case of this study, it can be assumed that the hydrodynamics is involved at several levels in the mass transfer phenomenon:

- By promoting the turbulence in the liquid phase, it can reduce the space gradient of concentration in the liquid phase between the surface of the QQ media and the bulk, and thus, accelerate the mass transfer phenomenon.
- At the local scale it can enhance the QQ media motion, and therefore favor the fast renewal of the liquid boundary layer around the QQ media.
- At the global scale, it affects the proportion of fluidized QQ media in the reactor, affecting, in particular, the exchange surface between the QQ media and the liquid phase.

Therefore, it can be assumed that the effect of hydrodynamics on the global mass transfer is complex because of the coupling of all these phenomena.

The fluidization rates determined in Chapter III under different conditions are recalled in Table V-7, and the corresponding fluidized surfaces S_{FM} and volumes V_{FM} are deduced in each case. Also, the amount m_0 of Rose Bengal Lactone initially adsorbed on the QQ media prior to each experiment is indicated, since variations could be observed from one experiment to another.

Table V-7 : QQ media properties in the QQ-ALMBR under different air flowrates.

SADm (Nm ³ .h ⁻¹ .m ⁻²)	0.75			0.90			1.00		
QQ media	Beads	Hollow cylinders	Sheets	Beads	Hollow cylinders	Sheets	Beads	Hollow cylinders	Sheets
m_0 (mg)	156.8	155.8	159.9	141.8	137.3	147.4	138.1	200	194
Total exchange surface S_s (m ²)	0.086	0.115	0.200	0.086	0.115	0.200	0.086	0.135	0.234
Total volume of QQ media V_s (10 ⁻⁵ m ³)					5.85				
Total number of QQ media N_{TM}	2600	298	585	2600	298	585	2600	298	585
Fluidization rate (%)	6.2	26.2	30.1	10.9	53.2	47.8	16.1	63.3	55.9
Fluidized surface S_{FM} (m ²)	0.0062	0.0354	0.0704	0.0109	0.0718	0.1118	0.0161	0.0845	0.1308
Fluidized volume V_{FM} (10 ⁻⁵ m ³)	0.31	1.53	1.76	0.64	3.11	2.79	0.94	3.70	3.27
Fluidized number media N_{FM}	161	78	176	283	158	279	418	188	327

V.5.3.1. *Effect of the hydrodynamics on the solid-liquid mass transfer*

Using the camera and the image processing, the concentration of Rose Bengal Lactone overtime was monitored when stained QQ media were introduced in the ALMBR, under the conditions presented in Table V-7. The results are presented in Figure V-15, in terms of normalized amount of Rose Bengal Lactone ($\frac{C_l(t)V_l}{m_0}$) released to the liquid overtime.

It is first possible to observe that the overall aspect of the curves describes a quick increase at the beginning and then tend to reach a stable value. This kind of trend is logical since the mass transfer is in this case driven by the difference of concentrations between the solid and the liquid, which tends to be attenuated overtime, inducing a slowdown of the phenomenon. The overall mass transfer phenomenon appears to be relatively slow, since all the experiments lasted more than 24 h.

The time necessary to approach the equilibrium (the moment t_e at which the normalized concentration reaches 96 % of its final value) was measured for each condition and the results are gathered in Table V-8. When comparing the times t_e for the three shapes of QQ media, minimal differences are observed between the three different air flowrates, suggesting that the global transfer dynamics is not significantly affected by the aeration in the investigated range of air flowrates.

Table V-8 : Time t_e required to reach 96 % of the equilibrium of solid-liquid mass transfer for the three shapes of QQ media.

	Beads			Hollow cylinders			Sheets		
SADm (Nm³.h⁻¹.m⁻²)	0.75	0.90	1.00	0.75	0.90	1.00	0.75	0.90	1.00
t_e (h)	32.8	27.2	31.6	6.8	8.2	8.9	3.6	4.3	4.4

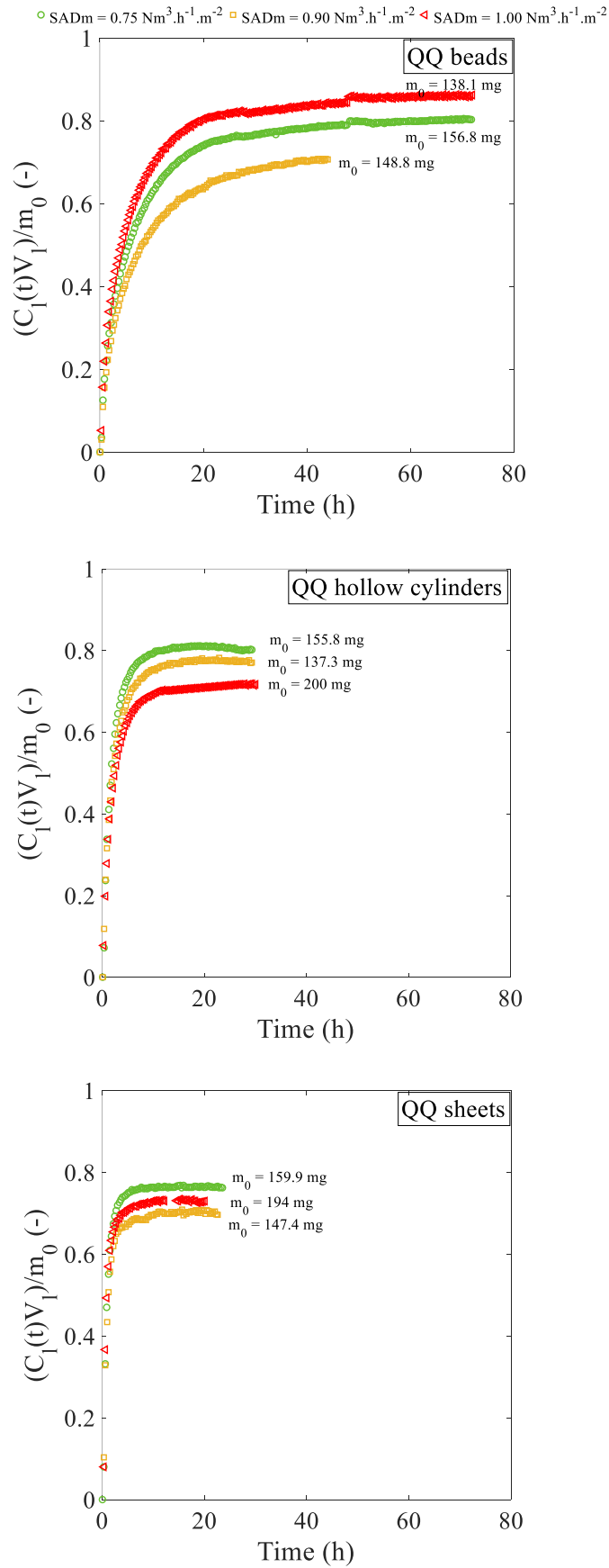


Figure V-15 : Effect of the hydrodynamics on the normalized released amount of Rose Bengal Lactone in the liquid phase for the three different shapes of QQ media.

In addition, the solid-liquid mass transfer parameters (k_{sl} and $k_{sl}S_{exchange}$, where $S_{exchange}$ is the exchange surface between the QQ media and the liquid phase) were determined considering the initial conditions ($t \rightarrow 0$) and according to the approach previously explained (Equations V-18 and V-19). The initial slopes of the curves $C_l(t)$ were determined over the 10 first points (the first 90 s of the operation) for each condition, and one example is presented in Figure V-16 for the mass transfer from the QQ beads to the liquid under the three investigated air flowrates.

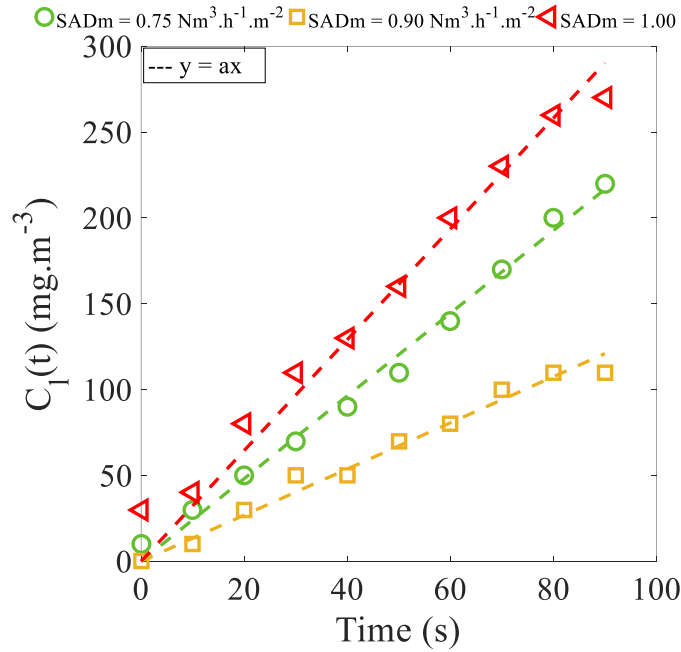


Figure V-16 : Initial (over the first 90 s) evolution of the concentration of Rose Bengal Lactone in the liquid phase from QQ beads under three air flowrates.

For the three air flowrates, a linear trend curve in which a is the slope is determined, to further deduce the mass transfer parameters as in Equation V-19. The correlation parameters as well as the mass transfer parameters are gathered in Table V-9 for this case. Using the same approach, the mass transfer parameters obtained for the QQ hollow cylinders and sheets are presented in Table V-9 as well.

Table V-9 : Parameters of the kinetics model and Sherwood numbers for the solid-liquid mass transfer of Rose Bengal Lactone from the QQ media to the liquid under different air flowrates (*the Sh numbers were calculated with the diffusion coefficient $D = 3.92 \times 10^{-10} \text{ m}^2 \cdot \text{s}^{-1}$*).

SADm ($\text{Nm}^3 \cdot \text{h}^{-1} \cdot \text{m}^{-2}$)	0.75	0.90	1.00
Linear correlation parameters ($y = ax$) for QQ beads			
a ($\text{mg} \cdot \text{m}^{-3} \cdot \text{s}^{-1}$)	2.408	1.344	3.226
R^2	0.9919	0.9788	0.9722
Solid-Liquid mass transfer parameters for QQ beads			
$k_{sl} S_{exchange}$ ($10^{-8} \text{ m}^3 \cdot \text{s}^{-1}$)	1.00	0.62	1.52
k_{sl} (considering S_s) ($10^{-7} \text{ m} \cdot \text{s}^{-1}$)	1.17	0.72	1.78
k_{sl} (considering S_{FM}) ($10^{-7} \text{ m} \cdot \text{s}^{-1}$)	18.82	6.81	11.04
L (10^{-3} m)		3.50	
Sh (considering S_s) (-)	1.04	0.66	1.59
Sh (considering S_{FM}) (-)	16.80	6.08	9.86
Solid-Liquid mass transfer parameters for QQ hollow cylinders			
$k_{sl} S_{exchange}$ ($10^{-8} \text{ m}^3 \cdot \text{s}^{-1}$)	2.16	1.70	1.87
k_{sl} (considering S_s) ($10^{-7} \text{ m} \cdot \text{s}^{-1}$)	1.88	1.48	1.39
k_{sl} (considering S_{FM}) ($10^{-7} \text{ m} \cdot \text{s}^{-1}$)	7.16	2.86	2.20
L (10^{-3} m)		0.90	
Sh (considering S_s) (-)	0.43	0.35	0.32
Sh (considering S_{FM}) (-)	1.65	0.66	0.50
Solid-Liquid mass transfer parameters for QQ sheets			
$k_{sl} S_{exchange}$ ($10^{-8} \text{ m}^3 \cdot \text{s}^{-1}$)	4.03	3.23	4.58
k_{sl} (considering S_s) ($10^{-7} \text{ m} \cdot \text{s}^{-1}$)	2.02	1.62	1.95
k_{sl} (considering S_{FM}) ($10^{-7} \text{ m} \cdot \text{s}^{-1}$)	6.63	3.37	3.50
L (10^{-3} m)		0.50	
Sh (considering S_s) (-)	0.26	0.21	0.25
Sh (considering S_{FM}) (-)	0.85	0.43	0.45

The observation of the transferred flux $k_{sl} S_{exchange}$ reveals no clear effect of the aeration, in the investigated range, since different trends are described for the three shapes of QQ media.

The determination of the mass transfer coefficient k_{sl} requires dividing the transferred flux that was measured by the exchange surface $S_{exchange}$ to compare the transfer kinetics. However, in the present case, the exact exchange surface is hard to evaluate, since it depends on the fluidization of the QQ media, as previously mentioned. Therefore, two possible limit-cases could be considered for discussion: in the first case, the exchange surface corresponds to the total surface S_s of QQ media introduced in the reactor whether they are fluidized or settled. In the second case, the exchange surface only corresponds to the surface S_{FM} of the fluidized QQ media. The mass transfer coefficients were calculated in both cases (Table V-9) and also represented as a function of the aeration for the three shapes of QQ media in Figure V-17.

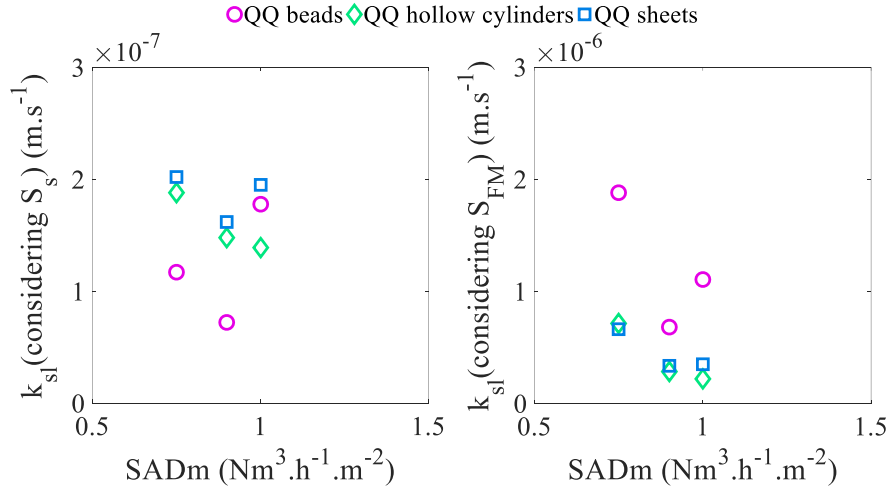


Figure V-17 : Mass transfer coefficients under different air flowrates and for the three shapes of QQ media.

Significant differences can be observed between the two considered cases. In the first case, where the totality of QQ media introduced (with the surface S_s) in the reactor take part to the global transfer, the mass transfer coefficients roughly range between 0.5×10^{-7} and $2.0 \times 10^{-7} \text{ m.s}^{-1}$. On the other hand, in the second case, where the assumption that only the fluidized QQ media (with the surface S_{FM}) participate to the global transfer, the mass transfer coefficients range between 0.2×10^{-6} and $2.0 \times 10^{-6} \text{ m.s}^{-1}$. These observations are consistent, and actually indicate that in the second case, where the number of QQ media transferring (only the fluidized ones) is lower, the mass transfer should be much faster to reach the same transferred flux as in the first case. However, the effect of the air flowrate in the investigated range on the mass transfer coefficient is still hardly identifiable, in both the considered cases.

In sum, these results show that the effect of the air flowrate on the solid-liquid mass transfer is not visible in the investigated conditions, because of the complexity of the mechanisms that are dependent on the aeration and the difficulty to assess with certainty the exchange surface. Indeed, the two considered cases are “extreme” cases, which are most likely not representative of the reality since the settled QQ media can also take part to the global transfer, and also because there is an alternation phenomenon in the fluidization (the QQ media in suspension are not necessarily the same during the whole operation). Thus, the effective exchange surface $S_{exchange}$ between the QQ media and the liquid phase should be comprised between the fluidized surface and the total surface of QQ media ($S_{FM} < S_{exchange} < S_s$).

V.5.3.2. Effect of QQ media shape on the mass transfer

Because the initial conditions were different from one experiment to another, and the levels reached at the equilibrium were different for the three shapes of QQ media (Figure V-15), the concentration curves were normalized with respect to the final value ($\frac{C_l(t)}{C_l(t_\infty)}$) and presented in Figure V-18, in order to only take into account the dynamics of the transfer phenomenon (independently from the transferred amounts).

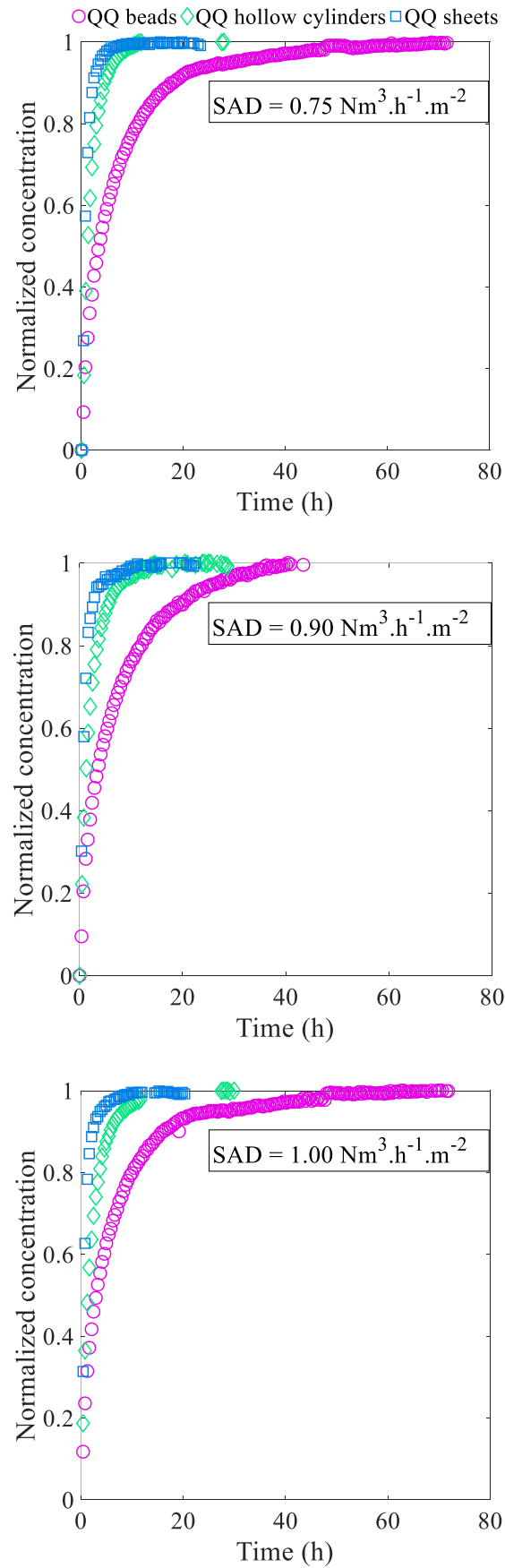


Figure V-18 : Effect of the shape of the QQ media on the normalized concentrations of Rose Bengal Lactone in the liquid phase for the three different air flowrates.

The effect of the QQ media shape can be firstly determined by visualizing the curves, since it clearly appears that the overall dynamics is faster for the QQ sheets than for the QQ hollow cylinders and beads. This can be confirmed by the comparison of the times t_e necessary to reach 96 % of the equilibrium presented in Table V-8. It appears that the time to reach the equilibrium for the QQ beads is approximately 3 times and 9 times greater than the one for the QQ hollow cylinders and sheets, in the investigated range of air flowrates. In the case of QQ beads, the curves presented in Figure V-18 reveal that the equilibrium is not completely reached and that the mass transfer keeps on evolving very slowly, which can be due to their thicker diameter and thus slower internal mass transfer.

The mass transfer parameters determined in Table V-9 show that significant differences are obtained in the transferred flux $k_{sl}S_{exchange}$ for the three shapes. As an example, for an SADm of $1.00 \text{ Nm}^3 \cdot \text{h}^{-1} \cdot \text{m}^{-2}$ (corresponding to the highest fluidization rates) the transferred flux $k_{sl}S_{exchange}$ in presence of QQ sheets is up to 3 and 4 times greater than that of QQ beads and QQ hollow cylinders, respectively. In terms of mass transfer coefficient k_{sl} the differences between the three shapes of QQ media depend on which of the two aforementioned cases is considered.

In sum, it appears that for the same volume of QQ media introduced in the reactor, the mass transfer phenomenon is considerably enhanced in presence of QQ sheets compared to the other shapes, in terms of time to reach the equilibrium as well as transferred flux. In addition, the times t_e needed to reach the equilibrium for QQ sheets is only around 4 h, which represents one third of the residence time (12 h) of the ALMBR (Chapter IV), whereas the time needed for the QQ beads (about 30 h) is at least 2.5 times greater than the residence time. These results suggest that, among the three shapes of QQ media, sheets would be the most favorable shape to enhance the mass transfer phenomenon from the QQ media to the liquid phase, and thus to fastly mitigate fouling via the QQ activity.

V.5.3.3. *Identification of the prevailing mechanism*

The Sherwood numbers were determined according to the Equation V-8 for each QQ media shape, and gathered in Table V-9. Again, two cases were considered, corresponding to the two exchange surfaces.

When the total surface S_s is taken into account, the Sherwood numbers range from 0.2 and 1.6 for the different QQ media shapes under the different air flowrates. According to the literature, the fact that the Sherwood numbers are lower than 0.5 (in this case for QQ hollow cylinders and sheets) indicates that the diffusion mechanism is very fast compared to the external mass transfer step in the investigated conditions, and that the diffusion time can be negligible. However, for the QQ beads ($0.6 < Sh < 1.6$) the internal diffusion is not negligible, which confirms the fact that the equilibrium was never completely reached in the investigated conditions.

When the fluidized surface S_{FM} is considered, the Sherwood numbers are much greater and range from 0.4 to 17. In most cases, the Sherwood numbers are comprised between 0.5 and 10 (except for the QQ

beads under $0.75 \text{ Nm}^3\cdot\text{h}^{-1}\cdot\text{m}^{-2}$) which, according to the literature, indicates that there is no clear prevalence of one mechanism over the other. However, in the particular case of the beads under an SADm of $0.75 \text{ Nm}^3\cdot\text{h}^{-1}\cdot\text{m}^{-2}$, the Sherwood number is worth 16.80 (> 10) which refers to a slow diffusion step.

In all the cases (whatever is the considered exchange surface), the Sherwood numbers obtained for the QQ beads is much greater than for the other two shapes, which undeniably shows that the diffusion into the QQ beads is slower because of their diameter.

V.5.3.4. Concluding remarks on the solid-liquid mass transfer from the QQ media to the liquid phase

The development of the camera technique turned out to be relevant to study the solid-liquid mass transfer from the QQ media to the liquid phase of the aerated part of the ALMBR.

The comparison of the investigated air flowrates led to the conclusion that no notable effect on the solid-liquid mass transfer coefficient was observed in the studied conditions. This result could be explained by the fluctuations in the fluidization of QQ media during the experiment and the difficulty to evaluate the effective exchange surface, which made difficult the precise determination of a mass transfer coefficient.

Concerning the effect of the QQ media shape, it was found that the QQ sheets gave rise to greater mass transfer phenomenon with the shortest time to reach the equilibrium and the greatest transferred flux. With the view to applying QQ to reduce membrane biofouling, QQ sheets can therefore be the most appropriate shape in the case of exo-enzyme-producing QQ bacteria (*Pseudomonas* sp. 1A1, for example). Indeed, the exo-enzyme produced in the core of the QQ sheets could rapidly transfer out of it to reach and degrade the AHLs present in the mixed liquor.

Finally, the determination of the Sherwood number in the investigated conditions, demonstrated that the overall phenomenon is clearly limited by the external mass transfer step over the internal diffusion in the QQ media. Nevertheless, when comparing the three shapes of QQ media it appears that the diffusion can again be a little more important in the case of QQ beads, the same way it was for the liquid-solid mass transfer (Figure V-13), because of their greater diameter.

V.6. Conclusions and perspectives

In this chapter, an attempt was made to characterize quantitatively the mass transfer phenomena that can be involved in the application of QQ, whether it is based on an endo-enzyme-producing QQ bacteria or an exo-enzyme-producing one. For that purpose, two main kinds of mass transfer were distinguished for the study: the liquid-solid mass transfer to mimic the transport of AHLs from the mixed liquor to the inner part of QQ media; and the solid-liquid mass transfer to mimic the transport of exo-enzymes from the QQ media to the mixed liquor. Using a model (dye) molecule under different hydrodynamics conditions, the mass transfer kinetics were characterized to come to the following main conclusions:

- First, the selected tools for the characterization of the mass transfer turned out to be efficient for the study of the mass transfer. The experimental setups as well as the theoretical approaches allowed getting relevant information about both kinds of mass transfer.
- The study of the liquid-solid mass transfer in jar-tests allowed determining mass transfer coefficients in the order of magnitude of 10^{-6} m.s^{-1} . The results brought into light that both of the QQ sheets and hollow cylinders can be the appropriate shapes to favor for an efficient mass transfer of AHLs from the mixed liquor to the entrapped endo-enzyme producing bacteria, in terms of transferred flux under similar hydrodynamics conditions. For the QQ beads, the liquid-solid mass transfer was found to be less efficient because their specific shape makes the internal diffusion step weigh more heavily on the overall transfer phenomenon.
- The study of the solid-liquid mass transfer in the aerated ALMBR was performed under different air flowrates for the three shapes of QQ media. The effect of the air flowrate on the mass transfer coefficient was hardly quantifiable because of the difficulty to assess the effective exchange surface. However, the effect of the QQ shape could be determined and the most favorable shape appears to be QQ sheets in terms of transferred flux. In the case of exo-enzyme-producing bacteria entrapped in the QQ media, the transfer of exo-enzymes could be more efficient for QQ sheets than for QQ hollow cylinders and beads.
- The investigation of the two kinds of mass transfer gave interesting insights for the QQ application. Actually, the mass transfer coefficient for liquid-solid transfer (in the jar-test) was found to be in the order of magnitude of 10^{-6} , whereas the solid-liquid transfer (in the aerated ALMBR) was 10^{-7} . The two mass transfer coefficients are not directly comparable because they were obtained under different hydrodynamic conditions, but this indicates that the mechanical stirring can provide better hydrodynamics conditions to foster the mass transfer.
- In all the cases, the QQ beads were found to give rise to the smallest transferred flux compared to the other two shapes. However, when considering the fluidized surface S_{FM} the mass transfer coefficient for QQ beads is greater, which means that this shape could be valuable in that case, by

increasing the surface (decreasing the diameter) and increasing their fluidization (increasing the air flowrate, decreasing their diameter and/or density).

These findings are of great importance because they open the way to an optimized application of QQ. In order to take the present results to the next step, the following propositions could be addressed as the subject for future research:

- This study provided valuable information about the different mass transfer mechanisms and their kinetics, but the QQ reaction kinetics is still unknown so far. Therefore, the study of the kinetics of the biochemical reaction could be relevant to know to which extent the optimization of the mass transfer step is important for the overall reaction.
- The study of the two kinds of mass transfer (liquid-solid and solid-liquid) was here conducted under different operating conditions due to technical limitations. A complete comparison of these two phenomena under the exact same hydrodynamic conditions could be interesting and may result in the selection of one type of QQ bacteria (either endo-enzyme or exo-enzyme-producing bacteria) for a more efficient biofouling mitigation.
- This study was performed using a dye molecule as a tracer providing global trends. Even though the trends are reliable, it is important keeping in mind that the values themselves are specific to the model molecule that was used. Thus, it could be of great interest conducting the same kind of experiments with the actual molecules involved in the QQ reaction: AHLs as a substrate, and QQ acylase or QQ lactonase as enzymes (Chapter I).
- In the case of the endo-enzyme-producing bacteria, the AHLs are expected to transfer into the QQ media. Besides, the AHLs were proved to be present in the mixed liquor of the MBR as well as they can be embedded in the structure of the biofilm formed on the membrane surface. Thus, it could be interesting to characterize the mass transfer from the membrane surface to the QQ media in addition to these results. For that purpose, a qualitative attempt was made in the present work by staining the membrane with the Rose Bengal Lactone before introducing it in the MBR in presence of fresh QQ media. The QQ media were then visually observed, and it can be seen in Figure V-19 that the Rose Bengal tends to transfer into the QQ media overtime. Also, it appears that the color is more pronounced at the surface of the QQ beads than in their inner part, which illustrates the previously mentioned internal diffusion limitation.

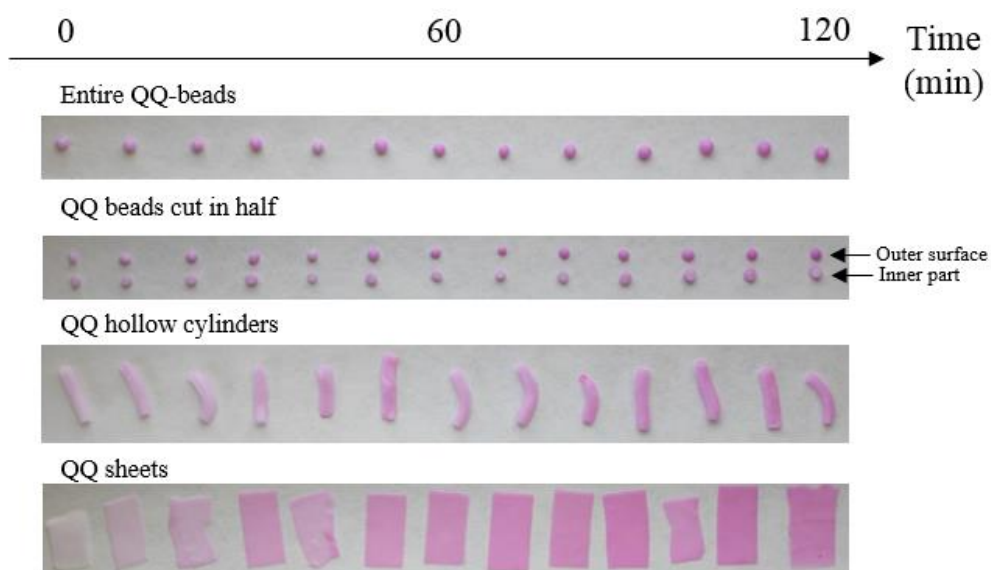


Figure V-19 : Transfer of the Rose Bengal Lactone from the surface of the membrane to the QQ media in the MBR under an SADm of $0.75 \text{ Nm}^3 \cdot \text{h}^{-1} \cdot \text{m}^{-2}$.

CHAPTER VI. EFFECT OF QQ MEDIA ON FOULING AND GENERAL DISCUSSION

RESUME EN FRANCAIS

Ce chapitre présente d'une part des résultats complémentaires de filtration, dans le but d'évaluer l'effet physique des « QQ media » sur la réduction du colmatage, et d'autre part, le lien logique existant entre tous les résultats de cette étude.

Les résultats obtenus en menant la filtration d'une suspension modèle (bentonite) dans le pilote de laboratoire, font l'objet de la première partie du chapitre. En caractérisant l'évolution du colmatage de la membrane par des mesures de perméabilité sous différentes conditions (deux différentes aérations et en présence ou non de « QQ media »), les résultats ont tout d'abord révélé qu'une différence de débit d'air entre 0.75 et 1.00 Nm³.h⁻¹.m⁻², en termes de SADm, avait peu d'effet sur le colmatage de la membrane. En présence de « QQ media », les performances de filtration ont été modifiées et des effets différents ont pu être observés suivant les conditions d'aération. Sous un SADm de 0.75 Nm³.h⁻¹.m⁻², l'ajout de « QQ media » n'a pas eu d'effet notable sur un retardement ou une réduction du phénomène de colmatage, dans les conditions opératoires considérées. Cependant, sous un SADm de 1.00 Nm³.h⁻¹.m⁻², le colmatage de la membrane a été réduit de, respectivement, 30 et 60 % en présence de « QQ media » en forme de cylindres creux et feuilles.

Par ailleurs, ces observations sur le colmatage de la membrane sont expliquées en discutant les phénomènes physiques liés à l'addition de « QQ media » au bioréacteur à membrane. En effet, les résultats obtenus dans les chapitres précédents ont été synthétisés et le lien logique entre ces résultats discuté. Une cohérence entre les différentes approches choisies dans cette étude (caractérisation hydrodynamique des phases gaz, liquide et solide, distribution des temps de séjour, temps de mélange) a ainsi été mise en évidence. Grâce à cela, il a été conclu que l'effet physique des « QQ media » pour réduire le colmatage est d'autant plus important que le taux de fluidisation est grand et que la distance des « QQ media » par rapport à la membrane est petite.

Enfin, plusieurs temps caractéristiques ont pu être déterminés tout au long de cette étude, et ont été rassemblés dans ce chapitre. En comparant ces temps, une discussion est proposée sur le fait de cibler l'étape de transfert de matière impliquée dans le processus global du QQ, comme une étape-clé à optimiser en vue d'une réduction plus efficace du colmatage.

VI.1. Introduction

The subject of this work is the application of QQ (supported by QQ media) to MBRs with the original aim to deeply understand the physical phenomena involved in it, in order to go towards an optimized technique for biofouling mitigation. So far, these physical phenomena (hydrodynamics, mass transfer) were separately considered and the effects of suspended QQ media as well as other operating parameters such as air flowrate, reactor geometry...were evaluated. However, these physical aspects are in reality interdependent and thus, cannot be completely dissociated one from another. Therefore, the need to verify the consistency of the results and their good accordance is crucial to draw firm conclusions from this work. Most of the results of this study were obtained under model conditions that definitely allowed the comparison of the different shapes of QQ media and the assessment of the effect of the operating conditions. In order to complement the previous findings, the objective of the present chapter is three-fold:

- Firstly, to characterize the membrane fouling and assess the impact of the addition of QQ media on it. With this view, the strategy is to perform filtration experiments in the ALMBR using a model suspension in order to evaluate the physical effect of the QQ media on the cake fouling. To characterize this effect, the experiments will be performed under different operating conditions (two different SADm (0.75 and $1.00 \text{ Nm}^3 \cdot \text{h}^{-1} \cdot \text{m}^{-2}$) and in presence or not of QQ media), and the permeability during the operation will be selected as the comparative criterion.
- Secondly, to identify the mechanisms involved in the effect of QQ media on fouling mitigation by summarizing the most important data from this study and find out the logical relationships that link all the observed trends together.
- Finally, considering the expected double anti-fouling effect of QQ (physical and biological), some ways of improvement for an efficient fouling control will be discussed, in particular, by presenting the characteristic times of the system, and open the discussion about the key-parameters to target for an optimized QQ application.

VI.2. Membrane fouling in the ALMBR/qq-ALMBR

In order to evaluate the extent of membrane fouling, filtration experiments were performed with a model suspension (bentonite) in the ALMBR with and without the addition of QQ media.

A bentonite suspension was prepared (around $1.0 \text{ g} \cdot \text{L}^{-1}$), characterized (size distribution) and introduced in the ALMBR under different operating conditions (two different air flowrates and in presence or not of QQ media). The reactor was run for 3 hours at a constant permeate flowrate ($1.5 \text{ L} \cdot \text{h}^{-1}$) and with a recirculation flowrate of $4 \text{ L} \cdot \text{h}^{-1}$ from the aerobic tank to the anoxic tank. In order to evaluate the fouling development, a pressure sensor was used to monitor the permeate pressure and then to deduce the TMP

variations overtime. From the TMP and permeate volume monitoring, the permeability could be obtained overtime, therefore, indicating the extent of membrane fouling.

The experiments were performed under the SADm of 0.75 and 1.00 $\text{Nm}^3 \cdot \text{h}^{-1} \cdot \text{m}^{-2}$ in order to evaluate the effect of the aeration with two sufficiently distant values. In addition, these conditions were found to be favorable for the fluidization of QQ media. More details about the whole experimental procedure (preparation of the suspension, size distribution measurement, experimental setup...etc.) are given in Chapter II.

VI.2.1. *Fouling in the ALMBR*

The results obtained in the ALMBR with no QQ media under an aeration of 0.75 $\text{Nm}^3 \cdot \text{h}^{-1} \cdot \text{m}^{-2}$ are first presented as an example in order to validate the repeatability of the method. The effect of the aeration on membrane fouling in the ALMBR is further investigated.

VI.2.1.1. *Example of results obtained under an SADm of 0.75 $\text{Nm}^3 \cdot \text{h}^{-1} \cdot \text{m}^{-2}$*

The example developed hereafter was obtained with a bentonite suspension of 1.02 $\text{g} \cdot \text{L}^{-1}$ with an average particle diameter of $17.8 \pm 0.5 \mu\text{m}$. The experiment was run under an SADm of 0.75 $\text{Nm}^3 \cdot \text{h}^{-1} \cdot \text{m}^{-2}$ and the raw results were processed according to the procedure presented in Chapter II. The evolution of the permeability (determined with a precision of around $\pm 15\%$) overtime is presented in Figure VI-1.

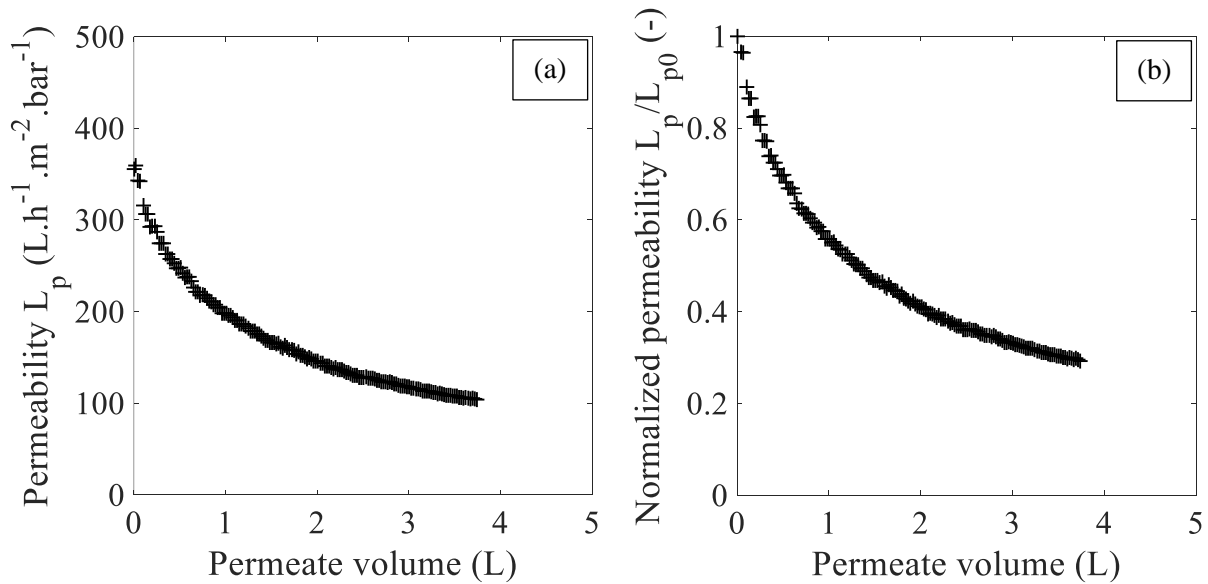


Figure VI-1 : (a) Permeability and (b) normalized permeability versus the permeate volume obtained for the filtration of bentonite in the ALMBR under an SADm of 0.75 $\text{Nm}^3 \cdot \text{h}^{-1} \cdot \text{m}^{-2}$.

In Figure VI-1, the trend of the curves is consistent with the expectations since the permeability describes an overall decrease with the increase volume of permeate, as the membrane tends to foul. Figure VI-1 also reveals that the extent of fouling is quite severe under these conditions, since the permeability loss is about 70 % after 3 h of filtration. In addition, it can be observed that the fouling phenomenon is quite quick at the beginning of the operation (with 40 % decrease in the permeability after only 35 min of operation), and then tends to slow down.

In order to characterize the reversibility of the fouling, the membrane permeability to water was measured before and after the mechanical cleaning of the membrane, and using the Equations VI-1 to VI-3.

In Equations VI-1 to VI-3, R_m , R_t and R_{irr} are respectively the membrane resistance, the total resistance and the irreversible fouling resistance, in a way that the condition expressed as in Equation VI-4 is fulfilled. The Equation VI-4 describes the model of resistances-in-series which was used as an additional indicator of the fouling extent, and in which R_{rev} is the resistance corresponding to the reversible part of fouling (removed by mechanical cleaning of the membrane).

$$L_{p,initial} = \frac{1}{\mu R_m} \quad \text{VI-1}$$

$$L_{p,fouled} = \frac{1}{\mu R_t} \quad \text{VI-2}$$

$$L_{p,cleaned} = \frac{1}{\mu(R_m + R_{irr})} \quad \text{VI-3}$$

$$R_t = R_m + R_{rev} + R_{irr} \quad \text{VI-4}$$

The proportion of each of the resistances was determined for this example of experiment and presented in Figure VI-2, in terms of percentages (the total resistance R_t corresponding to 100 %). Figure VI-2 illustrates that the fouling resulting from the experiment is quite important, since the cake resistance ($R_{rev} + R_{irr}$) is worth more than 6 times the membrane resistance R_m . However, most of this fouling was reversible and the irreversible part was only 1 % of the total resistance measured at the end of the operation.

To conclude, the selected criteria are relevant and indicative of a reversible cake-fouling phenomenon. Therefore, these indicators were kept to analyze all of the experiments in order to allow their comparison, and hence, the effect of the QQ media will be further evaluated on the reversible cake type of fouling.

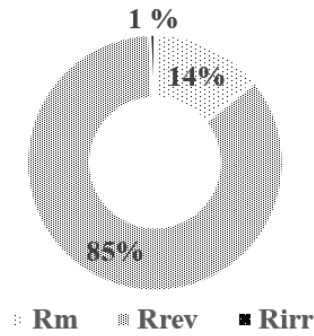


Figure VI-2 : Proportions of resistances resulting from the filtration of bentonite in the ALMBR under an SADm of $0.75 \text{ Nm}^3 \cdot \text{h}^{-1} \cdot \text{m}^{-2}$.

VI.2.1.2. *Repeatability of the experiment*

The repeatability of the experiment allows to assess the reliability of the results and the level of confidence with which the main conclusions can be drawn. For that purpose, the filtration experiment under the SADm of $0.75 \text{ Nm}^3 \cdot \text{h}^{-1} \cdot \text{m}^{-2}$ was repeated. The data of the two experiments (1 and 2) are presented in Table VI-1.

Table VI-1 : Initial conditions and results for the two identical experiments run in the ALMBR under an SADm of $0.75 \text{ Nm}^3 \cdot \text{h}^{-1} \cdot \text{m}^{-2}$.

Experiment n°	1	2	Discrepancy between the two experiments (%)
Feed (bentonite suspension) concentration (g.L ⁻¹)	1.02	0.98	4
$L_{p,initial}(20^\circ\text{C}) (\text{L} \cdot \text{h}^{-1} \cdot \text{m}^{-2} \cdot \text{bar}^{-1})$	367 ± 55	298 ± 45	19
$L_{p,fouled}(20^\circ\text{C}) (\text{L} \cdot \text{h}^{-1} \cdot \text{m}^{-2} \cdot \text{bar}^{-1})$	52 ± 8	43 ± 7	17
$L_{p,cleaned}(20^\circ\text{C}) (\text{L} \cdot \text{h}^{-1} \cdot \text{m}^{-2} \cdot \text{bar}^{-1})$	351 ± 53	336 ± 50	4

The raw results of these two experiments were processed to obtain the permeability curves presented in Figure VI-3.

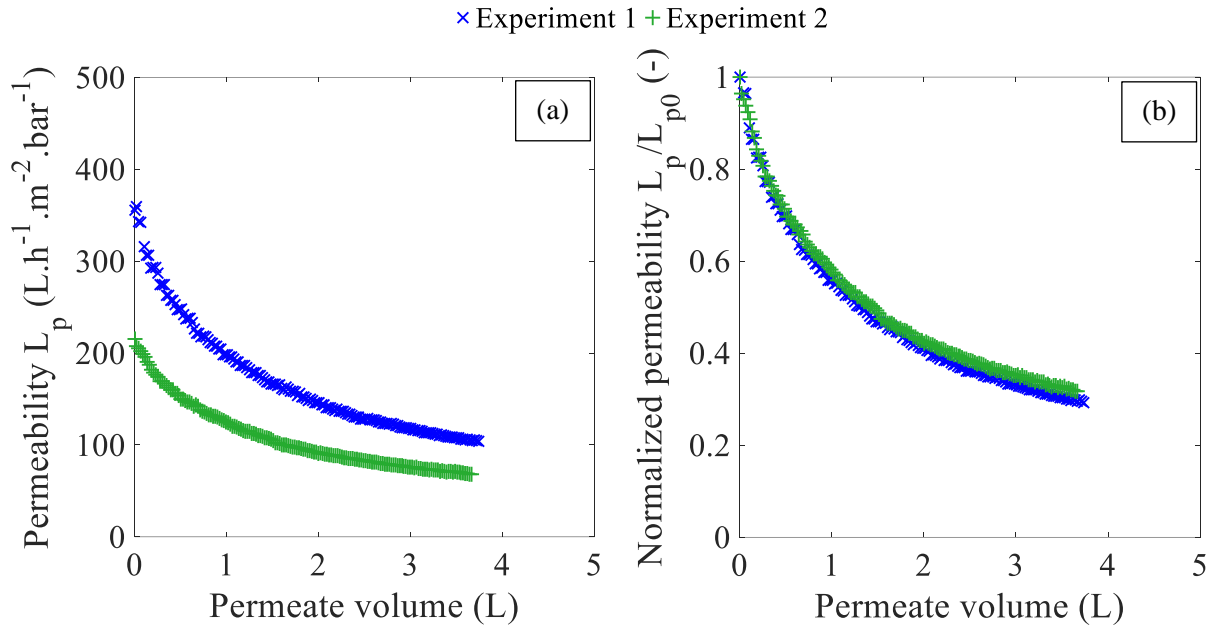


Figure VI-3 : Repeatability of the experiment conducted in the ALMBR under an SADm of 0.75 Nm³.h⁻¹.m⁻², in terms of permeability and normalized permeability versus the permeate volume.

The significant gap between the two curves observed in Figure VI-3(a), can obviously be attributed to difference in initial the permeabilities. Therefore, the permeability curves are not directly comparable, but the normalized ones are (Figure VI-3(b)), since they purely indicate the kinetics of fouling without taking into account the values of the initial permeability. When observing Figure VI-3(b), it appears that the two normalized permeability curves are very close.

In conclusion, these results confirm the repeatability of the experiment and shows that the experiments are still exploitable even though the initial permeabilities are different from one experiment to another.

VI.2.1.2.1. Effect of the aeration on fouling in the ALMBR

The effect of the air flowrate on the fouling phenomenon in the ALMBR was investigated by running two filtration experiments: one with the SADm of 0.75 Nm³.h⁻¹.m⁻² and the second one with the SADm of 1.00 Nm³.h⁻¹.m⁻². These experiments were performed with the aim to determine the role of aeration in membrane fouling, as well as, to further evaluate how this role can be affected or not in presence of QQ media.

The initial conditions of the two experiments are presented in Table VI-2.

Table VI-2 : Initial conditions for the experiments run in the ALMBR under two different air flowrates.

Experiment run under SADm ($\text{Nm}^3 \cdot \text{h}^{-1} \cdot \text{m}^{-2}$)	0.75	1.00	Discrepancy between the two experiments (%)
Feed (bentonite suspension) concentration	1.02	1.00	2
Initial permeability to water $L_{p,initial}(20^\circ \text{C})$ ($\text{L} \cdot \text{h}^{-1} \cdot \text{m}^{-2} \cdot \text{bar}^{-1}$)	367 ± 55	450 ± 68	23

The two filtration experiments were run during 3 h, and the raw results (presented in the Appendix A-VI-1) were processed as described previously to result in the normalized permeability curves presented in Figure VI-4.

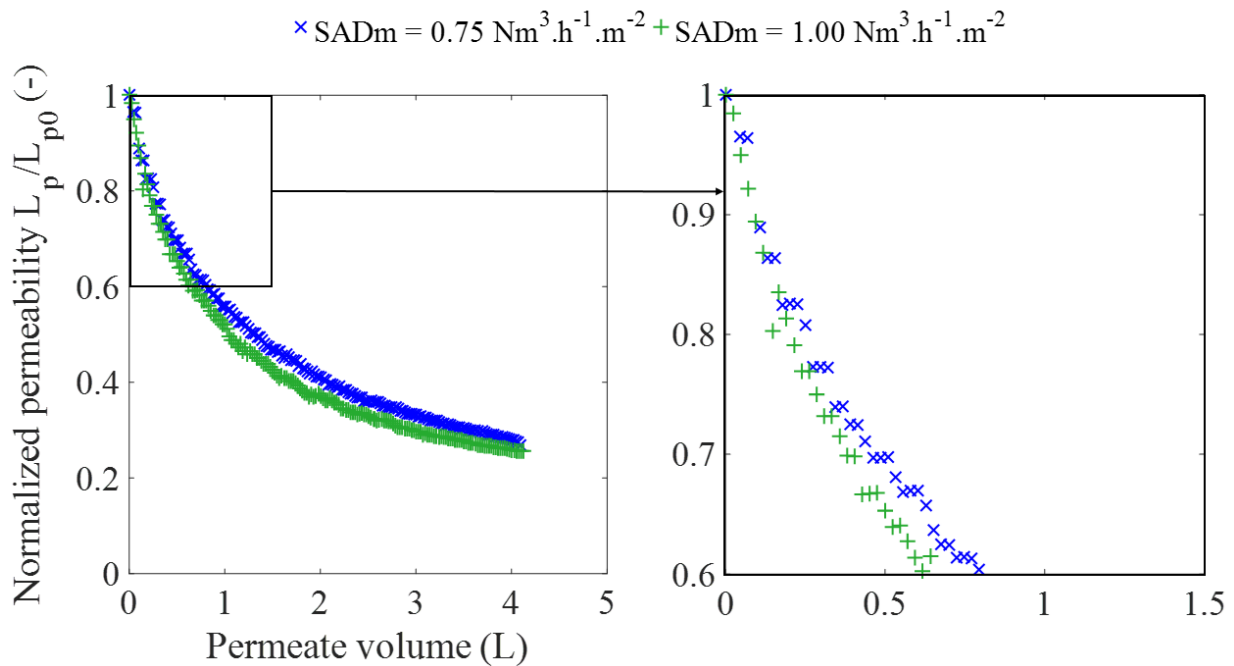


Figure VI-4 : Normalized permeability curves obtained for the experiments conducted in the ALMBR under the SADm of 0.75 and $1.00 \text{ Nm}^3 \cdot \text{h}^{-1} \cdot \text{m}^{-2}$.

The two curves present a similar trend as well as a very small gap that can be considered as negligible given the precision of the measurement of the permeability (around $\pm 15\%$). Overall, the normalized permeability curve obtained for the SADm of $1.00 \text{ Nm}^3 \cdot \text{h}^{-1} \cdot \text{m}^{-2}$ is on average 8 % below the one obtained

under $0.75 \text{ Nm}^3.\text{h}^{-1}.\text{m}^{-2}$, which indicates that no significant difference in the fouling phenomenon is caused by a variation of air flowrate from 0.75 to $1.00 \text{ Nm}^3.\text{h}^{-1}.\text{m}^{-2}$.

This result may seem surprising, since the aeration in MBRs is generally meant to reduce fouling. This non-substantial effect of the aeration can be attributed to the fact that the investigated conditions give rise to too fast a fouling phenomenon, in which case the variation of SADm from 0.75 to $1.00 \text{ Nm}^3.\text{h}^{-1}.\text{m}^{-2}$ makes no significant difference.

VI.2.2. *Fouling in the QQ-ALMBR*

Membrane fouling in the QQ-ALMBR was investigated under two different SADm (0.75 and $1.00 \text{ Nm}^3.\text{h}^{-1}.\text{m}^{-2}$), with a riser width D_r of 15 mm and in presence of 0.45 % v/v of the three shapes of QQ media. The initial conditions for the different experiments are gathered in Table VI-3. The effect of the addition of QQ media was discussed based on the complementary criteria deduced from the experimental curves and also presented in Table VI-3.

Table VI-3 : Initial conditions and comparison criteria deduced from the experiments run in the ALMBR/ QQ-ALMBR under different operating conditions.

	ALMBR		QQ beads-ALMBR		QQ hollow cylinders-ALMBR		QQ sheets-ALMBR	
SADm ($\text{Nm}^3.\text{h}^{-1}.\text{m}^{-2}$)	0.75	1.00	0.75	1.00	0.75	1.00	0.75	1.00
Feed (bentonite suspension) concentration (g.L^{-1})	1.02	1.00	1.00	1.00	0.98	0.98	1.00	1.00
$L_{p,init}(20^\circ\text{C})$ ($\text{L.h}^{-1}.\text{m}^2.\text{bar}^{-1}$)	367	451	306	381	351	430	332	405
Time to lose 40 % of the initial permeability during the experiment ($\frac{L_p}{L_{p0}} = 0.6$) (min)	35	28	26	30	34	40	36	55

VI.2.2.1. *Effect of QQ media on fouling in the QQ-ALMBR*

In order to discuss the effect of the addition of QQ media on the fouling phenomenon, the experimental results are directly presented in terms of normalized permeability as a function of the permeate volume in Figure VI-5.

The observation of Figure VI-5 firstly reveals that the effect of QQ media depends on the aeration conditions, as different trends were obtained under the two investigated flowrates.

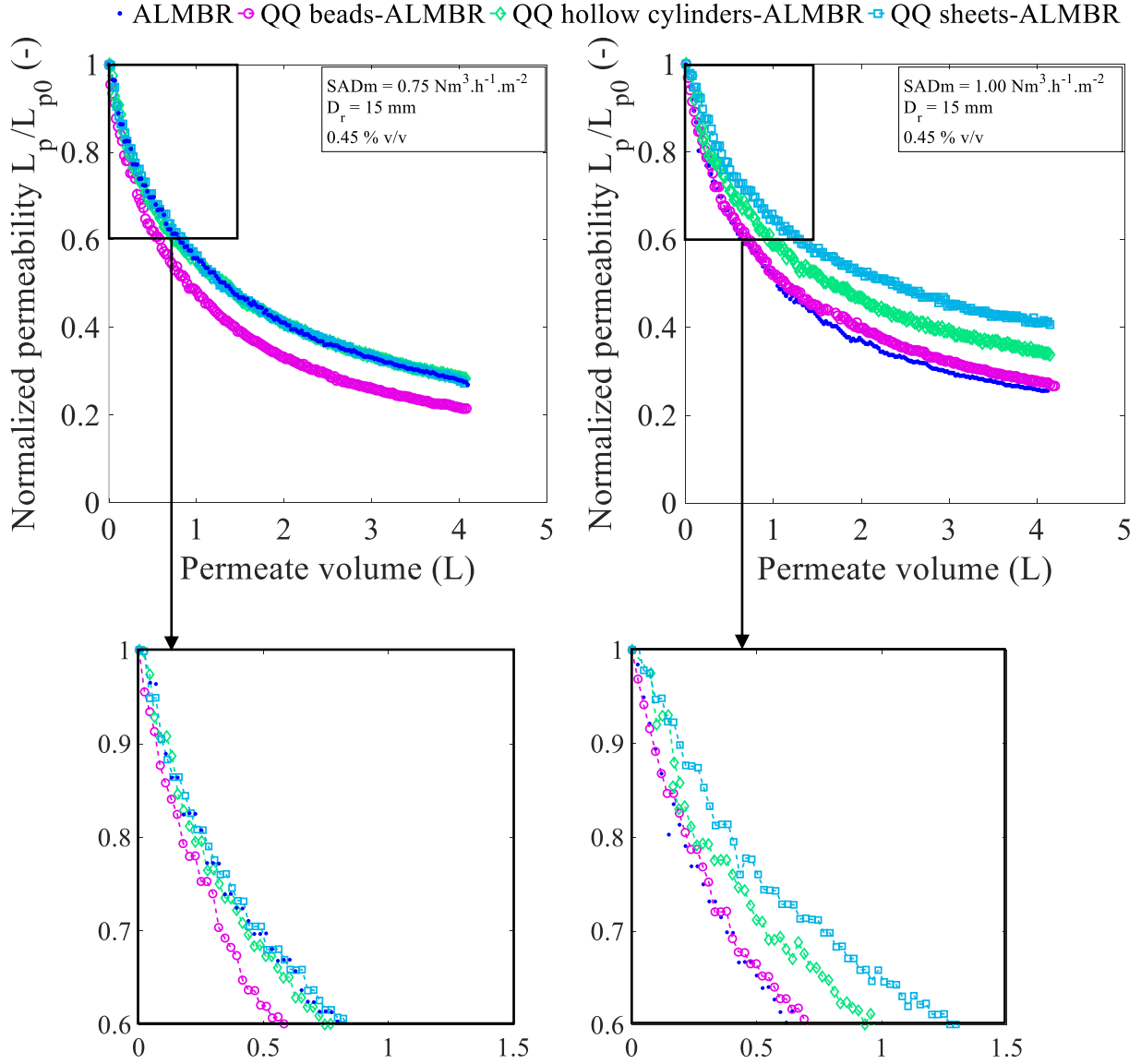


Figure VI-5 : Normalized permeability curves obtained for the experiments conducted in the ALMBR/QQ-ALMBR under the different operating conditions.

When the filtration experiments were performed under the SADm of $0.75 \text{ Nm}^3.\text{h}^{-1}.\text{m}^{-2}$ (Figure VI-5), it can be noticed that the normalized permeability curves obtained in presence of QQ hollow cylinders and sheets were almost perfectly superimposed with the one obtained in the ALMBR. However, the normalized permeability in presence of QQ beads was substantially (17 % on average) lower than the one of ALMBR and the time to lose 40 % of the permeability was shortened by more than 25 % in comparison to the ALMBR.

Under the SADm of $1.00 \text{ Nm}^3.\text{h}^{-1}.\text{m}^{-2}$, the normalized permeability in presence of the QQ hollow cylinders and sheets were considerably above the one obtained in the ALMBR (respectively 23 and 39 % on average), whereas the one in presence of QQ beads was very close (with only 5 % on average) to

the curve corresponding to the ALMBR. The time necessary to lose 40 % of the initial permeability was considerably extended with the addition of QQ hollow cylinders and sheets, by respectively 43 % and 96 %.

Based on these observations, it seems that among the investigated operating conditions, the most favorable ones are offered in presence of QQ sheets under an air flowrate of $1.00 \text{ Nm}^3 \cdot \text{h}^{-1} \cdot \text{m}^{-2}$, whereas the least favorable ones correspond to the addition of QQ beads under an air flowrate of $0.75 \text{ Nm}^3 \cdot \text{h}^{-1} \cdot \text{m}^{-2}$.

VI.2.2.2. *Effect of the aeration on fouling in the QQ-ALMBR*

The results are reconfigured in Figure VI-6 to discuss the effect of aeration on the fouling phenomenon in presence of QQ media in the reactor. In presence of QQ media, the highest SADm in this case ($1.00 \text{ Nm}^3 \cdot \text{h}^{-1} \cdot \text{m}^{-2}$) leads to less pronounced fouling.

In the ALMBR, the effect of the aeration was not substantial on the membrane fouling. Therefore, these results indicate that the addition of QQ media (whatever the shape) impact this trend, which is plausible since it can be imagined that part of the energy brought by the aeration is dissipated in the transport of QQ media rather than totally in the liquid phase.

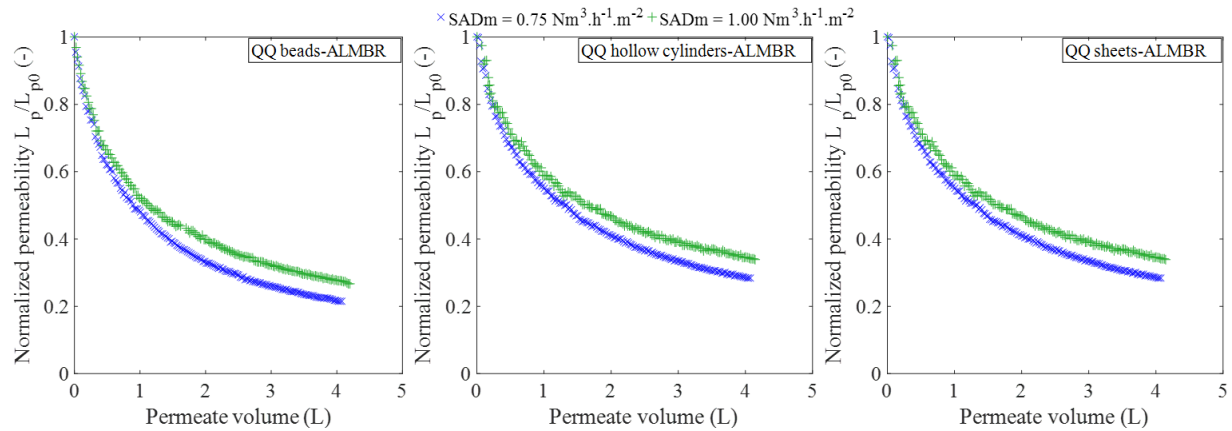


Figure VI-6 : Normalized permeability curves obtained for the experiments conducted in the QQ-ALMBRs under the air flowrates of 0.75 and $1.00 \text{ Nm}^3 \cdot \text{h}^{-1} \cdot \text{m}^{-2}$.

VI.2.3. *Concluding remarks on membrane fouling in the ALMBR/ QQ-ALMBR*

The filtration experiments conducted under two air flowrates (SADm of 0.75 and $1.00 \text{ Nm}^3 \cdot \text{h}^{-1} \cdot \text{m}^{-2}$) allowed identifying the effect of QQ media on fouling mitigation and the following main conclusions can be drawn:

- In the ALMBR, the two investigated aeration conditions (SADm of 0.75 and 1.00 Nm³.h⁻¹.m⁻²) gave rise to similar results in terms of membrane fouling.
- In the QQ-ALMBRs, the highest air flowrate was found to offer more favorable conditions for fouling mitigation, with respectively 30 % a 60 % increase of the permeability in presence of sheets.
- Among the investigated conditions, it appears that the most advantageous conditions for an effective fouling mitigation are obtained in presence of QQ sheets under the SADm of 1.00 Nm³.h⁻¹.m⁻², with up to a 60 % increase of the permeability.

These results show the consequence of the addition of QQ media on membrane fouling under different conditions, however these observations need to be put in relationship with the previous results of this study, in order to identify the physical mechanisms involved in the fouling mitigation. In the following, the link between the different physical aspects previously studied avec the fouling mitigation will be established.

VI.3. Mechanisms involved in the physical effect of QQ media for membrane fouling mitigation

In the following, the most important data from this study will be summarized and the consistency of the results will be evaluated by investigating the logical relationships linking the observed trends together.

VI.3.1. *Summary and consistency of the results*

The key-results of the study are summarized in Table VI-4 for their analysis. These results were obtained in the same air-lift configuration, with a riser width D_r of 15 mm and under air flowrates going from 0.75 to 1.00 Nm³.h⁻¹.m⁻², for which the fluidization of QQ media was made possible.

In Table VI-4, the effect of QQ media on the physical parameters and the membrane fouling in the QQ-ALMBR was evaluated in terms of percentage with respect to the same properties measured in the ALMBR.

Table VI-4 : Summary of the main experimental results obtained at a volume fraction of 0.45 % v/v.

QQ media	Beads			Hollow cylinders			Sheets		
SADm (Nm ³ .m ⁻¹ .m ⁻²)	0.75	0.90	1.00	0.75	0.90	1.00	0.75	0.90	1.00
Inherent behavior of the QQ media									
Fluidization									
Total number of introduced media (-)		2600			298			585	
Fluidization rate (%)	6	11	16	26	53	63	30	48	56
Number of fluidized media (-)	161	283	418	78	158	188	177	279	327
Surface of one particle of QQ media (10 ⁻⁶ m ²)		38.5			455.8			400.0	
Total surface of introduced media (m ²)		0.100			0.136			0.234	
Surface of fluidized media (m ²)	0.006	0.011	0.016	0.036	0.072	0.086	0.071	0.112	0.131
Position with respect to the membrane surface (mm) at:									
The middle of the membrane (Window II)	6.5	7.1	9.2	2.1	2.8	1.2	0	0.1	0.9
OO media velocity in the riser (m.s⁻¹) at:									
The middle of the membrane (Window II)	0.42	0.44	0.31	0.25	0.35	0.28	0.21	0.24	0.20
Time for the OO media to rise along the membrane (s)									
	0.8	0.7	1.0	1.3	0.9	1.1	1.5	1.3	1.6
Effect of QQ media on the hydrodynamics (% with respect to the ALMBR)									
On the gas phase									
Gas hold-up in the riser of the ALMBR	-15	-45	-10	x	x	x	x	x	x
Average bubble size in the riser	2.3	6.4	-6.5	7.2	-1.4	-4.0	7.0	5.7	-11.1
Average bubble velocity in the riser	9.7	6.7	-2.0	20.5	-10.9	9.5	10.8	16.9	5.8
On the liquid phase in the riser									
Average liquid velocity	-4	-12	-28	-21	-7	-9	-67	-49	-49
Maximal velocity of the flow profile at:									
The top of the membrane (Window I)	0	-28	-36	0	6	-4	-82	-56	-72
The middle of the membrane (Window II)	-18	-17	-36	-53	-30	-20	-65	-57	-44
The bottom of the membrane (Window III)	-6	-10	-23	-12	-5	-27	-65	-38	-41
Proportion of shear stress peaks ≥ 0.5 Pa at:									
The top of the membrane (Window I)	0	Inf*	-81	52	Inf*	-44	-75	Inf*	-100
The middle of the membrane (Window II)	-16	-46	-82	-49	-71	-31	-76	-78	-38
The bottom of the membrane (Window III)	Inf*	53	15	Inf*	43	17	Inf*	-89	-92
Effect of QQ media on the circulation and mixing performances (% with respect to the ALMBR)									
Mixing time of the aerobic tank of the ALMBR	-3	-7	-21	-18	-31	-33	-16	4	-17
Effective volume of the aerobic tank of the ALMBR	-16	-3	0	-20	-1	0	-13	-3	0
Recirculation flowrate from the aerobic to the anoxic tank of the ALMBR	-45	-38	0	-38	-20	-55	-97	-89	-60
Mass transfer from the QQ media to the liquid phase of the ALMBR									
Solid-liquid transferred flux (10 ⁻⁸ m ³ .s ⁻¹)	1.00	0.62	1.52	2.16	1.70	1.87	4.03	3.23	4.58
Solid-liquid mass transfer coefficient with the total surface S_g (10 ⁻⁷ m.s ⁻¹)	1.17	0.72	1.78	1.88	1.48	1.39	2.02	1.62	1.95
Effect of QQ media on the membrane fouling (% with respect to the ALMBR)									
Time to lose 40 % of the initial permeability	-26	x	7	-3	x	43	3	x	96

*Infinite increase with respect to the (vacant) ALMBR where the considered parameter was nil.

x: Not measured.

VI.3.1.1. Inherent behavior of the QQ media

The inherent behavior of the QQ media in the ALMBR was analyzed in terms of fluidization rate, QQ media velocity and QQ media position with respect to the membrane surface.

When QQ media were introduced in the reactor, it was demonstrated that the fluidization rate increased with the increasing aeration, for the three shapes of QQ media. However, at the same volume fraction (0.45 % v/v) and under the same air flowrate, it appears that the greatest fluidization rates were obtained for QQ sheets.

In the literature, the physical effect of QQ media on fouling reduction was assumed to be due to the direct contact of QQ media with the membrane surface [12,14], in which case the number of fluidized QQ media and the surface of contact of the QQ media with the membrane can be two key-parameters.

Within this scope, complementary data were extracted for a deeper discussion (Table VI-4). Indeed, it appears in Table VI-4 that considering the number of fluidized QQ media (N_{FM}), complementary assumptions can be proposed, in addition to those on the effect of the fluidization rate. As a matter of fact, to reach the same volume fraction of 0.45 % v/v, the total number of beads (2600) introduced in the reactor is greater than that of hollow cylinders (298) and sheets (585). Therefore, considering the fluidization rate, the greatest number of fluidized media is for QQ beads (418 particles in suspension) under an air flowrate of $1.00 \text{ Nm}^3 \cdot \text{h}^{-1} \cdot \text{m}^{-2}$. From this result, it can be assumed that under these specific conditions (volume fraction of 0.45 % v/v and air flowrate of $1.00 \text{ Nm}^3 \cdot \text{h}^{-1} \cdot \text{m}^{-2}$), the probability of contact between the QQ media and the membrane surface could be higher in presence of beads, rather than in presence of the other two shapes. However, when considering the contact surface, the surface of fluidized QQ sheets remains definitely greater than for the other two shapes, under all the considered conditions.

Given the filtration results, this means that the observed effect of QQ sheets on fouling mitigation was favored by their shape and surface, that lead to an effective contact with the membrane.

The results corresponding to the other volume fractions (0.10 and 0.06 % v/v) are presented in Appendix A-VI-2, and the same conclusions as for 0.45 % v/v can be drawn in terms of fluidization.

In addition to the fluidization phenomenon, the inherent behavior of QQ media was also assessed in terms of particle velocity and position. Concerning the position, the QQ sheets were observed to rise closer to the membrane surface than the other two shapes, under all the investigated conditions (first section of Table VI-4), which again suggests an enhanced probability for the sheets to have a direct contact with the membrane surface. The QQ hollow cylinders are the second shape with the closest position to the membrane surface. Finally, the QQ sheets describe the lowest rising velocity, which can be linked to the longest time “spent” in the vicinity of the membrane, in comparison to the two other shapes.

At this stage, it can be confirmed that the physical effect of QQ sheets is due to a “sweeping” action which is made possible thanks to their specific shape, allowing them to rise very close to the membrane at a relatively low velocity, thus allowing the prolonged contact with the membrane surface.

VI.3.1.2. Relation between the hydrodynamics in the reactor and the inherent behavior of QQ media in the reactor

The hydrodynamics in the reactor was investigated in presence of QQ media, distinguishing the gas phase and the liquid phase, in order to highlight their effect (Chapter III). The results are summarized in the second part of Table VI-4.

The effect of the addition of QQ media on the gas phase was investigated in terms of gas hold-up and bubbles properties (size and velocity) in the riser. The results show that the effect of QQ cannot be considered as significant, since the variations remain in the range of the error linked to the measurement techniques used to characterize the gas phase. Therefore, it can be concluded that the QQ media do not substantially impair the gas phase in the ALMBR, which suggests that, in the investigated conditions, the benefits of air bubbles for the MBR operation are maintained in presence of QQ media.

Concerning the effect of QQ in the liquid phase, the liquid velocity and the membrane shear stress were measured under different operating conditions. The maximum velocity of the local flow profiles that were measured at different heights (window I, II and III), were found to be reduced in presence of QQ media, in most cases. However, the most noticeable decrease in the maximal velocity is by far obtained in presence of QQ sheets, with – 38 % to – 82 %, depending on the localization and the air flowrate. For the hollow cylinders and beads, no clear tendency on the liquid velocity appeared. Nonetheless, the results concerning the QQ sheets are clearly consistent with the fluidization properties. As a matter of fact, it seems logical that the QQ sheets, with their greater fluidization rate and surface have the more significant effect on the liquid velocity. Given the greater number of fluidized sheets in the reactor (about twice as high as for the QQ hollow cylinders under the same flowrate), and given their larger surface in comparison to the QQ beads and hollow cylinders, they behave as more numerous and larger obstacles for the liquid flow in the riser. This result is also in good accordance with the proper velocities of the QQ media, since the QQ sheets were observed to have the lowest rising velocity in the riser.

The effect of QQ media on the membrane shear stress was also examined. Again, the QQ sheets appear to be the shape that induces the most noticeable effect, since the reduction of the proportion of peaks having an intensity of at least 0.5 Pa is higher for QQ hollow cylinders and beads. This observation is in accordance with the previous results, as the membrane shear stress is directly related to the local liquid velocity in the vicinity of the membrane. Therefore, the QQ sheets with their important fluidization rate and surface slow down the liquid flow in the riser, and more specifically in the vicinity of the membrane, where there were proved to rise, under the studied conditions.

In sum, the effect of the QQ media on the hydrodynamics parameters seems to be consistent and can be explained by the fluidization results, especially, considering the case of QQ sheets that clearly stands out from the other QQ media shapes. Regarding the QQ hollow cylinders and beads, their effect can be non-negligible on the liquid phase, but at a less generalized extent than that of QQ sheets. In conclusion, the behavior of the liquid phase is undeniably modified in presence of QQ media, and more specifically QQ sheets, which is the trends observed in the effect on fouling mitigation.

VI.3.1.3. Relation between the circulation and mixing performance and the inherent behavior of QQ media in the reactor

The influence of QQ media on the circulation and mixing performance of the ALMBR was studied distinguishing two scales of time corresponding to different characteristic phenomena of the reactor: the short-term effect with the determination of the mixing time (at the scale of the biological kinetics), and the long-term effect with the RTD analysis (at the scale of the process kinetics). The key-results of this study (Chapter IV) are summarized in Table VI-4, in terms of percentage of reduction or increase in comparison to the ALMBR (with no QQ media).

The mixing time in the aerobic tank was reduced in presence of QQ media, in most cases. The correlation between the fluidized QQ beads and cylinders and the mixing time presented in Figure VI-7 show that the greater the number of media in suspension, the more the mixing time is reduced, and thus the more the short-term mixing of the aerobic tank is improved. For the QQ sheets, the singular point obtained for the SADm of $0.90 \text{ Nm}^3 \cdot \text{h}^{-1} \cdot \text{m}^{-2}$ (pointed in Figure VI-7) may be attributed to an experimental error, and complementary experiments would be needed for confirmation. Nevertheless, in all the cases, the most significant gain in the mixing time is obtained for the highest air flowrate of the investigated range ($1.0 \text{ Nm}^3 \cdot \text{h}^{-1} \cdot \text{m}^{-2}$). When considering this overall trend, it seems logical that an increase in the number of QQ media in suspension, promotes the mixing performance, by creating secondary circulation phenomena.

The RTD analysis allowed characterizing the mixing performance at the long-term operation, and one of the main conclusions highlighted by this study (Chapter IV) was that at the lower air flow rates, the presence of QQ media could be correlated to low-mixing or dead zones in the aerobic tank, which was assumed to be due to the low fluidization of QQ media under these conditions. In order to confirm this assumption, the relation between fluidized QQ media and effective volume (in terms of percentage with respect to the ALMBR) is presented in Figure VI-8. For the three shapes of QQ media, the effective volume increases with the increasing number of media in suspension. This result seems logical and consistent with the mixing time results, since the greater is the number of fluidized QQ media, the better is their spatial distribution in the reactor preventing dead zones from being created at the bottom of the reactor, where the non-fluidized media tend to accumulate.

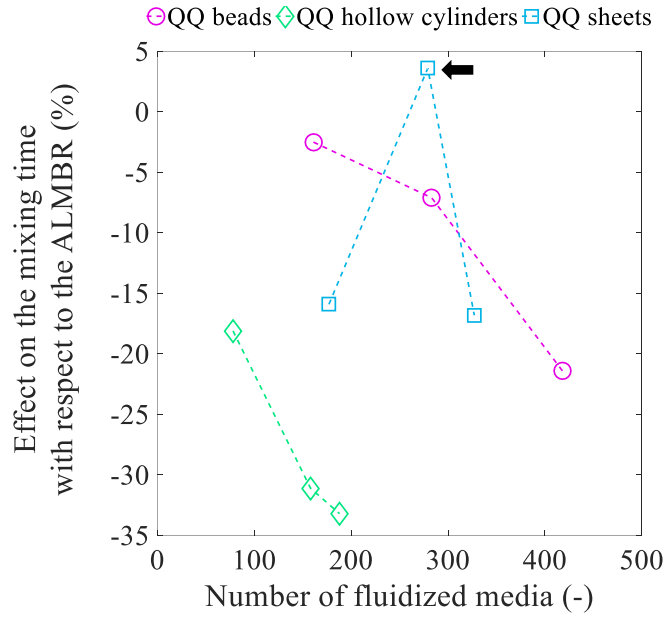


Figure VI-7 : Correlation between the number of fluidized QQ media and the mixing time in the aerobic tank of the ALMBR.

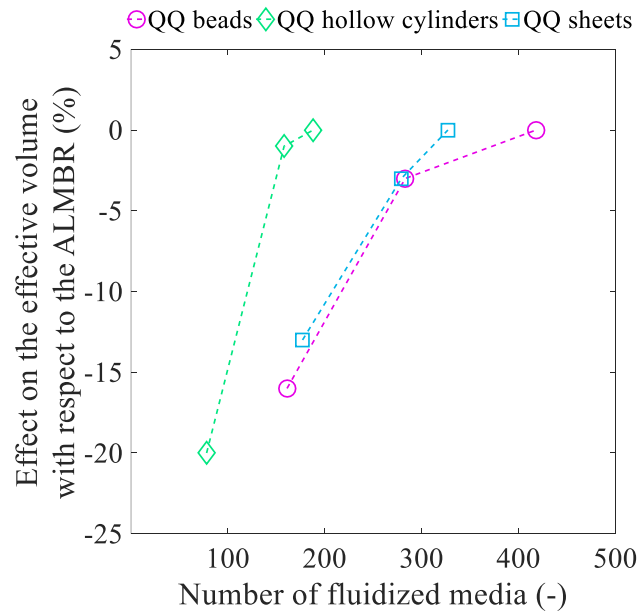


Figure VI-8 : Correlation between the number of fluidized QQ media and the effective volume in the aerobic tank of the ALMBR.

VI.3.1.4. *Relation between circulation, mixing and hydrodynamics in the QQ-ALMBR*

The first parts of this study were globally dedicated the flowing behavior of the ALMBR/ QQ-ALMBR at different scales of space and time. Different methods were used for the complete characterization of the system, and the concept of velocity was the common key-parameter. Actually, the hydrodynamics characterization allowed determining the liquid velocity as well as the QQ media velocity in the riser part of the ALMBR, using optical methods (PIV and shadowgraphy, respectively). In addition, in the circulation and mixing performance analysis, the circulation time t_c (time necessary for the liquid flow to complete one loop from the riser to the down-comer), which can be used to deduce the flowing velocity in the riser. Making the assumption that the liquid flowrate Q_l is conserved from the riser to the down-comer, the equality can be written as in Equation VI-5, where U_{lr} and U_{ld} are the liquid velocities in the riser and down-comer, respectively, and A_r and A_d are the cross-sections of the riser and down-comer parts, respectively. The gas hold-up in the down-comer is nil.

$$Q_l = (1 - \varepsilon_g)U_{lr}A_r = U_{ld}A_d \quad \text{VI-5}$$

Considering that the liquid height h_D in both the riser and down-comer parts is the same, the Equation VI-5 can be re-written as in Equation VI-6, where t_{cr} and t_{cd} are the times necessary for the liquid flow to complete the distance h_D at the velocities U_{lr} and U_{ld} , respectively. In addition, the times t_{cr} and t_{cd} are also linked as in the Equation VI-7, where t_c is the total circulation time presented in Chapter IV, and that was measured by visually tracking QQ media in the liquid flow in the air-lift. Knowing the distance “travelled” by the QQ media when completing a loop in the air-lift, the corresponding air-lift circulation velocity could be deduced and is presented in Table VI-5.

$$Q_l = \frac{h_D}{t_{cr}}A_r = \frac{h_D}{t_{cd}}A_d \quad \text{VI-6}$$

$$t_c = t_{cr} + t_{cd} \quad \text{VI-7}$$

Therefore, from the combination of these equations, the liquid velocity in the riser can be deduced for comparison with other methods. The different velocities presented in Table VI-5 are globally all in the same order of magnitude. However, it can be observed that the mean liquid velocity deduced from the circulation time as well as the QQ media velocity are always higher than the liquid velocity measured with PIV. It can be assumed that the liquid flow velocity measured with the PIV technique is underestimated, which may be attributed to one of the limitations of PIV. As a matter of fact, PIV measurement consists in a 2D-measurement and only concerns one plane of the liquid flow. In our case, the middle plane was chosen to perform the measurements (Chapter II) and was maybe not fully representative of the whole reactor. Therefore, one way to overcome this limitation could be to perform

measurements at different planes of the liquid flow, or to select other measurement techniques, in order to have more accurate 3D-information about the liquid flow.

Table VI-5 : QQ media and liquid velocities measured with different methods.

	QQ beads- ALMBR			QQ hollow cylinders- ALMBR			QQ sheets- ALMBR		
SADm ($\text{Nm}^3.\text{h}^{-1}.\text{m}^{-2}$)	0.75	0.90	1.00	0.75	0.90	1.00	0.75	0.90	1.00
QQ media velocity (II) (shadowgraphy + image processing) (m.s^{-1})	0.42	0.44	0.31	0.25	0.35	0.28	0.21	0.24	0.20
Average liquid velocity in the riser (PIV) (m.s^{-1})	0.12	0.15	0.14	0.10	0.16	0.18	0.04	0.09	0.10
Maximal liquid velocity in the riser (II) (PIV) (m.s^{-1})	0.14	0.19	0.16	0.08	0.16	0.20	0.06	0.10	0.14
Air-lift circulation velocity in the riser (Visualization of particle) (m.s^{-1})	0.19	0.22	0.25	0.20	0.23	0.25	0.17	0.19	0.25

VI.3.1.5. *Relation between the hydrodynamics and the mass transfer*

In the literature, the hydrodynamics was reported to promote the mass transfer by fostering the turbulence and the fluidization of particles (in the case of suspended particles) [162]. More specifically, the Equation V-9 (presented in Chapter V), was proposed as a law describing the promotion of the mass transfer phenomenon (represented by the Sherwood number Sh) by the increase of the convective forces and turbulence (represented by the Reynolds number Re).

In this study, the effect of the air flowrate (in terms of SADm) on the solid-liquid mass transfer was not clearly visible (Chapter V). With the results previously presented (in Chapters I and V), an attempt was made in order to assess the relationship between the hydrodynamics and the solid-liquid mass transfer. The Sherwood number corresponding to the transfer from the QQ media to the liquid phase were calculated for the three shapes of QQ media and under the three investigated air flowrates, and considering the two cases for the exchange surface (Table V-9). The liquid flow induced under these same aeration conditions were characterized in Chapter III by determining the average liquid velocity in the riser U_{lr} and the corresponding liquid-Reynolds number Re_l in the riser. In Figure VI-9, a significant dispersion can be observed and the improvement of the solid-liquid mass transfer by the turbulence is not clearly perceptible. These dispersions can be attributed to the fact that the QQ media describe different behaviors in terms of hydrodynamics as well as mass transfer. Therefore, the definition of one single law might be difficult. Also, the hydrodynamics is involved at many levels in the mass transfer (renewal of the liquid, promotion of convective forces, fluidization of QQ media). For these reasons, a relationship linking these two aspects exists but its exact identification is still hardly achievable with the data acquired so far, and deeper research is still required.

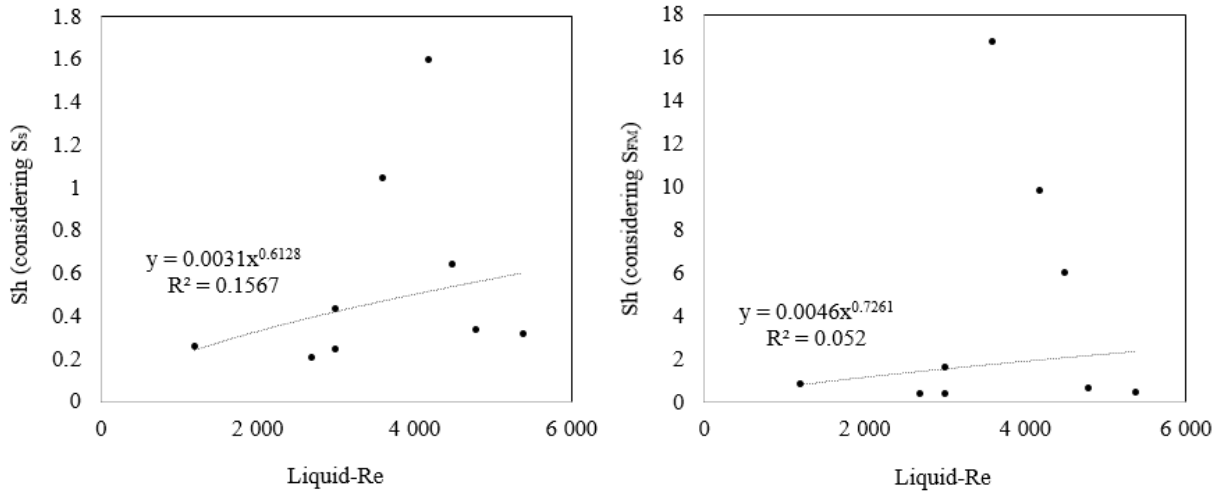


Figure VI-9 : Correlation between the Sherwood number and the liquid-Reynolds number obtained for the mass transfer of Rose Bengal Lactone from three shapes of QQ media to the liquid phase of the ALMBR (*Sherwood number calculated in Table V-9*).

VI.3.2. Relationship between the fouling mitigation effect and the physical aspects of QQ media

With the perspective to promote fouling mitigation through the addition of suspended QQ, it is essential to link all of the obtained results and finally conclude about the optimal conditions for QQ application.

Under the air flowrate of $0.75 \text{ Nm}^3 \cdot \text{h}^{-1} \cdot \text{m}^{-2}$, the QQ beads were found to be weakly fluidized (6.2 % of the particles, corresponding to 161 beads in suspension), to rise relatively far from the membrane surface with an average distance of 6.5 mm. However, the few beads in suspension were found to have an important rising velocity reaching $0.42 \text{ m} \cdot \text{s}^{-1}$ but an insignificant effect on the liquid flow in the riser, and an uneven effect on the membrane shear stress. Under the same air flowrate of $0.75 \text{ Nm}^3 \cdot \text{h}^{-1} \cdot \text{m}^{-2}$, the QQ hollow cylinders were demonstrated to be more importantly fluidized (2.6 % corresponding to 78 particles in suspension), to rise more closely to the membrane surface (2.1 mm) at a relatively low velocity ($0.25 \text{ m} \cdot \text{s}^{-1}$), and to induce a considerable decrease in the liquid flow. Regarding the QQ sheets, the fluidization was even more important (30.4 % corresponding to 177 sheets in suspension), and they were found to rise in the very vicinity of the membrane surface (0 mm) with a rising velocity of $0.21 \text{ m} \cdot \text{s}^{-1}$. Given this information and the observed results, it can be assumed that under the air flowrate of $0.75 \text{ Nm}^3 \cdot \text{h}^{-1} \cdot \text{m}^{-2}$, the number of fluidized QQ media are globally not important enough to mitigate fouling though a mechanical effect with vigorous collisions between the media and the membrane surface. In the case of beads, the fouling is even more severe, which can be attributed to the fact that the QQ beads in suspension (161 particles) have a high rising velocity that can promote the transport and deposition of particles from the mixed liquor to the membrane surface.

Under the air flowrate of $1.00 \text{ Nm}^3 \cdot \text{h}^{-1} \cdot \text{m}^{-2}$, the fluidization rate of the three shapes of QQ media was greater resulting in a number of QQ beads, hollow cylinders and sheets in suspension of 418, 188 and 327, respectively. The rising velocity of QQ beads was lower under this air flowrate reaching $0.31 \text{ m} \cdot \text{s}^{-1}$, their effect on the slowdown of the liquid flow was more pronounced but their distance to the membrane was greater (9.2 mm), which can explain the fact that the fouling mitigation was not fully successful in these conditions. The QQ hollow cylinders, were found to rise closer to the membrane surface (1.2 mm) with a velocity of $0.28 \text{ m} \cdot \text{s}^{-1}$, and the QQ sheets even closer (0.9 mm) with a lower velocity ($0.20 \text{ m} \cdot \text{s}^{-1}$). Concerning the membrane shear stress, it was found to be globally reduced in presence of QQ media under $1.00 \text{ Nm}^3 \cdot \text{h}^{-1} \cdot \text{m}^{-2}$, especially with QQ sheets. Therefore, these results suggest that the QQ sheets and hollow cylinders reduce membrane fouling by rising close to the membrane surface thus, preventing the deposition of particles from the mixed liquor on it. The greater is the number of media in suspension and the closer to the membrane they rise (in this case, QQ sheets), the better is the physical effect on fouling mitigation.

VI.4. Interest of the study for membrane fouling mitigation through a biological effect

It is worth keeping in mind that QQ has a potential double-effect to mitigate fouling: a biological effect (disruption of the bacterial communication by QQ enzyme-producing bacteria) and a physical effect (cake erosion) that was assumed to be due to the direct contact of QQ media with the membrane surface, resulting in the removal of the biomass deposited on it.

The present study addressed a key physical step involved in the global application of QQ mediated by QQ media: the **mass transfer** which ensures the “meeting” between the molecular compounds involved in the enzymatic reaction (the QQ enzymes and their substrates (AHLs)).

The kinetics of mass transfer was found to be relatively slow, with transfer coefficients in the order of magnitude of $10^{-7} \text{ m} \cdot \text{s}^{-1}$ (Table VI-4), which suggests that it can be the governing step. The mass transfer was studied from the liquid to the QQ media and from the QQ media to the liquid. In both cases, the shape, and more specifically the surface, of QQ media was found to be an important parameter affecting the transferred flux. Consequently, the QQ sheets were found to be the most favorable shape owing to their great surface exchange. However, in the investigated conditions, the effect of hydrodynamics was not clearly perceivable.

Therefore, the challenge for an optimal QQ application from the biological perspective can be summarized as a question of time, and more specifically, in the fact that the reaction should take place efficiently and relatively quickly, in comparison with the other mechanisms of the QQ-MBR.

In the present study, time was recurrently the underlying issue of the different addressed questions, and some of the characteristic times of the QQ-ALMBR system have been determined and are gathered in the timescale presented in Figure VI-10.

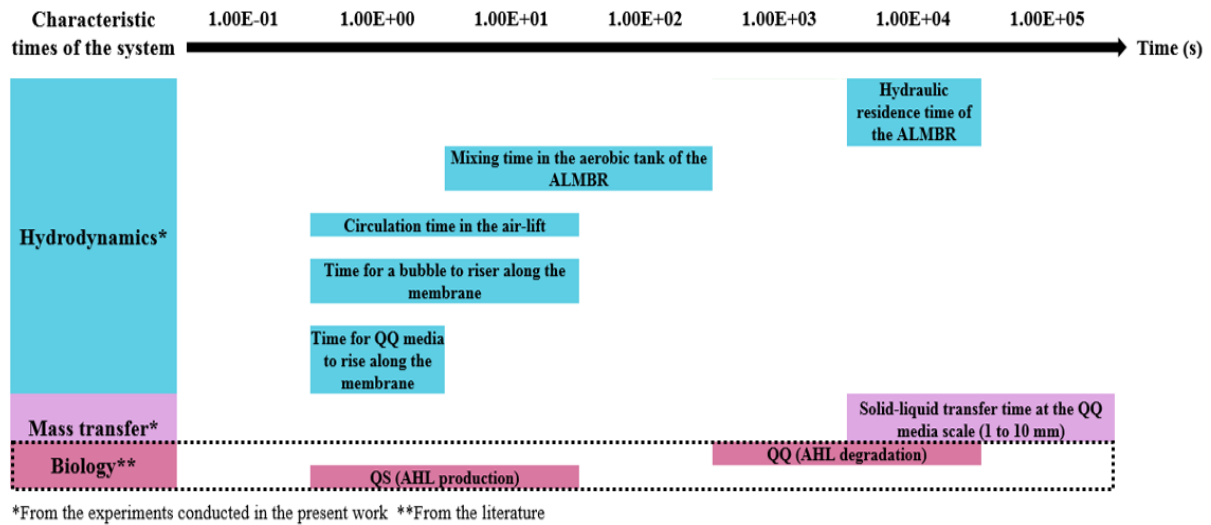


Figure VI-10 : Characteristic times of the QQ-ALMBR operation.

The characteristic times related to the QQ-ALMBR operation were classified based on their order of magnitude and distinguishing the physical phenomena (hydrodynamics and mass transfer) from the biological phenomena (QS and QQ reaction). For the physical phenomena, the times were measured/deduced from the experiments conducted in **this study**. Concerning the fouling time, it is of crucial importance keeping in mind that it is actually fully dependent on the operating conditions (permeate flux, aeration, membrane configuration...) and that the fouling phenomenon involves several mechanisms at different scales of time (pore-clogging, biofilm production). Hence, the definition of one global characteristic fouling time is not possible.

Concerning the biological data, their determination can be difficult since several parameters such as the microbial population nature and growth, the operating conditions, the nutrients, the temperature and pH, can affect the biological activity. Nevertheless, some biological data were found in the literature and given for informative purpose. As an example, the AHLs synthesis was reported by Parsek et al. (1999) [163] to take 3 to 30 s to produce 1 mole of AHLs in presence of 1 mg of RhII protein which catalyzes the synthesis. On the other hand, the degradation of AHLs was measured several times to characterize the QQ activity of QQ bacteria applied to MBRs, according to a standard test consisting in measuring the decreasing concentration of one model AHL (C8-HSL) (initially at the concentration of around 200 nM) during 30 to 200 min [56], which results in a degradation time in the order of magnitude of 10^3 to 10^4 s.

Even though more information would be needed about the biological aspects involved in the QQ application, the elements presented in Figure VI-10 open the discussion on the necessity to optimize the QQ application, maybe by adapting the physical parameters to the biological ones. As an example, it can be seen on Figure VI-10 that the production of AHLs can be a relatively quick phenomenon, as well as the mixing time. Given that the AHLs are produced by the biomass in the mixed liquor, this means that the signal molecules can potentially spread quickly in the reactor, promoting the bacterial communication, and thus the production of biofilm. On the other hand, the degradation of AHLs seems to be slower and limited by the mass transfer from the liquid to the QQ media or *vice-versa* (depending on the QQ bacteria), which makes the global degradation even slower. Therefore, one way of improvement could be to reduce as much as possible the delay between the AHLs production and their degradation, by accelerating the mass transfer step.

VI.5. Conclusions and perspectives

The present chapter allowed opening a global discussion on the effect of QQ media addition in the ALMBR and the interest of its double-effect (physical and biological) to reduce membrane fouling. The following statements can be retained as main conclusions:

- The effect of QQ media was not observable under the SADm of $0.75 \text{ Nm}^3 \cdot \text{h}^{-1} \cdot \text{m}^{-2}$ owing to their low fluidization under these conditions (only up to 30 % of fluidized QQ media). However, for the SADm of $1.00 \text{ Nm}^3 \cdot \text{h}^{-1} \cdot \text{m}^{-2}$, membrane fouling was successfully reduced in presence of QQ hollow cylinders and sheets with a final permeability increased by **30 %** and **60 %** with respect to the vacant ALMBR, respectively, after 3 h of operation.
- The effect of the aeration on the membrane fouling was not clearly visible in the investigated conditions, which can be attributed to the fact that the selected conditions gave rise to too severe a fouling phenomenon.
- The results obtained in the previous parts of the study were summarized in this chapter and appeared to be consistent. On that basis, logical and reliable relationships between these results and the observed effect could be identified.
- In sum, among the three shapes of QQ media, QQ beads were found to be weakly fluidized and to rise far away from the membrane surface, which resulted in no positive effect to mitigate membrane fouling under the investigated conditions. QQ hollow cylinders could mitigate membrane fouling under the SADm of $1.00 \text{ Nm}^3 \cdot \text{h}^{-1} \cdot \text{m}^{-2}$, thanks to the significant fluidization rate. The QQ sheets were found to be the most efficient to reduce membrane fouling under the SADm of $1.00 \text{ Nm}^3 \cdot \text{h}^{-1} \cdot \text{m}^{-2}$, and their effect was attributed to their great fluidization rate and their closeness to the membrane surface when rising.
- The biological effect induced by QQ application was not studied *per se* but the mass transfer step was identified as a key-parameter to target in future research in order to accelerate QS inhibition, and therefore, prevent more effectively biofilm from being produced.

GENERAL CONCLUSION AND PERSPECTIVES

Membrane fouling is a widely investigated subject in the field of membrane processes, and the development of innovative methods for its mitigation and control, represents today a major challenge in both the research and the industrial scenes. In this context, Quorum Quenching (QQ) appeared in 2009 as a promising technology for biofouling mitigation through an original double-action: a biological action consisting in preventing biofilm production by disrupting the bacterial communication, and a physical action (washing effect) due to the addition of suspended media carrying the QQ activity (QQ media). These particular specificities raised several questions such as: the impact of the addition of QQ media on hydrodynamics of the reactor, the mass transfer involved in the QQ reaction, as well as, the mechanisms involved in the physical washing effect of QQ media.

The general objective of this study was to provide clues for a better understanding of the phenomena involved in the QQ application, from an original and purely physical perspective. In particular, the aforementioned questions were addressed in order to bring potential ways of improvement for future QQ application.

In Chapter I, the state of the art was presented by overviewing literature concerning the application of QQ to MBRs from 2009 to 2018. The results of the different studies were analyzed and harmonized based on original criteria such as the short-term fouling (quick increase of TMP at the beginning of the operation), the long-term fouling (slow increase of the TMP), the amount of produced biofilm/EPS. From these studies, the effect of the operating conditions on the QQ efficiency could also be identified: in particular, the bacterial QQ was found to be more efficient using free-moving carriers (QQ media) and the QQ activity was found to increase with the initial amount of QQ bacteria entrapped in the media. Above all, this chapter allowed establishing the strategy of the present study, on the basis of the gaps identified (hydrodynamics and mass transfer).

As presented in Chapter II, this study relied on an experimental approach, conducted in an air-lift membrane bioreactor (ALMBR). This particular configuration of MBR was selected because it was reported in the literature to have favorable hydrodynamics conditions, and more specifically, enhanced membrane shear stress reducing the fouling phenomenon.

The hydrodynamics characterization was achieved at different scales of space and time and using several techniques: the global scale was studied by measuring the fluidization rate of the QQ media, the gas hold-up, the average liquid velocity, the RTD and the mixing time. The techniques used for this part of the study were essentially visualization and/or tracer techniques. At the local scale, the bubble size and velocity, the QQ media position and velocity, as well as the liquid velocity field were characterized using optical techniques (laser + camera). The mass transfer part was conducted using a model dye mimicking the molecules involved in the QQ reaction: the signal molecules (AHLs) and the QQ enzymes. The mass transfer was quantified by measuring the light intensity correlated to the variations of dye concentration, either by spectrophotometry or by a camera technique. Finally, filtration

experiments were conducted in the ALMBR using a model suspension (bentonite) and the fouling phenomenon was quantified under different conditions (aeration, presence of not of QQ media) by measuring the permeability variation during the operation.

In this study the decision was made to perform experiments under given conditions in order to highlight the differences generated by the addition of QQ media, as well as to compare the QQ media shape and the hydrodynamics conditions.

The main conclusions of this study are given hereafter:

- In Chapter III, the hydrodynamics characterization of the ALMBR/qq-ALMBR was performed. At the global scale, the ALMBR was found to present typical features of air-lift reactors (ALRs) or ALMBRs, since the increase of the gas hold-up (up to 10 %) and the liquid velocity in the riser (up to 0.2 m.s^{-1}) with the superficial gas velocity (from 0 to 0.01 m.s^{-1}) was consistent with the literature. The fluidization of qq media was found to strongly depend on the ALMBR configuration (no fluidization for a riser width of 7 mm). The fluidization rate was demonstrated to increase with the air flowrate, and could reach up to 100 % for qq sheets and hollow cylinders under $1.0 \text{ Nm}^3.\text{h}^{-1}.\text{m}^{-2}$ and at a volume fraction of 0.06 % v/v. Among the three shapes of qq media, the qq sheets exhibited the best fluidization behavior. When the qq media were added to the ALMBR, the gas hold-up was not affected, however, a slowdown (up to 50 %) of the liquid flow in the riser was obtained in presence of qq sheets added at a volume fraction of 0.45 % v/v.

At the local scale, the bubbles were characterized in terms of size and velocity. The bubble velocity described a slight increase (from 0.4 to 0.6 m.s^{-1}) with the superficial gas velocity for the two riser widths. However, the bubble size kept unchanged in the investigated range of air flowrates. The position of the qq media was studied and the qq sheets were found to rise very close to the membrane (0 to 1 mm away), in comparison to qq hollow cylinders and beads (between 1 and 9 mm away). The bubble size and velocity were not considerably impaired in presence of qq media. However, the liquid velocity and, consequently, the membrane shear stress were reduced locally (down to 80 %) in presence of qq sheets.

- In Chapter IV, the circulation and mixing performances of the ALMBR/qq-ALMBR were evaluated. The mixing time of the ALMBR was found to decrease (from 60 to 30 s) with the aeration until the critical SADm of $0.75 \text{ Nm}^3.\text{h}^{-1}.\text{m}^{-2}$. The mixing time could be slightly reduced in presence of qq media. The ALMBR under its continuous mode, was found to operate as two completely stirred tanks-in-series with different volumes and a recirculation flow between the two tanks. The ALMBR described no specific dysfunctions such as dead volume or short-circuiting. In presence of qq media, the long-term mixing was found to be impaired. In particular, the qq media created dead volumes (up

to 20 %) because of their tendency to settle down to the bottom of the reactor, and by clogging the recirculation pipe between the two tanks.

- In Chapter V, the mass transfer from the QQ media to the liquid phase (solid-liquid) and *vice versa* was characterized. The importance of the QQ media shape was clearly highlighted in this part of the study. The liquid-solid mass transfer was studied ex-situ (in jar-tests) and the results revealed that the transferred flux was greater for QQ sheets and hollow cylinders than for beads, because of their greater exchange surface and their smaller thickness that made the internal diffusion very quick compared to the external transfer step. The solid-liquid mass transfer was studied in-situ (in the ALMBR) under different aeration conditions. Among the QQ media, the sheets were identified as the most favorable shape in terms of transferred flux. However, the effect of the hydrodynamics on the mass transfer was hardly quantifiable because of the complexity of mechanisms governed by the aeration in the ALMBR (liquid circulation, macro and micro-mixing, fluidization of QQ media). In the investigated conditions, the liquid-solid mass transfer coefficient was found to be in the order of magnitude of 10^{-6} , whereas the solid-liquid mass transfer was 10^{-7} m.s^{-1} . These values indicate that the mass transfer can be considered as very slow in comparison to the other phenomena of the process: mixing, circulation, fouling.

- Lastly, Chapter VI presented the filtration results and highlighted how the QQ media could exert a physical effect to reduce membrane fouling. The effect of the QQ media on membrane fouling under the SADm of $0.75 \text{ Nm}^3.\text{h}^{-1}.\text{m}^{-2}$ was not visible in the investigated conditions. Under the highest investigated flowrate (SADm = $1.00 \text{ Nm}^3.\text{h}^{-1}.\text{m}^{-2}$), the QQ sheets and hollow cylinders induced a fouling mitigation of 60 and 30 %, respectively (in terms of total permeability at the end of operation). These results, put in relationship with the previous ones, revealed that the physical effect of QQ media (sheets more specifically) was not only due to punctual collisions with the membrane (as it was assumed in the literature) but also to the rising motion and the prolonged contact with the membrane surface while rising (“sweeping” effect). Given the great surface of QQ sheets, their effect to reduce membrane fouling could also be assumed to be attributed to a “flotation-like” phenomenon, which means that part of the particles in the mixed liquor can be carried by the QQ sheets while rising, and thus prevented from depositing on the membrane surface.

In sum, this study brought new insights to the application of QQ to MBRs. The mechanisms by which the QQ media could affect the MBR operation and the membrane fouling could be identified. This study contributed to a better understanding of a promising technology for membrane fouling by raising new questions and opening new discussions. However, some aspects can still be improved and constitute an interesting continuation to the present work.

In that way, a few recommendations and perspectives for future research are proposed in the following:

- On a **technical level** and with the view to apply QQ at the industrial scale, the design of the ALMBR appeared as a crucial aspect to optimize for the fluidization. In order to favor the QQ media fluidization, the location of the air spargers is a key-parameter. Therefore, it is highly recommended to always keep the air spargers under the bed of QQ media, as well as to optimize the height of the membrane modules. By this way, the QQ media would be completely fluidized for an enhanced effect on fouling mitigation.

- On the **methodology level**, the mass transfer was studied using a mimic molecule as a first approach. However, the mass transfer phenomenon strongly depends on the nature of the molecules involved (solute, solvent) and the nature of their interactions. Hence, this study could be taken further by studying the mass transfer of the actual molecules involved in the QQ reaction: the AHLs and/or the QQ enzymes, which would allow more accurate conclusions. In particular, the use of a mimic was valid in our case to study the convective mass transfer in the reactor and to compare the different shapes of QQ media, but the use of AHLs would be valuable to determine the actual diffusion coefficient, and thus describe more reliably the diffusion of the molecules into the QQ media.

- On a **scientific level**, this study demonstrated that the fluidization of QQ media was a key-phenomenon to promote (by increasing the aeration) to enhance their physical washing effect. In addition, it appeared that their distance to the membrane is determining. Thus it could be of great interest to understand more deeply the mechanisms involved in that physical effect by characterizing, for example, the trajectory of QQ media, the frequency of contact with the membrane surface, the effective surface contact between the QQ media and the membrane, the horizontal velocity of QQ media (towards the membrane), the turbulence,...etc.

- Also, some of the biological kinetics involved in the QQ application still need deeper understanding such as the production of AHLs, the production of QQ enzymes, the enzymatic degradation, and the production of biofilm. This information is of critical importance to emphasize the preventive aspect of QQ, which means rapidly and effectively disrupting the QS communication before the production of biofilm.

- Obviously, this study showed the major importance of the shape of QQ media as it was found to play a key-role in several ways (fluidization, hydrodynamics, and mass transfer). Therefore, the development of new shapes could be the subject of future research. In particular, QQ media with lower density (to foster the fluidization), greater porosity (to entrap more QQ bacteria) and greater surface exchange (to improve the mass transfer) could be designed and assessed for their efficiency to mitigate fouling.

APPENDICES

Appendix A-II-1: Quantification of AHLs

In the literature, several methods were reported for the quantification of AHLs, as reviewed by Wang et al. (2011) [164] in the figure hereafter.

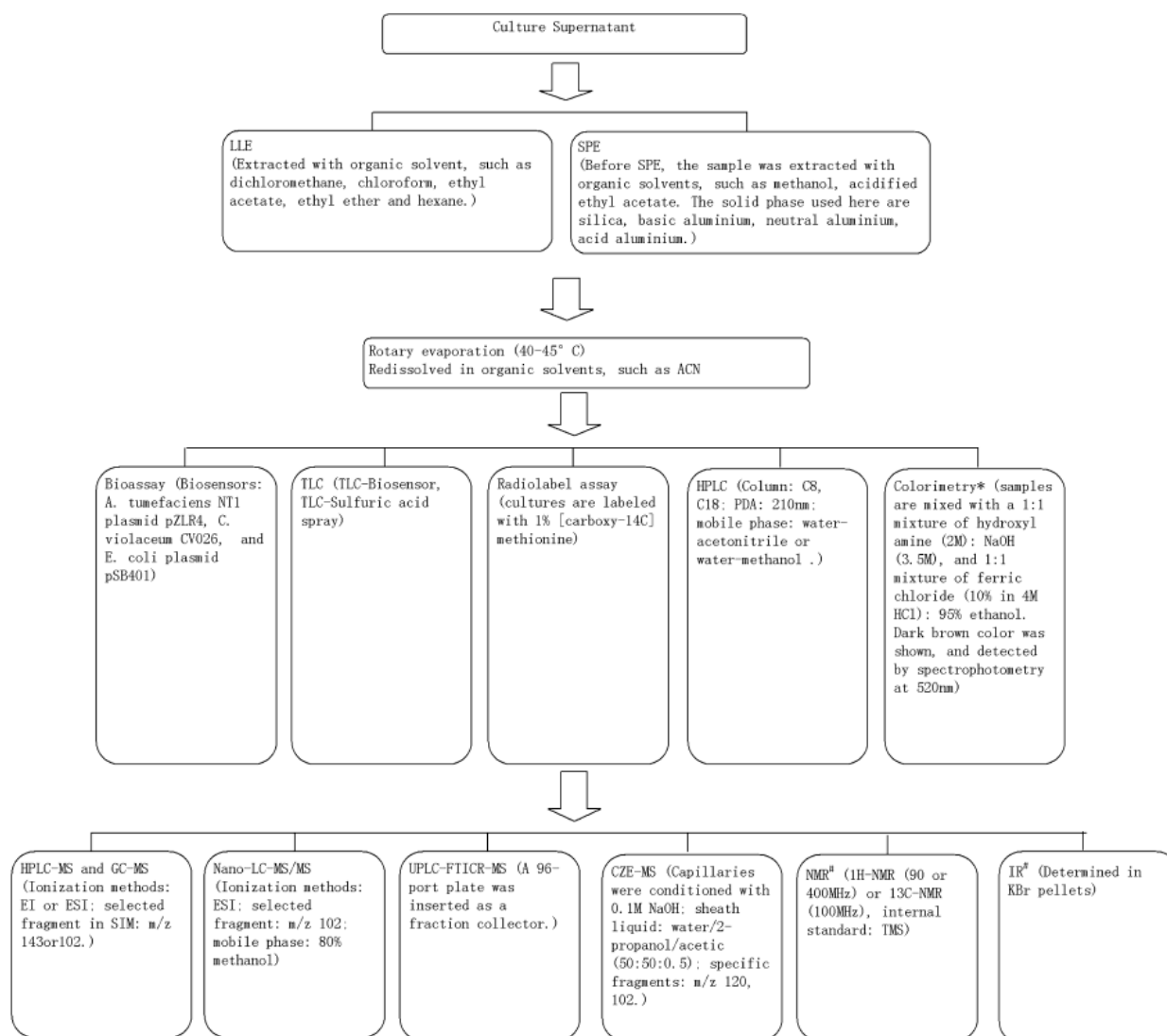


Figure A-II-1-VI-11 : Flow-chart of extraction, purification, identification and quantification of AHLs [164].

From these methods, the bioassay based on the bioluminescent reporter strain *A.tumefaciens* A136 was tested in the present study (more details about the principle of the methods are given in the literature [12,50]), and an example of calibration curve giving the relationship between the bioluminescence intensity and the concentration of C8-HSL is given in the figure hereafter.

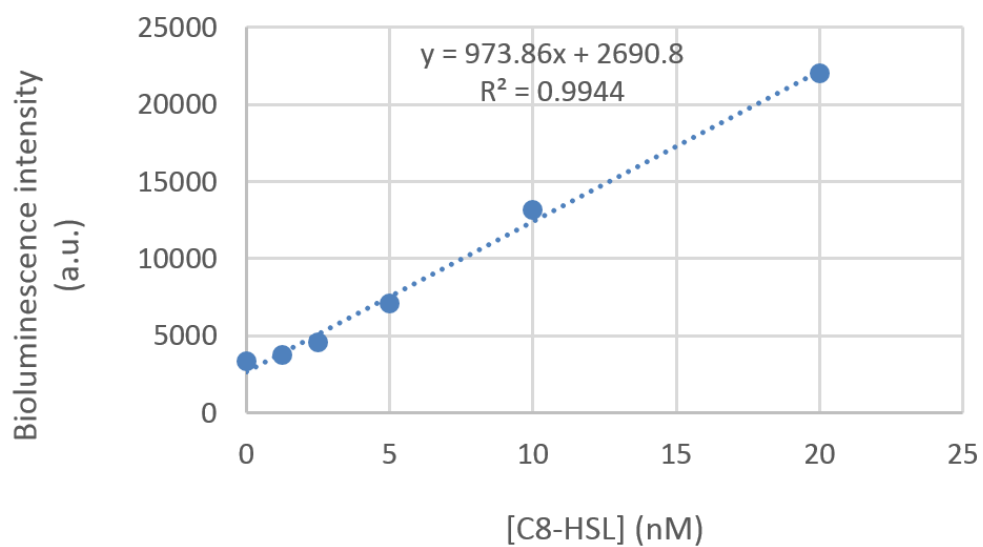


Figure A-II-1-2: Calibration curve of the *A.tumefaciens* A136-based bioluminescence assay for the quantification of AHLs.

Appendix A-III-1: Calculation of the terminal falling velocity of the QQ media in water

The method proposed by Heywood was selected for the determination of the terminal falling velocity of QQ media. It was developed for non-spherical solid particles in free-fall in a fluid and having a projected area A_p and a volume V_p .

This theory is based on the circle-equivalent diameter d_a , which is the diameter of the spherical particle having the same projected area A_p and can be determined using the following equation:

$$d_a = \sqrt{\frac{4A_p}{\pi}}$$

Then the shape factor k' is then determined using the equation below (k' is worth $\frac{\pi}{6}$ for spherical particles):

$$k' = \frac{V_p}{d_a^3}$$

The equivalent-Galilei number Ga_{eq} is then calculated using the following equation, where g is the gravitational constant, μ_l the viscosity of the liquid (water in our case), and ρ_s and ρ_l the density of the solid and the liquid, respectively.

$$Ga_{eq} = \frac{6k'(\rho_s - \rho_l)\rho_l g d_a^3}{\mu_l^2}$$

The equivalent-Reynolds number Re_{eq} is deduced then as a function of the equivalent-Galilei number using one of the following correlations, depending on the ranges.

Stokes	$Re_{eq} = \frac{Ga_{eq}}{18}$	$Re_{eq} < 1$ $Ga_{eq} < 27.5$
Van Allen	$Re_{eq} = \frac{Ga_{eq}}{18} [1 + 0.15 Re_{eq}^{0.687}]^{-1}$	$1 < Re_{eq} < 10^3$ $27.6 < Ga_{eq} < 4.4 \times 10^5$
Newton	$Re_{eq} = (Ga_{eq})^{0.5}$	$10^3 < Re_{eq} < 5 \times 10^5$ $4.4 \times 10^5 < Ga_{eq} < 1.1 \times 10^{11}$

Since the previous correlations were defined for spherical particles, the equivalent-Reynolds number has to be corrected taking into account the shape of the particle and according to the equation below where $Re_{eq,corr}$ is the corrected Reynolds number and Δ is determined on the basis of the values of Ga_{eq} and k' as in the Table A-III-1-1.

$$\log(Re_{eq,corr}) = \log(Re_{eq}) + \Delta$$

Table A-III-1-1: Values of Δ for the correction of the equivalent-Reynolds number.

$\log(\frac{1}{3} Ga_e)$	$k'=0,4$	$k'=0,3$	$k'=0,2$	$k'=0,1$
-2	-0,022	-0,002	+0,032	+0,131
-1	-0,023	-0,003	+0,030	+0,131
0	-0,025	-0,005	+0,026	+0,129
1	-0,027	-0,010	+0,021	+0,122
2	-0,031	-0,016	+0,012	+0,111
2,5	-0,033	-0,020	0,000	+0,080
3	-0,038	-0,032	-0,022	+0,025
3,5	-0,051	-0,052	-0,056	-0,040
4	-0,068	-0,074	-0,089	-0,098
4,5	-0,083	-0,093	-0,114	-0,146
5	-0,097	-0,110	-0,135	-0,186
5,5	-0,109	-0,125	-0,154	-0,224
6	-0,120	-0,134	-0,172	-0,255

Finally, the terminal falling velocity of the particle U_{tp} is determined with via the following equation:

$$U_{tp} = \frac{\mu_l Re_{eq,corr}}{\rho_l d_a}$$

The data and results for the three shapes of QQ media are presented in Table A-III-1-2.

Table A-III-1-2: Data and results of the terminal falling velocity for the three shapes of QQ media in water at 20°C.

Properties of the solid particles (QQ media)			
QQ media	Beads	Hollow cylinders	Sheets
Dimensions (10^{-3} m)	Diameter = 3.5	Outer diameter = 3.5 Length = 27	Length = 20 Width = 10
A_p (10^{-6} m ²)	9.6	94.5	200
V_p (10^{-9} m ³)	22.5	198.5	100
ρ_s (kg.m ⁻³)	1074	1060	1063
Properties of the liquid phase (water)			

ρ_l (kg.m ⁻³)	998.2		
μ_l (20°C) (Pa.s)	1.002×10 ⁻³		
Results			
d_a (10 ⁻³ m)	3.5	11.0	16.0
k'	0.5	0.15	0.02
Ga_{eq}	3.2×10 ⁴	2.3×10 ⁵	1.2×10 ⁵
Re_{eq}	238	805	541
$\Delta *$	0.0041	0.0697	0.009
$Re_{eq,corr}$	240	345	552
U_{tp} (10 ⁻² m.s ⁻¹)	5.8	5.0	2.0

*The values of Δ could not be directly read on the Table A-III-1-1 but were determined by extrapolation based on the values highlighted, and on the graphs presented in Figures A-III-1-1 and A-III-1-1.

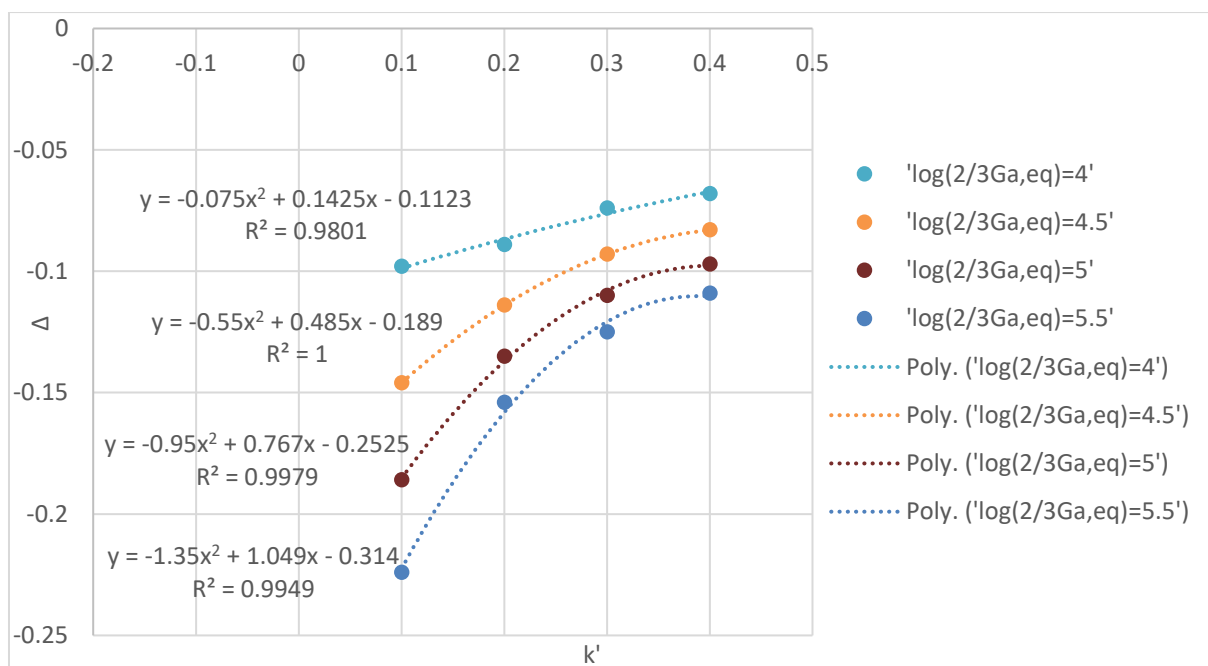


Figure A-III-1-VI-12 : Correlations between the correction factor Δ and the shape factor k' , deduced from the values in Table A-III-1-1.

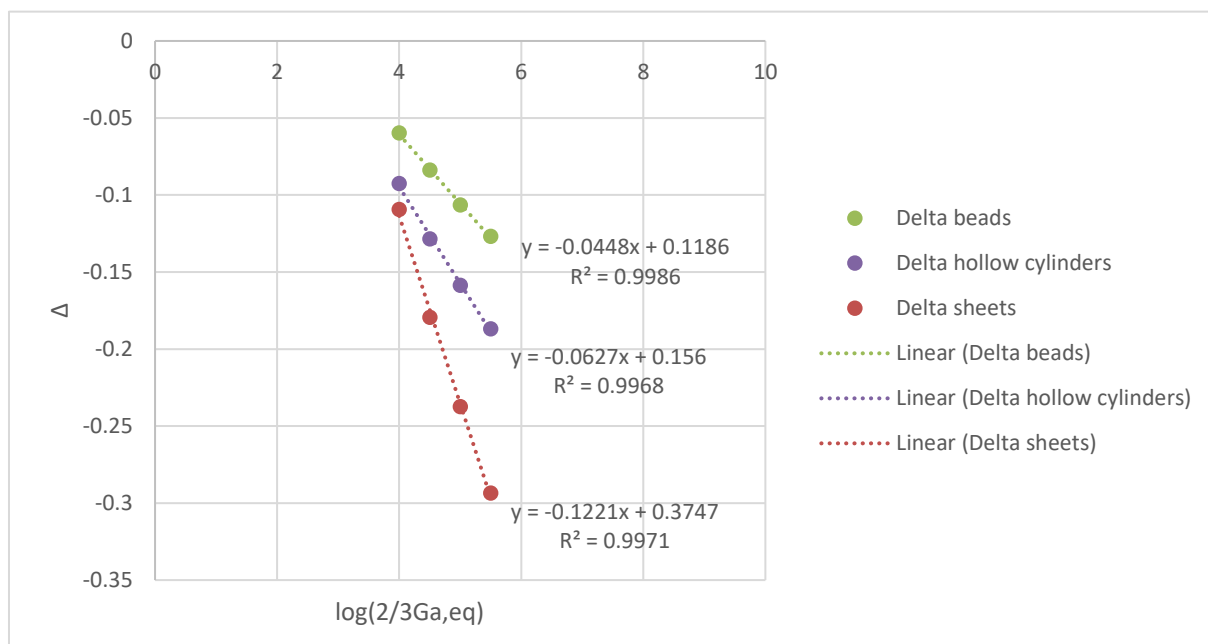


Figure A-III-1-VI-13 : Correlations between the correction factor Δ and the equivalent-Galilei number, deduced from the values in Table A-III-1-1.

The terminal falling velocity (in Table A-III-1-1) was found to decrease with the projected area of the QQ media.

Appendix A-III-2: Effect of baffles height on the fluidization of QQ media for a riser width D_r of 7 mm

Some complementary experiments were performed in order to investigate more how the air-lift geometry can affect the fluidization of QQ media. As it was demonstrated in the hydrodynamics characterization, no fluidization was observed when the riser width was set to 7 mm. Thus, the effect of the baffles height was investigated in presence of 0.45 % v/v of QQ beads. The different investigated conditions are gathered in Table A-III-2-1.

Table A-III-2-VI-6: Different heights of baffles tested for the study of the fluidization of QQ media under a riser width D_r of 7 mm.

Height of the baffles with respect to the bottom of the reactor (cm)	h_0	h_1	h_2	h_3	h_4
	6.5	9	11	13	15

Similarly to what was described in Chapter II, the fluidization rate of the QQ beads under each condition was determined by counting the QQ media on photos, and the results are presented in Figure A-III-2-1.

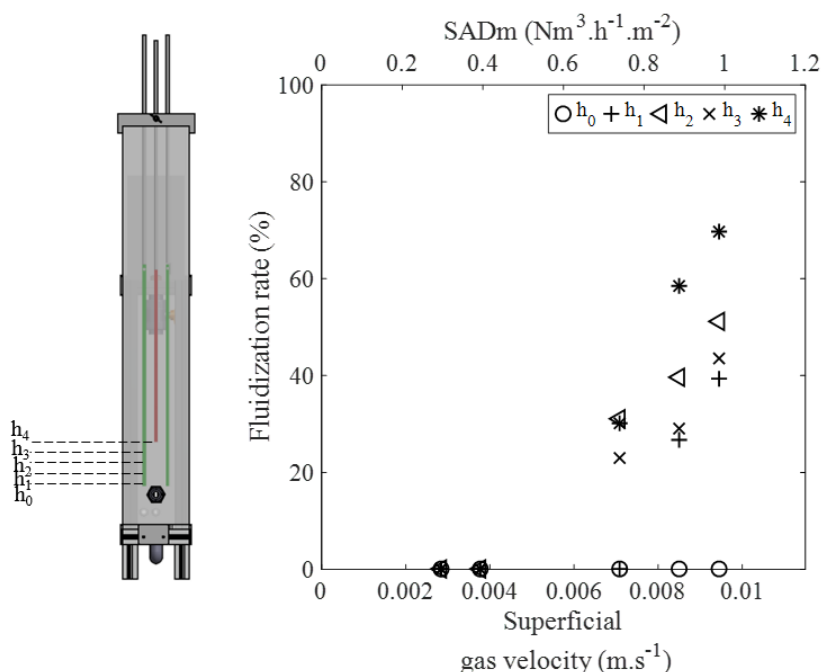


Figure A-III-2-1: Effect of the baffles position on the fluidization of QQ beads with a volume fraction of 0.45 % v/v and a riser width (D_r) of 7 mm.

These results confirm that the air-lift configuration has a key impact on the fluidization of QQ media. As it is presented in Figure A-III-2-1, the raise of baffles increases considerably the fluidization phenomenon for the same air flowrate. This result is of great interest and shows that a future perspective of research could be the investigation of an optimal geometry that promotes the fluidization of QQ media.

Appendix A-IV-1: Application of the usual RTD models

- *Tanks-in-series model*

This model was selected because the considered ALMBR is actually composed of tank-in-series. The first step to apply this model is to determine the number N of tanks in series using the following equation:

$$N = \frac{\mu^2}{\sigma^2}$$

From the first and second moments of the RTD functions, it was deduced that the ALMBR could be modeled by 1.3 and 1.5 tanks under the air flowrates of 0.75 and 0.90 $\text{Nm}^3 \cdot \text{h}^{-1} \cdot \text{m}^{-2}$, respectively, whereas 3.9 tanks-in-series were necessary to model the ALMBR under the SADm of 1.00 $\text{Nm}^3 \cdot \text{h}^{-1} \cdot \text{m}^{-2}$. Using these numbers of tanks-in-series, the theoretical RTD functions were determined in each case according to the following equation:

$$E(\theta) = N \frac{(N\theta)^{N-1}}{(N-1)!} e^{-N\theta}$$

The experimental and theoretical RTD profiles (red curves) are presented in Figure A-IV-1-1. The theoretical curves describe similar shapes to the experimental ones. However, in all the cases, significant discrepancies are still noticeable between the experimental and theoretical profiles. In sum, the present model is not suitable to model the ALMBR due to the fact that it is based on the succession of identical tanks, which is not in accordance with the geometry of the considered ALMBR. Besides, the numbers of tanks that were determined were decimal, which makes no physical sense and confirms the non-suitability of the model.

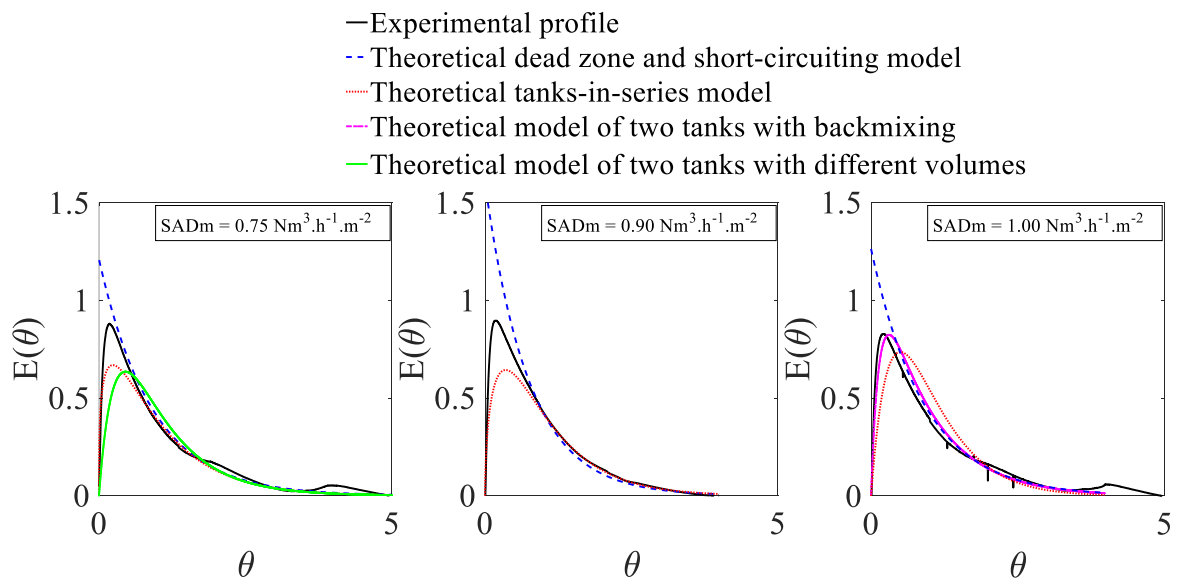


Figure A-IV-1-1: Usual models applied to the ALMBR under different air flowrates.

- *Tanks-in-series with back-mixing model*

Because of the recycling flow that takes place in the ALMBR, this model was selected to be tested. The back-mixing rate R was first determined using the equation below and considering two ($N = 2$) tanks-in-series.

$$\sigma^2 = \frac{N(1 + 2R) - 2R(1 + R) \left[1 - \left(\frac{R}{1 + R} \right)^N \right]}{N^2}$$

The model could only be applied when the SADm was $1.00 \text{ Nm}^3 \cdot \text{h}^{-1} \cdot \text{m}^{-2}$, because the rate R was found to be negative in the other cases. A theoretical $E(\theta)$ curve was determined using the following equations.

$$w = \sqrt{1 + R}$$

$$r_i = 1 + \frac{2(1 - w \cos \psi_i)}{w^2 - 1}$$

$$\psi_i(N + 1) + 2 \arctan \frac{\sin \psi_i}{w - \cos \psi_i} = i\pi$$

$$E(\theta) = 2N \frac{w^{N+1}}{w^2 - 1} \sum_{i=1}^N (-1)^{i+1} \frac{\sin^2 \psi_i}{(1 + Nr_i)} \exp(-N\theta r_i)$$

The theoretical RTD curve is plotted in Figure A-IV-1-1 (pink curve). The comparison of the experimental and theoretical profiles reveals important differences, which indicates the non-adequacy of this model to describe the ALMBR. Again, the hypothesis of two identical tanks does not correctly represent the geometry of the ALMBR.

- *Model of two tanks-in-series with different volumes*

This model offers the advantage of being based on the succession of two tanks with different volumes, and therefore could be modulated to fit the geometry of the studied ALMBR. The condition to apply this model is that the mean residence time equals the theoretical hydraulic retention time ($\mu = \tau$), which was only verified in the present study when the SADm is $0.75 \text{ Nm}^3 \cdot \text{h}^{-1} \cdot \text{m}^{-2}$. For this particular case, given the variance of the RTD function, the ratio of volumes α was calculated according to the following equation:

$$\sigma^2 = \frac{1 + \alpha^2}{(1 + \alpha)^2}$$

The ratio found α was found to be 3.5 (indicating that the first tank is 3.5 times greater than the second one), which is not in accordance with the actual geometry of the ALMBR. Also, when comparing the

theoretical $E(\theta)$ curve (obtained by the equation below and plotted as the green curve in Figure A-IV-1-1) to the experimental one, the model does not seem to correctly describe the ALMBR.

$$E(\theta) = \frac{1 + \alpha}{1 - \alpha} [\exp(-(1 + \alpha)\theta) - \exp(-(1 + \frac{1}{\alpha})\theta)]$$

- *Model of completely mixed reactor with dead zones and short-circuiting*

Finally, the model of completely mixed reactor with dead zones and short-circuiting was applied by determining the two parameters of the model m and n , using the following equations.

$$m = \frac{\mu}{\tau}$$

$$\sigma^2 = m^2 \tau^2 \left(\frac{2}{n} - 1 \right)$$

Using these parameters, the theoretical RTD functions were determined by the equation below (blue dotted curves in Figure A-IV-1-1). It appears that this model is not suitable either to describe the behavior of the ALMBR.

$$E(\theta) = \frac{n^2}{m} \exp\left(-\frac{n}{m}\theta\right) + (1 - n)\delta(t)\tau$$

In conclusion, the application of the usual models reveals that neither of them is completely adequate to correctly model the behavior of the ALMBR under the three considered air flowrates. This finding can be explained by the fact that the models are relatively simple models taking into account one phenomenon at the time (dysfunction, recycling flow, tanks-in-series), when the ALMBR addressed in the present study is in reality a more complex combination of all of these phenomena. Additionally, the dispersion model was also tried and did not result in a good model of the ALMBR which is, besides, in accordance with what was reported in the literature about MBRs being closer to completely mixed reactors. Therefore, it is possible to conclude that a more complete model is needed in order to describe the flowing behavior of the ALMBR.

Appendix A-IV-2: Criterion for the specific RTD model

In Chapter III, a specific model was developed to describe the flowing behavior in the ALMBR/QQ-ALMBR. The model was expressed by a theoretical RTD function $E_{th}(\theta)$ depending on three main parameters (m , n and Q_r). These parameters were adjusted to fit the experimental data. The minimization of the discrepancies between the theoretical and the experimental profiles was mathematically translated to a minimal value of $|E_{th}(\theta) - E_{exp}(\theta)|$, which graphically refers to two very close curves.

This criterion was chosen rather than a relative error $|\frac{E_{th}(\theta) - E_{exp}(\theta)}{E_{exp}(\theta)}|$ because it directly indicate the gap between the two curves, and it is more a reliable comparative tool when considering several curves.

An example is provided in the following for demonstration, with arbitrary values. The figure below presents two arbitrary curves (theoretical and experimental), and the average value $|y_{th}(x) - y_{exp}(x)|$ as well as the relative error $|\frac{y_{th}(x) - y_{exp}(x)}{y_{exp}(x)}|$ are calculated in two cases, according to the equations below, where p is the number of experimental points.

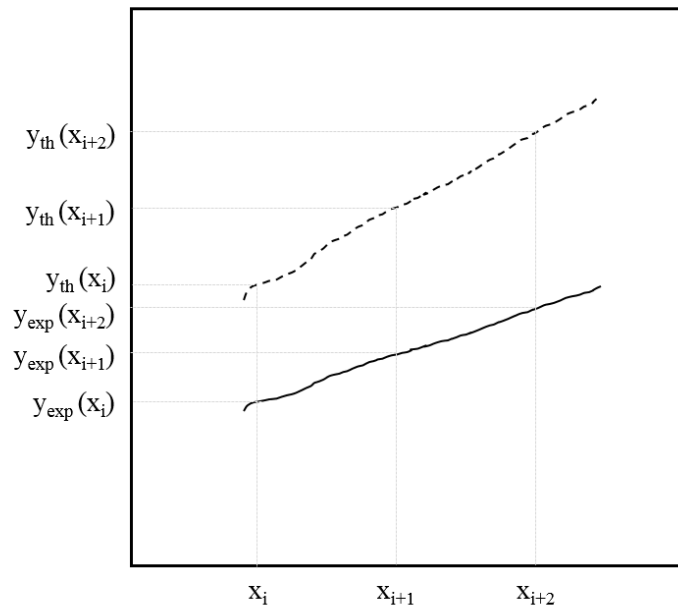


Figure A-IV-2-VI-14 : Illustrative example for the determination of the gap between an experimental and a theoretical curve.

$$\text{Average } |y_{th}(x) - y_{exp}(x)| = \frac{\sum_{i=1}^p |y_{th}(x_i) - y_{exp}(x_i)|}{p}$$

$$Average \left| \frac{y_{th}(x) - y_{exp}(x)}{y_{exp}(x)} \right| = \frac{\sum_{i=1}^p \frac{|y_{th}(x_i) - y_{exp}(x_i)|}{y_{exp}(x_i)}}{p}$$

For the illustration, $p = 3$ and $i = 1, 2, 3$.

Table A-IV-2-VI-7 : Example for the determination of the gap between an experimental and a theoretical curve.

Case 1					
$y_{exp}(x_1)$	$y_{exp}(x_2)$	$y_{exp}(x_3)$	$y_{th}(x_1)$	$y_{th}(x_2)$	$y_{th}(x_3)$
10	20	30	15	25	35
<i>Average</i> $ y_{th}(x) - y_{exp}(x) = 5$					
<i>Average</i> $\left \frac{y_{th}(x) - y_{exp}(x)}{y_{exp}(x)} \right = 25 \%$					
Case 2					
$y_{exp}(x_1)$	$y_{exp}(x_2)$	$y_{exp}(x_3)$	$y_{th}(x_1)$	$y_{th}(x_2)$	$y_{th}(x_3)$
20	30	40	25	35	45
<i>Average</i> $ y_{th}(x) - y_{exp}(x) = 5$					
<i>Average</i> $\left \frac{y_{th}(x) - y_{exp}(x)}{y_{exp}(x)} \right = 18 \%$					

In both cases the average value $|y_{th}(x) - y_{exp}(x)|$ was worth 5 which means that the curves were just as close to each other, however, the relative gap *Average* $\left| \frac{y_{th}(x) - y_{exp}(x)}{y_{exp}(x)} \right|$ was lower in the case 2 than in the case 1, because the values of the experimental function $y_{exp}(x)$ are taken into account. Therefore, the average value $|y_{th}(x) - y_{exp}(x)|$ is more reliable criterion for comparison.

Appendix A-VI-2: Fluidization rates of QQ media introduced at three volume fractions

Table A-VI-2-VI-8 : Fluidization rates, numbers and surfaces of the QQ media.

QQ media	Beads			Hollow cylinders			Sheets		
Volume fraction of 0.45 % v/v									
SADm (Nm ³ .m ⁻¹ .m ⁻²)	0.75	0.90	1.00	0.75	0.90	1.00	0.75	0.90	1.00
N_{TM} (-)	2600			298			585		
<i>Fuidization rate</i> (%)	6.2	10.9	16.1	26.2	53.2	63.3	30.4	47.8	55.9
N_{FM} (-)	161	283	418	78	158	188	177	279	327
Surface of one particle of QQ media (10 ⁻⁶ m ²)	38.5			455.8			400.0		
S_{TM} (m ²)	0.100			0.136			0.234		
S_{FM} (m ²)	0.006	0.011	0.016	0.036	0.072	0.086	0.071	0.112	0.131
Volume fraction of 0.10 % v/v									
SADm (Nm ³ .m ⁻¹ .m ⁻²)	0.75	0.90	1.00	0.75	0.90	1.00	0.75	0.90	1.00
N_{TM} (-)	578			65			130		
<i>Fuidization rate</i> (%)	4.9	12.2	14.5	55.7	59.6	82.9	49.6	74.4	84.1
N_{FM} (-)	28	70	84	36	39	54	65	97	109
Surface of one particle of QQ media (10 ⁻⁶ m ²)	38.5			455.8			400.0		
S_{TM} (m ²)	0.022			0.030			0.052		
S_{FM} (m ²)	0.001	0.003	0.003	0.017	0.018	0.025	0.026	0.039	0.044
Volume fraction of 0.06 % v/v									
SADm (Nm ³ .m ⁻¹ .m ⁻²)	0.75	0.90	1.00	0.75	0.90	1.00	0.75	0.90	1.00
N_{TM} (-)	347			39			78		
<i>Fuidization rate</i> (%)	6.3	7.8	8.3	38.8	82.0	100	68.0	100	100
N_{FM} (-)	22	27	29	15	32	39	48	78	78
Surface of one particle of QQ media (10 ⁻⁶ m ²)	38.5			455.8			400.0		
S_{TM} (m ²)	0.013			0.018			0.031		
S_{FM} (m ²)	0.001	0.001	0.001	0.007	0.015	0.018	0.019	0.031	0.031

REFERENCES

1. Wisniewski, C. Membrane bioreactor for water reuse. *Desalination* **2007**, *203*, 15–19, doi:10.1016/j.desal.2006.05.002.
2. Wang, Z.; Ma, J.; Tang, C. Y.; Kimura, K.; Wang, Q.; Han, X. Membrane cleaning in membrane bioreactors: A review. *J. Membr. Sci.* **2014**, *468*, 276–307, doi:10.1016/j.memsci.2014.05.060.
3. Lin, H.; Peng, W.; Zhang, M.; Chen, J.; Hong, H.; Zhang, Y. A review on anaerobic membrane bioreactors: Applications, membrane fouling and future perspectives. *Desalination* **2013**, *314*, 169–188, doi:10.1016/j.desal.2013.01.019.
4. Xiong, Y.; Liu, Y. Biological control of microbial attachment: a promising alternative for mitigating membrane biofouling. *Appl. Microbiol. Biotechnol.* **2010**, *86*, 825–837, doi:10.1007/s00253-010-2463-0.
5. Feng, L.; Wu, Z.; Yu, X. Quorum sensing in water and wastewater treatment biofilms. http://www.jeb.co.in/journal_issues/201304_apr13_supp/paper_20.pdf **2013**.
6. Kim, H.-W.; Oh, H.-S.; Kim, S.-R.; Lee, K.-B.; Yeon, K.-M.; Lee, C.-H.; Kim, S.; Lee, J.-K. Microbial population dynamics and proteomics in membrane bioreactors with enzymatic quorum quenching. *Appl. Microbiol. Biotechnol.* **2012**, *97*, 4665–4675, doi:10.1007/s00253-012-4272-0.
7. Waheed, H.; Hashmi, I.; Khan, S. J.; Kim, S. R.; Arshad, M.; Nasir, H. Microbial population dynamics and profiling of quorum sensing agents in membrane bioreactor. *Int. Biodeterior. Biodegrad.* **2015**, doi:10.1016/j.ibiod.2015.12.014.
8. Jo, S. J.; Kwon, H.; Jeong, S.-Y.; Lee, S. H.; Oh, H.-S.; Yi, T.; Lee, C.-H.; Kim, T. G. Effects of Quorum Quenching on the Microbial Community of Biofilm in an Anoxic-Oxic MBR for Wastewater Treatment. *J. Microbiol. Biotechnol.* **2016**, doi:10.4014/jmb.1604.04070.
9. Kim, S.-R.; Lee, K.-B.; Kim, J.-E.; Won, Y.-J.; Yeon, K.-M.; Lee, C.-H.; Lim, D.-J. Macroencapsulation of quorum quenching bacteria by polymeric membrane layer and its application to MBR for biofouling control. *J. Membr. Sci.* **2015**, *473*, 109–117, doi:10.1016/j.memsci.2014.09.009.
10. Jahangir, D.; Oh, H.-S.; Kim, S.-R.; Park, P.-K.; Lee, C.-H.; Lee, J.-K. Specific location of encapsulated quorum quenching bacteria for biofouling control in an external submerged membrane bioreactor. *J. Membr. Sci.* **2012**, *411–412*, 130–136, doi:10.1016/j.memsci.2012.04.022.
11. Oh, H.-S.; Yeon, K.-M.; Yang, C.-S.; Kim, S.-R.; Lee, C.-H.; Park, S. Y.; Han, J. Y.; Lee, J.-K. Control of Membrane Biofouling in MBR for Wastewater Treatment by Quorum Quenching Bacteria Encapsulated in Microporous Membrane. *Environ. Sci. Technol.* **2012**, *46*, 4877–4884, doi:10.1021/es204312u.
12. Lee, S.; Lee, S. H.; Lee, K.; Kwon, H.; Nahm, C. H.; Lee, C.-H.; Park, P.-K.; Choo, K.-H.; Lee, J.-K.; Oh, H.-S. Effect of the Shape and Size of Quorum Quenching Media on Biofouling Control in Membrane Bioreactors for Wastewater Treatment. *J. Microbiol. Biotechnol.* **2016**, doi:10.4014/jmb.1605.05021.
13. Lee, S.; Park, S.-K.; Kwon, H.; Lee, S. H.; Lee, K.; Nahm, C. H.; Jo, S. J.; Oh, H.-S.; Park, P.-K.; Choo, K.-H.; Lee, C.-H.; Yi, T. Crossing the Border between Laboratory and Field: Bacterial Quorum Quenching for Anti-Biofouling Strategy in an MBR. *Environ. Sci. Technol.* **2016**, doi:10.1021/acs.est.5b04795.
14. Lee, S. H.; Lee, S.; Lee, K.; Nahm, C. H.; Kwon, H.; Oh, H.-S.; Won, Y.-J.; Choo, K.-H.; Lee, C.-H.; Park, P.-K. More Efficient Media Design for Enhanced Biofouling Control in a Membrane Bioreactor: Quorum Quenching Bacteria Entrapping Hollow Cylinder. *Environ. Sci. Technol.* **2016**, *50*, 8596–8604, doi:10.1021/acs.est.6b01221.
15. Branda, S. S.; Vik, S.; Friedman, L.; Kolter, R. Biofilms: the matrix revisited. *Trends Microbiol.* **2005**, *13*, 20–26, doi:10.1016/j.tim.2004.11.006.
16. Flemming, H.-C.; Schaule, G.; Griebe, T.; Schmitt, J.; Tamachkierowa, A. Biofouling—the Achilles heel of membrane processes. *Desalination* **1997**, *113*, 215–225, doi:10.1016/S0011-9164(97)00132-X.
17. Wisniewski, C.; Grasmick, A. Floc size distribution in a membrane bioreactor and consequences for membrane fouling. *Colloids Surf. Physicochem. Eng. Asp.* **1998**, *138*, 403–411, doi:10.1016/S0927-7757(96)03898-8.
18. Lade, H.; Diby, P.; Ji Hyang, K. N-Acyl Homoserine Lactone-Mediated Quorum Sensing with Special Reference to Use of Quorum Quenching Bacteria in Membrane Biofouling Control. *BioMed Res. Int.* **2014**, doi:10.1155/2014/162584.
19. Lade, H.; Paul, D.; Kweon, J. H. Quorum Quenching Mediated Approaches for Control of Membrane Biofouling. *Int. J. Biol. Sci.* **2014**, *10*, 550–565, doi:10.7150/ijbs.9028.
20. Siddiqui, M. F.; Rzechowicz, M.; Harvey, W.; Zularisam, A. W.; Anthony, G. F. Quorum sensing based membrane biofouling control for water treatment: A review. *J. Water Process Eng.* **2015**, *7*, 112–122, doi:10.1016/j.jwpe.2015.06.003.
21. Fuqua, W. C.; Winans, S. C.; Greenberg, E. P. Quorum sensing in bacteria: the LuxR-LuxI family of cell density-responsive transcriptional regulators. *J. Bacteriol.* **1994**, *176*, 269–275.

22. Lim, S.; Kim, S.; Yeon, K.-M.; Sang, B.-I.; Chun, J.; Lee, C.-H. Correlation between microbial community structure and biofouling in a laboratory scale membrane bioreactor with synthetic wastewater. *Desalination* **2012**, *287*, 209–215, doi:10.1016/j.desal.2011.09.030.
23. Luxmy, N.; Nakajima, F.; Yamamoto, K. Analysis of bacterial community in membrane-separation bioreactors by fluorescent in situ hybridization (FISH) and denaturing gradient gelelectrophoresis (DGGE) techniques Available online: <http://www.iwaponline.com/wst/04110/wst041100259.htm> (accessed on Oct 15, 2015).
24. Miller, M. B.; Bassler, B. L. Quorum Sensing in Bacteria. *Annu. Rev. Microbiol.* **2001**, *55*, 165–199, doi:10.1146/annurev.micro.55.1.165.
25. Parsek, M. R.; Greenberg, E. P. Acyl-homoserine lactone quorum sensing in Gram-negative bacteria: A signaling mechanism involved in associations with higher organisms. *Proc. Natl. Acad. Sci.* **2000**, *97*, 8789–8793, doi:10.1073/pnas.97.16.8789.
26. Waters, C. M.; Bassler, B. L. Quorum sensing: cell-to-cell communication in bacteria. *Annu. Rev. Cell Dev. Biol.* **2005**, *21*, 319–346, doi:10.1146/annurev.cellbio.21.012704.131001.
27. Whitehead, N. A.; Barnard, A. M. L.; Slater, H.; Simpson, N. J. L.; Salmond, G. P. C. Quorum-sensing in Gram-negative bacteria. *FEMS Microbiol. Rev.* **2001**, *25*, 365–404, doi:10.1111/j.1574-6976.2001.tb00583.x.
28. Williams, P. Quorum sensing, communication and cross-kingdom signalling in the bacterial world. *Microbiology* **2007**, *153*, 3923–3938, doi:10.1099/mic.0.2007/012856-0.
29. Davies, D. G.; Parsek, M. R.; Pearson, J. P.; Iglewski, B. H.; Costerton, J. W.; Greenberg, E. P. The Involvement of Cell-to-Cell Signals in the Development of a Bacterial Biofilm. *Science* **1998**, *280*, 295–298, doi:10.1126/science.280.5361.295.
30. Hall-Stoodley, L.; Stoodley, P. Developmental regulation of microbial biofilms. *Curr. Opin. Biotechnol.* **2002**, *13*, 228–233, doi:10.1016/S0958-1669(02)00318-X.
31. Hammer, B. K.; Bassler, B. L. Quorum sensing controls biofilm formation in *Vibrio cholerae*. *Mol. Microbiol.* **2003**, *50*, 101–104, doi:10.1046/j.1365-2958.2003.03688.x.
32. Labbate, M.; Queck, S. Y.; Koh, K. S.; Rice, S. A.; Givskov, M.; Kjelleberg, S. Quorum Sensing-Controlled Biofilm Development in *Serratia liquefaciens* MG1. *J. Bacteriol.* **2004**, *186*, 692–698, doi:10.1128/JB.186.3.692-698.2004.
33. Parsek, M. R.; Greenberg, E. P. Sociomicrobiology: the connections between quorum sensing and biofilms. *Trends Microbiol.* **2005**, *13*, 27–33, doi:10.1016/j.tim.2004.11.007.
34. Rice, S. A.; Koh, K. S.; Queck, S. Y.; Labbate, M.; Lam, K. W.; Kjelleberg, S. Biofilm Formation and Sloughing in *Serratia marcescens* Are Controlled by Quorum Sensing and Nutrient Cues. *J. Bacteriol.* **2005**, *187*, 3477–3485, doi:10.1128/JB.187.10.3477-3485.2005.
35. Shrout, J. D.; Chopp, D. L.; Just, C. L.; Hentzer, M.; Givskov, M.; Parsek, M. R. The impact of quorum sensing and swarming motility on *Pseudomonas aeruginosa* biofilm formation is nutritionally conditional. *Mol. Microbiol.* **2006**, *62*, 1264–1277, doi:10.1111/j.1365-2958.2006.05421.x.
36. Waters, C. M.; Lu, W.; Rabinowitz, J. D.; Bassler, B. L. Quorum Sensing Controls Biofilm Formation in *Vibrio cholerae* through Modulation of Cyclic Di-GMP Levels and Repression of vpsT. *J. Bacteriol.* **2008**, *190*, 2527–2536, doi:10.1128/JB.01756-07.
37. Xia, S.; Zhou, L.; Zhang, Z.; Li, J. Influence and mechanism of N-(3-oxooxetanoyl)-L-homoserine lactone (C8-oxo-HSL) on biofilm behaviors at early stage. *J. Environ. Sci.* **2012**, *24*, 2035–2040, doi:10.1016/S1001-0742(11)61060-7.
38. Yeon, K.-M.; Cheong, W.-S.; Oh, H.-S.; Lee, W.-N.; Hwang, B.-K.; Lee, C.-H.; Beyenal, H.; Lewandowski, Z. Quorum Sensing: A New Biofouling Control Paradigm in a Membrane Bioreactor for Advanced Wastewater Treatment. *Environ. Sci. Technol.* **2009**, *43*, 380–385, doi:10.1021/es8019275.
39. Kim, S.-R.; Oh, H.-S.; Jo, S.-J.; Yeon, K.-M.; Lee, C.-H.; Lim, D.-J.; Lee, C.-H.; Lee, J.-K. Biofouling Control with Bead-Entrapped Quorum Quenching Bacteria in Membrane Bioreactors: Physical and Biological Effects. *Environ. Sci. Technol.* **2013**, *47*, 836–842, doi:10.1021/es303995s.
40. Maqbool, T.; Khan, S. J.; Waheed, H.; Lee, C.-H.; Hashmi, I.; Iqbal, H. Membrane biofouling retardation and improved sludge characteristics using quorum quenching bacteria in submerged membrane bioreactor. *J. Membr. Sci.* **2015**, *483*, 75–83, doi:10.1016/j.memsci.2015.02.011.
41. Siddiqui, M. F.; Sakinah, M.; Singh, L.; Zularisam, A. W. Targeting N-acyl-homoserine-lactones to mitigate membrane biofouling based on quorum sensing using a biofouling reducer. *J. Biotechnol.* **2012**, *161*, 190–197, doi:10.1016/j.jbiotec.2012.06.029.
42. Weerasekara, N. A.; Choo, K.-H.; Lee, C.-H. Hybridization of physical cleaning and quorum quenching to minimize membrane biofouling and energy consumption in a membrane bioreactor. *Water Res.* **2014**, *67*, 1–10, doi:10.1016/j.watres.2014.08.049.
43. Dong, Y.-H.; Wang, L.-H.; Zhang, L.-H. Quorum-Quenching Microbial Infections: Mechanisms and Implications. *Philos. Trans. Biol. Sci.* **2007**, *362*, 1201–1211.

44. Rasmussen, T. B.; Givskov, M. Quorum sensing inhibitors: a bargain of effects. *Microbiology* **2006**, *152*, 895–904, doi:10.1099/mic.0.28601-0.
45. Siddiqui, M. F.; Sakinah, M.; Ismail, A. F.; Matsuura, T.; Zularisam, A. W. The anti-biofouling effect of Piper betle extract against *Pseudomonas aeruginosa* and bacterial consortium. *Desalination* **2012**, *288*, 24–30, doi:10.1016/j.desal.2011.11.060.
46. Jiang, W.; Xia, S.; Liang, J.; Zhang, Z.; Hermanowicz, S. W. Effect of quorum quenching on the reactor performance, biofouling and biomass characteristics in membrane bioreactors. *Water Res.* **2013**, *47*, 187–196, doi:10.1016/j.watres.2012.09.050.
47. Kim, J.-H.; Choi, D.-C.; Yeon, K.-M.; Kim, S.-R.; Lee, C.-H. Enzyme-Immobilized Nanofiltration Membrane To Mitigate Biofouling Based on Quorum Quenching. *Environ. Sci. Technol.* **2011**, *45*, 1601–1607, doi:10.1021/es103483j.
48. Yeon, K.-M.; Lee, C.-H.; Kim, J. Magnetic Enzyme Carrier for Effective Biofouling Control in the Membrane Bioreactor Based on Enzymatic Quorum Quenching. *Environ. Sci. Technol.* **2009**, *43*, 7403–7409, doi:10.1021/es901323k.
49. Czajkowski, R.; Jafra, S. Quenching of acyl-homoserine lactone-dependent quorum sensing by enzymatic disruption of signal molecules. *Acta Biochim. Pol.* **2009**, *56*, 1–16.
50. Oh, H.-S.; Kim, S.-R.; Cheong, W.-S.; Lee, C.-H.; Lee, J.-K. Biofouling inhibition in MBR by *Rhodococcus* sp. BH4 isolated from real MBR plant. *Appl. Microbiol. Biotechnol.* **2013**, *97*, 10223–10231, doi:10.1007/s00253-013-4933-7.
51. Köse-Mutlu, B.; Ergön-Can, T.; Koyuncu, İ.; Lee, C.-H. Quorum quenching MBR operations for biofouling control under different operation conditions and using different immobilization media. *Desalination Water Treat.* **2015**, *0*, 1–11, doi:10.1080/19443994.2015.1086899.
52. Ergön-Can, T.; Köse-Mutlu, B.; Koyuncu, İ.; Lee, C.-H. Biofouling control based on bacterial quorum quenching with a new application: Rotary microbial carrier frame. *J. Membr. Sci.* **2017**, *525*, 116–124, doi:10.1016/j.memsci.2016.10.036.
53. Hasnain, G.; Khan, S. J.; Arshad, M. Z.; Abdullah, H. Y. Combined Impact of Quorum Quenching and Backwashing on Biofouling Control in a Semi-Pilot Scale MBR Treating Real Wastewater - Recherche Google. *J. Chem. Soc. Pak.* **2017**.
54. Weerasekara, N. A.; Choo, K.-H.; Lee, C.-H. Biofouling control: Bacterial quorum quenching versus chlorination in membrane bioreactors. *Water Res.* **2016**, *103*, 293–301, doi:10.1016/j.watres.2016.07.049.
55. Cheong, W.-S.; Lee, C.-H.; Moon, Y.-H.; Oh, H.-S.; Kim, S.-R.; Lee, S. H.; Lee, C.-H.; Lee, J.-K. Isolation and Identification of Indigenous Quorum Quenching Bacteria, *Pseudomonas* sp. 1A1, for Biofouling Control in MBR. *Ind. Eng. Chem. Res.* **2013**, *52*, 10554–10560, doi:10.1021/ie303146f.
56. Cheong, W.-S.; Kim, S.-R.; Oh, H.-S.; Lee, S. H.; Yeon, K.-M.; Lee, C.-H.; Lee, J.-K. Design of Quorum Quenching Microbial Vessel to Enhance Cell Viability for Biofouling Control in Membrane Bioreactor. *J. Microbiol. Biotechnol.* **2014**, *24*, 97–105, doi:10.4014/jmb.1311.11008.
57. Waheed, H.; Pervez, S.; Hashmi, I.; Khan, S. J.; Kim, S.-R. High-performing antifouling bacterial consortium for submerged membrane bioreactor treating synthetic wastewater. *Int. J. Environ. Sci. Technol.* **2017**, *1*–10, doi:10.1007/s13762-017-1392-1.
58. Xiao, Y.; Waheed, H.; Xiao, K.; Hashmi, I.; Zhou, Y. In tandem effects of activated carbon and quorum quenching on fouling control and simultaneous removal of pharmaceutical compounds in membrane bioreactors. *Chem. Eng. J.* **2018**, doi:10.1016/j.cej.2018.02.073.
59. Yavuztürk Gül, B.; Koyuncu, I. Assessment of new environmental quorum quenching bacteria as a solution for membrane biofouling. *Process Biochem.*, doi:10.1016/j.procbio.2017.05.030.
60. Gül, B. Y.; Imer, D. Y.; Park, P.-K.; Koyuncu, I. Assessment of a novel anti-biofouling microorganism (*Bacillus* sp. T5) for control of membrane biofouling and its effect on bacterial community structure in membrane bioreactors. *Water Sci. Technol.* **2017**, wst2017592, doi:10.2166/wst.2017.592.
61. Ham, S.-Y.; Kim, H.-S.; Cha, E.; Park, J.-H.; Park, H.-D. Mitigation of membrane biofouling by a quorum quenching bacterium for membrane bioreactors. *Bioresour. Technol.* **2018**, doi:10.1016/j.biortech.2018.03.007.
62. Yu, H.; Liang, H.; Qu, F.; He, J.; Xu, G.; Hu, H.; Li, G. Biofouling control by biostimulation of quorum-quenching bacteria in a membrane bioreactor for wastewater treatment. *Biotechnol. Bioeng.* **2016**, n/a–n/a, doi:10.1002/bit.26039.
63. Dong, Y.-H.; Zhang, L.-H. Quorum sensing and quorum-quenching enzymes. *Scopus* **2005**.
64. Fetzner, S. Quorum quenching enzymes. *J. Biotechnol.* **2014**, doi:10.1016/j.jbiotec.2014.09.001.
65. Park, S.-Y.; Hwang, B.-J.; Shin, M.-H.; Kim, J.-A.; Kim, H.-K.; Lee, J.-K. N-acylhomoserine lactonase producing *Rhodococcus* spp. with different AHL-degrading activities. *FEMS Microbiol. Lett.* **2006**, *261*, 102–108, doi:10.1111/j.1574-6968.2006.00336.x.

66. Uroz, S.; Oger, P. M.; Chapelle, E.; Adeline, M.-T.; Faure, D.; Dessaux, Y. A Rhodococcus qsdA-Encoded Enzyme Defines a Novel Class of Large-Spectrum Quorum-Quenching Lactonases. *Appl. Environ. Microbiol.* **2008**, *74*, 1357–1366, doi:10.1128/AEM.02014-07.
67. Uroz, S.; Chhabra, S. R.; Cámara, M.; Williams, P.; Oger, P.; Dessaux, Y. N-Acylhomoserine lactone quorum-sensing molecules are modified and degraded by Rhodococcus erythropolis W2 by both amidolytic and novel oxidoreductase activities. *Microbiology* **2005**, *151*, 3313–3322, doi:10.1099/mic.0.27961-0.
68. Wang, L.-H.; Weng, L.-X.; Dong, Y.-H.; Zhang, L.-H. Specificity and Enzyme Kinetics of the Quorum-quenching N-Acyl Homoserine Lactone Lactonase (AHL-lactonase). *J. Biol. Chem.* **2004**, *279*, 13645–13651, doi:10.1074/jbc.M311194200.
69. Mohammed Sakr, M.; Mohamed Anwar Aboshanab, K.; Mabrouk Aboulwafa, M.; Abdel-Haleem Hassouna, N. Characterization and Complete Sequence of Lactonase Enzyme from *Bacillus weihenstephanensis* Isolate P65 with Potential Activity against Acyl Homoserine Lactone Signal Molecules. *BioMed Res. Int.* **2013**, *2013*, e192589, doi:10.1155/2013/192589.
70. Sio, C. F.; Otten, L. G.; Cool, R. H.; Diggle, S. P.; Braun, P. G.; Bos, R.; Daykin, M.; Cámara, M.; Williams, P.; Quax, W. J. Quorum Quenching by an N-Acyl-Homoserine Lactone Acylase from *Pseudomonas aeruginosa* PAO1. *Infect. Immun.* **2006**, *74*, 1673–1682, doi:10.1128/IAI.74.3.1673-1682.2006.
71. Romero, M.; Diggle, S. P.; Heeb, S.; Cámara, M.; Otero, A. Quorum quenching activity in *Anabaena* sp. PCC 7120: identification of AiiC, a novel AHL-acylase. *FEMS Microbiol. Lett.* **2008**, *280*, 73–80, doi:10.1111/j.1574-6968.2007.01046.x.
72. Xu, F.; Byun, T.; Dussen, H.-J.; Duke, K. R. Degradation of N-acylhomoserine lactones, the bacterial quorum-sensing molecules, by acylase. *J. Biotechnol.* **2003**, *101*, 89–96, doi:10.1016/S0168-1656(02)00305-X.
73. Nahm, C. H.; Choi, D.-C.; Kwon, H.; Lee, S.; Lee, S. H.; Lee, K.; Choo, K.-H.; Lee, J.-K.; Lee, C.-H.; Park, P.-K. Application of quorum quenching bacteria entrapping sheets to enhance biofouling control in a membrane bioreactor with a hollow fiber module. *J. Membr. Sci.* **2017**, *526*, 264–271, doi:10.1016/j.memsci.2016.12.046.
74. Meng, F.; Chae, S.-R.; Drews, A.; Kraume, M.; Shin, H.-S.; Yang, F. Recent advances in membrane bioreactors (MBRs): Membrane fouling and membrane material. *Water Res.* **2009**, *43*, 1489–1512, doi:10.1016/j.watres.2008.12.044.
75. Pollice, A.; Brookes, A.; Jefferson, B.; Judd, S. Sub-critical flux fouling in membrane bioreactors — a review of recent literature. *Desalination* **2005**, *174*, 221–230, doi:10.1016/j.desal.2004.09.012.
76. Zhang, J.; Chua, H. C.; Zhou, J.; Fane, A. G. Factors affecting the membrane performance in submerged membrane bioreactors. *J. Membr. Sci.* **2006**, *284*, 54–66, doi:10.1016/j.memsci.2006.06.022.
77. Cho, B. D.; Fane, A. G. Fouling transients in nominally sub-critical flux operation of a membrane bioreactor. *J. Membr. Sci.* **2002**, *209*, 391–403, doi:10.1016/S0376-7388(02)00321-6.
78. Hwang, B.-K.; Lee, W.-N.; Yeon, K.-M.; Park, P.-K.; Lee, C.-H.; Chang, in-S.; Drews, A.; Kraume, M. Correlating TMP Increases with Microbial Characteristics in the Bio-Cake on the Membrane Surface in a Membrane Bioreactor. *Environ. Sci. Technol.* **2008**, *42*, 3963–3968, doi:10.1021/es7029784.
79. Li, C.; Cabassud, C.; Guigui, C. Effects of carbamazepine in peak injection on fouling propensity of activated sludge from a MBR treating municipal wastewater. *J. Membr. Sci.* **2015**, *475*, 122–130, doi:10.1016/j.memsci.2014.10.017.
80. Li, C.; Cabassud, C.; Reboul, B.; Guigui, C. Effects of pharmaceutical micropollutants on the membrane fouling of a submerged MBR treating municipal wastewater: Case of continuous pollution by carbamazepine. *Water Res.* **2015**, *69*, 183–194, doi:10.1016/j.watres.2014.11.027.
81. Massé, A.; Spérandio, M.; Cabassud, C. Comparison of sludge characteristics and performance of a submerged membrane bioreactor and an activated sludge process at high solids retention time. *Water Res.* **2006**, *40*, 2405–2415, doi:10.1016/j.watres.2006.04.015.
82. Domínguez, L.; Rodríguez, M.; Prats, D. Effect of different extraction methods on bound EPS from MBR sludges. Part I: Influence of extraction methods over three-dimensional EEM fluorescence spectroscopy fingerprint. *Desalination* **2010**, *261*, 19–26, doi:10.1016/j.desal.2010.05.054.
83. Bouhabila, E. H.; Ben Aim, R.; Buisson, H. Fouling characterisation in membrane bioreactors. *Sep. Purif. Technol.* **2001**, *22–23*, 123–132, doi:10.1016/S1383-5866(00)00156-8.
84. Teychene, B.; Guigui, C.; Cabassud, C.; Amy, G. Toward a better identification of foulant species in MBR processes. *Desalination* **2008**, *231*, 27–34, doi:10.1016/j.desal.2007.12.006.
85. Brelles-Mariño, G.; Bedmar, E. J. Detection, purification and characterisation of quorum-sensing signal molecules in plant-associated bacteria. *J. Biotechnol.* **2001**, *91*, 197–209, doi:10.1016/S0168-1656(01)00330-3.

86. Li, X.; Fekete, A.; Englmann, M.; Götz, C.; Rothballer, M.; Frommberger, M.; Buddrus, K.; Fekete, J.; Cai, C.; Schröder, P.; Hartmann, A.; Chen, G.; Schmitt-Kopplin, P. Development and application of a method for the analysis of N-acylhomoserine lactones by solid-phase extraction and ultra high pressure liquid chromatography. *J. Chromatogr. A* **2006**, *1134*, 186–193, doi:10.1016/j.chroma.2006.09.047.
87. Jahn, A.; Nielsen, P. H. Extraction of extracellular polymeric substances (EPS) from biofilms using a cation exchange resin. *Water Sci. Technol.* **1995**, *32*, 157–164, doi:10.1016/0273-1223(96)00020-0.
88. Teychene, B.; Guigui, C.; Cabassud, C. Engineering of an MBR supernatant fouling layer by fine particles addition: A possible way to control cake compressibility. *Water Res.* **2011**, *45*, 2060–2072, doi:10.1016/j.watres.2010.12.018.
89. Waheed, H.; Xiao, Y.; Hashmi, I.; Stuckey, D.; Zhou, Y. Insights into quorum quenching mechanisms to control membrane biofouling under changing organic loading rates. *Chemosphere* **2017**, *182*, 40–47, doi:10.1016/j.chemosphere.2017.04.151.
90. Chisti, M. Y. *Airlift bioreactors*; Elsevier Applied Science, 1989; ISBN 978-1-85166-320-0.
91. Merchuk J.C.; Gluz M. Bioreactors, Air-lift Reactors. *Encycl. Bioprocess Technol.* **2002**, doi:10.1002/0471250589.ebt029.
92. Khalili-Garakani, A.; Mehrnia, M. R.; Mostoufi, N.; Sarrafzadeh, M. H. Analyze and control fouling in an airlift membrane bioreactor: CFD simulation and experimental studies. *Process Biochem.* **2011**, *46*, 1138–1145, doi:10.1016/j.procbio.2011.01.036.
93. Khalili-Garakani, A.; Mehrnia, mr; Mostoufi, N.; Sarrafzadeh, M. Flow Characteristics in an Airlift Membrane Bioreactor. *Chem. Prod. Process Model.* **2009**, *4*.
94. Böhm, L.; Drews, A.; Prieske, H.; Bérubé, P. R.; Kraume, M. The importance of fluid dynamics for MBR fouling mitigation. *Bioresour. Technol.* **2012**, *122*, 50–61, doi:10.1016/j.biortech.2012.05.069.
95. Prieske, H.; Böhm, L.; Drews, A.; Kraume, M. Optimised hydrodynamics for membrane bioreactors with immersed flat sheet membrane modules. *Desalination Water Treat.* **2010**, *18*, 270–276, doi:10.5004/dwt.2010.1784.
96. Jacob, M. *Réutilisation des eaux usées épurées par association de procédés biologiques et membranaires*; Toulouse, INSA, 2011;
97. Chapter 3 - Design A2 - Judd, Simon. In *The MBR Book*; Judd, C., Ed.; Elsevier Science: Oxford, 2006; pp. 123–162 ISBN 978-1-85617-481-7.
98. Judd, S. *The MBR Book: Principles and Applications of Membrane Bioreactors for Water and Wastewater Treatment*; Elsevier, 2011; ISBN 978-0-08-046510-4.
99. Couvert, A.; Bastoul, D.; Roustan, M.; Chatellier, P. Hydrodynamic and mass transfer study in a rectangular three-phase air-lift loop reactor. *Chem. Eng. Process. Process Intensif.* **2004**, *43*, 1381–1387, doi:10.1016/j.cep.2003.06.001.
100. Drandev, S.; Penev, K. I.; Karamanev, D. Study of the hydrodynamics and mass transfer in a rectangular air-lift bioreactor. *Chem. Eng. Sci.* **2016**, *146*, 180–188, doi:10.1016/j.ces.2016.02.041.
101. Xu, Y.; Zhu, N.; Sun, J.; Liang, P.; Xiao, K.; Huang, X. Evaluating oxygen mass transfer parameters for large-scale engineering application of membrane bioreactors. *Process Biochem.* **2017**, *60*, 13–18, doi:10.1016/j.procbio.2017.05.020.
102. Martinelli, L.; Guigui, C.; Line, A. Characterisation of hydrodynamics induced by air injection related to membrane fouling behaviour. *Desalination* **2010**, *250*, 587–591, doi:10.1016/j.desal.2009.09.029.
103. Pollet, S. *Caractérisation du colmatage et de l'hydrodynamique dans les bioréacteurs à membranes : influence de la configuration du module et de l'aération*; Toulouse, INSA, 2009;
104. Bessière-Pacurar, C. *Compréhension et quantification des mécanismes hydrodynamiques locaux liés à l'aération au sein de faisceaux de fibres creuses immergées*; Toulouse, INSA, 2010;
105. Chisti, M. Y.; Halard, B.; Moo-Young, M. Liquid circulation in airlift reactors. *Chem. Eng. Sci.* **1988**, *43*, 451–457, doi:10.1016/0009-2509(88)87005-2.
106. Hills, J. H. The operation of a bubble column at high throughputs: I. Gas holdup measurements. *Chem. Eng. J.* **1976**, *12*, 89–99, doi:10.1016/0300-9467(76)87002-5.
107. Freitas, C.; Fialová, M.; Zahradnik, J.; Teixeira, J. A. Hydrodynamic model for three-phase internal- and external-loop airlift reactors. *Chem. Eng. Sci.* **1999**, *54*, 5253–5258, doi:10.1016/S0009-2509(99)00256-0.
108. Wicaksana, F.; Fane, A. G.; Chen, V. Fibre movement induced by bubbling using submerged hollow fibre membranes. *J. Membr. Sci.* **2006**, *271*, 186–195, doi:10.1016/j.memsci.2005.07.024.
109. Bello, R. A.; Robinson, C. W.; Moo-Young, M. Liquid circulation and mixing characteristics of airlift contactors. *Can. J. Chem. Eng.* **1984**, *62*, 573–577, doi:10.1002/cjee.5450620501.
110. Prieske, H.; Drews, A.; Kraume, M. Prediction of the circulation velocity in a membrane bioreactor. *Desalination* **2008**, *231*, 219–226, doi:10.1016/j.desal.2007.12.010.
111. Heijnen, J. J.; Hols, J.; van der Lans, R. G. J. M.; van Leeuwen, H. L. J. M.; Mulder, A.; Weltevrede, R. A simple hydrodynamic model for the liquid circulation velocity in a full-scale two- and three-phase

- internal airlift reactor operating in the gas recirculation regime - ScienceDirect Available online: <https://www.sciencedirect.com/science/article/pii/S0009250997000705> (accessed on Apr 18, 2018).
112. Fan, L.-S.; Hwang, S.-J.; Matsuura, A. Hydrodynamic behaviour of a draft tube gas-liquid-solid spouted bed. *Chem. Eng. Sci.* **1984**, *39*, 1677–1688, doi:10.1016/0009-2509(84)80101-3.
 113. Heck, J.; Onken, U. Characteristics of solid suspensions in a bubble column without and with draft tube. *Chem. Eng. Technol.* **2004**, *11*, 335–340, doi:10.1002/ceat.270110144.
 114. Immich, M.; Onken, U. Prediction of minimum gas velocity in suspended bubble columns and airlift reactors. *Chem. Eng. Sci.* **1992**, *47*, 3379–3386, doi:10.1016/0009-2509(92)85048-G.
 115. Petrovic, D. L. J.; Pošarac, D.; Duduković, A.; Skala, D. Minimum fluidization velocity of large particles in a draft tube airlift reactor - ScienceDirect Available online: <https://www.sciencedirect.com/science/article/pii/S000925099380275U> (accessed on Apr 24, 2018).
 116. Nakao, K.; Azakami, F.; Furumoto, K.; Yoshimoto, M.; Fukunaga, K. Measurement and Correlation of Critical Gas and Liquid Velocities for Complete Circulation of Solid Particles in External Loop Airlift Bubble Columns. *Can. J. Chem. Eng.* **2003**, *81*, 444–450, doi:10.1002/cjce.5450810315.
 117. Pjontek, Macchi, A. Hydrodynamic comparison of spherical and cylindrical particles in a gas-liquid-solid fluidized bed at elevated pressure and high gas holdup conditions - ScienceDirect Available online: <https://www.sciencedirect.com/science/article/pii/S003259101300795X> (accessed on Apr 24, 2018).
 118. Clift, R.; Grace, J. R.; Weber, M. E. *Bubbles, Drops, and Particles*; Courier Corporation, 1978; ISBN 978-0-486-44580-9.
 119. Davies, R. M.; Taylor, S. G. The mechanics of large bubbles rising through extended liquids and through liquids in tubes. *Proc R Soc Lond A* **1950**, *200*, 375–390, doi:10.1098/rspa.1950.0023.
 120. Jensen, K. D. Flow measurements. *J. Braz. Soc. Mech. Sci. Eng.* **2004**, *26*, 400–419, doi:10.1590/S1678-58782004000400006.
 121. Yeo, A. P. S.; Law, A. W. K.; Fane, A. G. Factors affecting the performance of a submerged hollow fiber bundle. *J. Membr. Sci.* **2006**, *280*, 969–982, doi:10.1016/j.memsci.2006.03.029.
 122. Laborie, S. Approche intégrée du dessalement d’eau de mer : Distillation membranaire sous vide pour la réduction des rejets salins et possibilités de couplage avec l’énergie solaire Available online: <http://www.theses.fr/146662520> (accessed on Apr 22, 2018).
 123. Ducom, G.; Puech, F. P.; Cabassud, C. Air sparging with flat sheet nanofiltration: a link between wall shear stresses and flux enhancement. *Desalination* **2002**, *145*, 97–102, doi:10.1016/S0011-9164(02)00392-2.
 124. Yamanoi, I.; Kageyama, K. Evaluation of bubble flow properties between flat sheet membranes in membrane bioreactor. *J. Membr. Sci.* **2010**, *360*, 102–108, doi:10.1016/j.memsci.2010.05.006.
 125. Couvert, A.; Bastoul, D.; Roustan, M.; Line, A.; Chatellier, P. Prediction of liquid velocity and gas hold-up in rectangular air-lift reactors of different scales. *Chem. Eng. Process. Process Intensif.* **2001**, *40*, 113–119, doi:10.1016/S0255-2701(00)00130-6.
 126. Ducom, G. *Etude de procédés hybrides pour la nanofiltration de macroémulsions : couplage avec une déstabilisation chimique et avec un écoulement gaz / liquide*; Toulouse, INSA, 2001;
 127. Liu, N.; Zhang, Q.; Chin, G.-L.; Ong, E.-H.; Lou, J.; Kang, C.-W.; Liu, W.; Jordan, E. Experimental investigation of hydrodynamic behavior in a real membrane bio-reactor unit. *J. Membr. Sci.* **2010**, *353*, 122–134, doi:10.1016/j.memsci.2010.02.042.
 128. Liu, R.; Huang, X.; Wang, C.; Chen, L.; Qian, Y. Study on hydraulic characteristics in a submerged membrane bioreactor process. *Process Biochem.* **2000**, *36*, 249–254, doi:10.1016/S0032-9592(00)00210-7.
 129. Liu, R.; Huang, X.; Sun, Y. F.; Qian, Y. Hydrodynamic effect on sludge accumulation over membrane surfaces in a submerged membrane bioreactor. *Process Biochem.* **2003**, *39*, 157–163, doi:10.1016/S0032-9592(03)00022-0.
 130. Liu, X.; Wang, Y.; Waite, T. D.; Leslie, G. Numerical simulation of bubble induced shear in membrane bioreactors: Effects of mixed liquor rheology and membrane configuration. *Water Res.* **2015**, *75*, 131–145, doi:10.1016/j.watres.2015.02.009.
 131. Yan, X.; Xiao, K.; Liang, S.; Lei, T.; Liang, P.; Xue, T.; Yu, K.; Guan, J.; Huang, X. Hydraulic optimization of membrane bioreactor via baffle modification using computational fluid dynamics. *Bioresour. Technol.* **2015**, *175*, 633–637, doi:10.1016/j.biortech.2014.10.133.
 132. Yan, X.; Wu, Q.; Sun, J.; Liang, P.; Zhang, X.; Xiao, K.; Huang, X. Hydrodynamic optimization of membrane bioreactor by horizontal geometry modification using computational fluid dynamics. *Bioresour. Technol.* **2016**, *200*, 328–334, doi:10.1016/j.biortech.2015.10.050.
 133. Freitas, C.; Teixeira, J. A. Hydrodynamic studies in an airlift reactor with an enlarged degassing zone. *Bioprocess Eng.* **1998**, *18*, 267–279, doi:10.1007/s004490050441.

134. Cahyadi, A.; Fane, A. G.; Chew, J. W. Correlating the hydrodynamics of fluidized media with the extent of membrane fouling mitigation: Effect of bidisperse GAC mixtures. *Sep. Purif. Technol.* **2018**, *192*, 309–321, doi:10.1016/j.seppur.2017.10.019.
135. Klein, J.; Vicente, A. A.; Teixeira, J. A. Hydrodynamics of a Three-phase Airlift Reactor with an Enlarged Separator — Application to High Cell Density Systems. *Can. J. Chem. Eng.* **2003**, *81*, 433–443, doi:10.1002/cjce.5450810314.
136. Lu, W.-J.; Hwang, S.-J.; Chang, C.-M. Liquid velocity and gas holdup in three-phase internal loop airlift reactors with low-density particles. *Chem. Eng. Sci.* **1995**, *50*, 1301–1310, doi:10.1016/0009-2509(95)98842-3.
137. Ojha, A.; Al Dahhan, M. Investigation of local gas holdup and bubble dynamics using four-point optical probe technique in a split-cylinder airlift reactor. *Int. J. Multiph. Flow* **2018**, *102*, 1–15, doi:10.1016/j.ijmultiphaseflow.2017.12.001.
138. Kramers, H.; Baars, G. M.; Knoll, W. H. A comparative study on the rate of mixing in stirred tanks. *Chem. Eng. Sci.* **1953**, *2*, 35–42, doi:10.1016/0009-2509(53)80006-0.
139. Ascanio, G. Mixing time in stirred vessels: A review of experimental techniques. *Chin. J. Chem. Eng.* **2015**, *23*, 1065–1076, doi:10.1016/j.cjche.2014.10.022.
140. Behin, J. Modeling of modified airlift loop reactor with a concentric double-draft tube. *Chem. Eng. Res. Des.* **2010**, *88*, 919–927, doi:10.1016/j.cherd.2010.01.004.
141. Behin, J.; Farhadian, N. Residence time distribution measurements in a two dimensional rectangular airlift reactor by digital image processing. *Exp. Therm. Fluid Sci.* **2013**, *51*, 244–250, doi:10.1016/j.expthermflusci.2013.08.004.
142. Sanchez miron; Ceron Garcia; Garcia Camacho; Molina Grima; Chisti Mixing in Bubble Column and Airlift Reactors - Semantic Scholar Available online: /paper/Mixing-in-Bubble-Column-and-Airlift-Reactors-S%3%A1nchez/b0597b6dca109c1453f78e287a3166a86356596c (accessed on Apr 1, 2018).
143. Rahman-Al Ezzi, A. A.; Najmuldeen, G. F. Gas Hold-Up, Mixing Time and Circulation Time in Internal Loop Airlift Bubble Column - PDF Available online: <http://sciencedocbox.com/Chemistry/67874774-Gas-hold-up-mixing-time-and-circulation-time-in-internal-loop-airlift-bubble-column.html> (accessed on Mar 1, 2018).
144. Čurlin, M.; Matić, M.; Matošić, M.; Mijatović, I.; Kurtanjek, Ž. Effects of hydraulic residence time and mixing on wastewater treatment in a membrane bioreactor. *Chem. Biochem. Engineering Quarterly* **2004**, *18*, 97–104.
145. Xu, Z.; Yu, J. Hydrodynamics and mass transfer in a novel multi-airlifting membrane bioreactor. *Chem. Eng. Sci.* **2008**, *63*, 1941–1949, doi:10.1016/j.ces.2007.12.026.
146. Bando, Y.; Hayakawa, H.; Nishimura, M. Effects of Equipment Dimensions on Liquid Mixing Time of Bubble Column with Draft Tube. *J. Chem. Eng. Jpn.* **1998**, *31*, 765–770, doi:10.1252/jcej.31.765.
147. Levenspiel, O. *Chemical Reaction Engineering*; Third.; John Wiley & Sons: Department of Chemical Engineering, Oregon State University, 1999; ISBN 0-471-25424-X.
148. Wang, Y.; Sanly; Brannock, M.; Leslie, G. Diagnosis of membrane bioreactor performance through residence time distribution measurements — a preliminary study. *Desalination* **2009**, *236*, 120–126, doi:10.1016/j.desal.2007.10.058.
149. Wang, Y.; Ong, K. W.; Brannock, M. W. D.; Leslie, G. L. Evaluation of membrane bioreactor performance via residence time distribution: effects of membrane configuration and mixing. *Water Sci. Technol. J. Int. Assoc. Water Pollut. Res.* **2008**, *57*, 353–359, doi:10.2166/wst.2008.114.
150. Brannock, M. W. D.; Wang, Y.; Leslie, G. Evaluation of full-scale membrane bioreactor mixing performance and the effect of membrane configuration. *J. Membr. Sci.* **2010**, *350*, 101–108, doi:10.1016/j.memsci.2009.12.016.
151. Gavrilescu, M.; Tudose, R. Z. Residence time distribution of liquid phase in an external-loop airlift bioreactor. *Bioprocess Eng.* **1996**, *14*, 183–193, doi:10.1007/BF01464733.
152. Wilke, C. R.; Chang, P. Correlation of diffusion coefficients in dilute solutions. *AIChE J.* **1**, 264–270, doi:10.1002/aic.690010222.
153. Cussler, E. L. *Diffusion: Mass Transfer in Fluid Systems*; Cambridge University Press, 2009; ISBN 978-0-521-87121-1.
154. Ravn, L.; Christensen, A. B.; Molin, S.; Givskov, M.; Gram, L. Methods for detecting acylated homoserine lactones produced by Gram-negative bacteria and their application in studies of AHL-production kinetics. *J. Microbiol. Methods* **2001**, *44*, 239–251, doi:10.1016/S0167-7012(01)00217-2.
155. Furusawa, T.; Smith, J. M. Fluid-Particle and Intraparticle Mass Transport Rates in Slurries. **1973**.
156. Dotto, G. L.; Buriol, C.; Pinto, L. A. A. Diffusional mass transfer model for the adsorption of food dyes on chitosan films. *Chem. Eng. Res. Des.* **2014**, *92*, 2324–2332, doi:10.1016/j.cherd.2014.03.013.
157. SUN, L.-M.; MEUNIER, F.; BRODU, N.; MANERO, M.-H. Adsorption - Aspects théoriques. *Ref TIP452WEB - Opérations Unit. Génie Réaction Chim.* **2016**.

158. Dotto, G. L.; Moura, J. M.; Cadaval, T. R. S.; Pinto, L. A. A. Application of chitosan films for the removal of food dyes from aqueous solutions by adsorption. *Chem. Eng. J.* **2013**, *214*, 8–16, doi:10.1016/j.cej.2012.10.027.
159. Sanger, P.; Deckwer, W.-D. Liquid—Solid Mass Transfer in Aerated Suspensions. *Chem. Eng. J.* **1981**, *22*, 179–186, doi:10.1016/0300-9467(81)80013-5.
160. Noyes, A. A.; Whitney, W. R. THE RATE OF SOLUTION OF SOLID SUBSTANCES IN THEIR OWN SOLUTIONS. *J. Am. Chem. Soc.* **1897**, *19*, 930–934, doi:10.1021/ja02086a003.
161. Wu, F.-C.; Tseng, R.-L.; Huang, S.-C.; Juang, R.-S. Characteristics of pseudo-second-order kinetic model for liquid-phase adsorption: A mini-review. *Chem. Eng. J.* **2009**, *151*, 1–9, doi:10.1016/j.cej.2009.02.024.
162. Bong, Y. Solid-liquid mass transfer in agitated vessels with high solids concentration, School of Civil, Environmental and Chemical Engineering RMIT University: Melbourne, Australia, 2013.
163. Parsek, M. R.; Val, D. L.; Hanzelka, B. L.; Cronan, J. E.; Greenberg, E. P. Acyl homoserine-lactone quorum-sensing signal generation. *Proc. Natl. Acad. Sci.* **1999**, *96*, 4360–4365, doi:10.1073/pnas.96.8.4360.
164. Wang, J.; Quan, C.; Wang, X.; Zhao, P.; Fan, S. Extraction, purification and identification of bacterial signal molecules based on N-acyl homoserine lactones. *Microb. Biotechnol.* **2011**, *4*, 479–490, doi:10.1111/j.1751-7915.2010.00197.x.